

**I. OPTIMIZATION OF INTERDIGITATED BACK CONTACT SILICON  
HETERO-JUNCTION (IBC-SHJ) SOLAR CELL FABRICATION PROCESS;  
II. PASSIVE TUNING OF OPTICAL COUPLERS**

by

Ugochukwu J. Nsofor

A dissertation submitted to the Faculty of the University of Delaware in partial fulfillment of the requirements for the degree of Doctor of Philosophy in Electrical & Computer Engineering

Winter 2019

© 2019 Ugochukwu J. Nsofor  
All Rights Reserved

**I. OPTIMIZATION OF INTERDIGITATED BACK CONTACT SILICON  
HETERO-JUNCTION (IBC-SHJ) SOLAR CELL FABRICATION PROCESS;  
II. PASSIVE TUNING OF OPTICAL COUPLERS**

by

Ugochukwu J. Nsofor

Approved: \_\_\_\_\_

Kenneth E. Barner, Ph.D.  
Chair of the Department of Electrical & Computer Engineering

Approved: \_\_\_\_\_

Levi T. Thompson, Ph.D.  
Dean of the College of Engineering

Approved: \_\_\_\_\_

Douglas J. Doren, Ph.D.  
Interim Vice Provost for Graduate and Professional Education

I certify that I have read this dissertation and that in my opinion it meets the academic and professional standard required by the University as a dissertation for the degree of Doctor of Philosophy.

Signed:

---

Steven S. Hegedus, Ph.D.  
Professor in charge of dissertation

I certify that I have read this dissertation and that in my opinion it meets the academic and professional standard required by the University as a dissertation for the degree of Doctor of Philosophy.

Signed:

---

Shouyuan Shi, Ph.D.  
Member of dissertation committee

I certify that I have read this dissertation and that in my opinion it meets the academic and professional standard required by the University as a dissertation for the degree of Doctor of Philosophy.

Signed:

---

Robert L. Opila, Ph.D.  
Member of dissertation committee

I certify that I have read this dissertation and that in my opinion it meets the academic and professional standard required by the University as a dissertation for the degree of Doctor of Philosophy.

Signed:

---

Ujjwal K. Das, Ph.D.  
Member of dissertation committee

## **ACKNOWLEDGMENTS**

I wish to acknowledge the grace of God that has preserved and sustained me through the many challenges, twists and turns of the past 5.5 years, and the rigors of graduate study. Looking back, I am quite astonished at the many accomplishments I have attained courtesy of His grace and mercy.

I wish to extend a profound gratitude to my advisor, Dr. Steven S. Hegedus for the opportunity to work and complete my PhD research at the Institute of Energy Conversion (IEC). I appreciate the confidence and trust you conferred on me all through my time at IEC. Your knowledge, style of teaching, broader perspectives, experience and personality is a rare combination to find. I appreciate all the avenues you created for easy access to you and for knowledge sharing. In the same vein, I would also like to specially thank Dr. Ujjwal Das who worked side by side with me during my research work. I am grateful for the valuable time you spent with me during training, trouble shooting and planning experiments. Your vast knowledge and humble approach to problem solving is truly remarkable. Special thanks to Dr. Shouyuan Shi for guiding my research on directional couplers and agreeing to be on my doctoral committee. Many thanks to Dr. Robert Opila for graciously agreeing to be on my committee despite many other engagements and for the inputs on my XPS study. I appreciate the kind personalities and the enormous talents of the staffs at IEC that provided me the opportunity of improving myself immensely. I appreciate the time Dr. Kevin Dobson, Wayne Buchanan, Shannon Fields, Christopher Thompson, Brian McCandless, Gregory Hanket, Sharon Stewart, Dr. William Shafarman and Dr. Robert

Birkmire spent directly or indirectly in assisting me with details of my research. Thank you for creating and promoting a nurturing environment that allowed me to thrive effortlessly during my time at IEC.

I wish to express my deepest gratitude to my family – immediate and extended, for the love and support. My lovely wife Ada Josephine Nsofor, my adorable son Obichukwu Jason Nsofor, my parents Nze Wilfred and Lolo Louisa E.O. Nsofor, my siblings Dr. Chinedu Nsofor, Engr. Uchenna Nsofor, Ifeoma Nsofor Eze, Chibuzor Nsofor, Chigozie Nsofor, my sisters in-law Blessing Nsofor and Esther Nsofor, my brother in-law Emeka Eze, my nieces Tochukwu Nsofor, Chimamanda Nsofor and my nephews Somtochukwu Eze and Chiemezie Nsofor. Your presence in my life continues to stir and motivate me to become the best version of myself. Your prayers and good wishes towards me are greatly appreciated. I also wish to appreciate Dr. and Dr. (Mrs.) Aloysius Onwuka and family for the hospitality and love you expressed towards me each time I visited and for making your home a place of solace for me.

Permit me to thank all the faculty that took turns to lecture and mentor me during the course of this program – Dr. Steven Hegedus, Dr. Dennis Prather, Dr. Daniel Weile, Dr. James Kolodzey, Dr. Michael Hochberg, Dr. Keith Goosen, Dr. Jones Scott, Dr. John Rabolt, Dr. Robert Hunsperger, Dr. Kenneth Lutz, Dr. Janusz Murakowski, Dr. Gareth Schneider and Adj. Prof David Young.

My time here would not have been possible if not for the kind and loving community of family and friends that encouraged and supported me. Worthy of mention are Mr. Sanni and Pastor Temitope Ibrahim – Nwannedinamba, The Curran family who made their home my home - Sean, Dennis, Susie, Cathy, Aidan and Seth; Jamie and Tina King, Dr. Wilson Khaemba, Dr. Francis and Beatrice Tannian; Dr.

Okechukwu Ogbuu, Dr. Uwadiae Obahiagbon, Martins Ezuma, Kenechukwu Uzo, Kingsley Ezeanaka and Patrick Ihejirika – my brothers in the struggle, Dr. Olufemi Bolarinwa, Tosan Omatsola and Dr. Olufemi Akanbi who went out of their way to support me morally and financially while I was applying to grad schools, Rosemarie McDonald – my Jamaican mom, Alex Mwale and Ian Johnstone – my friends from another mother, St. Thomas Moore Oratory Family, Potter’s House Family, the Black Graduate Students Association (BGSA), Office of International Students and Scholars (OISS) and my fellow graduate student ambassadors.

### **Special Acknowledgement**

This material is based upon work supported by the US Department of Energy’s Office of Energy Efficiency and Renewable Energy (EERE) under Solar Energy Technologies Office (SETO) Agreement Number DE-EE0007534, and the Air Force Office of Scientific Research (AFOSR) Award Number FA9550-14-1-0198. Neither the United States Government nor any agency thereof, nor any of their employees, makes any warranty, expressed or implied, or assumes any legal liability or responsibility for the accuracy, completeness, or usefulness of any information, apparatus, product, or process disclosed, or represents that its use would not infringe privately owned rights. Reference herein to any specific commercial product, process, or service by trade name, trademark, manufacturer, or otherwise does not necessarily constitute or imply its endorsement, recommendation, or favoring by the United States Government or any agency thereof. The views, opinions, and/or findings contained in this manuscript are those of the author and should not be interpreted as representing the official views or policies, either expressed or implied, of the United States Government or any agency thereof.

## TABLE OF CONTENTS

LIST OF TABLES .....	xi
LIST OF FIGURES .....	xiii
ABSTRACT .....	xxiii

### Chapter

1	INTRODUCTION .....	1
1.1	Overview of Solar Radiation .....	5
1.2	Solar Cell Technology .....	8
1.2.1	Crystalline Silicon Solar Cell Operating Principles .....	9
1.2.1.1	Homojunction Cells .....	10
1.2.1.2	Heterojunction Cells .....	12
1.3	High Efficiency Crystalline Silicon Architecture .....	13
1.3.1	Homojunction with Both Side Contact .....	14
1.3.2	Heterojunction with Both Side Contact .....	14
1.3.3	Homojunction with Back Side Contact .....	14
1.3.4	Heterojunction with Back Side Contact .....	15
1.4	Research Motivation and Objectives .....	16
1.4.1	Optimization of SHJ and IBC-SHJ solar cell fabrication .....	16
1.4.2	Passive Tuning of Optical Couplers .....	17
1.5	Dissertation Outline .....	18
2	EXPERIMENTAL TECHNIQUES .....	20
2.1	Device Fabrication .....	20
2.1.1	Plasma Enhance Chemical Vapor Deposition (PECVD) .....	21
2.1.2	Physical Vapor Deposition (PVD) .....	24
2.1.3	Photolithography .....	26
2.1.4	Wet and Dry Etch .....	28

2.1.5	Laser Processing for Dicing, Contact Formation and Isolation ..	30
2.2	Material Characterization .....	32
2.2.1	Optical Characterization .....	32
2.2.1.1	Ultraviolet-Visible Spectrophotometry (UV-VIS) .....	32
2.2.1.2	Variable Angle Spectroscopic Ellipsometry (VASE) ..	33
2.2.1.3	Fourier Transform Infrared (FTIR) .....	36
2.2.1.4	Raman Spectroscopy .....	39
2.2.1.5	X-ray Photoelectron Spectroscopy (XPS) .....	41
2.2.1.6	Optical and Scanning Electron Microscopy .....	45
2.2.1.7	Optical Emission Spectroscopy (OES).....	48
2.2.2	Electrical Characterization .....	49
2.2.2.1	Effective Minority Carrier Lifetime Measurement .....	49
2.2.2.2	Current-Voltage (J-V) Characterization .....	52
2.2.2.3	Diode Analysis .....	55
2.2.2.4	Quantum Efficiency Analysis and Spectral Response ..	58
2.2.2.5	Temperature Dependent Conductivity Measurement...	62
2.3	Summary .....	64
3	ANALYSIS OF SILICON WAFER PREPARATION FOR SOLAR CELL FABRICATION .....	65
3.1	Introduction .....	65
3.2	Sample Preparation.....	66
3.3	Effect of Saw Damage Removal .....	66
3.4	Effective Lifetime with Quinhydrone Methanol Solution .....	68
3.5	Experimental Matrix for Simplifying Wafer Cleaning Steps.....	69
3.6	XPS Analysis of Cleaning Steps .....	71
3.6.1	XPS Analysis after Organic Removal Step (XPS-1).....	72
3.6.2	XPS Analysis after HNA SDE Step (XPS-2).....	73
3.6.3	XPS Analysis after TMAH Texture (XPS-3).....	75
3.7	Effect of TMAH Residue Removal.....	79
3.8	Summary .....	82
4	IMPROVING THE CHEMICAL AND FIELD EFFECT PASSIVATION OF CRYSTALLINE SILICON SOLAR CELL.....	83

4.1	Introduction .....	83
4.2	Optical Emission Spectroscopic (OES) Study of PECVD Plasma Kinetics.....	84
4.3	Hydrogen Plasma Post-Deposition Treatment .....	92
4.4	Bi-Layer Deposition of Intrinsic Amorphous Silicon .....	97
4.5	Reducing Process Dependent Voc and Jsc losses .....	104
4.5.1	Doped Layer Characterization.....	108
4.5.2	Indium Tin Oxide (ITO) Optimization.....	120
4.6	Summary .....	121
5	CELL STRUCTURES AND PERFORMANCE .....	123
5.1	Front Heterojunction (FHJ) Solar Cell.....	123
5.1.1	Front Emitter Junction Passivation.....	124
5.1.2	Doped Layer Optimization .....	127
5.1.3	Improving Light Trapping Scheme .....	129
5.2	Interdigitated Back Contact Silicon Heterojunction (IBC-SHJ) Solar Cell .....	133
5.2.1	Laser Processed IBC Cells .....	134
5.2.1.1	Laser Fired Contact (LFC) .....	135
5.2.1.2	Plasma Masked Laser Process (PMLP).....	141
5.2.1.3	All Laser Process (ALP).....	149
5.2.1.4	Direct Laser Isolation for Patterning Metal Contacts. ....	153
5.2.2	All PECVD-Masked Process (APMP) .....	157
5.3	Summary .....	163
6	PASSIVE TUNING OF OPTICAL COUPLERS FOR DUAL OUTPUT MODULATORS .....	165
6.1	Introduction .....	165
6.2	Ti-indiffused LiNbO <sub>3</sub> Channel Waveguide.....	166
6.3	Electro-optic (EO) Modulation .....	168
6.4	Balance Detection System.....	170
6.5	Directional Couplers.....	172
6.5.1	Design and Fabrication of Directional Couplers .....	173
6.5.2	Addressing Fabrication Tolerance.....	176

6.5.3	Effect of Thin Film Additive Cladding .....	178
6.5.4	Passive Tuning of Optical Couplers .....	182
6.6	Summary .....	183
7	CONCLUSION AND FUTURE PERSPECTIVES .....	185
7.1	Conclusion .....	185
7.2	Future Perspective .....	189
7.2.1	Manufaturable IBC-SHJ Solar Cells .....	189
7.2.2	Tuning of Optical Couplers .....	190
7.3	List of Publications .....	190
7.4	List of Patent Applications .....	192
	REFERENCES .....	193
Appendix		
A	AM1.5 AND AM0 .....	204
B	PECVD GROWTH RATE DEPENDENCE ON PLASMA VOLTAGE .....	206
C	COPYRIGHT FOR PUBLISHED MATERIAL .....	208

## LIST OF TABLES

Table 2.1:	Laser parameters used for laser isolation, direct and indirect laser ablation, and LFC in this study .....	31
Table 2.2:	Scan parameters used for high and low resolution XPS analysis.....	44
Table 3.1:	Cleaning sequences to study the effects of TMAH texturing and TMAH residue removal step [ <sup>63</sup> ].....	79
Table 4.1:	Experimental set up for studying the effect of varying input parameters on plasma transient behavior. Highlighted number represents our standard process conditions. ....	88
Table 4.2:	Process conditions for studying the effect of varying $H_{\alpha}$ conc. and $V_{pl}$ on passivation [ <sup>77</sup> ].....	95
Table 4.3:	Implied Voc from varying plasma voltage condition during hydrogen plasma treatment. Reference sample has i-layer without hydrogen plasma treatment [ <sup>77</sup> ]. ....	97
Table 4.4:	Average $iV_{oc}$ and measured Voc trends from multiple samples after doped layer deposition and metallization.....	105
Table 4.5:	Input parameter variations for p-doped layer study. ....	110
Table 4.6:	Input parameter variations for n-doped layer study. ....	110
Table 4.7:	Activation energies and conductivities for varying p-doped layers. ....	113
Table 4.8:	Activation energies and conductivities for varying n-doped layers. ....	113
Table 4.9:	Microstructure parameters for different p-doped layers.....	116
Table 4.10:	Microstructure parameters for different n-doped layers.....	117
Table 4.11:	P-doped layers ranked according to their conductivity, microstructure parameter and $\Delta V_{oc}$ . ....	119

Table 4.12:	N-doped layers ranked according to their conductivity, microstructure parameter and $\Delta V_{OC}$ .	119
Table 5.1:	2X2 Matrix for cells with SD and ID deposition methods for intrinsic and p-doped a-Si:H layers.	125
Table 5.2:	Measured cell parameters for cells A, B, C and D made from MC1652-02, MC1650-01, MC1657-20 and MC1642-09 respectively.	125
Table 5.3:	Descriptions and measured cell parameters for cells E to J with unique p- and n-doped layer deposition conditions. Initial $iV_{oc}$ before doped layers. All had the new ID i-layer stack on front and back.	127
Table 5.4:	2x2 matrix for light trapping experiment comparing polished vs textured wafers, and front vs both side ITO.	130
Table 5.5:	Descriptions and measured cell parameters for cells K to N with different wafer surface finish and ITO depositions. Cells K to N were made from MC1679:23, 24, 10 and 11 respectively.	131
Table 5.6:	Summary of device iterations geared towards solving process dependent technical difficulties with PMLP structures. These steps have led to over 3-fold improvement in cell efficiency.	148
Table 5.7:	Isolation resistances after patterning of Ni coated samples.	155
Table 5.8:	Isolation resistances after patterning of Ti/Sb/Ni coated samples.	155
Table 5.9:	Summary of IBC structures, outlining their fabrication processes, advantages and challenges. The process steps described here pertain to the rear side, as the front side is the same for all cases.	162
Table 5.10:	Summary of IBC structures, outlining their present conversion efficiencies and primary limitations.	163
Table 6.1:	PECVD growth recipes for index tuning study showing gas flow rates, thicknesses and refractive index for silicon nitride with different silane to ammonia ratios.	180

## LIST OF FIGURES

Figure 1.1:	Global new investment in renewable energy by region, 2017, \$BN [ <sup>6</sup> ]....	2
Figure 1.2:	Trends in U.S. Renewable Energy Generation Technologies [ <sup>3</sup> ].....	3
Figure 1.3:	Nameplate Capacities of Renewable Energy Sources in the U.S. [ <sup>3</sup> ].....	4
Figure 1.4:	Additions and Retirements of U.S. Electricity Generating Capacity in 2016 [ <sup>3</sup> ].....	5
Figure 1.5:	Electromagnetic spectrum of solar radiation. Solar spectrum received above the atmosphere (yellow region) matches that of a black body (an ideal absorber and radiator of energy at all wavelength), while the solar spectrum on the earth surface (red region) is significantly attenuated by the reflection and absorption action of atmospheric greenhouse gases. ....	6
Figure 1.6:	Average annual ground solar energy across the globe showing African and Central America with higher intensities. ....	7
Figure 1.7:	Solar Irradiation across the United States. ....	7
Figure 1.8:	Schematics of a Solar Cell.....	8
Figure 1.9:	Summary of the Operation of Photovoltaic Systems .....	9
Figure 1.10:	Share of photovoltaic (PV) market by technology (2017) [ <sup>3</sup> ]. Si-based cells still represent more than 90% of the market. ....	10
Figure 1.11:	Band diagram of a c-Si p-n homojunction showing the charge gradient in the space charge region (SCR). $E_C$ is the conduction band minimum, $E_V$ is the valence band maximum, $E_F$ is the Fermi level and $qV_{bi}$ (eV) is the built in potential.....	11
Figure 1.12:	Band diagram of a c-Si heterojunction showing the valence band ( $\Delta E_V$ ) and conduction band ( $\Delta E_C$ ) offsets .....	13

Figure 1.13: High conversion efficiency c-Si architectures with their corresponding record efficiencies: a) Homojunction with both side contact [ <sup>10</sup> ], b) Heterojunction with both side contact [ <sup>11</sup> ], c) Homojunction with back side contact [ <sup>12</sup> ] and d) Heterojunction with back side contact [ <sup>13</sup> ].	16
Figure 2.1: Left image - Multi-chamber, plasma-enhanced chemical vapor deposition (MC PECVD) system operated in dc and RF mode and used to grow intrinsic a-Si:H, doped a-Si:H, a-SiNx:H and a-SiC:H films. Right Image - Single-chamber, plasma-enhanced chemical vapor deposition (SC PECVD) system operated in RF mode and used to deposit amorphous dielectric films on optical waveguides.	22
Figure 2.2: Multi-chamber system SCADA for monitoring and operating the system.	23
Figure 2.3: Electron beam (e-beam) evaporation system used for thin film metallization.	25
Figure 2.4: Photolithography schematics showing the different steps involved in pattern transfer using photolithography	27
Figure 2.5: Cross sections of an anisotropic wet etch of silicon with potassium hydroxide (KOH) showing the crystallography etches of silicon along crystal planes {100}, {110} and {111}. The etching creates V-grooves with flat sloping {111}-oriented sidewalls, theta degree from the horizontal plane, an undercut (delta) and {100}-oriented base.	29
Figure 2.6: Schematic of a UV-VIS spectrophotometry [ <sup>36</sup> ]	33
Figure 2.7: Variable Angle Spectroscopic Ellipsometry from J. A. Woollam, complete with Auto-retarder [ <sup>38</sup> ]	35
Figure 2.8: A FTIR Spectroscopy system by Thermo Scientific used for vibrational spectroscopic study.	36
Figure 2.9: A typical Raman spectral for a silicon sample showing TA, LA, LO, TO, Si-H Wagging and Stretching modes, and two-phonon excitation (left graph), De-convoluted TO spectral with three Gaussians showing the crystalline phase at 520 cm <sup>-1</sup> and 510 cm <sup>-1</sup> , and the amorphous phase at 480 cm <sup>-1</sup> (right graph).	40
Figure 2.10: A Thermo Scientific DXR Raman Microscope complete with a 532 nm laser source used for Raman Spectroscopy.	41

Figure 2.11: Schematic diagram illustrating the principle of operation of XPS.....	42
Figure 2.12: A Thermo Scientific K-Alpha <sup>+</sup> Surface Analysis tool used for XPS Analysis. ....	44
Figure 2.13: a) Image and b) working principles of an optical microscopy.....	46
Figure 2.14: Schematics of an SEM showing key components.....	47
Figure 2.15: Schematics showing the three major components of OES illustrating how OES works.....	49
Figure 2.16: Sinton instrument WCT120 lifetime tester used for PCD and QSSPC measurement [ <sup>58</sup> ].....	52
Figure 2.17: Schematic of a four-point probe for J-V measurement.....	53
Figure 2.18: Sample J-V curve showing important cell parameter.....	54
Figure 2.19: Equivalent circuit of a solar cell showing a diode in parallel with a current source. ....	55
Figure 2.20: Light and dark JV characteristics for a well-behaved CIGS device (a) Standard JV (b) shunt characterization, G (c) r(J) with fit used to determine n and R <sub>s</sub> (d) ln(J+J <sub>sc</sub> ) with fit used to determine n and J <sub>0</sub> . [ <sup>62</sup> ] 58	58
Figure 2.21: Sample quantum efficiency diagram of a solar cell.....	59
Figure 2.22: Sample spectral response diagram of a solar cell.....	60
Figure 2.23: Optical setup for QE measurement. A) Light source, B) Filter wheel, C) Monochrometer, D) Light chopper, E) Collimating lens, F) Bias light setup, G) Focusing lens, H) Sample stage. ....	61
Figure 2.24: A Tenney Engineering Inc. enclosure for temperature dependent conductivity measurement, complete with a programmable electrometer, voltage source and channel scanner. ....	63
Figure 3.1: Experimental flow chart for saw damage removal study [ <sup>63</sup> ].....	67
Figure 3.2: Effect of SDE on effective minority carrier lifetime and iV <sub>OC</sub> measurement in quinhydrone methanol solution for: a) samples with KOH SDE and b) samples without KOH SDE. Each data point represents an average of 2 samples [ <sup>63</sup> ]. ....	68

Figure 3.3: Processing sequence for the four batches of samples used for the wafer cleaning/texturing experiment [63].	71
Figure 3.4: XPS-1 Qualitative Survey for Groups 1, 2, 3 and 4 showing peaks for Silicon (2s, 2p and plasmonic peaks), Carbon 1s, Oxygen (1s and Auger KLL peak) and Fluorine 1s.	72
Figure 3.5: XPS survey spectral for group1 condition showing peaks for silicon, carbon, oxygen and fluorine: a) after organic removal step, and b) after HNA SDE [63].	74
Figure 3.6: High-resolution silicon XPS scans for group 2 condition: a) after piranha dips for XPS-1 and b) after HNA SDE for XPS-2 [63].	74
Figure 3.7: a) Chemically polished c-Si surface used for this experiment, b) c-Si surface after TMAH texturing step showing v-grooves and c) Illustration of light trapping scheme.	75
Figure 3.8: Silicon peaks for XPS-3 scans for groups 1- 4 conditions after TMAH texturing step [63].	76
Figure 3.9: XPS-3 Qualitative Survey for Groups 1, 2, 3 and 4 showing high peaks for Silicon (2s at ~145 eV, 2p at ~99 eV), reduced peaks for Carbon 1s (285 eV), Oxygen 1s (~530 eV) and no peak for Fluorine 1s (~688 eV).	76
Figure 3.10: Percentage composition of elemental species (Si, C, O and F) across all four conditions showing their variation with chemical treatment of the silicon samples: a) after XPS-1, b) after XPS-2, and c) after XPS-3 [63].	77
Figure 3.11: $\tau_{\text{eff}}$ and $iV_{\text{OC}}$ for i.a-Si:H passivated surfaces on four different wafer preparation sequences. All processing sequence includes HNA SDE, TMAH texture and TMAH residue removal steps. Error bar shows the range of data from four samples used for lifetime measurement [63].	78
Figure 3.12: Time dependent behavior of $\tau_{\text{eff}}$ from quinhydrone-methanol immersion experiment on the merits of TMAH texturing and TMAH residue removal step [63].	80
Figure 3.13: $\tau_{\text{eff}}$ and $iV_{\text{OC}}$ result from 10 nm i.a-Si:H passivated surfaces of four selected conditions to demonstrate the effect of TMAH residue removal step [63].	81

Figure 4.1: a) OES survey spectral and b) Typical a-Si:H plasma during deposition using a DC plasma. ....	85
Figure 4.2: OES survey spectral showing the effect of electron energy distribution, EED on DC (black and red lines) and RF (blue line) sources on the peak intensity of the plasma species (upper section), and the peak position for Ar used as purge and vent gas (lower section). ....	87
Figure 4.3: OES spectral for varying a) DC current, b) RF power, c) pressure and d) hydrogen dilution ratio, at $T_{\text{sub}}$ of 200 °C. For each parameter variation, other parameters were fixed at 123mA, 1.25 T and H dilution of 2.5. ....	89
Figure 4.4: Parameter combinations to reduce DC plasma transient behavior at $T_{\text{sub}}$ of 200 °C: a) std. i.a-Si:H (ref. condition), b) low plasma current, c) high hydrogen dilution ratio and d) high pressure. ....	90
Figure 4.5: Parameter combinations to increase DC plasma transient behavior at $T_{\text{sub}}$ of 250 °C: a) std. i.a-Si:H (ref. condition), b) high plasma current, c) low hydrogen dilution ratio, and d) low pressure. ....	91
Figure 4.6: Effect of varying a) dc plasma current, b) pressure and c) hydrogen flow, on $H_{\alpha}$ conc. and $V_{\text{pl}}$ [77]. ....	94
Figure 4.7: a) $\tau_{\text{eff}}$ and $iV_{\text{oc}}$ of both side i.a-Si:H passivation samples treated with hydrogen plasma with varying $H_{\alpha}$ conc. and $V_{\text{pl}}$ before thermal annealing. b) Change in $iV_{\text{oc}}$ after thermal annealing as a function of the $V_{\text{pl}}$ during hydrogen plasma treatment [77]. ....	95
Figure 4.8: i.a-Si:H passivation of n-type crystalline silicon surface: a) prior art; b) according to Sanyo patent. ....	99
Figure 4.9: i.a-Si:H passivation of n-type crystalline silicon surface developed at IEC: a) low $V_{\text{pl}}$ LCHP-i in contact with the c-Si surface; b) high $V_{\text{pl}}$ HCLP-i in contact with the c-Si surface. ....	100
Figure 4.10: Variation of $\tau_{\text{eff}}$ and $iV_{\text{oc}}$ with thickness for single deposition, SD (open symbols) and bi-layer deposition, ID (closed symbols), before and after the HPT [86]. Numbers on the x-axis refer to total i-layer thickness in nm. ....	100
Figure 4.11: $E_g$ variation with thickness for SD and ID with and without HPT [86].	102

Figure 4.12: FTIR absorption coefficient spectral for: a) 4 nm SD i.a-Si:H film, b) 12 nm SD i.a-Si:H film and c) 12 nm ID i.a-Si:H film showing improved microstructure properties for ID film [ <sup>86</sup> ]. This trend is consistent for samples with HPT.....	104
Figure 4.13: Variation of microstructure parameter with increasing thickness for SD and ID films after HPT [ <sup>86</sup> ]. .....	104
Figure 4.14: Effective minority carrier lifetime for both-side p, n and i-layer (w/ and w/o HPT) passivation. Dashed line shows the standard reporting condition for the minority carrier density of 1E15.....	106
Figure 4.15: Effective minority carrier lifetime for both side i/p, i/n and i-layer (w/o HPT) passivation.....	107
Figure 4.16: Effective minority carrier lifetime for both side i/p, i/n and i-layer (w/ HPT) passivation. ....	107
Figure 4.17: Current-voltage relationship for a) p-doped layers, and b) n-doped layers, showing straight lines, typical for ohmic conductors, for all doped layer variation studied. ....	112
Figure 4.18: Temperature dependent conductivity plots for a) p-doped layers and b) n-doped layers for all doped layer conditions studied.....	113
Figure 4.19: Infrared spectra for p-doped layers showing: a) Raw; and fitted data for: b) std-p, c) std-p +HPT, d) bi-layer w/incr. H <sub>2</sub> dilution, e) low/high/nc-Si, and f) low V <sub>pl</sub> .....	114
Figure 4.20: Infrared spectra for n-doped layers showing: a) Raw; and fitted data for: b) std-n, c) std-n +HPT, d) bi-layer w/incr. H <sub>2</sub> dilution, e) low/high/nc-Si, and f) low V <sub>pl</sub> .....	115
Figure 4.21: Loss in iVoc after p-i-N-i-p structure different p-doped-layer variance and a reference condition with a single deposited i-layer without HPT.....	118
Figure 5.1: Measured quantum efficiencies for cell A (green), cell B (red), cell C (blue) and cell D (black) showing their respective optical response.....	126
Figure 5.2: Light JV curves for cells E to J. Insert shows cell architecture with front and backside ITO.....	129

Figure 5.3: Light JV curves for cells K to N showing different diode characteristics for FHJ cells on different surface finish and ITO depositions. ....	131
Figure 5.4: External quantum efficiency (EQE) measurement on all 4 cells from Table 5.5. Cells on polished surface show poor short and long wavelength response irrespective of backside ITO due to high front surface reflection and poor internal light trapping. Cells on textured surface show better short wavelength response due to reduced front surface reflection and improved long wavelength response for the cell with backside ITO due to rear contact reflection. ....	133
Figure 5.5: a.) Device architecture for IBC-SHJ with LFC through the n-strip, b.) SEM image of laser spots using 25.5% laser power optimized for LFC. ....	137
Figure 5.6: Light and dark JV curve of an IBC-SHJ solar cell with laser-fired contact through Ti/Sb/Al metal stack (MC1658-05). Insert shows cell parameters. Reported $iV_{oc}$ measured after i-layer passivation. ....	137
Figure 5.7: Changes in (a) $V_{oc}$ and (b) FF of FHJ cells as a function of laser energy delivered per unit area during LFC through n.a-Si:H (red symbols) and a-SiN <sub>x</sub> :H (black symbols) [ <sup>100</sup> ]. ....	139
Figure 5.8: Estimated (a) Ideality factor, $n$ , and (b) recombination current, $J_0$ , for dark JV (blue and black symbols) and light JV (red and orange symbols) for cells with either a-SiN <sub>x</sub> :H (black and orange symbols) or n.a-Si:H (blue and red symbols) rear dielectric layer as a function of $E_A$ [ <sup>100</sup> ]. ....	140
Figure 5.9: Modified IBC-SHJ device structure with the addition of an i.a-Si:H/n.a-Si:H BSF to repel minority carrier around the laser processed area. The device fabrication process involves laser ablation of the i/p.a-Si:H layer, (indicated by red vertical region in the middle of the n region), followed by an a-SiN <sub>x</sub> :H etch (left) and metal deposition to contact the n.a-Si:H layer (right). ....	142
Figure 5.10: Light and dark JV curve of an IBC-SHJ solar cell with PMLP fabrication process (MC1679-02). Insert shows cell parameters. Reported $iV_{oc}$ measured after plasma mask deposition of n- and p-doped layers. ....	144
Figure 5.11: a) Front view and b) back view of the n-strip shadow mask used during PECVD masked deposition. ....	144

Figure 5.12: 3-Terminal front HJ test structure for diagnosing plasma leakage during PECVD masked deposition.....	145
Figure 5.13: Light JV curves for the 3-terminal front HJ test structure with and without HNA etch of plasma leakage films. ....	146
Figure 5.14: Light and dark JV curve of an IBC-SHJ solar cell with PMLP2 fabrication process (MC1699-18). Insert shows cell parameters. Reported $iV_{oc}$ measured after plasma mask deposition of p- and n-doped layers, laser ablation and chemical etching. ....	147
Figure 5.15: Fabrication process-flow for an all laser process (ALP) for making an IBC-SHJ solar cell. ....	151
Figure 5.16: Process flow and final device cross-section for both the ALP and PMLP fabrication sequences. ....	152
Figure 5.17: Test structure for direct laser isolation experiment of Ni and Ti/Sb/Ni stack metal on a well-passivated c-Si surface. ....	154
Figure 5.18: Left: Optical microscopy image of laser ablation region with exposed nitride pattern (blue coloration), Right: SEM image showing complete metal isolation along the laser scribed line with 27% laser power. ....	156
Figure 5.19: PECVD and PVD deposition masks used in making the IBC-SHJ discussed in this section. They are defined on a 150- $\mu\text{m}$ Si wafer using combination of laser patterning and chemical etching. a) n-strip mask, b) p-strip mask, and c) gap mask for metal deposition. ....	158
Figure 5.20: a) Front surface with AR coating and b) rear interdigitated emitter and base pattern of a complete IBC-SHJ cell.....	160
Figure 5.21: Fabrication process flow for an in-situ PECVD mask deposition process for making an IBC-SHJ solar cell. ....	160
Figure 5.22: Light and dark JV curve of an IBC-SHJ solar cell with APMP fabrication process (MC1661-11). Insert shows cell parameters. Reported $iV_{oc}$ measured after plasma mask deposition of nitride, p- and n-doped layers, and chemical etching.....	161
Figure 6.1: a) Patterned titanium stripe on LNB sample before diffusion, b) After titanium-indiffusion, and c) Optical simulation of guided mode in the titanium-indiffused region. ....	167

Figure 6.2:	Index profile across the titanium-diffused region (core) and LiNbO <sub>3</sub> substrate (left). Incident beam of light guided by total internal reflection (TIR) through the core. The core is formed by graded refractive indices in the x- and y-axes corresponding to ordinary and extraordinary axes respectively in a z-cut LiNbO <sub>3</sub> substrate (right). ....	168
Figure 6.3:	Left: Schematic showing the modulation of a beam of light as it passes through a Pockels cell of length, L to which an electric field, E is applied resulting in a $\Delta\phi$ change in phase on the optical beam; Right: Illustration of a phase modulation using an EO modulator in a Mach Zehnder Interferometer (MZI) configuration. ....	170
Figure 6.4:	a) A photonic link with a single receiver detection system where signal mixing is done with a MZI [112], b) Illustration of signal modulation using MZI configuration. ....	171
Figure 6.5:	a) Photonic link with a dual output receiver system where signal mixing is done with a directional coupler [113], b) Illustration of laser RIN cancellation in a balanced detection system. ....	172
Figure 6.6:	Schematic diagram of a directional coupler structure for optical splitting. Lower panels indicate computed cross-sectional mode profiles at the positions indicated by dash lines [102]. ....	173
Figure 6.7:	Beam propagation method showing an illustration of a 3 dB splitting between waveguides with a) 30 $\mu\text{m}$ spacing between output ports, and b) 127 $\mu\text{m}$ spacing between output ports. ....	174
Figure 6.8:	A fiber alignment system with 6 degree of freedom in the X, Y, Z, yaw, pitch and roll axes used for waveguide alignment during optical measurement. ....	175
Figure 6.9:	Experimental (solid) and simulated (dashed) results of directional coupler structures with varying coupling lengths [102]. ....	176
Figure 6.10:	Illustration of improved mode interaction by the addition of a thin film cladding layer [102]. ....	177
Figure 6.11:	Simulated effects of different cladding materials on the change in effective index of the odd and even modes in coupled Ti:LiNbO <sub>3</sub> waveguides [102]. ....	179
Figure 6.12:	Correlation of increasing Si <sub>3</sub> N <sub>4</sub> thickness with change in effective index and coupling length [102]. ....	181

Figure 6.13: Improved coupling observed with increasing $\text{Si}_3\text{N}_4$ cladding layer.....	183
Figure A.1: Spectral distribution of sunlight for space (AM0) and terrestrial (AM1.5G and AM1.5D) applications as estimated by the American Society of Testing and Materials (ASTM).....	205
Figure A.2: Growth rate dependence on plasma voltage for i.a-Si:H deposition. Data was collected for varying deposition conditions over a period of 12 months. ....	207

## ABSTRACT

The commercial dominance of Si solar cells has been driven by progress in their conversion efficiencies coupled with their long-term durability and widespread knowledge-base for making standardized devices. Recent record efficiency Si solar cells have utilized a relatively new device architecture incorporating Si heterojunction (SHJ) – due to their remarkable high open circuit voltage ( $V_{oc}$ ) and low thermal budget. The focus of my research involves the optimization of SHJ fabrication processing to improve conversion efficiency and application to another high efficiency concept – the interdigitated back contact (IBC) structure.

SHJ cells, unlike conventional Si cells made from diffused junctions, have their junctions formed by growing thin-doped and intrinsic amorphous silicon (i.a-Si:H) layers on the silicon surface. Thus, the i.a-Si:H/c-Si interface is an integral part of the junction, which places great emphasis on the purity of the wafer surface. Excellent surface passivation is contingent on a well-prepared surface free from organic contaminants, particles and metallic ions, thus enabling low surface recombination and high open circuit voltage ( $V_{oc}$ ). This work began with a systematic study on the optimal conditions for silicon surface preparation to ensure excellent passivation at the a-Si:H/c-Si interface of SHJ solar cells. X-ray photoelectron spectroscopy (XPS) was utilized to analyze the elemental composition of impurities on the wafer surface. Passivation quality, characterized by effective minority carrier life time ( $\tau_{eff}$ ) and implied  $V_{oc}$  ( $iV_{oc}$ ), was determined using either quinhydrone-methanol solution or ~10 nm of i-a-Si:H deposited using DC plasma process. This study outlines

the critical steps in the cleaning process, supporting a wafer cleaning approach that is concise and repeatable while creating minimal chemical waste.

Excellent passivation at the i.a-Si:H/c-Si interface was achieved using bilayer deposition of i-a-Si:H films with post deposition hydrogen plasma treatment (HPT). Correlation between the hydrogen plasma composition and passivation quality was studied using optical emission spectroscopy (OES) during the PECVD process. Fourier transform infrared (FTIR) and Variable angle spectroscopic ellipsometry (VASE), both non-invasive techniques, were used to characterize the ~10 nm films to evaluate the Si-H bonding and optical properties. Development of bilayer deposition of i-a-Si:H with HPT has led to state-of-the-art  $iV_{oc}$  exceeding 750 mV. Temperature dependent conductivity measurements of several p- and n-doped layers were studied. Deposition conditions at low plasma voltage were found to have better combination of microstructure parameters, conductivities and  $\Delta V_{oc}$ . Improvements from these layers were transferred to Front HJ and IBC-SHJ structures with conversion efficiencies up to 20% and 15.1 % respectively. Challenges and technical difficulties with the IBC-SHJ structures were also highlighted and possible remedies were proffered.

As an additional research focus, my prior work on the design and fabrication of a dual output modulator for balance detection systems is presented and results of developing a novel method to passively tune the splitting ratio of a Ti-diffused lithium niobate ( $LiNbO_3$ ) 3-dB directional coupler by the addition of a silicon-rich nitride cladding material is highlighted. The sensitivity to slight variations in the fabrication process conditions usually presents a challenge to achieving precise and repeatable 3-dB splitting in a directional coupler made of Ti-diffused  $LiNbO_3$  waveguides. In the Mach-Zehnder Interferometer (MZI) modulation configuration used in this work, this

deviation in splitting ratio results in poor extinction ratio and low modulation depth. To mitigate this problem, different techniques that involve changing the effective index of the two waveguides were explored and a new approach involving post-fab trimming was developed.

## **Chapter 1**

### **INTRODUCTION**

Fossil fuels such as natural gas, crude oil and coal have been the main drivers of global energy for decades. However, with steadily increasing world energy demand [1], limited minable years ahead [2] coupled with worldwide agreement to reduce the impact of greenhouse gas emissions, the fossil fuel era is gradually coming to an end. As the need to diversify energy production intensifies, solar energy technologies have emerged as promising candidates to boost renewable energy quota. In 2016, solar PV experienced a 52% increase in installed capacity in the United States and continues to be one of the fastest growing renewable energy sources worldwide [3]. Interest in renewable energy sources such as wind and solar continues to soar with increasing growth of photovoltaic installations [4] and the attainment of grid parity (which occurs when an alternative energy source generates power at a cost that is less or equal to the price of purchasing power from the electricity grid) by a number of countries [5].

The 2018 Global Trends in Renewable Energy Investment report conducted by the Frankfurt School-United Nation Environment Programme (FS-UNEP) for Climate and Sustainable Energy Finance shows a radical shift from fossil fuel to renewable energy sources. The current pace of change in the energy mix can no longer be described as an evolution but a revolution. In 2017 alone, a record 157 gigawatts of renewable power was installed and commissioned worldwide [6]. This is about 10% increase from the 143 GW that was commissioned a year earlier and more than double the 70 GW of new generating capacity for combined fossil fuel. In 2017, worldwide

solar power accounted for about 98 GW, which is roughly 62% of the 157 GW of renewable energy generating capacity commissioned and 38% of the net power capacity coming on stream from combined renewable and fossil fuel. It is anticipated that by 2050, solar photovoltaic systems would take up about 20% share of global energy demand [7]

Enabling this improvement in renewable energy capacity is a surge in investment around the world from China, the United States, Europe, Australia and even many developing countries, most of which show sharp increases in renewable energy investment in 2017. Figure 1.1 shows a representation of the percentage share of global investment in renewable energy deployment in 2017 with China in front as the current world's leading investor in renewable energy.

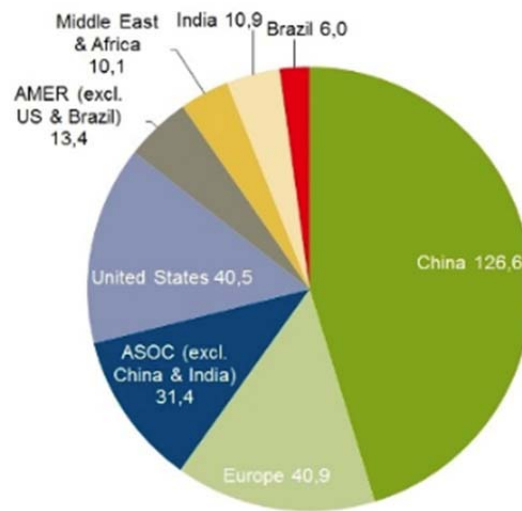


Figure 1.1: Global new investment in renewable energy by region, 2017, \$BN [6]

The Renewable Energy Data Book, published by the U.S. National Renewable Energy Laboratory (NREL) show similar trends in the U.S. as both installed capacity and electricity generation grew by double digits in 2016. The report confirms that 67% of U.S. electricity capacity addition in 2016 came from renewable electricity and for the first time in the U.S, the combined generation from solar and wind exceed that of hydropower [3]. The number of alternative fueling stations increased to more than 27,000 stations, a roughly 18% increase from 2015 numbers.

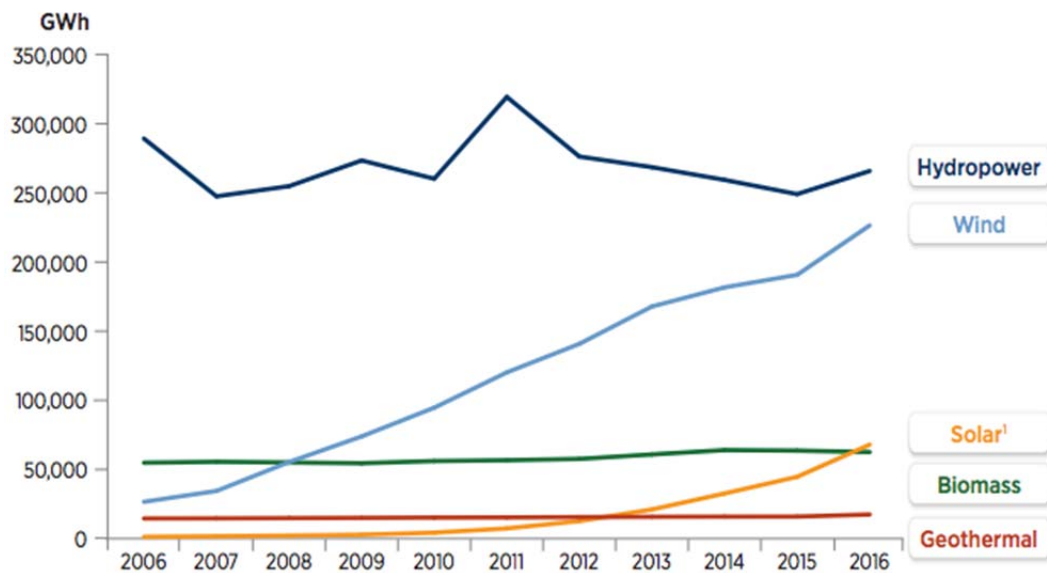


Figure 1.2: Trends in U.S. Renewable Energy Generation Technologies [3]

The last decade has seen marked improvement in renewable energy share in the U.S. with significant increases in photovoltaic and wind energy deployment as shown in Figures 1.2 and 1.3. At the same time there have been significant cut backs and accelerated closure of existing fossil powered plants as depicted in Figure 1.4.

This improvement in renewable energy capacity can be attributed to falling costs and improved reliability of solar power [8], more deployment of wind power and a strong commitment to addressing climate change [6].

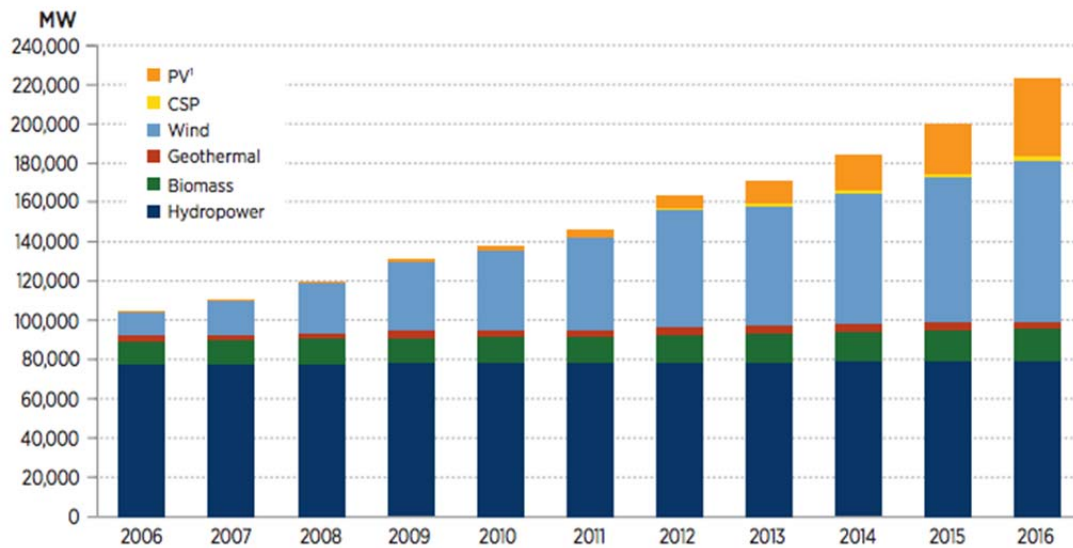


Figure 1.3: Nameplate Capacities of Renewable Energy Sources in the U.S. [3]

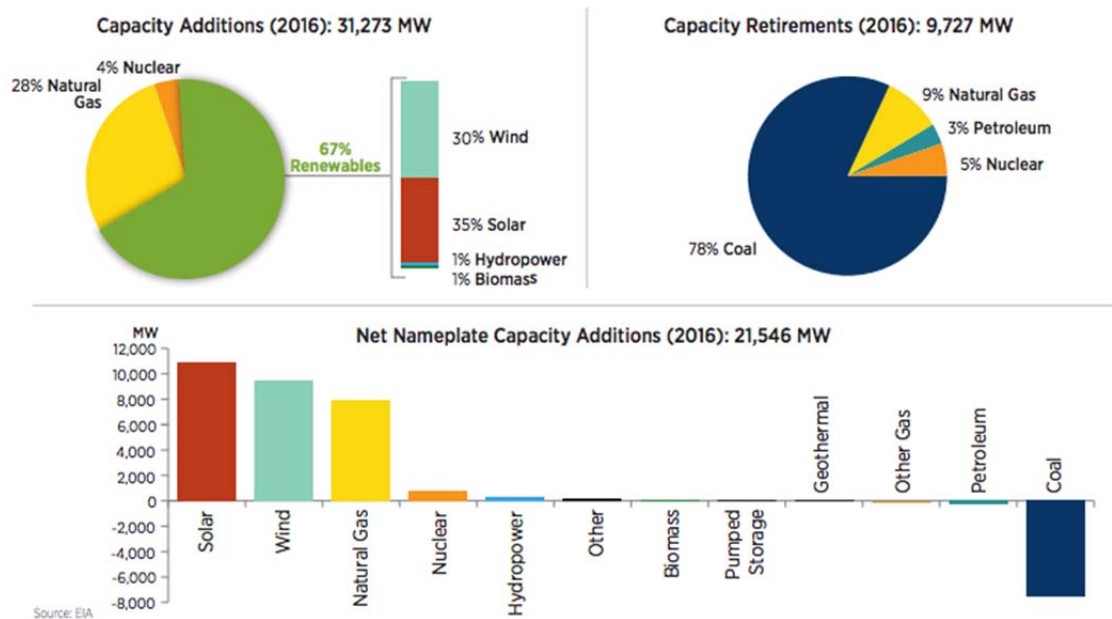


Figure 1.4: Additions and Retirements of U.S. Electricity Generating Capacity in 2016 [3]

In total the world has invested \$2.9 trillion in green energy sources since 2004 with approximately \$280 billion invested in renewables in 2017 alone, with solar power taking a huge portion, at roughly \$160 billion, making it the most funded technology in 2017.

## 1.1 Overview of Solar Radiation

Solar cells are fueled by free solar radiation which is the electromagnetic (EM) energy from the sun, which warms our planet, brightens the day, promotes plant metabolism and acts as one of the primary drivers of our weather. About half of this radiation falls in the visible short-wave portion of the EM spectrum while the other half is in the near infrared or in the ultraviolet portion of the EM spectrum as shown in Figure 1.5. Solar irradiance is the power per unit area (in  $W/m^2$ ) from the sun over a

given wavelength range. When integrated over time gives solar irradiation or insolation (in kWh/m<sup>2</sup>/hr), useful for estimating the amount of available sunlight within an area and for planning the deployment of solar power systems.

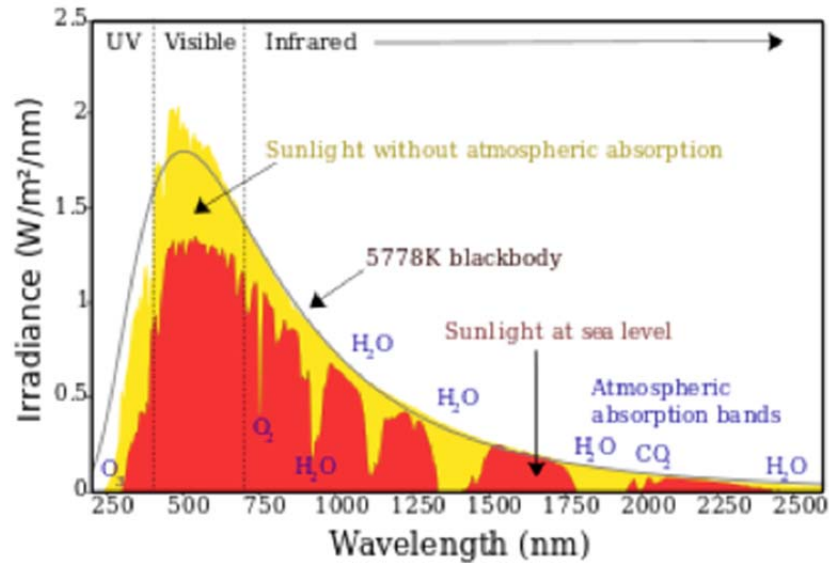


Figure 1.5: Electromagnetic spectrum of solar radiation. Solar spectrum received above the atmosphere (yellow region) matches that of a black body (an ideal absorber and radiator of energy at all wavelength), while the solar spectrum on the earth surface (red region) is significantly attenuated by the reflection and absorption action of atmospheric greenhouse gases.

The average amount of sunlight reaching an area varies with respect to its location on the globe. The average value incident on the earth's surface is about 5.75 kWh/m<sup>2</sup>/day (if we assume 30% of the Sun's energy is lost in the atmosphere and an average of 12 hours sunlight a day). Most countries in African, Central America and Southeast Asia experience above average solar irradiation all year round as depicted in Figure 1.6. However, considering the fraction of radiant light reaching the earth

surface that is required for energy conversion, it is fair to say that solar energy is widely distributed across the globe.

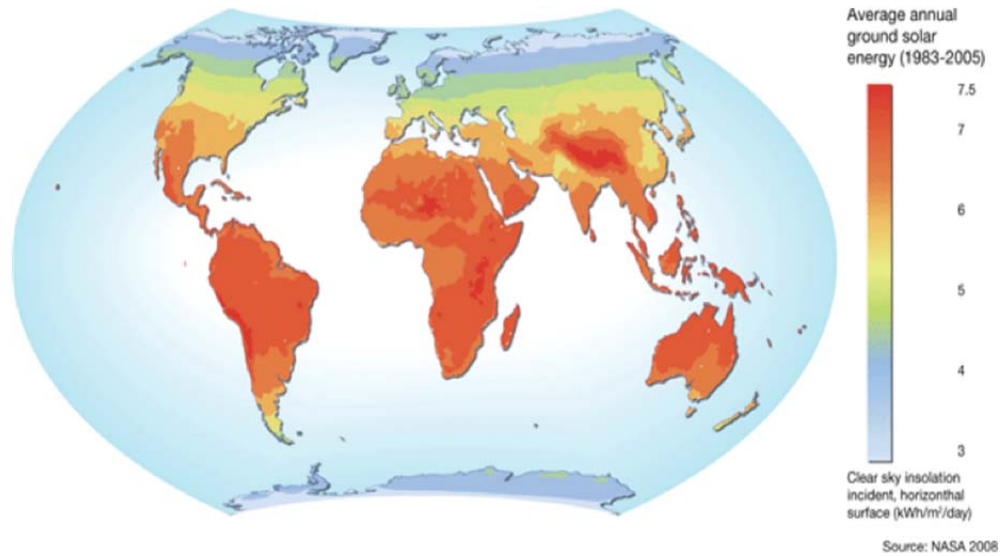


Figure 1.6: Average annual ground solar energy across the globe showing African and Central America with higher intensities.

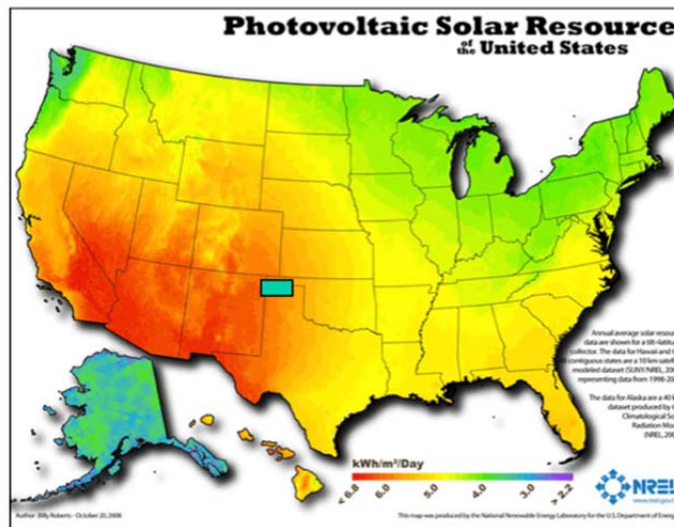


Figure 1.7: Solar Irradiation across the United States.

Take the U.S. for example, an area of land about 11 million acres (the green area NW of Texas in Figure 1.7), roughly  $\sim 0.6\%$  of its land mass and a mere fraction of the state of Texas, is sufficient to generate the annual U.S electricity consumption (4000 TW-hr) using today's photovoltaic system.

Thus, it is easy to see why solar energy is very attractive. Sunlight is free, readily available to all and stupendously abundant. Estimated at over 165,000 TW, solar resources dwarf current and future projections of global power usage. Therefore the ongoing surge in investment, research efforts and deployment is certainly justified. Solar energy is definitely the technology of today and the foreseeable future.

## 1.2 Solar Cell Technology

Solar power is the conversion of radiant light and heat from sunlight into electricity, either directly using photovoltaic (PV) system, indirectly using concentrated thermal solar power, or a combination.

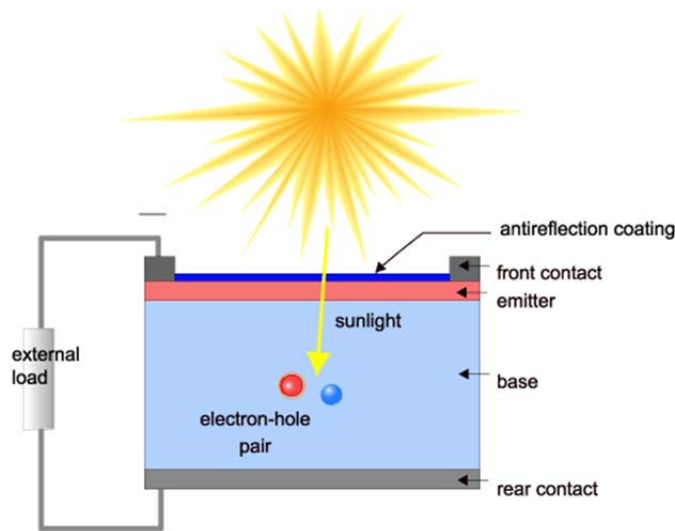


Figure 1.8: Schematics of a Solar Cell

When photons are incident upon and subsequently absorbed by a photovoltaic device, they generate electron-hole pairs, which get separated by an electric field at the junction and collected through respective metal contacts. Figure 1.8 shows a schematic cross section of a solar cell with emitter, base and contacts. The whole process can be summarized in 3 steps – light absorption, carrier generation and carrier collection, as illustrated in Figure 1.9.

***Light Absorption + Carrier Generation + Carrier Collection***

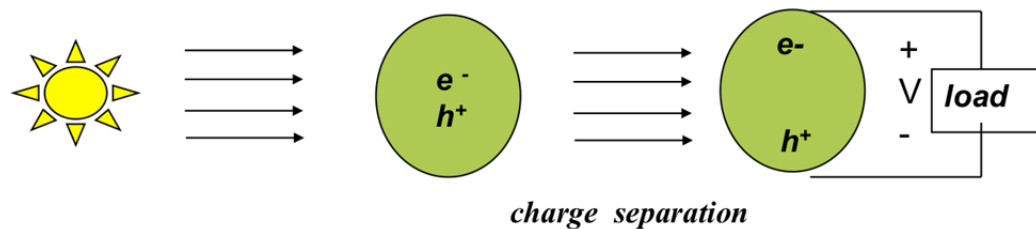


Figure 1.9: Summary of the Operation of Photovoltaic Systems

**1.2.1 Crystalline Silicon Solar Cell Operating Principles**

Silicon is the material of choice for over 90% of the world PV market. It is the second most abundant element in the earth crust; other materials of interest for alternative solar cells are much rarer. It can be easily manufactured to high purity with low structural defects, is durable and chemically stable, its surfaces are easily passivated, and it can be easily doped p- or n-type. Silicon has the highest efficiency for single junction cells and is a matured technology partially owing to its ubiquitous usage in the microelectronics industry and subsequent knowledge base and technology infrastructure. Thus, it is no surprise that of the many materials used for solar cell fabrication, crystalline silicon (c-Si) has had a majority share of the PV market for decades.

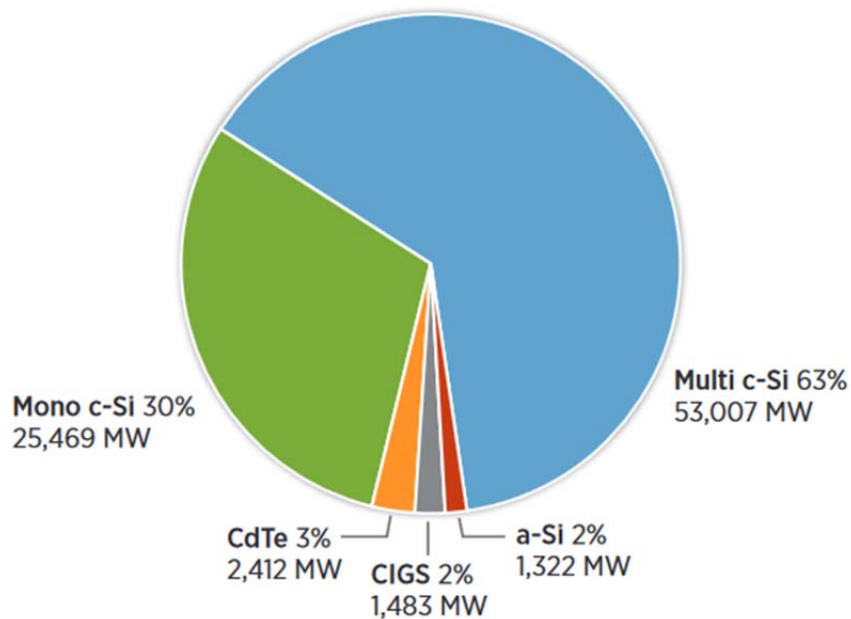


Figure 1.10: Share of photovoltaic (PV) market by technology (2017) [3]. Si-based cells still represent more than 90% of the market.

### 1.2.1.1 Homojunction Cells

Most c-Si solar cells are typically manufactured with a  $\sim 150 \mu\text{m}$  thick boron doped p-type wafer as the base and a  $< 0.2 \mu\text{m}$  phosphorous diffused n-type emitter to form a PN diode. The field effect of the emitter and anti-reflection coating (ARC) from silicon nitride ( $\text{SiN}_x$ ) provides front surface passivation. Contact to the device is made on the front side with screen-printed silver (Ag) grids fired through the  $\text{SiN}_x$  dielectric layer and on the rear side with Aluminum (Al). As the p-type and n-type regions of the diode exist within the same c-Si lattice, this device uses a homojunction to separate charge carriers under illumination. The band diagram of the common p-n homojunction without bias is shown in Figure 1.11.

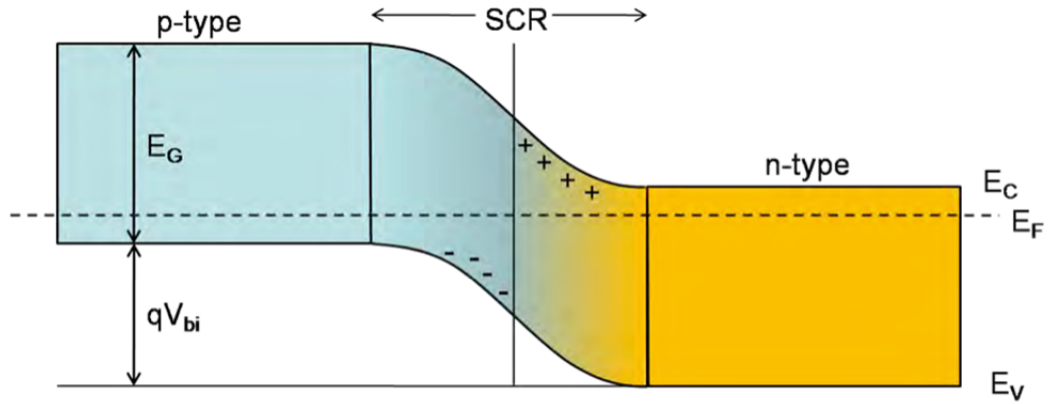


Figure 1.11: Band diagram of a c-Si p-n homojunction showing the charge gradient in the space charge region (SCR).  $E_C$  is the conduction band minimum,  $E_V$  is the valence band maximum,  $E_F$  is the Fermi level and  $qV_{bi}$  (eV) is the built in potential.

When an external circuit is connected to the illuminated cell with a constant voltage  $V$ , current will flow through the cell according to equation 1.1:

$$J = J_o \left[ \exp\left(\frac{qV}{nKT}\right) - 1 \right] - J_{sc} \quad 1.1$$

Where

$$J_o = qN_c N_v \exp\left(\frac{-E_G}{KT}\right) \left( \frac{1}{N_A} \sqrt{\frac{D_n}{\tau_n}} + \frac{1}{N_D} \sqrt{\frac{D_p}{\tau_p}} \right) \quad 1.2$$

And the short circuit current density due to collected photo-carriers is

$$J_{sc} = qG(L_n + L_p) \quad 1.3$$

The current density through the circuit, saturation current density and short circuit current density are denoted as  $J$ ,  $J_o$  and  $J_{sc}$  respectively.  $K$  is Boltzmann's constant,  $T$  is absolute temperature,  $q$  is the charge of an electron,  $N_c$  ( $N_v$ ) is the density of state in the conduction (or valence) band,  $N_A$  ( $N_D$ ) is the density of acceptors (or donors),  $D_n$  ( $D_p$ ) is the diffusivity of electron (or hole) and  $\tau_n$  ( $\tau_p$ ) is the effective lifetime of

electron (or hole). When the cell is operated at open circuit,  $J=0$ , the voltage across the terminal of the cell is termed open circuit voltage and can be derived from Eqn. 1.1 as:

$$V_{OC} = \frac{nKT}{q} \ln \left( \frac{J_{SC}}{J_0} + 1 \right) \quad 1.4$$

Improving the  $V_{OC}$  requires a reduction in the saturation current  $J_0$  according to Eqn. 1.4. As can be seen from Eqn. 1.2, reducing the saturation current can be achieved with an increase in effective lifetime. Improving  $J_{SC}$  on the other hand involves optimization of the front surface optical properties - reducing front surface reflection and absorption at the amorphous silicon layers and the back surface properties – increasing the back surface internal reflection and reducing back surface recombination losses.

### 1.2.1.2 Heterojunction Cells

In a silicon heterojunction (SHJ) structure, the junction is not formed by contact of opposite doping types within the same crystal lattice. Instead, the junction is formed through deposition of thin doped amorphous silicon film of opposite polarity to that of the absorber. Since the junction is formed at the c-Si surface, the wafer purity is critical. A good wafer cleaning step and surface passivation is usually introduced prior to the doped layer passivation to reduce the interface defect density ( $D_{it}$ ). The c-Si wafers used in this work have very good bulk quality with very high bulk lifetime ( $\tau_{eff} > 5$  ms) hence; cell performance is limited by surface recombination. A significant aspect of c-Si solar cell research focuses on improving c-Si surface passivation. A core part of this dissertation will focus on my work on improving surface passivation using very thin (~10 nm thick) hydrogenated intrinsic and doped amorphous silicon layers. The term heterojunction applies since the junction is

between crystalline and amorphous phases, which have a band gap energy difference of approximately 0.7 eV. The band bending resulting from this band offset creates a strong field that repels electrons from recombining at the p-type emitter and holes from recombining at the n-type base contact thus providing a field effect passivation. The current record efficiency single junction cell is a SHJ device with an Interdigitated back contact architecture from Kaneka having cell efficiency record of 26.7 % and a  $V_{oc}$  of 744 mV [9].

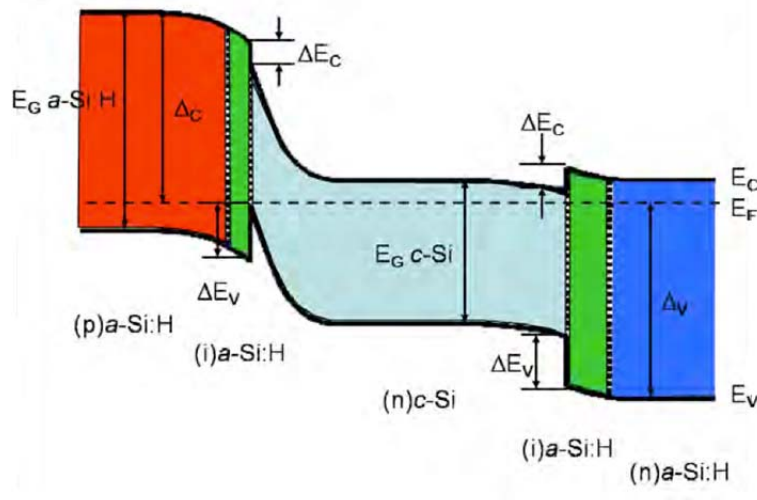


Figure 1.12: Band diagram of a c-Si heterojunction showing the valence band ( $\Delta E_V$ ) and conduction band ( $\Delta E_C$ ) offsets

### 1.3 High Efficiency Crystalline Silicon Architecture

Many different solar cell architectures have been studied over the years in order to achieve high conversion efficiency. I will briefly review four architectures that have led to recent record conversion efficiency. These architectures can be grouped into two categories; i) how the junctions are formed and ii) where and how the p and n metal contacts are formed.

### **1.3.1 Homojunction with Both Side Contact**

This c-Si architecture involves the formation of a PN junction by a high temperature diffusion process as described in section 1.2.1.1. The p and n contacts are formed on either side of the solar cell. Most commercially available c-Si solar cells are made using this architecture because it is a mature and easily manufacturable technology. However, the high thermal budget, shading loss from front surface metal grids and low open circuit voltage due to low valence band offset are undesirable. This architecture is shown in Fig. 1.13 a.

### **1.3.2 Heterojunction with Both Side Contact**

This c-Si architecture involves the formation of a PN heterojunction by growing thin doped amorphous silicon film of opposite polarity to that of the absorber as described in section 1.2.1.2. The heterojunction architecture is very popular due to its high open circuit voltage ( $V_{oc}$ ) emanating from a high valence band offset between the crystalline and amorphous phases of the c-Si/a-Si:H interface. The p and n contacts are formed on either side of the solar cell in this architecture as well. This architecture is more cost effective because the doped layers are deposited usually by low temperature plasma enhanced chemical vapor deposition (PECVD) process. However, they still suffer from shading loss from front surface metal grids. This architecture is shown in Figure 1.13 b.

### **1.3.3 Homojunction with Back Side Contact**

This c-Si architecture combines a very robust technology (the homojunction) with an all back metal contact (the Interdigitated back contact, IBC). The IBC structure helps to eliminate shading loss from front surface metal grid and allows for optimizing of the front surface primarily for optical gains leading to better short circuit

current ( $J_{sc}$ ). This architecture however, still retains some of the undesirable features of the homojunction – high thermal budget and low  $V_{oc}$ . It is depicted in Figure 1.13 c.

#### **1.3.4 Heterojunction with Back Side Contact**

This c-Si cell architecture is the future of high efficiency Si solar cells. It combines the high  $V_{oc}$  of heterojunction architecture with the high  $J_{sc}$  of the IBC structure to improve the overall efficiency of the cell. The three most recent record efficiency Si cell reports have been of this architecture, formally known as IBC silicon heterojunction (IBC-SHJ) [9, 13]. It was first demonstrated by the IEC group at the University of Delaware in 2007 [14]. Despite the demonstrated record efficiency, it is technologically immature and lacks a commercial champion partly due to process complexity. Thus, significant IBC-SHJ research and development has focused on addressing the critical challenge of simplifying the downstream patterning of the p (emitter) and n (base) strip on the backside while maintaining exceptional passivation quality. In the past, photolithography has been used to define the emitter and base contacts with multiple alignments and etch-steps [15]. This, however, results in negative impact on yield and is not considered manufacturable. Currently at IEC, we are investigating the viability of using laser-processing techniques to dope and/or define the emitter and base regions on the backside. This approach will make this architecture more cost effective and manufacturable. IBC-SHJ structure is show in Fig. 1.13 d.

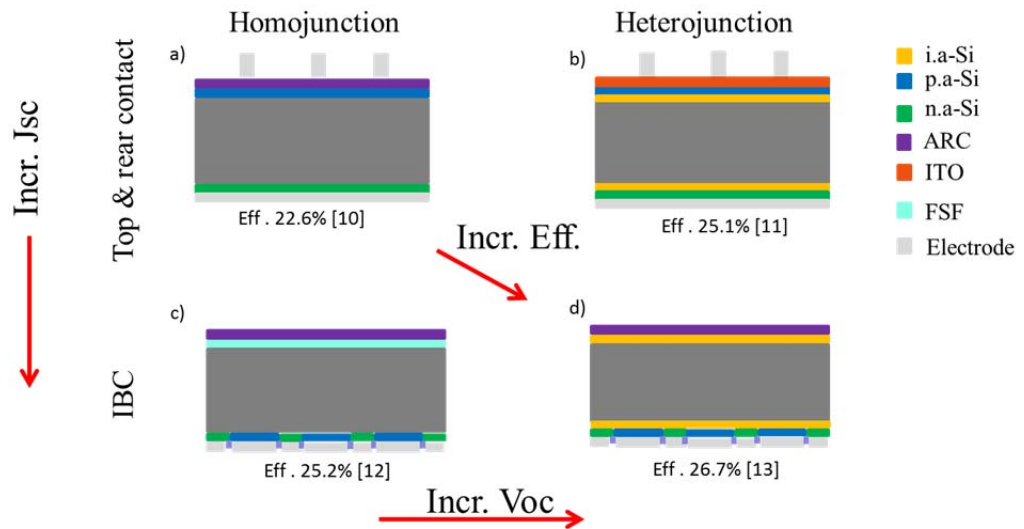


Figure 1.13: High conversion efficiency c-Si architectures with their corresponding record efficiencies: a) Homojunction with both side contact [10], b) Heterojunction with both side contact [11], c) Homojunction with back side contact [12] and d) Heterojunction with back side contact [13].

## 1.4 Research Motivation and Objectives

This section outlines the motivation for the work conducted during my doctoral research and objectives for each aspect of the work.

### 1.4.1 Optimization of SHJ and IBC-SHJ solar cell fabrication

IBC solar cells (Figure 1.13 c) have achieved high efficiency due to their high short circuit current ( $J_{sc}$ ) inherent from the IBC design. It was first developed and commercialized by SunPower who uses conventional diffuse junctions and contact regions, and held the record efficiency of commercial Si solar cell on the market up until 3 years ago. The other high efficiency approach for Si wafer cells is the heterojunction (HJ), which uses ~10 nm layers of hydrogenated intrinsic amorphous silicon to achieve excellent silicon surface passivation and junction formation

resulting in high open circuit voltage (Voc). The HJ cell has been in commercial production for over a decade pioneered by Sanyo (now acquired by Panasonic and Tesla) and recently also Sunpreme and others. The value of integrating these two technologies for making high efficiency IBC-SHJ cell have been proposed and demonstrated previously [14]. However, after nearly a decade of research and development on IBC-SHJ cells, there is yet to be a commercial product or demonstration of a manufacturable device. The difficulty to rapidly pattern the rear doped regions and contacts without damaging the underlying passivation continues to pose a significant challenge to low cost manufacturing. Traditionally, patterning of Si non-PV devices involves photolithography, which can be relatively benign but is very slow and gives much higher resolution than is needed for PV applications. To address this challenge we have optimized the passivation quality of our standard SHJ cells and combined it with an optimized laser-based patterning process. This allows us to merge the highest efficiency Si solar cell structure (IBC-SHJ) with low cost rapid patterning to enable high efficiency manufacturable cells and module.

To ensure very high Voc and lessen the potential damage to the underlying passivation due to laser processing, we have developed an excellent a-Si:H/ c-Si interface passivation and relatively benign laser steps. Our efforts to improve the Si surface passivation have resulted in methods and techniques that ensure state-of-the-art high-implied Voc (iVoc) comparable to those of record efficiency cells, and excellent chemical and field effect passivation from doped layers.

#### **1.4.2 Passive Tuning of Optical Couplers**

The second section of this dissertation focuses on my earlier work on the design and fabrication of a dual output modulator for balance detection systems.

Ideally, a 3-dB directional coupler splits an incoming optical signal in half and gives equal outputs to both output ports of a directional coupler. However, slight variations in the fabrication process conditions usually present a challenge to achieving precise and repeatable 3-dB splitting in the directional coupler made of Ti-indiffused lithium niobate waveguides. In the Mach-Zehnder Interferometer (MZI) modulators used in this work, this deviation in splitting ratio results in low modulation depth and poor extinction ratio. To allay this problem, different techniques that involve changing the effective index of the two waveguides have been developed. These techniques however are complex and introduce a number of fabrication steps. The motivation in this work was to develop a novel and simple method for controlling the splitting ratio using a post-fab trimming of the splitting ratio by varying the thickness of a cladding layer through etching.

## **1.5 Dissertation Outline**

This dissertation is divided into seven main chapters. Chapter 1 provides an introduction to solar cell technology, history and architectures. It also highlights the motivation and objectives of this research. Chapter 2 gives a description of the many material deposition and characterization techniques used in the design, fabrication and characterization of solar cells and optical couplers. Experimental techniques and device analysis methods for solar cells are also presented in this chapter. Chapter 3 discusses the methodology and critical nature of silicon wafer preparation. It details the systematic study that was carried out in order to determine the optimal condition for silicon surface preparation. The effects of the many solvent and chemical treatment that c-Si undergoes during cleaning were analyzed using x-ray photoelectron spectroscopy. Surface purity and passivation quality were quantified by effective

minority carrier lifetime and implied open circuit voltage, and was used to achieve a simplified wafer cleaning procedure. Chapter 4 highlights the experimental methods we explored to improve the passivation at the crystalline silicon/amorphous silicon (c-Si/a-Si) interface. Optical emission spectroscopy study of the plasma condition was applied, after which other techniques like hydrogen plasma post deposition treatment and bi-layer deposition were shown as viable methods to improve passivation. To minimize the loss in passivation after doped layer deposition, a comprehensive study on doped layer properties is also presented here. Chapter 5 presents result from front heterojunction cells and laser processed IBC-SHJ cells showing how improved surface passivation and processing steps translate to high conversion efficiencies in finished cells. Challenges with laser and shadow mask processed IBC cells and the steps we took to remedy those challenges are also highlighted here. Chapter 6 addresses a different aspect of my research – Passive tuning of optical couplers. The benefits and challenges of a balanced detection system are presented. Directional coupler design and device fabrication steps are then discussed with emphasis on how to balance the splitting ration between both arms of a directional coupler using a cladding material. A 3D finite-difference Eigenmode (FDE) solver (Lumerical) [<sup>16</sup>] was used to investigate the impact of additive cladding layer to the coupling ratio. The properties of different cladding and their effects on the mode profile, loss, and effective indices of the odd and even modes are also presented here. Finally, chapter 7 gives a summary of the dissertation and offers some future perspectives for research and development on both topics – IBC-SHJ and Optical couplers.

## Chapter 2

### EXPERIMENTAL TECHNIQUES

This chapter covers various experimental techniques and methods that were used in the study of this dissertation, including the fabrication techniques for processing silicon and lithium niobate wafers. The material characterization methods used to characterize the electrical and optical properties of the structures, and the device analysis tools used to verify device performance are also discussed.

#### 2.1 Device Fabrication

Various techniques have been developed to fabricate crystalline silicon/amorphous silicon (c-Si/a-Si:H) heterojunction (HJ) solar cells, interdigitated back contact silicon heterojunction (IBC-SHJ) solar cells, Titanium-diffused lithium niobate based waveguides and modulators. Many of these techniques and processes were inherited from the integrated circuit (IC) and microelectronics industry, where they have been used to enable the fabrication of complex devices, structures and systems in micro- and nanometer scale [17, 18]. They include: i) chemical vapor deposition system like the plasma enhanced chemical vapor deposition (PECVD) and hot-wire chemical vapor deposition (HW-CVD), used for growing thin dielectric film like silicon dioxide (SiO<sub>2</sub>), amorphous silicon nitride (a-SiN:H), amorphous silicon carbide films (a-SiC:H), intrinsic and doped amorphous silicon (a-Si:H); ii) Physical vapor deposition methods like evaporation (using electron-beam or thermal source) and sputtering, used for depositing metal contact and transparent conductive oxides; iii) Wet and dry

etch which relies on chemical solutions, vapor phase or plasma-based method to selectively removed materials from a substrate; iv) Photolithography (UV and electron beam) technique used for defining patterns, in IBC-SHJ solar cells and waveguides and v) Laser processing for dicing, contact formation and contact isolation on silicon wafers. These wide ranges of semi-conductor processing techniques were employed in fabricating the SHJ, IBC-SHJ solar cells and optical couplers that are presented in this work. In this chapter, I offer an introduction to these techniques and processes while explaining their significant benefits.

### **2.1.1 Plasma Enhance Chemical Vapor Deposition (PECVD)**

Silicon deposition by CVD was first reported as early as 1909 [<sup>19</sup>] and 1927 [<sup>20</sup>] using hydrogen reduction of tetrachlorosilane ( $\text{SiCl}_4$ ). This was followed by the widespread use of thin silicon films in the electronics industry accelerated by the CVD of Si-based photocells [<sup>21</sup>] and rectifiers [<sup>22</sup>] after World War II. Improvements in CVD have been most rapid when other thin film deposition technologies have proved problematic or inadequate for depositing multiple thin films or when conformal coating of large surface areas is required [<sup>23</sup>]. Despite the various developments in CVD, the major stimulus to the technology was indisputably provided by the rapid development of the microelectronics industry since the mid-1970s, which requires very thin high purity films with accurate control of film uniformity, composition and doping.

Chemical vapor deposition is a vacuum deposition process used for growing high quality thin film on a substrate material by a chemical reaction of vapor-phase precursors. Unlike physical vapor deposition (PVD), which involves the adsorption of

molecular or atomic species on a substrate, the chemical reaction of precursors in CVD takes place in the gas phase and on the substrate [23]. The process is often initiated or supported by plasma (as in plasma-enhanced CVD), heat (Hot-wire CVD) or high frequency radiation such as UV (photo-assisted CVD) [24-26]

In a typical CVD, one or more volatile precursor reacts and/or decomposes in vacuum to produce the desired film on an exposed substrate (wafer surface). By varying the process conditions like temperature, pressure, power density and gas flow rate, CVD can be harnessed to deposit materials in monocrystalline, polycrystalline, amorphous and epitaxial form. A single- and multi-chamber plasma-enhanced CVD that operates in either dc or RF (with frequency of 13.56 MHz) mode were used to deposit high quality a-Si:H and dielectric films for this dissertation.

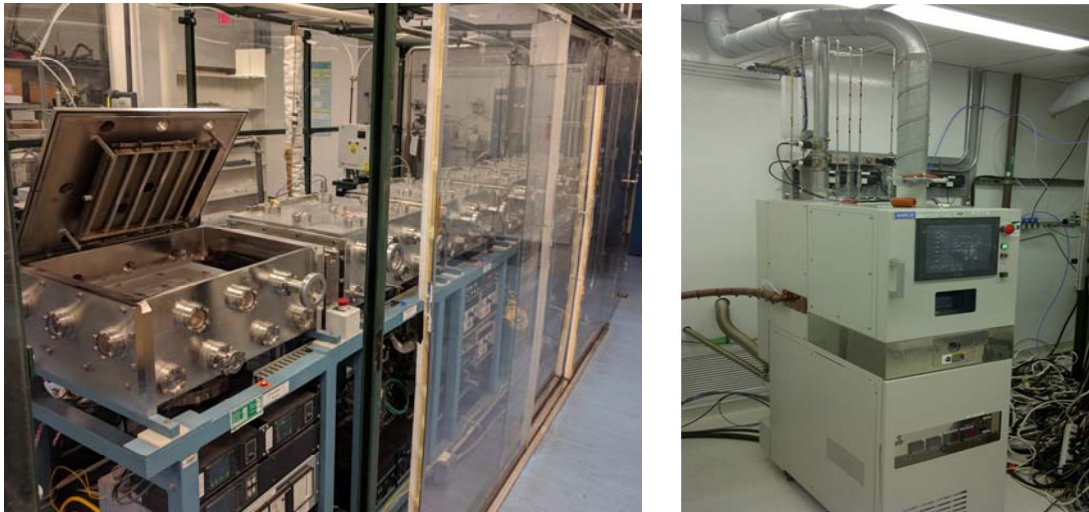


Figure 2.1: Left image - Multi-chamber, plasma-enhanced chemical vapor deposition (MC PECVD) system operated in dc and RF mode and used to grow intrinsic a-Si:H, doped a-Si:H, a-SiN<sub>x</sub>:H and a-SiC:H films. Right Image - Single-chamber, plasma-enhanced chemical vapor deposition (SC PECVD) system operated in RF mode and used to deposit amorphous dielectric films on optical waveguides.

This MC system, shown in Figure 2.1 with four reaction chambers and two load locks, allows us to grow specific film in a dedicated chamber in order to maintain film quality and reduce cross contamination. Substrates are loaded through either of the load locks and transferred between different chambers by gears similar to a commercial production line. A cut out of the MC-system SCADA interface that allows for monitoring and control of the system is shown in Figure 2.2.

In this dissertation, the PE-CVD was mostly used for intrinsic and doped amorphous silicon (i.a-Si:H, n-a-Si:H and p-a-Si:H), silicon nitride (a-SiN:H) and silicon carbide (a-SiC:H) thin film depositions. Silane ( $\text{SiH}_4$ ) and hydrogen ( $\text{H}_2$ ) are used as source gases for intrinsic layers, while diborane ( $\text{B}_2\text{H}_6$ ), phosphine ( $\text{PH}_3$ ), ammonia ( $\text{NH}_3$ ) or methane ( $\text{CH}_4$ ) is added for p-type doping, n-type doping, nitride or carbide respectively.

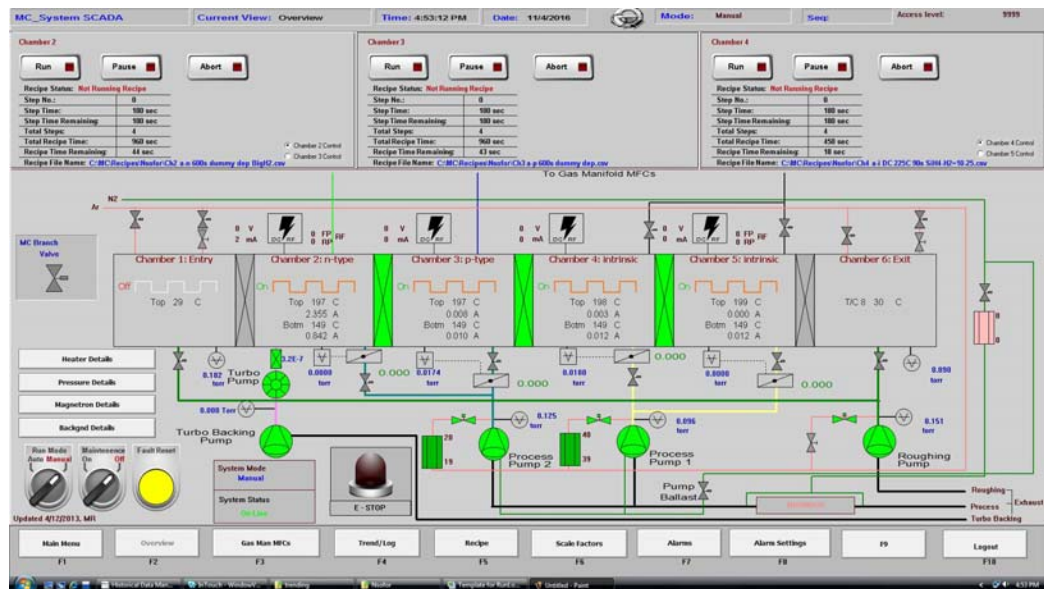


Figure 2.2: Multi-chamber system SCADA for monitoring and operating the system.

### 2.1.2 Physical Vapor Deposition (PVD)

Another category of thin film deposition method is the physical vapor deposition (PVD), which involves a variety of vacuum deposition techniques used to produce metallic thin film and coatings. It typically involves a process in which a material, in the form of an ingot, goes from condensed phase to vapor phase and then back to condensed phase as it coats a substrate. The two most common thin film PVD techniques are evaporation and sputtering. The metal layers of early semiconductor devices were deposited using evaporation technique [27]. While still widely used in research, evaporation has been displaced by sputtering and electroplating in silicon technologies due to the increased need for conformal film deposition and the difficulty to produce well-controlled alloys with evaporation technique.

Evaporation involves heating a source material (using resistive, inductive or electron beam system) inside a high vacuum chamber until it starts to evaporate, producing vapor pressure in the chamber. The evaporated material constitutes a cloud of vapor, which travels freely through vacuum (typically  $\sim 10^{-6}$  Torr) to reach the substrate and coat it as thin films [28]. The evaporator used for metal deposition in this work uses electron beam system. Most kinetic energy of the electrons is transformed into thermal energy as they bombard the surface of the ingot. The increasing surface temperature of the ingot results in the formation of a liquid melt, and consequently causes the material to evaporate under vacuum. The material utilization efficiency of this method is higher than other methods, and it offers more structural and morphological control of films.



Figure 2.3: Electron beam (e-beam) evaporation system used for thin film metallization.

Sputtering on the other hand involves the bombardment of a target material with high-energy particles that are to be deposited on a substrate. The substrates to be coated are placed in a vacuum chamber containing an inert gas – usually Argon – and a negative electric charge is placed on the target material to be deposited causing the plasma in the chamber to glow. Langmuir developed sputtering in the 1920s [29] as a thin film deposition technique. When compared to evaporation, sputtering has better step coverage, induces less radiation damage and much better for producing alloys and compound materials. Several different methods of plasma vapor deposition coating systems are widely used, including ion beam and ion-assisted sputtering, reactive sputtering in an Oxygen gas environment, gas flow and magnetron sputtering [30].

Metal depositions for this dissertation were carried out using an e-beam deposition system shown in Figure 2.3. Here, the electron beam is created by a

filament, and directed and focused by a permanent magnet set onto the target. Samples were loaded onto a sample holder, which can accommodate up to 9 pieces of 1-inch square substrates. A crystal monitor during the deposition monitors the thickness of the film. This system was used for the deposition of aluminum, nickel, silver, titanium and antimony films for solar cell studies, while a similar e-beam evaporation system was used for depositing titanium stripes for optical waveguides. ITO deposition on the other hand was done using a sputtering system from an ITO target using Ar or O<sub>2</sub>-Ar gas mixture.

### **2.1.3 Photolithography**

The use of photolithography in semiconductor has evolved from contact printing (in the early 1960s) through proximity printing to projection printing (from the mid-1970s to today). Photolithography literally means the art of writing on stones with light. It is sometimes referred to as optical lithography or ultraviolet (UV) lithography. It is a process used in micro-fabrication for pattern transfer of parts of a thin film or the bulk of a substrate. The pattern transfer is achieved using light to inscribe a geometric pattern on a photo-mask to a light-sensitive chemical (photoresist) on the substrate. It is the most complicated, expensive and critical process in most microelectronic device processing [<sup>29</sup>]. The resolution (the minimum feature size that can be exposed) of a photolithography system depends on the aligner, which could be either a contact, proximity or projection printer.

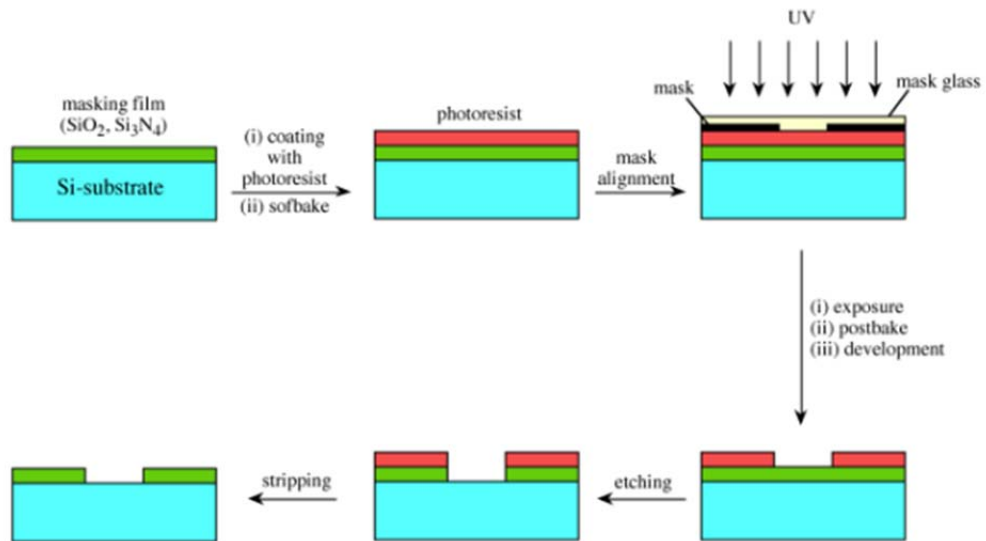


Figure 2.4: Photolithography schematics showing the different steps involved in pattern transfer using photolithography

The photolithography process depicted in Figure 2.4 shows the different steps involved in pattern transfer. The process comprises of the following basic steps:

1. The wafer is uniformly coated with a photoresist using a spinner that is programmed to rotate around 1000-3000 revolutions per minute (rpm). Each photoresist has a specific spinning recipe that determines the final thickness of the photoresist layer.
2. The photoresist is then soft-baked (or pre-baked) to dry the photoresist and remove excess solvent. An unbaked photoresist will lose solvent at room temperature due to evaporation, thereby changing the photoresist composition with time. Thus, the soft bake helps to stabilize the photoresist film.
3. The wafer and mask are aligned using a mask aligner set up and the set up is exposed with UV light through a mask having the desired pattern. In more advanced sub-micron technologies, this mask setup could take the form of a complex optical system.

4. The photoresist is developed using a developer, and the irradiated area (for a positive resist) or the unirradiated area (for a negative resist) is washed away leaving behind the mask pattern on the wafer.

5. The photoresist on the wafer is hard-baked to improve adhesion to the wafer so that it can withstand subsequent processing steps.

After these steps, the sample then undergoes further processing (like wet or dry etch, ion implantation or thin film deposition) wherein the patterned photoresist acts as a protective layer. The remaining photoresist is finally stripped away afterward using a solvent (acetone in our case).

Photolithography was used in this dissertation in defining the titanium stripes, which forms the waveguides and directional couplers. Photolithography process has also been shown as a viable tool for defining the emitter (p-region) and base (n-region) contacts on the rear side of an IBC-SHJ solar cell [31].

#### **2.1.4 Wet and Dry Etch**

After forming a photoresist image on the surface of a wafer, etching is carried out to complete the pattern transfer process. Etching is the chemical removal of materials from a wafer during microfabrication. In most cases the photoresist material is sufficient to act as an etch mask after it is hard baked. In other cases, an etch mask may be required to improve selectivity during etch. Selectivity describes the ability of an etchant to etch a material at a faster rate or in preference to an underlying material. A poorly selective etch removes the top layer, but also attacks the underlying layer, while a highly selective etch leaves the underlying layer intact. Every device manufacturing process involves some form of etch process to effectively transfer patterns to a wafer. An etch could either be isotropic (if it etches uniformly and

produce round sidewalls) or anisotropic (if it etches in one direction and produce vertical sidewalls).

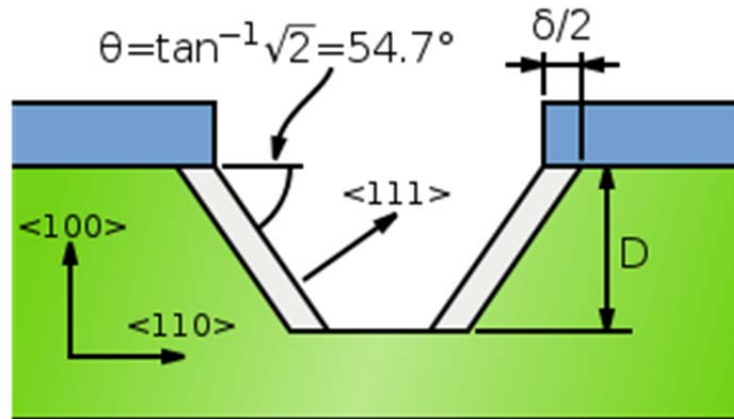


Figure 2.5: Cross sections of an anisotropic wet etch of silicon with potassium hydroxide (KOH) showing the crystallography etches of silicon along crystal planes  $\{100\}$ ,  $\{110\}$  and  $\{111\}$ . The etching creates V-grooves with flat sloping  $\{111\}$ -oriented sidewalls, theta degree from the horizontal plane, an undercut (delta) and  $\{100\}$ -oriented base.

Wet etch typically uses chemical solutions to perform the etching action. It lacks anisotropy, has poor process control and can easily contaminate the wafer surface. It however has good selectivity and rarely damage the wafer [32]. Dry etch on the other hand is a more physical approach, though in some case it is assisted by plasma (as in the inductively coupled plasma - reactive ion etch, ICP-RIE). The source gas usually contains chlorine, fluorine or oxygen to etch silicon, compound of silicon (like silicon nitride or oxide) or organics respectively. With increased need for process control, dry etch has found usefulness in many microelectronics fabrications. Plasma is much easy to control than simple immersion wet etching. Another form of dry etch is ion milling which uses energetic ions of noble gases, mostly  $\text{Ar}^+$ , to bombard the

wafer knocking off atoms from the wafer surface. Dry etch generally has high anisotropy and better controllability; however, they are prone to damaging the wafer due to high-energy ion hitting the wafer surface. The greater the degree of bombardment, the higher the etch anisotropy, but the lower the selectivity.

Wet etch, synonymous to Figure 2.5, was used in this study to uniformly etch oxide, etch silicon and texture silicon during wafer cleaning using hydrofluoric acid (HF), HNA (a mixture of 10% HF with Nitric acid) and tetramethylammonium hydroxide (TMAH) respectively.

### **2.1.5 Laser Processing for Dicing, Contact Formation and Isolation**

Laser is an acronym for Light Amplification by Stimulated Emission of Radiation. The invention of LASER was foreshadowed by the creation of the MASER (Microwave Amplification by Stimulated Emission of Radiation) by Charles H. Townes, Herbert J. Zeiger and James P. Gordon at Columbia University [<sup>33</sup>] following Einstein's prediction of stimulated emission of light at specific wavelengths with the aid of electrons. However, it was not until 1960 that Theodore H. Maiman, a physicist at Hughes Research Laboratory in Malibu, California developed the first LASER using photographic flash lamps as the source of the laser pump. Advanced laser processing techniques are currently used in semi-conductor industry to enable rapid, high precision manufacturing of devices beyond the limits of traditional systems. Laser is being used on a wide range of process in the IC industry for photomask writing, wafer dicing, marking, trimming and inspection [<sup>34</sup>].

Laser processing has been proposed as a viable approach to simplify the IBC-SHJ solar cell fabrication by reducing the complexities of multiple photolithography process. Thus, making the process more manufacturable and cost effective. Laser

processing can be applied in one of five ways: 1) Laser dicing of wafers for achieving precise dimensions; 2) laser patterning to isolate the emitter (p-type) and base (n-type) regions; 3) laser ablation to carefully open up a path way for metal contact to the emitter or base region; 4) laser fired contact (LFC) to selectively dope the n-type Si base region using a pentavalent element (Antimony, Sb) and; 5) laser fired emitter (LFE) to selectively dope the emitter region using a trivalent element (Gallium, Ga) for p-type Si. The latter, though theoretically plausible, is not practically viable, as the damage created by the laser firing process constitutes a significant recombination site for minority carriers. Condition 1 is easily achieved using a 532 nm visible laser. Conditions 2, 3 and 4 are currently being studied using a 355 nm UV laser with 25 nm pulse width. Experiments have been designed for investigating the potentials of laser isolation and laser fired contacts with minimal damage to the underlying passivation. A list of different lasers and parameters used in this study is highlighted in Table 2.1.

Table 2.1: Laser parameters used for laser isolation, direct and indirect laser ablation, and LFC in this study

Lab	Wavelength	Pulse width	Power	Uses
UVa	355 nm	5 ps	35 mW	i/p ablation w/less heat diffusion
UVa	355 nm	25 ns	8 W	Direct metal ablation and LFC
UVa	532 nm	1 ns	8W	Indirect ablation and LFE
IEC	532 nm	7 ns	~200 mW	Wafer dicing and LFC

Some of the results involving the use of such laser processing for IBC-SHJ solar cells are reported in this dissertation.

## **2.2 Material Characterization**

This section covers the material characterization techniques, both optical and electrical, that were employed to determine the properties of the thin films used for fabricating solar cells and optical couplers. It also includes relevant device performance measurements.

### **2.2.1 Optical Characterization**

#### **2.2.1.1 Ultraviolet-Visible Spectrophotometry (UV-VIS)**

The UV-VIS spectroscopy [<sup>35</sup>] measures the transmittance and reflectance of a substance by radiating it with light of different wavelengths, which covers the visible, adjacent near ultraviolet and near infrared ranges.

The basic parts of a spectrophotometer (Figure 2.6) [<sup>36</sup>] are a light source (often an incandescent bulb for the visible wavelengths, or a deuterium arc lamp in the ultraviolet), a holder for the sample, a diffraction grating or monochromator to separate light of the different wavelengths, and a photon detector. The detector is typically a photodiode or a CCD. Photodiodes are used with monochromators, which filter the light so that only light of a single wavelength reaches the detector. Diffraction gratings are used with CCDs, which collects light of different wavelengths on different pixels.

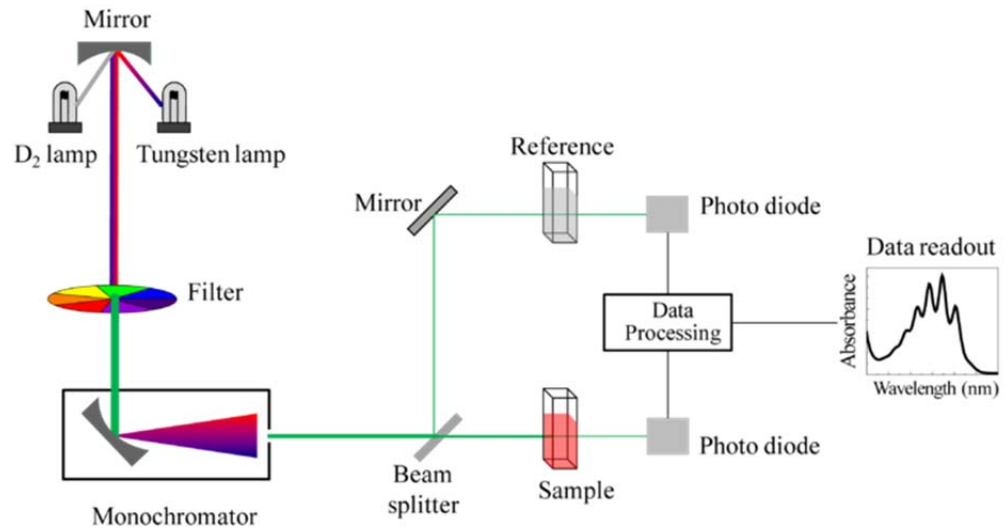


Figure 2.6: Schematic of a UV-VIS spectrophotometry [36]

UV-VIS spectroscopy was used in this dissertation to measure the reflection and transmission of thin film layer (e.g. intrinsic and doped a-Si:H) on glass to obtain thickness, growth rate and band-gap. It is also used to characterize the hemispherical reflection of textured wafers in order to determine a suitable silicon-texturing recipe.

### 2.2.1.2 Variable Angle Spectroscopic Ellipsometry (VASE)

The use of ellipsometry was first reported in 1886 when Paul Drude utilized a similar technique while studying Sb<sub>2</sub>S<sub>3</sub> crystals [37]. Since then, it has gained widespread interest as the need to characterize complex structure increases. Ellipsometry is a non-invasive and very sensitive surface characterization tool used for measuring the optical properties of thin films. It uses the relative phase change from a beam of reflected polarized light to derive psi ( $\psi$ ) and delta ( $\Delta$ ), which are related to the ratio of Fresnel reflection coefficients ( $R_p$ ) and ( $R_s$ ) for the parallel and

perpendicular polarized light respective. The relationship between these terms is given as:

$$\rho = \frac{R_p}{R_s} = \tan(\psi)e^{i\Delta} \quad (2.1)$$

VASE, unlike single wave ellipsometry, uses broadband light source, which spans across infrared, visible and ultraviolet spectral region. Thus, the dielectric function tensor or complex refractive index over a wide spectral region can be extracted and used in characterizing thin films. Variable angle capability in VASE enables the acquisition of large amount of data points for measured samples at multiple angles of incidence. This spectral acquisition angles of incidence and range allows for accurate determination of the optical properties of single and multi-layer films. Since ellipsometry is an indirect technique, the measured phase difference ( $\Delta$ ) and amplitude ratio ( $\psi$ ), for both varying angle and wavelength, cannot be directly converted to optical constants. A layer model for the each film or each individual film on a multilayers material is required. In this study, samples were fitted with a Tauc Lorentz model to estimate the thickness, optical constant (n and k) and band gap of the thin films.

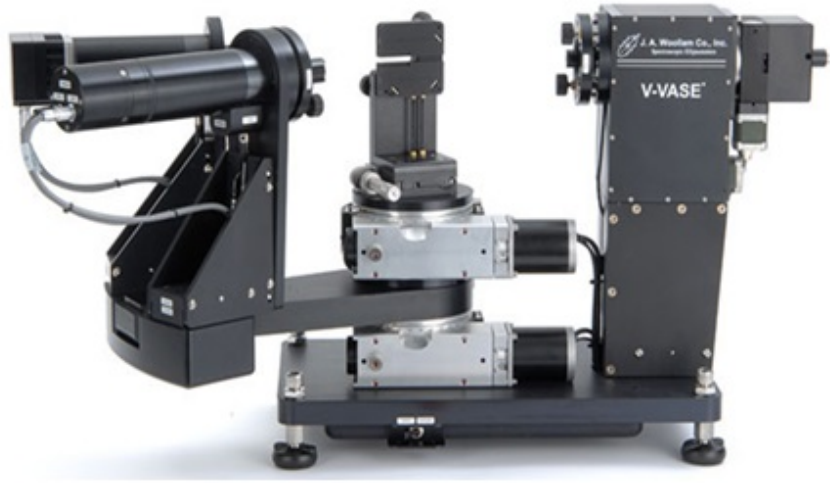


Figure 2.7: Variable Angle Spectroscopic Ellipsometry from J. A. Woollam, complete with Auto-retarder [38]

Ellipsometry measurements for this dissertation were performed using a Variable Angle Spectroscopic Ellipsometry from J. A. Woollam Co. depicted in Figure 2.7. The system comes with a 75W HS-190 monochromator (optimized for speed, wavelength accuracy and light throughput), fiber optic cable with a broad spectral range of 240-1700 nm and an auto retarder. This version comes with a rotating analyzer and a fixed angle input polarizer. Thus the monochromator beam does not necessarily need to be perfectly unpolarized as is the case with the rotating polarizer set up. The optical properties of the intrinsic and doped amorphous silicon on c-Si used for the SHJ and IBC-SHJ solar cells, and the silicon-rich silicon nitride used for the passive tuning of optical couplers were all done using VASE, and in some cases, in comparison with UV-VIS spectroscopy.

### 2.2.1.3 Fourier Transform Infrared (FTIR)

Fourier-transform infrared spectroscopy (FTIR) is an optical technique used in thin film characterization to obtain and analyze the infrared spectrum of absorption or emission of a material. FTIR has a unique advantage over other dispersive spectrometers that measure intensity over a narrow spectral range at a given time. It has the unique capability of collecting high spectral-resolution data simultaneously over a wide range of wavelength.



Figure 2.8: A FTIR Spectroscopy system by Thermo Scientific used for vibrational spectroscopic study.

Chemical bonds of films absorb infrared energy at specific wavelengths (or wavenumber). Thus, the basic structure of different compounds can be identified by the spectral position of the infrared absorptions. A plot of infrared transmission against wavenumber gives a unique signature that corresponds to different materials.

Fourier transform technique on the other hand enables the fast processing and analyzing of the infrared spectral using a broadband source. Thus, instead of using a monochromatic beam of light through the test sample, Fourier transform techniques allows the passage of a beam generated by a broadband light source and measures how much of that beam is absorbed by the test sample. The beam is then modified repeatedly to contain a different combination of frequencies and fed as input into the system. Each time, the corresponding infrared absorption spectral data is acquired. All the data sets are then analyzed to infer the absorption at each wavelength.

The absorption spectra as a function of light intensities and film thickness is given by Beer Lambert relation expressed in Eqns. 2.2-2.3:

$$I = I_0 e^{-\alpha t} \quad 2.2$$

$$\alpha = \frac{\ln\left(\frac{I_0}{I}\right)}{t} = \frac{2.303 * A}{t} \quad 2.3$$

where  $\alpha$  is the absorption coefficient,  $A = \log(I_0/I)$  is the absorbance,  $I_0$  is the incident light intensity,  $I$  is the transmitted light intensity and  $t$  is the thickness of the measured film. In some FTIR systems, the sample is placed at a Brewster angle offset ( $\theta^0$ ) to limit the reflection at the sample to air interface. In which case, Eqn. 2.3 can be revised as:

$$\alpha = \log_e \cos \theta \frac{A}{t} \quad 2.4$$

Infrared spectroscopy has been widely used to learn about the hydrogen content and bonding configuration of hydrogenated amorphous silicon [39]. The infrared spectra for amorphous silicon consist of three absorption regions – two stretching mode (centered at  $\sim 2000 \text{ cm}^{-1}$  and  $\sim 2090 \text{ cm}^{-1}$ ), a doublet due to dihydride bending and scissor modes (around  $840 - 890 \text{ cm}^{-1}$ ) and a wagging mode (centered at  $640 \text{ cm}^{-1}$ ) [40-42]. The stretching modes were mainly studied while characterizing the amorphous silicon film due to the detector range of our FTIR system and the nature of the predominant amorphous silicon vibration. The monohydride and dihydride peaks are then fitted with the raw data to allow the estimation of the hydrogen concentration in each peak using Eqns. 2.5 and 2.6:

$$C_H = \frac{N_H}{N_{Si}} \times 100\% = \frac{N_H(\text{cm}^{-3})}{N_{Si}(\text{cm}^{-3}) = 5 \times 10^{22}(\text{cm}^{-3})} \times 100\% \quad 2.5$$

$$N_H = A_{Si-H} \int \frac{\alpha}{\omega} d\omega = A_{SiH} \int \frac{\alpha}{\omega_{2000}} d\omega + A_{SiH_2} \int \frac{\alpha}{\omega_{2090}} d\omega \quad 2.6$$

where  $C_H$  is the hydrogen content,  $N_H$  is the concentration of hydrogen atoms in the film,  $A$  is a proportionality constant and varies as the inverse of the vibration strength,  $\alpha$  is the absorption coefficient,  $\omega$  is the wavenumber and the integral over the absorption band of interest represents the integrated absorbance,  $I$ . The microstructure parameter  $R^*$ , defined as the relative contribution of the high stretching mode (HSM at  $2090 \text{ cm}^{-1}$ ) to the combined stretching modes (HSM and low stretching mode, LSM at  $2000 \text{ cm}^{-1}$ ), is then computed to characterize the nature of the Si-H bond according to Eqn. 2.7:

$$R^* = \frac{I_{HSM}}{I_{LSM} + I_{HSM}} \quad 2.7$$

A Thermo Scientific NICOLET 6700 FT-IR spectroscopy, shown in Figure 2.8 above, was used in this dissertation to determine the silicon to hydrogen bond structure in the intrinsic and doped amorphous silicon films.

#### 2.2.1.4 Raman Spectroscopy

Raman spectroscopy is another spectroscopic technique used to detect the vibrational modes in a material system. It is named after the Indian Physicist Sir C. V Raman, whose ground breaking work in the field of light scattering led to the discovery of the Raman Effect and earned him the 1930 Nobel Prize for Physics. The Raman effect describes the behavior of light as it transverse a transparent material. When a collimated beam of light, for example a laser light, is incident on a material, most of the photons undergo Rayleigh scattering (elastic scattering), while a small fraction is scattered inelastically, resulting in a frequency shift expressed as:

$$h\nu_s = h\nu_o \pm \Delta E \quad 2.8$$

where  $h\nu_s$  represents the energy of the scattered light,  $h\nu_o$  represents the energy of the incident light and  $\Delta E$  represents the energy shift equivalent to the energy of a phonon created (Stokes scattering) or annihilated (anti-Stokes scattering). This energy shift is closely related to the chemical bonds at the molecular level, thus it is used to identify the nature of the molecular bonds in a material.

Within the spectral range  $0 \sim 2500 \text{ cm}^{-1}$ , different peaks corresponding to different kinds of phonon modes can be identified [<sup>43</sup>] for silicon film: transverse-

acoustic mode (TA at 130  $\text{cm}^{-1}$ ), longitudinal-acoustic mode (LA at 330  $\text{cm}^{-1}$ ), longitudinal-optic mode (LO at 445  $\text{cm}^{-1}$ ), transverse-optic mode (TO between 480-520  $\text{cm}^{-1}$ ), Si-H Wagging mode ( $\sim 630 \text{ cm}^{-1}$ ), two-phonon excitation ( $\sim 950 \text{ cm}^{-1}$ ) and Si-H Stretching mode (between 2000-2100  $\text{cm}^{-1}$ ). The region of interest is the TO band, which can be further divided into three parts: a TO peak at 520  $\text{cm}^{-1}$  from the crystalline silicon contribution, a TO peak at 510  $\text{cm}^{-1}$  attributed to the grain boundaries effects of nano-crystalline silicon and another TO mode at about 480  $\text{cm}^{-1}$  from the contribution of amorphous silicon. These peaks are shown in Figure 2.9.

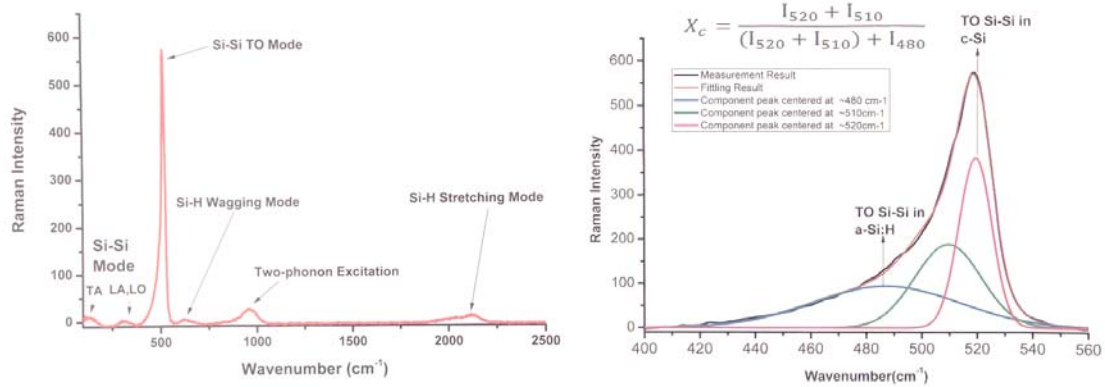


Figure 2.9: A typical Raman spectral for a silicon sample showing TA, LA, LO, TO, Si-H Wagging and Stretching modes, and two-phonon excitation (left graph), De-convoluted TO spectral with three Gaussians showing the crystalline phase at 520  $\text{cm}^{-1}$  and 510  $\text{cm}^{-1}$ , and the amorphous phase at 480  $\text{cm}^{-1}$  (right graph).

The crystalline ratio  $\chi_c$  of the sample can be defined by the contributions of the different phases to the TO mode according to Eqn. 2.9:

$$\chi_c = \frac{I_{520} + I_{510}}{(I_{520} + I_{510}) + I_{480}} \quad 2.9$$

where  $I_{xyz}$  represents the integral intensities of the peaks positioned at xyz. These peak positions are determined by a de-convolution of the Raman TO spectrum with three Gaussians.

A Thermo Scientific DXR Raman Microscope with a 532 nm laser, shown in Figure 2.10, was used in this dissertation to observe the Raman shift and the nature of i/p amorphous silicon interface for the doped layer optimization experiment.



Figure 2.10: A Thermo Scientific DXR Raman Microscope complete with a 532 nm laser source used for Raman Spectroscopy.

#### **2.2.1.5 X-ray Photoelectron Spectroscopy (XPS)**

Kai Siegbahn and his research group at the University of Uppsala, Sweden in the mid-1960s first developed Electron Spectroscopy for Chemical Analysis (ESCA) as a method for surface analysis [44]. The advent of commercial manufacturing of surface analysis tools in the early 1970s, necessitated by the growing IC industry, enabled the development of the present day X-ray Photoelectron spectroscopy (XPS).

XPS is a surface-sensitive and quantitative analysis technique that measures the elemental composition of elements that exist within a material. Since the mean free path of electrons in solids is very small, the detected electrons originate from only the top few atomic layers, making XPS a unique surface sensitive technique for elemental analysis. XPS works on the principle of photoelectric effect. By absorbing a photon from high-energy incident X-ray, an atom gains energy equal to  $h\nu$ . Core electrons with kinetic energy  $E_k$  are then ejected to regain the stable state of the atom as illustrated in Figure 2.11. These ejected electrons are collected and analyzed by the electron analyzer and a spectrum is obtained as a plot of the number of detected electron per energy interval versus kinetic energy and/or binding energy. The principle of energy conservation allows us to write the energy balance equation as:

$$h\nu = E_K + E_B + \Phi_{WF} \quad 2.10$$

where  $h\nu$  is the energy of the photon,  $E_K$  is the kinetic energy of the emitted electron,  $E_B$  is the binding energy of the atomic orbital from which the electron originates and  $\Phi_{WF}$  is the spectrometer work function.

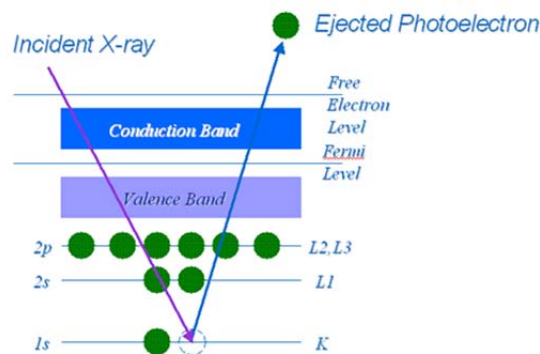


Figure 2.11: Schematic diagram illustrating the principle of operation of XPS

First, a quantitative analysis is carried out at low resolution to identify all the elements present on a test sample after which a more thorough, high resolution, qualitative analysis is carried out at a specific element peak corresponding to an element. The experimental data is then fitted with a model using CASA XPS software package [45] after loading the appropriate relative sensitivity factor (RSF) from an elemental library containing the RSFs for different XPS transitions [46]. The detection limit of the XPS used for this study is 0.1 atomic percent, therefore any chemical residues less than 0.1 atomic percent, which is less than a monolayer, cannot be detected [47]. Atomic percent by XPS was determined using the ratio of total area of an element detected to the area of all elements weighted by their sensitivity factor according to Eqn. 2.11:

$$\%E_x = \frac{AreaE_x/S_x}{\sum_i AreaE_i/S_i} \quad 2.11$$

where  $E_x$  represent an amount of element x,  $E_i$  represent an amount of each element detected, while  $S_x$  and  $S_i$  represents the sensitivity factors for element x and each of the elements detected.

Table 2.2: Scan parameters used for high and low resolution XPS analysis.

Parameters	Qualitative survey (low resolution)	Quantitative scan (high resolution)
Scan width	0-1200 eV	20-30 eV
Pass Energy	100 eV	20 eV
Channel step	1 eV	0.1 eV
No. of scan	1-5	10-30
Dwell time	10 ms	50 ms

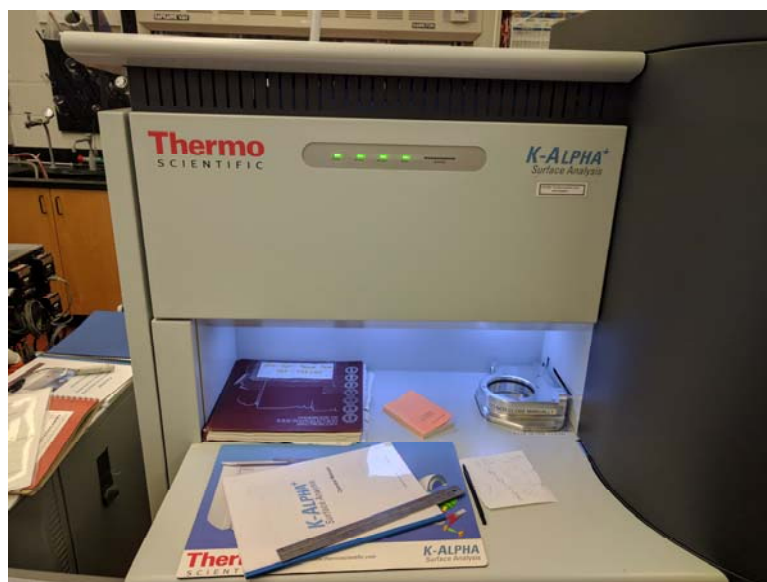


Figure 2.12: A Thermo Scientific K-Alpha<sup>+</sup> Surface Analysis tool used for XPS Analysis.

XPS surface analysis was carried out using a Thermo Scientific K-Alpha<sup>+</sup> surface analysis tool, shown in Figure 2.12, and was used to characterize crystalline silicon wafer's surface composition during wafer cleaning study.

#### **2.2.1.6 Optical and Scanning Electron Microscopy**

Microscopy is a technique that uses a microscope to view images of an object that is not within the range of resolution of the human eyes [<sup>48</sup>]. Microscopy has been used since the 16<sup>th</sup> century to image small objects and features. The first compound microscope was invented by Dutch spectacle-makers - Han Janssen and his son Zacharias Janssen [<sup>49</sup>]. However, Antonie Van Leeuwenhoek is generally considered to be the first acknowledged microscopist and microbiologist. Most of the early use of microscopy in science came from his pioneering work in microbiology [<sup>50, 51</sup>].

Optical Electron Microscopy is the passing of visible light that is transmitted or reflected from an object through a single lens or a network of lenses to allow the magnification of the object [<sup>52</sup>]. Figure 2.13 shows the image and working principle of an optical microscope.

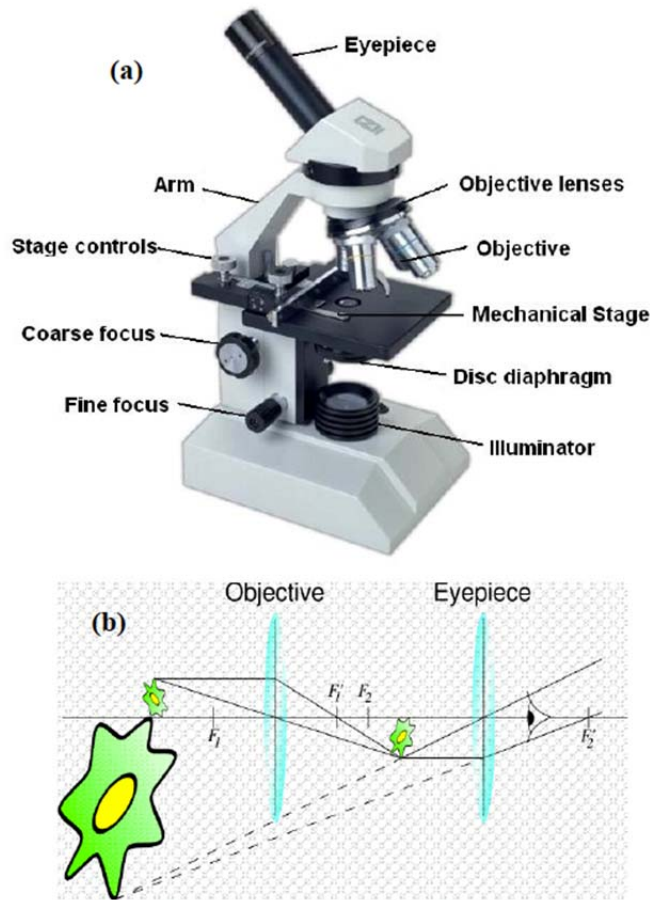


Figure 2.13: a) Image and b) working principles of an optical microscopy.

Scanning Electron Microscopy is used to view much smaller features in nano- and micrometer sizes using a stream of electron beam instead of light. Manfred von Ardenne pioneered SEM in the 1930s [53]. It was further developed by Charles Oatley and first commercialized by Cambridge Instruments. A beam of electrons is produced at the top of the microscope by heating a metallic filament (Figure 2.14), usually made of Tungsten or Lanthanum Hexaboride [54]. This beam is attracted through the anode, condensed by a magnetic condenser lens; passing through the scanning coils and then

focused as a very fine point on the sample by the magnetic objective lens. The scan coils are energized by varying the voltage and creates a magnetic field, which deflects the beam back and forth in a controlled pattern. Once the electron beam hits the sample, it produces secondary electrons from the sample, which carry the information about the specimen's surface such as topography. These electrons are collected by a secondary detector or a backscatter detector, converted to a voltage, amplified and sent to a viewing screen producing an image.

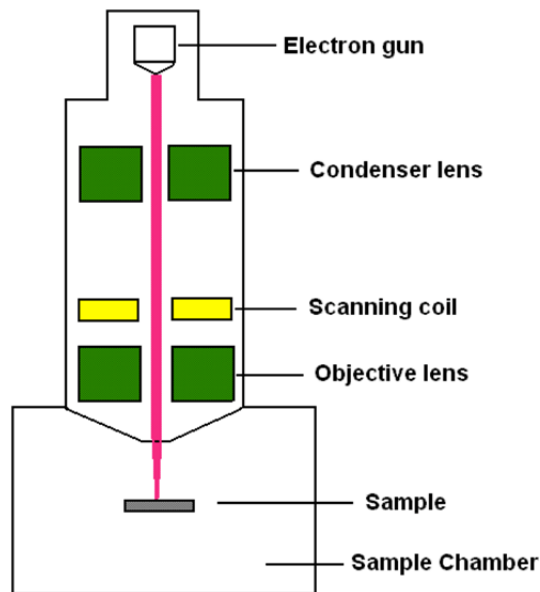


Figure 2.14: Schematics of an SEM showing key components

Both optical and scanning electron microscopies were used in this dissertation to examine the surface of semi-polished and textured c-Si wafers after texturing and waveguide patterns during photolithography.

### **2.2.1.7 Optical Emission Spectroscopy (OES)**

Optical Emission Spectroscopy is a widely used analytical technique predominantly used for metal analysis and to monitor plasma kinetics. It identifies plasma constituents by detecting and analyzing the intensity of light emitted from plasma at different wavelengths. The part of the electromagnetic spectrum, which is used by OES includes the visible spectrum and part of the ultraviolet spectrum.

Optical emission spectrometers cover the analysis of the chemical elements at the complete range from sub-ppm to percentage levels, from pure metals trace analysis to high-alloyed grades. All relevant elements can directly be analyzed simultaneously. The speed and the ease-of-use of this equipment make it so versatile and very well accepted and beneficial.

Typically the OES consist of three major components illustrated in Figure 2.15: 1) an electrical source to excite the atoms, strike plasma and thereby emit a characteristic light; 2) an optical system that transmit the multiple optical emission lines from the plasma into the spectrometer, where a diffraction grating in the spectrometer separates the incoming light into element-specific wavelengths. A corresponding detector measures the intensity of light for each wavelength. The intensity measured is typically proportional to the concentration of the excited species in the sample; and 3) a computer system that acquires the measured intensities and processes the data through a predefined calibration [<sup>55</sup>].

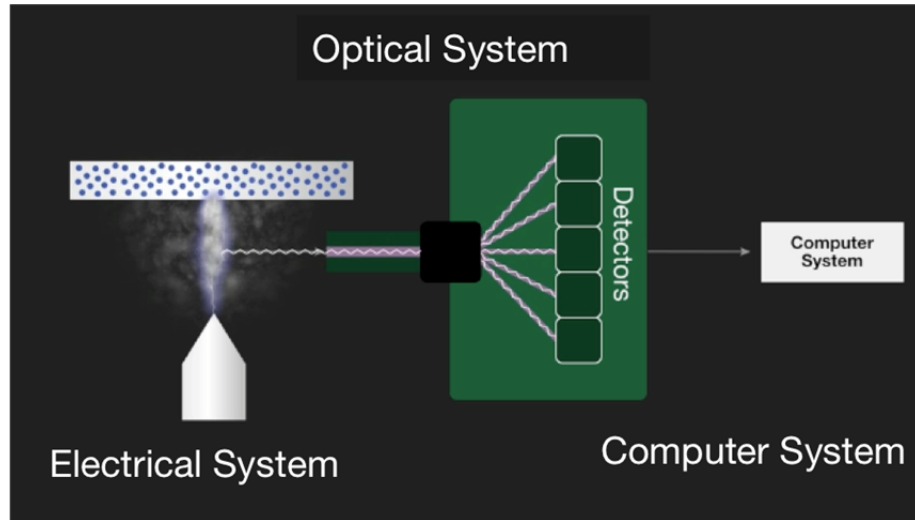


Figure 2.15: Schematics showing the three major components of OES illustrating how OES works.

In this dissertation, OES was used to study the plasma kinetics during the CVD process for intrinsic and doped amorphous silicon, and hydrogen plasma treatment to better inform our recipe formulation. The OES study was done in-situ during the CVD process.

## 2.2.2 Electrical Characterization

### 2.2.2.1 Effective Minority Carrier Lifetime Measurement

The effective minority carrier lifetime ( $\tau_{\text{eff}}$ ) measurement gives an indication of the effectiveness of the surface passivation on a c-Si surface. It is one of the early indications of final cell parameters. It measures how long a carrier will stay active in excited mode before recombination. It is not to be confused with radioactive lifetime, which denotes the average lifetime ( $1/e$  life) of a radioactive particle before decay. The lifetime in this case determines the steady state populations of electrons and holes,

i.e. the separation of quasi-Fermi levels and hence  $V_{OC}$  of the solar cell [56]. In this study, high quality Czochralski (CZ) wafers with bulk lifetime exceeding 5 ms were used and therefore the measured effective minority carrier lifetime is mainly determined by the quality of the surface passivation. The measured lifetime,  $\tau_{eff}$  can be decomposed to bulk  $\tau_b$  and surface  $\tau_s$  according to Eqn. 2.12:

$$\frac{1}{\tau_{eff}} = \frac{1}{\tau_b} + \frac{1}{\tau_s} \quad 2.12$$

The effective lifetime measurement is often done in either a transient decay mode, also called photo-conductance decay (PCD) or a quasi-steady-state photo-conductance (QSSPC) mode. For PCD method, the photo-generation is terminated abruptly. There will be no current flowing from the device. Therefore the rate of carrier density change is equal to the recombination rate according to Eqn. 2.13:

$$\frac{d(\Delta n)}{dt} = -\frac{\Delta n}{\tau_{eff}} \quad 2.13$$

The effective lifetime  $\tau_{eff}$  can be determined using Eqn. 2.13 if  $dn/dt$  and the excess carrier concentration  $\Delta n$  are measured. For QSSPC method, the illumination terminates slowly which is a quasi-steady process, so the QSS conditions prevail within the semiconductor, and effective lifetime is given as Eqn. 2.14:

$$\tau_{eff} = -\frac{\Delta n(t)}{G(t) - \frac{\partial(\Delta n)}{\partial t}} \quad 2.14$$

where  $G(t)$  is the generation rate, which is measured using a photo-detector.

Irrespective of the measuring mode methods, the excess electron concentration  $\Delta n$  is determined by measuring the conductance change of the c-Si wafer with illumination and time. The excess photo-conductance for a wafer of thickness  $W$  can

be measured using an inductor in a contactless fashion using Eqn. 2.15 expressed in terms of  $\Delta n$ :

$$\Delta\sigma_L = qW(\sigma_n + \sigma_p)\Delta n \quad 2.15$$

where  $\mu_n$  and  $\mu_p$  are the electron and hole mobility respectively.

The range of excess carrier concentration is varied from  $10^{13} \text{ cm}^{-3}$  (low injection level) to up to  $10^{17} \text{ cm}^{-3}$  (high injection level). However,  $\Delta n$  at  $10^{15} \text{ cm}^{-3}$  is usually reported since it represents approximately the excess carrier density in c-Si solar cells under general operational condition. In QSSPC mode, the separation between electron and hole quasi-Fermi levels, i.e.  $V_{oc}$  of the cell can be derived since  $\Delta n$  can be measured at steady state [57]. This  $V_{oc}$ , as derived from lifetime measurement, is called implied  $V_{oc}$  ( $iV_{oc}$ ), which is a very important indicator of the quality of surface passivation and is usually very close to the actual  $V_{oc}$  of the finished device if there is minimal  $V_{oc}$  degradation after p-n junction and contact formation. Thus, this sets the upper bar for the highest possible  $V_{oc}$  achievable by a device limited by its surface passivation.

In this dissertation, a commercially available Sinton instrument WCT 100 lifetime tester, shown in Figure 2.16, was used for both PCD and QSSPC measurements to estimate the effective minority carrier lifetime and implied open circuit voltage during the passivation study.



Figure 2.16: Sinton instrument WCT120 lifetime tester used for PCD and QSSPC measurement [58]

### 2.2.2.2 Current-Voltage (J-V) Characterization

The current-voltage (J-V) characteristic represents the most basic measurements made on a solar cell [59]. This measurement method uses a four-point probe, where the current of a solar cell is measured as a function of the applied voltage in the dark and light illumination. First-degree performance parameters ( $V_{oc}$ ,  $J_{sc}$ , FF and efficiency) of a solar cell are determined through this method. The measurement is performed under standard test condition (STC) as follows [60]: a) Air mass 1.5 spectrum (AM1.5) for terrestrial cells and Air mass 0 (AM0) for space cells (see appendix A for AM1.5 and AM0 definitions; b) Intensity of  $100 \text{ mW/cm}^2$  (or  $1 \text{ kW/m}^2$ , one sun illumination); c) Cell is mounted on a temperature controlled stage regulated by a chiller to maintain cell temperature at  $25 \text{ }^\circ\text{C}$ ; and d) Four-point probe method to eliminate the parasitic effects from the connecting wires ( $R_w$ ) and contacts

( $R_c$ ) to the measured device. The high input impedance ( $R_m$ ) of a voltmeter ( $\geq 10^{12}$  ohms) prevents the flow of current through the voltage path. Figure 2.17 shows a schematic of the four-point probe (Kelvin probe) used for JV measurement.

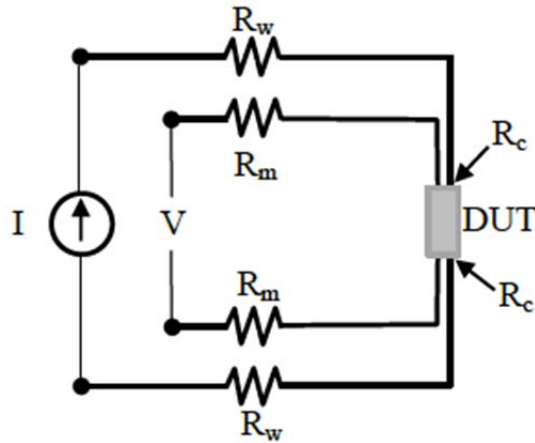


Figure 2.17: Schematic of a four-point probe for J-V measurement

Voltage is applied by a set of probes and current is measured by another set of probes. Thus, all points in the circuit are kept at equipotential and hence preventing any drop in voltage in the loop. A Keithley source-measure unit (SMU) Model 2400 [61] was used as the voltage source and current measurement unit. A J-V plot in the dark and under illumination yields the fundamental solar cell parameters. Figure 2.18 shows a typical J-V plot. The  $V_{OC}$  and  $J_{SC}$  are directly obtained from the curve at zero current and voltage respectively. The FF on the other hand is a measure of the “squareness” of the J-V curve and can be determined as the ratio of the maximum power density,  $P_{max}$  to the product of  $V_{oc}$  and  $J_{sc}$  according to Eqn. 2.16:

$$FF = \frac{P_{max}}{J_{sc} * V_{oc}} \quad 2.16$$

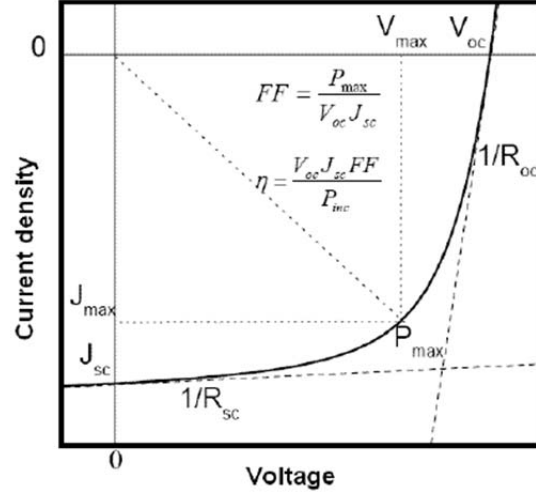


Figure 2.18: Sample J-V curve showing important cell parameter

The cell conversion efficiency, defined as the ratio of the  $P_{max}$  to the incident power density  $P_{light}$  is given by Eqn. 2.17:

$$Eff = \frac{P_{max}}{P_{light}} = \frac{V_{oc} * J_{sc} * FF}{P_{light}} \quad 2.17$$

Additionally, both the short-circuit ( $R_{sc}$ ) and open circuit ( $R_{oc}$ ) resistances can be evaluated using Eqn. 2.18 as follows:

$$R_{sc} = \left. \frac{dV}{dI} \right|_{sc}, \quad R_{oc} = \left. \frac{dV}{dI} \right|_{oc} \quad 2.18$$

In this dissertation, J-V characterization in the dark and under illumination was used to determine cell parameters for SHJ and IBC-SHJ solar cells.

### 2.2.2.3 Diode Analysis

For a more in-depth characterization of the solar cell, diode analysis is carried out to determine second-degree parameters like ideality factor ( $n$ ), reverse saturation current ( $J_0$ ), shunt conductance ( $G$ ), series and shunt resistance ( $R_s$  and  $R_{sh}$ ). A solar cell is a p-n junction, in which the metallurgical junction is formed between the crystalline silicon and the doped amorphous silicon, creating a built-in electric field. An ideal solar cell may be modeled by a current source in parallel with a diode; in practice no solar cell is ideal, so a shunt resistant and a series resistant component are added to the model as shown in Figure 2.19:

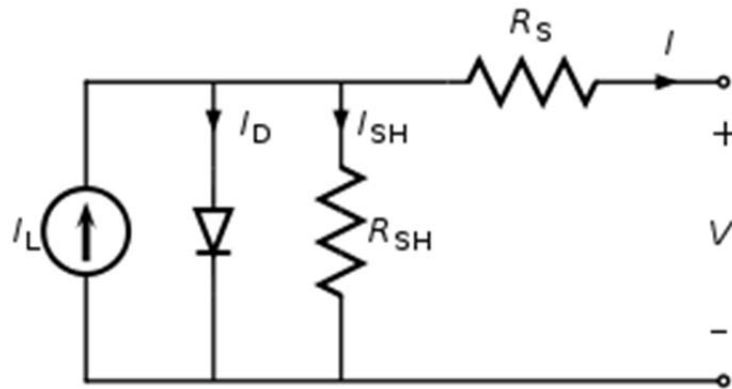


Figure 2.19: Equivalent circuit of a solar cell showing a diode in parallel with a current source.

According to the above equivalent circuit, the current produced by the solar cell can be expressed as the current from the current source, minus that which flows through the diode and shunt resistant as shown in Eqn. 2.19:

$$J = J_L - J_D - J_{SH} \quad 2.19$$

where  $J$  is the output current density,  $J_L$  is the photogenerated current density,  $J_D$  is the diode current density and  $J_{SH}$  is the shunt current density. The current through the circuit elements is governed by the voltage across them:

$$V_j = V + IR_s \quad 2.20$$

where  $V_j$  is the voltage across the diode and shunt resistor,  $V$  is the voltage across the output terminals,  $I$  is the output current and  $R_s$  is the series resistance. The current density through the diode is expressed using Shockley diode equation as:

$$J_D = J_o \left\{ \exp \left[ \frac{V_j}{nV_T} \right] - 1 \right\}, V_T = \frac{kT}{q} \approx 26 \text{ mV at } 25^\circ\text{C} \quad 2.21$$

where  $J_o$  is the reverse saturation current density,  $n$  is the diode ideality factor ( $n=1$  for an ideal diode),  $q$  is the charge of an electron,  $k$  is Boltzmann's constant,  $T$  is the absolute temperature and  $V_T$  is the thermal temperature. The current through the shunt resistor is expressed according to ohms law as:

$$I_{SH} = \frac{V_j}{R_{SH}} \quad 2.22$$

where  $R_{SH}$  is the shunt resistance in ohms. Thus the characteristic equation of a solar cell can be written as:

$$J = J_L - J_o \left\{ \exp \left[ \frac{V+IR_s}{nV_T} \right] - 1 \right\} - \frac{V+IR_s}{R_{SH}} \quad 2.23$$

These second-degree performance parameters of a solar cell ( $J_o$ ,  $n$ ,  $R_s$ ,  $R_{sh}$  and  $G$ ) can be extracted by further analysis and applying mathematical operation on the diode equation. Details of this analysis can be found in [62] but is summarized as follows:

1. A dark and illuminated J-V curve is plotted.
2. Plot  $dJ/dV$  ( $\text{mS}/\text{cm}^2$ ) for the dark curve to determine the shunt conductance from the  $dJ/dV$  near  $J_{sc}$ . The shunt resistance is then calculated as the inverse of the shunt conductance ( $R_{sh} = 1/G$ ). Low shunt conductance and high shunt resistance are indicators of a good cell.
3. Plot  $dV/dJ$  vs  $(J+J_{sc}-GV)^{-1}$ . The ideality factor,  $n$  is derived from the slope of this curve (Slope =  $nkT/q$ ) and the series resistance is derived from the intercept on the y-axis for both dark and light curves.
4. A semilog plot of  $(J+J_{sc}-GV)$  vs  $V-R_sJ$ . The ideality factor,  $n$  can again be derived from the slope of this curve (Slope =  $q/nkT$ ) and the intercept on the y-axis gives the  $J_0$  for both dark and light curves.  $n$  and  $J_0$  values from 3 and 4 can be compared for consistency.

The shunt conductance and series resistance are parasitic effects due to geometry and bulk properties of the cell. Thus, they contribute to power loss in the device. To correct for the shunt conductance,  $GV$  is subtracted from  $J+J_{sc}$  to remove the effect of the current contribution due to shunts in the device. To correct for the voltage drop across the series resistance,  $JR_s$  is subtracted from  $V$ . The actual bias across the junction is thus  $(V - JR_s)$ .

A representative output of the 4 steps in the analysis described above is shown in the Figure 2.20:

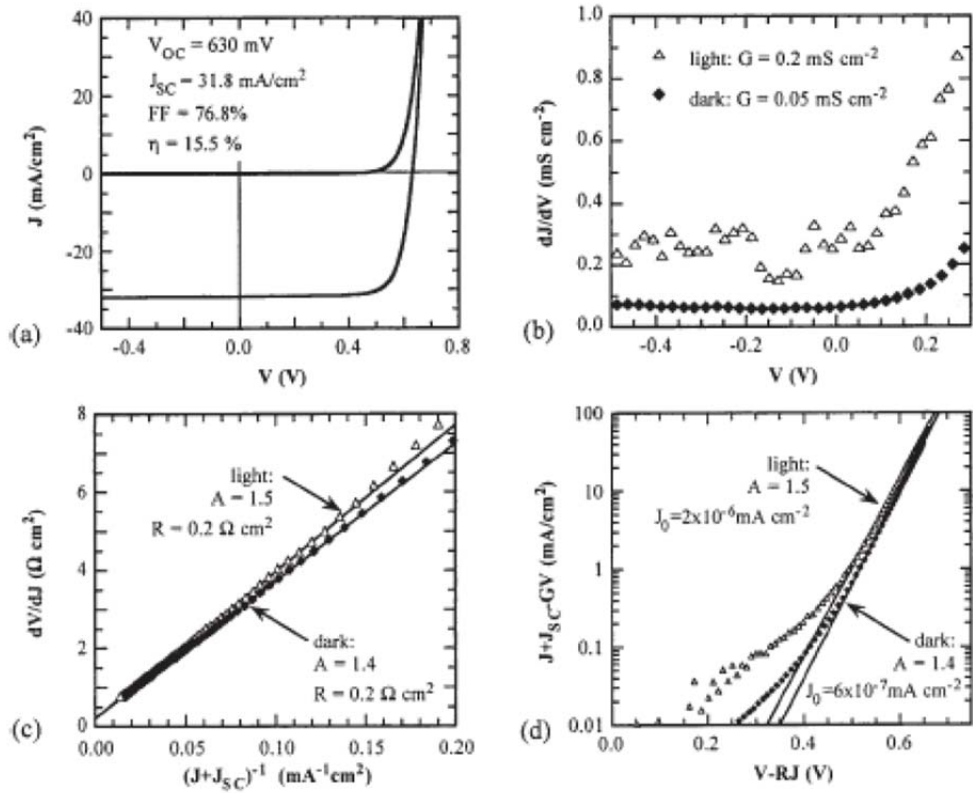


Figure 2.20: Light and dark JV characteristics for a well-behaved CIGS device (a) Standard JV (b) shunt characterization,  $G$  (c)  $r(J)$  with fit used to determine  $n$  and  $R_s$  (d)  $\ln(J+J_{sc})$  with fit used to determine  $n$  and  $J_0$ . [62]

#### 2.2.2.4 Quantum Efficiency Analysis and Spectral Response

The Quantum Efficiency (QE) is the ratio of the number of carriers collected by the solar cell to the number of photons of a given energy (wavelength) incident on the solar cell. Thus, it helps to estimate the wavelength dependent current generation in a device. If all photons of a certain wavelength are absorbed and the resulting minority carriers are collected, then the quantum efficiency at that particular wavelength is one. Ideally, the quantum efficiency for photons with energy below the band gap and photons transmitted through the cell is zero, so quantum efficiency has a

rectangular shape. But for most solar cells, it is not real rectangular shape (Figure 2.21) due to recombination effects or parasitic absorption.

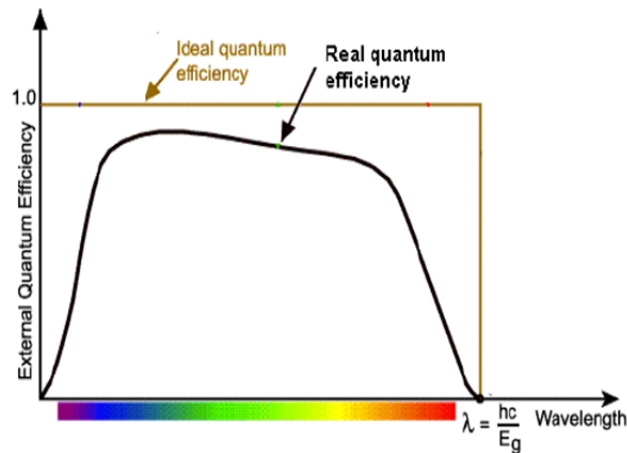


Figure 2.21: Sample quantum efficiency diagram of a solar cell

In most cases, the measured QE usually includes the effect of optical losses such as reflection. This is called “external” quantum efficiency (EQE). However, sometimes it is useful to look at the quantum efficiency of the light left after the reflected and transmitted light has been lost, which is called "internal" quantum efficiency (IQE).

The spectral response (SR) is similar to the quantum efficiency (QE). The SR represents the ratio of the current generated by the solar cell to the incident optical power [59] and has units of A/W. Overall, both QE and SR give the spectral dependence of the photocurrent collection. The actual measurement process involves the measurement of spectral response from which QE is calculated according to Eqn. 2.24:

$$SR = \frac{q\lambda}{hc} QE \quad 2.24$$

where  $h$  represents Planck's constant, and  $c$  and  $\lambda$  are the speed and wavelength of light. Figure 2.22 shows a sample spectral response of a solar cell.

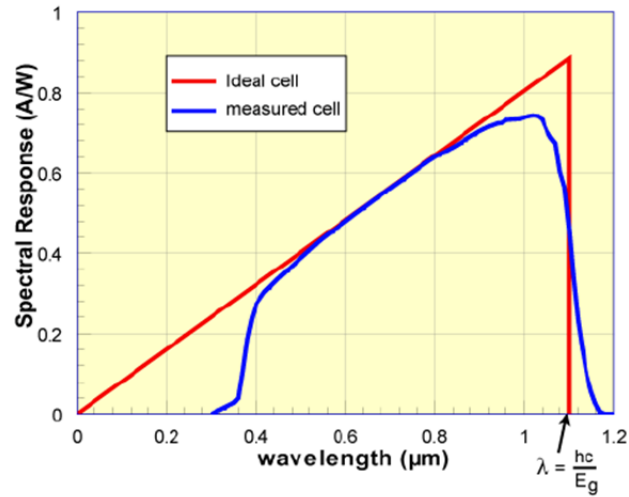


Figure 2.22: Sample spectral response diagram of a solar cell

The QE setup consists of an optical system which separates white light into monochromatic light by using a 200 W quartz tungsten halogen EHJ projector lamp, a filter wheel, an Oriel Corner Stone monochromator, a light chopper and a set of collimating lenses. The cell is mounted on an adjustable stage and electrical contacts are made to the cell by a set of four probes. The probes are connected to an electrical system, which consists of IV converter, Stanford Research Labs SR830 DSP lock-in amplifier, a voltmeter, an ammeter and an oscilloscope all interfaced to a computer running the control and data logging software. Figure 2.23 shows the optical set up for the QE measurement:

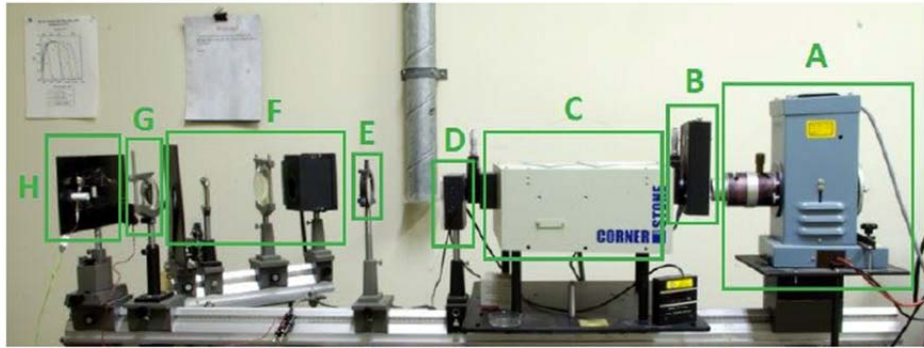


Figure 2.23: Optical setup for QE measurement. A) Light source, B) Filter wheel, C) Monochrometer, D) Light chopper, E) Collimating lens, F) Bias light setup, G) Focusing lens, H) Sample stage.

The light source is incident through a filter wheel which houses long pass filters that removes higher order wavelength interfering modes. This ensures that the monochromator receives light that is free from higher order modes. The monochromator splits the light into separate wavelengths using gratings, which reflects the spectrally dispersed light into a slit producing a Gaussian beam. The light at this point is incident on a light chopper, operating at 72 to 78 Hz. The light is then focused on the sample with a collimating and focusing lens. The QE setup also has the capability of applying light and voltage bias, which give further insight into losses and response of cells under light induced and voltage bias conditions.

QE measurements provide very useful information about the solar cell and the material from which it was made. The optical losses, bandgap, short circuit current density and sub-bandgap absorption can be determined from QE measurement. QE was used in this study to estimate the improvement in light absorption from front and rear surface optimization of SHJ solar cells.

### 2.2.2.5 Temperature Dependent Conductivity Measurement

Conductivity measurements were performed for p- and n-doped a-Si:H layers using a Keithley 617 programmable electrometer complete with a voltage source and channel scanner in a 2 point configuration, allowing a voltage sweep from 10V to -10V. A temperature sweep between 273 K and 393 K is achieved with the aid of a helium heat pump, while a window on the Tenney Engineering enclosure shown in Figure 2.24 allows for conductivity measurement under illumination. For conductivity measurement, doped a-Si:H films were deposited on Corning glass, after which two rectangular aluminum contacts are evaporated onto the layer. By applying a voltage  $V$  between the aluminum contacts, and measuring the corresponding current  $I$  through the films, the conductivity  $\sigma$  can be determined according to Eqn. 2.25:

$$\sigma = \frac{I * d}{V * l * t} \quad 2.25$$

where  $d$  is the distance between the aluminum contacts,  $l$  is the length of the aluminum contact, and  $t$  is the a-Si:H film thickness. To determine the activation energy, which gives an indication of the Fermi level position of the doped layer, dark conductivity measurements were carried out at temperatures ranging from 273 K to 393 K between the two electrodes. A plot of  $\sigma$  versus  $1/T$  is then plotted on a log scale. The Arrhenius equation, expressed in Eqn. 2.26, is then fitted to the equation of an exponential curve, Eqn. 2.27, to derive  $E_a$  and  $\sigma_o$ .

$$\sigma = \sigma_o \exp \left[ \frac{E_a}{k_B T} \right] \quad 2.26$$

$$y = A e^{mx} \quad 2.27$$

Alternatively,  $\ln(\sigma)$  versus  $1/T$  can be plotted on a linear scale and Eqn. 2.28 is fitted to the equation of a straight line, Eqn. 2.29, to derive  $E_a$  and  $\sigma_0$ .

$$\ln(\sigma) = \ln(\sigma_0) + \left[ \frac{E_a}{K_B} \right] \left[ \frac{1}{T} \right] \quad 2.28$$

$$y = c + mx \quad 2.29$$

where  $E_a$  is the activation energy,  $K_B$  is the Boltzmann constant,  $T$  is the temperature in kelvin,  $\sigma$  and  $\sigma_0$  are the conductivity at varying temperatures and at infinite temperature respectively,  $m$  is the slope,  $c$  is the intercept and  $A$  is constant.

In this study, temperature dependent conductivity measurement was performed on p and n doped a-Si:H films with varying deposition conditions.



Figure 2.24: A Tenney Engineering Inc. enclosure for temperature dependent conductivity measurement, complete with a programmable electrometer, voltage source and channel scanner.

### **2.3 Summary**

In this chapter, a detailed description of the experimental techniques and characterization methods used in this dissertation has been presented. The following chapters will feature experimental results that were achieved using these techniques.

## Chapter 3

### ANALYSIS OF SILICON WAFER PREPARATION FOR SOLAR CELL FABRICATION

#### 3.1 Introduction

Unlike conventional cells made from diffused junctions, SHJ cells have their junctions formed by growing thin-doped and intrinsic layers directly on the crystalline silicon surface. This places great emphasis on the purity of the wafer surface, as the a-Si/c-Si interface is an integral part of the junction. A key feature of SHJ cells is their very high  $V_{OC}$ , emanating from the band offset of the a-Si/c-Si hetero-structure. A contaminated silicon wafer surface however, could hinder the realization of this high  $V_{OC}$  by creating recombination sites. Thus, excellent surface passivation is contingent on a well-prepared surface free from organic contaminants, particles and metallic ions, which reduces surface recombination and enables very high  $V_{OC}$  necessary for achieving high efficiency devices. This assumes that the wafer's bulk lifetime is so high that it is not the limiting factor, which is a very good assumption for our monocrystalline n-type silicon wafers. A very aggressive and complex cleaning regime could be developed to yield a high purity surface, but this would lead to excess chemical waste, introduce variability from run to run, and undermine repeatability. Due to the critical nature of the surface property of the SHJ cell wafer, and the key role it plays in the overall cell performance, in this chapter I present a comprehensive study of different common wafer preparation steps, analyzing their relative significance in ensuring an optimal wafer surface for SHJ cell fabrication. Common

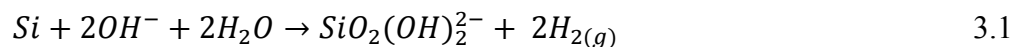
challenges with standard wafer cleaning procedures like variability and complexity are also highlighted in this chapter. Much of the results of this chapter were published in [63].

### 3.2 Sample Preparation

Chemically polished n-type Cz monocrystalline silicon wafers with (100) orientation, 140- $\mu\text{m}$  thicknesses and 4-5  $\Omega\text{-cm}$  resistivity were cut and processed as 25 $\times$ 25 mm square samples. Multiple samples were treated to unique wafer-cleaning sequences for reproducibility and effectiveness. Electronic grade ACS certified chemicals were supplied from Fisher Chemical, Aldrich Chemistry and J. T Baker, and were used as received. To effectively carry out this study, the wafer surface was characterized at different stages during the cleaning process in order to quantify the impact and value of each cleaning step. The cleaning procedure incorporates a wafer-texturing step, which serves to improve light trapping in the Si sample.

### 3.3 Effect of Saw Damage Removal

Initially the effects of surface damage etch (SDE), wafer degreasing, and metal ion removal were studied. SDE was carried out using potassium hydroxide (KOH). KOH, an anisotropic etchant of silicon, etches the {110}, {100} and {111} planes at a ratio of 400:200:1 at 85 $^{\circ}$  C [64]. Each surface of the Si wafer was etched by about 3 - 4  $\mu\text{m}$  in a 20% wt. aqueous KOH solution, leaving behind  $\text{K}^+$  ions on the wafer. Seidel et al. summarized the overall gross reaction of KOH with silicon as [65]:



Dust particle removal and wafer degreasing were performed in one of three methods: 1) a combination of acetone, methanol and isopropanol (AMI) in that order, heated ultrasonically at 55° C for 5 mins each; 2) pressurized CO<sub>2</sub> ice cleaning (ICE); or 3) DI water rinse designated as “None” in the flow chart below. Removal of metal ion contaminants from the KOH etch was achieved either by sequential RCA cleanings [66] – [RCA I (30% NH<sub>4</sub>OH: 30% H<sub>2</sub>O<sub>2</sub>: DI H<sub>2</sub>O – 1:1:5), followed by RCA II (conc. HCl: 30% H<sub>2</sub>O<sub>2</sub>: DI H<sub>2</sub>O – 1:1:5) both at 75° C for 10 mins each] or by Piranha (P) clean (conc. H<sub>2</sub>SO<sub>4</sub>: 30% H<sub>2</sub>O<sub>2</sub> – 3:1) for 5 mins at the intrinsic exothermic temperature of 80° C. The experimental design is shown in Figure 3.1:

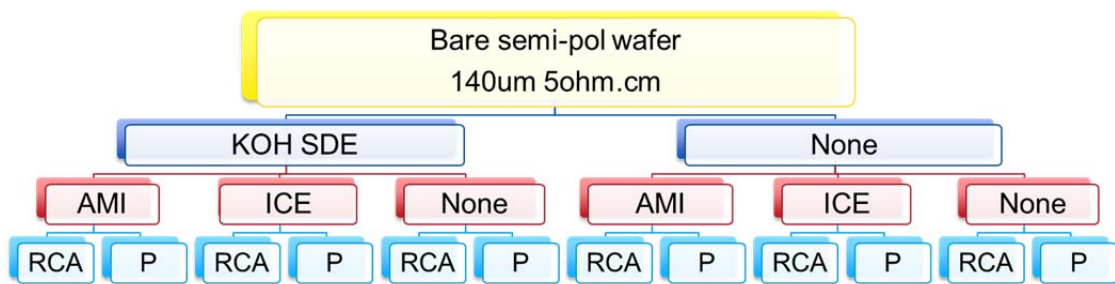


Figure 3.1: Experimental flow chart for saw damage removal study [63].

The experiment basically consists of two different groups of samples, one of which was treated with SDE and the other which was not treated with SDE. These two sets of samples were then treated to AMI, ICE or a simple DI water rinse. Finally, each of the three sub groups was treated to two types of wet chemical treatment – RCA I & II or Piranha. The samples were then passivated by immersion in 0.01 mol/dm<sup>3</sup> quinhydrone-methanol solution [67] at room temperature for approximately 20 mins before QSSPC lifetime measurement.

### 3.4 Effective Lifetime with Quinhydrone Methanol Solution

Quinhydrone-methanol solution was utilized in this study because it presents a quick and effective chemical surface passivation method for measuring the lifetime of Si wafers, with comparable passivation as i.a-Si:H layers [67]. In some cases, surface passivation was repeated with a 10 nm i.a-Si:H layer deposited on both sides of the wafers using a previously validated deposition recipe, to verify the efficacy of each cleaning process for solar cell fabrication. The result from SDE study shows striking difference for samples with and without KOH SDE. Figures 3.2a (w/ KOH SDE) and 3.2b (w/o KOH SDE) show the effective minority carrier lifetime and  $iV_{OC}$  from the sample sets shown in Figure 3.1 after 30 minutes in quinhydrone methanol solution.

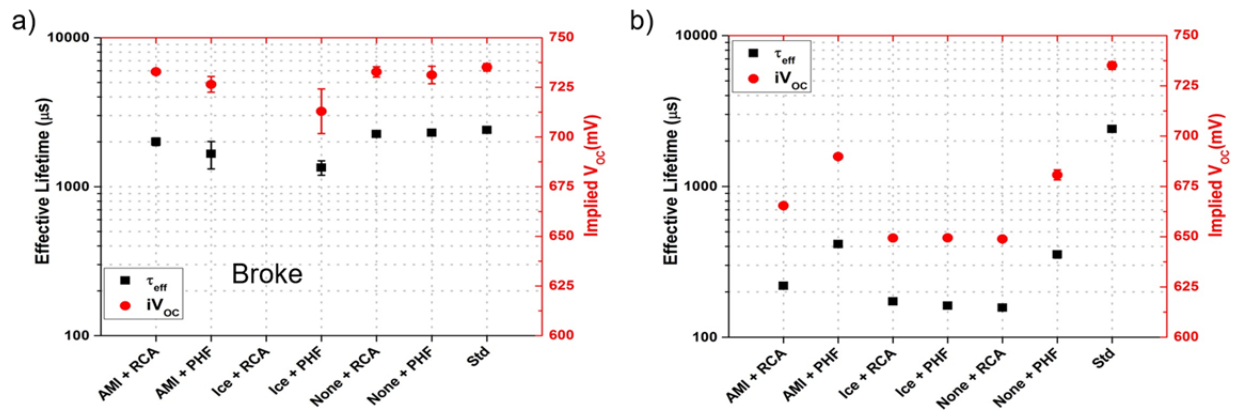


Figure 3.2: Effect of SDE on effective minority carrier lifetime and  $iV_{OC}$  measurement in quinhydrone methanol solution for: a) samples with KOH SDE and b) samples without KOH SDE. Each data point represents an average of 2 samples [63].

Results shown in Figure 3.2 above are averages from two samples used for each cleaning sequence. The KOH SDE clearly introduces a major difference between both sets of samples, with significantly higher measured effective lifetime and  $iV_{OC}$  in

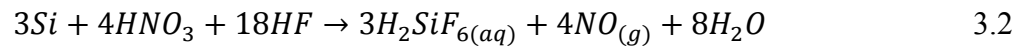
quinhydrone methanol solution (Figure 3.2a). This result shows that some form of SDE, which removes a few microns of contaminated layers, is crucial for achieving excellent passivation. This result also suggests that a simplified wafer cleaning approach can be achieved given the fact that samples with no wafer degreasing step (i.e. no AMI or ICE step) performed equally as those with either wafer degreasing steps or our standard baseline steps.

Other parameters studied showed secondary effects. Samples that received solvent treatment after SDE showed slightly improved reproducibility. However, this process did not appear to be crucial to producing high quality wafer surfaces. Samples that received pressurized CO<sub>2</sub> ice gun pre-treatment had a low yield ~50%, as several samples broke during this mechanical cleaning process. Those that survived the process showed slightly reduced lifetime and  $iV_{OC}$  as well as the largest sample-to-sample variation (see error bars in Figure 3.2a). For the wet chemical cleaning step, both RCA and Piranha performed similarly on the KOH SDE sample sets. RCA is a more complex two-step process requiring the heating of corrosive solutions. It is essential for removing the K<sup>+</sup> ion if KOH is used for SDE. In order to design a simplified cleaning procedure, KOH SDE was replaced with HNA (10% HF: conc. HNO<sub>3</sub> – 1:10) SDE, such that Piranha, a less complex wet chemical cleaning process, can be utilized.

### **3.5 Experimental Matrix for Simplifying Wafer Cleaning Steps**

In order to identify the process steps that are critical to producing high quality devices, an experimental matrix was designed towards simplifying the wafer cleaning process, and reducing the number of steps. The impacts of surface degreasing, organic removal and SDE on surface texturing were investigated. Four scenarios were

considered with no prior wafer treatments – Group 1 (AMI only), Group 2 (Piranha only), Group 3 (both AMI and Piranha, corresponding to our standard process), and Group 4 (DI water). In this experiment, KOH was substituted with HNA for the SDE in there to avoid the introduction of  $K^+$  and eliminate the need for more complex RCA cleaning. The overall reaction of HNA with Si is expressed as Eqn. 3.2 according to [68]:



Si solar cells require a textured surface to reduce reflection and increase internal light trapping. Optimal texturing for c-Si/a-Si heterojunction differs from diffused junctions due to specific junction formation mechanism and surface sensitivity. Here, orientation-dependent surface texturing was then carried out using a mixture of 8 ml, 25% w/w aqueous tetramethylammonium hydroxide (TMAH), 18 ml isopropanol (IPA) and 175 ml DI water, heated at 75-80° C and accompanied with ultrasonic agitation [69]. Texturing was accomplished in two phases – agitation-assisted creation of nucleation sites for 10-20 minutes and an etch step without agitation for another 10-20 minutes, making a total of ~ 40 minutes in TMAH. The samples were then rinsed in DI water with intermittent IPA spray, after which they were cleaned in piranha to completely remove TMAH residue and were dipped in 10% HF for oxide removal. The four different wafer-cleaning/texturing sequences used for this study are detailed below and illustrated in Figure 3.3 along with steps where XPS was measured:

Group 1: samples were treated with acetone, methanol and isopropanol (AMI) and rinsed in DI water.

Group 2: samples were treated with piranha ( $\text{H}_2\text{SO}_4$ :  $\text{H}_2\text{O}_2$  - 3:1) and rinsed in DI water.

Group 3: samples were treated with standard solvents plus piranha (AMI+P) and rinsed in DI water (Std. process).

Group 4: samples were only rinsed in DI water.



Figure 3.3: Processing sequence for the four batches of samples used for the wafer cleaning/texturing experiment [63].

### 3.6 XPS Analysis of Cleaning Steps

XPS was used to characterize the wafer surface at different stages during the cleaning process in order to quantify the impact and value of each step (see Figure 3.3). Of the various surface characterization techniques available, XPS was utilized because of its ability to detect electrons originating from the top few atomic layers, making it a unique surface sensitive technique for elemental analysis. After chemical treatment at IEC, samples are quickly loaded into a portable sample holder with a vacuum seal within seconds for transport to Brown Lab, where they are loaded into the XPS load lock to prevent oxides formation and adventitious carbon on the samples. All analysis was carried out under ultra-high vacuum (UHV) conditions with typical operational pressure of  $1 \times 10^{-9}$  mBar. The result from the XPS analysis of each cleaning step was then compared with effective minority carrier lifetime ( $\tau_{\text{eff}}$ ) and implied open circuit voltage ( $iV_{\text{OC}}$ ), estimated using QSSPC decay measurement on samples passivated with quinhydrone-methanol solution.

### 3.6.1 XPS Analysis after Organic Removal Step (XPS-1)

The first XPS analysis was carried out after the surface degreasing/ carbon contaminant removal step on all four different wafer-cleaning/texturing sequences – AMI (Group1), Piranha (Group2), AMI+Piranha (Group3) and DI water rinse (Group4). Figure 3.4 shows the qualitative survey spectrum for Groups 1 - 4 conditions with signals for silicon, carbon, oxygen and fluorine. Silicon 2s and 2p plasmonic peaks and Auger KLL peaks for oxygen and fluorine were also identified [70]. No peaks corresponding to metallic elements were observed from the survey scan irrespective of the cleaning condition. This suggests negligible metal ions on the wafer surface at the start of the cleaning process since group 4 samples, with only DI water, showed similar result.

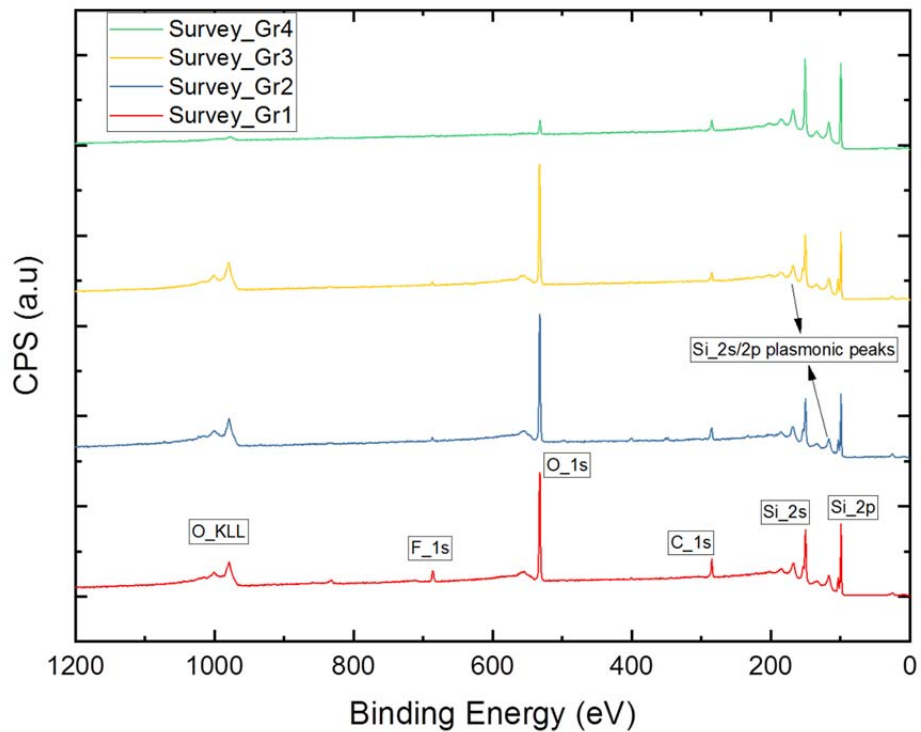


Figure 3.4: XPS-1 Qualitative Survey for Groups 1, 2, 3 and 4 showing peaks for Silicon (2s, 2p and plasmonic peaks), Carbon 1s, Oxygen (1s and Auger KLL peak) and Fluorine 1s.

Oxygen signals from samples exposed to solvent and/or Piranha showed higher peaks. This is attributed to the oxidizing action of  $H_2O_2$  and multiple rinses in DI water. Carbon signals for the AMI samples showed higher concentration due to carbon residue from the solvents. Samples exposed to only AMI showed higher fluorine content than samples with no prior chemical treatment. This trace amount of fluorine identified at this point is commonly attributed to outgassing of fluorine from the heated, Teflon™-coated sample holder cassettes used in this study [71]. Samples exposed to both AMI and Piranha showed lower fluorine content than the samples treated with only AMI, signifying the action of piranha on fluoride. Thus, a piranha step after AMI is crucial to removing carbon residue and outgassed fluoride.

### **3.6.2 XPS Analysis after HNA SDE Step (XPS-2)**

A second XPS analysis was carried out after HNA SDE to determine the elemental composition of impurities on the silicon samples at this point and their relative concentration. Figure 3.5 shows the survey spectrum for Group1 condition after organic removal step (XPS-1) and HNA SDE (XPS-2). The sharp drop in the oxygen peak in Figure 3.5b is attributed to the action of HNA, which results in an increase in the silicon peak, indicative of a purer surface. This justifies the motivation for this cleaning sequence: the nitric acid in the HNA solution oxidizes the silicon, while the hydrofluoric acid etches the oxidized compound according to [72].

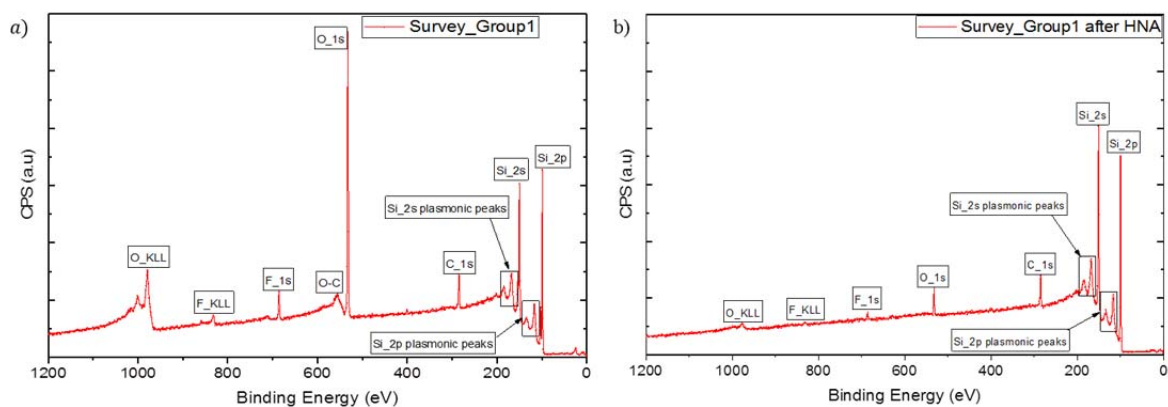


Figure 3.5: XPS survey spectral for group1 condition showing peaks for silicon, carbon, oxygen and fluorine: a) after organic removal step, and b) after HNA SDE [63].

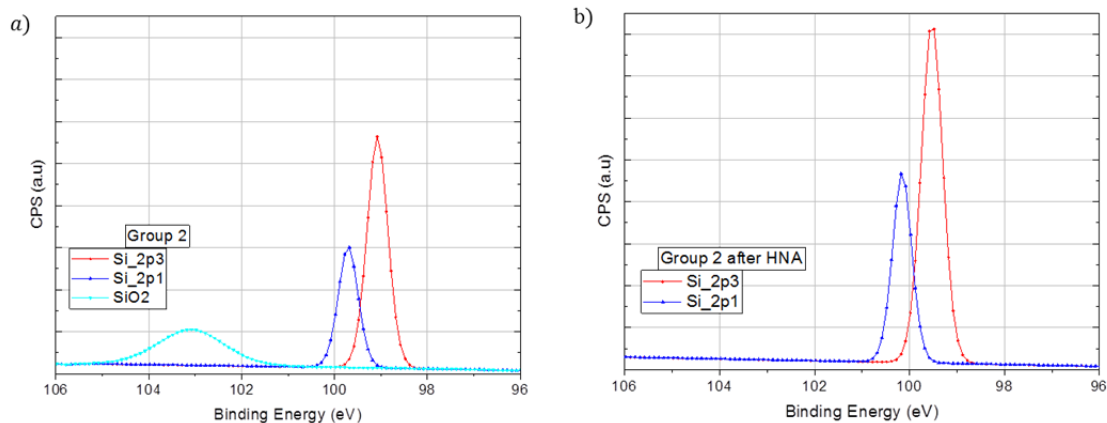


Figure 3.6: High-resolution silicon XPS scans for group 2 condition: a) after piranha dips for XPS-1 and b) after HNA SDE for XPS-2 [63].

Figure 3.6 shows the high-resolution scans for silicon after XPS-1 and XPS-2 respectively; comparing their silicon, oxide and silicate peaks to further illustrate this point. The silicon peak in Figure 3.6b, taken after XPS-2, shows stronger intensity when compared with the silicon peak in Figure 3.6a and shows no peak for oxide or

silicate at binding energy 103.5 eV. This confirms that a purer surface is achievable after HNA SDE.

### 3.6.3 XPS Analysis after TMAH Texture (XPS-3)

A third and final XPS analysis was carried out at the end of the cleaning process after texturing the samples with TMAH solution and the subsequent TMAH residue removal steps. The TMAH texturing step uses a 1% TMAH solution to achieve orientation dependent pyramids, which helps to reduce hemispherical reflection by improving the optical path length of incident light on the c-Si surface. Figure 3.7a and 3.7b shows a c-Si sample before and after TMAH texturing step, while Figure 3.7c show an illustration of how the textured surface reduces front reflection and improves light trapping.

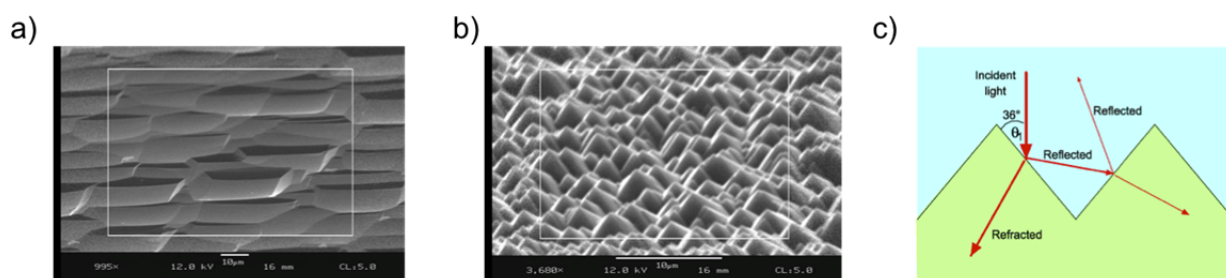


Figure 3.7: a) Chemically polished c-Si surface used for this experiment, b) c-Si surface after TMAH texturing step showing v-grooves and c) Illustration of light trapping scheme.

The sample surfaces showed high silicon signal at this point with a weak adventitious carbon peak. The survey scans and high-resolution scan for silicon on group 1-4 samples after TMAH texture is shown in Figure 3.8 and 3.9.

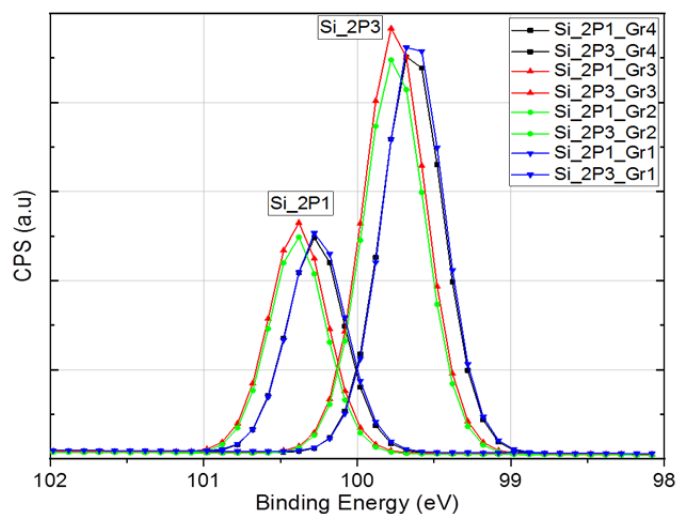


Figure 3.8: Silicon peaks for XPS-3 scans for groups 1- 4 conditions after TMAH texturing step [63].

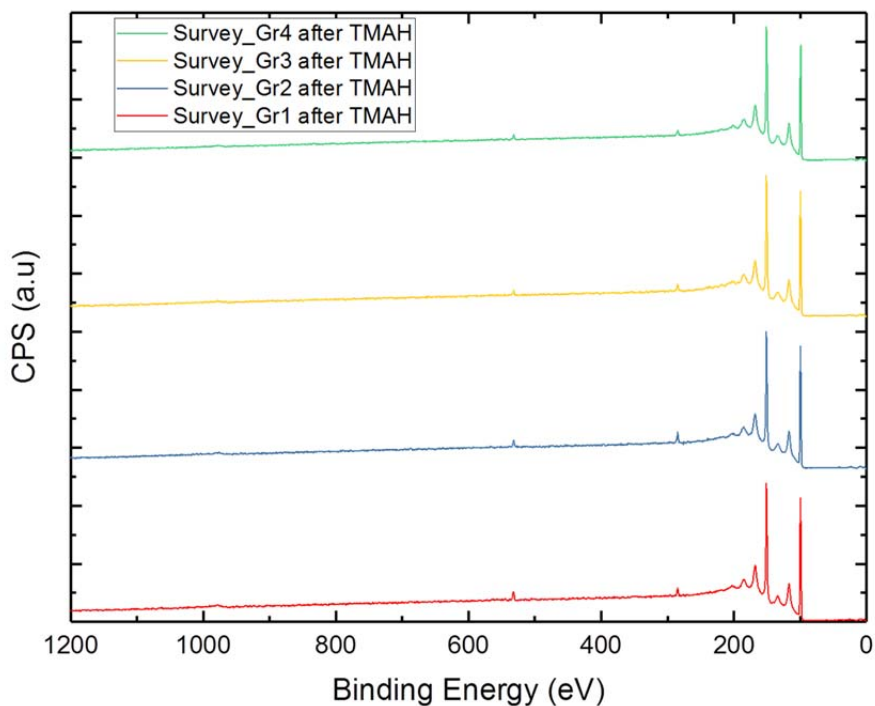


Figure 3.9: XPS-3 Qualitative Survey for Groups 1, 2, 3 and 4 showing high peaks for Silicon (2s at ~145 eV, 2p at ~99 eV), reduced peaks for Carbon 1s (285 eV), Oxygen 1s (~530 eV) and no peak for Fluorine 1s (~688 eV).

The silicon intensities across all four conditions appear uniform after XPS-3, an indication of equivalent surface quality. This buttresses the critical nature of HNA SDE, which uses HNA to remove few microns of Si including any contaminated layers from the wafer surface and TMAH texturing. Thus, these steps are very critical in removing surface contaminant, irrespective of prior chemical treatments. The shift in peak position in Figure 3.8 originates from internal drifts within the XPS equipment. Each pair of data that fits perfectly was taken at the same time.

To summarize the results from this study, the percentage composition of impurities aggregated by elements was determined and is shown in Figure 3.10. The result is comparable with XPS wafer-cleaning studies reported in literature [73], which often contain about 5, 10 and 1 atomic percentage of Oxygen, Carbon, and Fluorine respectively. The largest decrease in oxygen composition was achieved after HNA etch due to the action of HF, while carbon, oxygen and fluorine all experience further reduction after the TMAH texturing step.

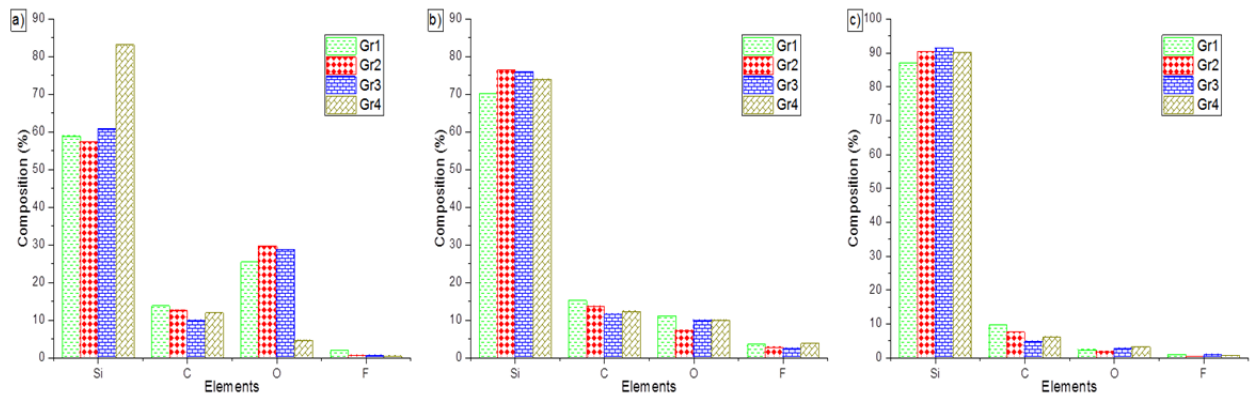


Figure 3.10: Percentage composition of elemental species (Si, C, O and F) across all four conditions showing their variation with chemical treatment of the silicon samples: a) after XPS-1, b) after XPS-2, and c) after XPS-3 [63].

The trace amounts of carbon and oxygen detected at this stage arguably originate from the ambient air in the lab. It can be inferred from Figures 3.10b and 3.10c that the HNA SDE and TMAH texturing steps are critical to achieving a uniform surface across all four conditions irrespective of any organic removal step.

To further verify that the surface purity resulting from all four conditions are equivalent after HNA SDE and TMAH texturing steps, 10 nm i.a-Si:H layer was deposited on the four batches of samples with different pre-treatments but completed with HNA etch, TMAH texturing, and TMAH residue removal. Figure 3.11 shows the  $\tau_{\text{eff}}$  and  $iV_{\text{oc}}$  to be approximately 2 ms and 740 mV respectively. This supports the XPS data, which shows that irrespective of the organic removal step or the lack thereof, the samples perform fairly uniformly following both HNA SDE and TMAH texturing. Thus, the initial solvent and/or piranha treatment steps are not crucial and can be excluded from the cleaning process.

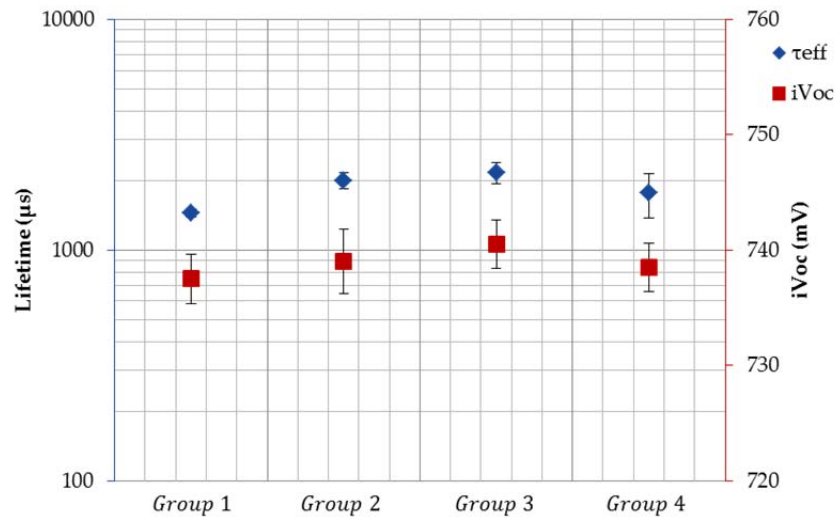


Figure 3.11:  $\tau_{\text{eff}}$  and  $iV_{\text{oc}}$  for i.a-Si:H passivated surfaces on four different wafer preparation sequences. All processing sequence includes HNA SDE, TMAH texture and TMAH residue removal steps. Error bar shows the range of data from four samples used for lifetime measurement [63].

### 3.7 Effect of TMAH Residue Removal

To further simplify this process, the merits and impact of the TMAH residue removal step were investigated more closely to determine the simplest wafer cleaning sequence without compromising passivation quality. Table 3.1 shows the six cleaning sequences chosen to depict the role of TMAH texturing and TMAH residue removal step on the final sample quality.

Table 3.1: Cleaning sequences to study the effects of TMAH texturing and TMAH residue removal step [63].

S/N	Description	Abbreviation
1	HF only	Hf
2	HF + HNA	HfHn
3	AMI + Piranha + HF + HNA	APHfHn
4	HF + TMAH	HfT
5	HF + TMAH + Piranha	HfTP
6	HF + HNA + TMAH + Piranha	HfHnTP

The first 3 treatments lack TMAH texturing step (T), while the other 3 treatment includes TMAH texturing step but with different pre- and/or post-TMAH treatments. Quinhydrone-methanol was used for the passivation study because of the ease of QH-MeOH process for passivation as compared with the CVD plasma process for i.a-Si:H passivation. To ensure oxide removal, all samples were dipped in HF just before the QH-MeOH immersion.  $\tau_{\text{eff}}$  and  $iV_{\text{OC}}$  was measured intermittently over an hour using Sinton QSSPC decay measurement.

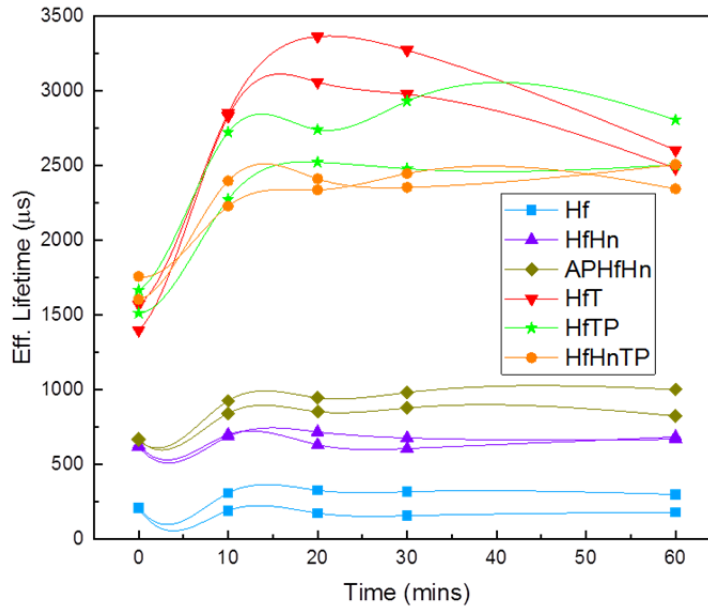


Figure 3.12: Time dependent behavior of  $\tau_{\text{eff}}$  from quinhydrone-methanol immersion experiment on the merits of TMAH texturing and TMAH residue removal step [63].

Figure 3.12 shows the  $\tau_{\text{eff}}$  for the six cleaning sequences chosen to depict the role of TMAH texturing and TMAH residue removal step on the final sample quality. It can be seen that the 3 pairs without TMAH texturing (Hf, HfHn and APHfHn) in Figure 3.12 all have lifetimes below 1 ms, while the 3 pairs with TMAH texturing (HfT, HfTP and HfHnTP) all have lifetime over 2 ms. In general, samples with TMAH texturing showed superior passivation in QH-MeOH immersion, irrespective of the TMAH residue removal steps. This corroborates the XPS data that shows significant differences on the surface elemental composition after TMAH texturing. The additional passivation observed on the samples with TMAH texturing step, but without TMAH residue removal, can be ascribed to the TMAH residue on the wafer surface. Figure 3.12 suggests that the passivated samples with TMAH residue (HfT)

are unstable as  $\tau_{\text{eff}}$  starts to degrade after  $\sim 25$  mins. This is evident from the fast decay associated with these samples. Other negative effects of TMAH residue on  $\tau_{\text{eff}}$  and  $iV_{\text{OC}}$  are not obvious in QH-MeOH as TMAH residue dissolves in methanol. However, with 10 nm i.a-Si:H layer, the effects of TMAH residue becomes more pronounced and marked with low  $\tau_{\text{eff}}$ ,  $iV_{\text{OC}}$  and wider error margin.

Based on the result from the QH-MeOH immersion study, the same experiment was repeated using 10 nm-thick i.a-Si:H layer deposited by dc plasma process on selected cleaning sequence to demonstrate that a simplified wafer cleaning approach can be used for solar cell fabrication. Figure 3.13 highlights the importance of TMAH texturing and the subsequent residue removal for samples passivated with 10 nm i.a-Si:H by the significant differences in  $\tau_{\text{eff}}$  and  $iV_{\text{OC}}$  between samples that lack either of these steps and samples with both steps.

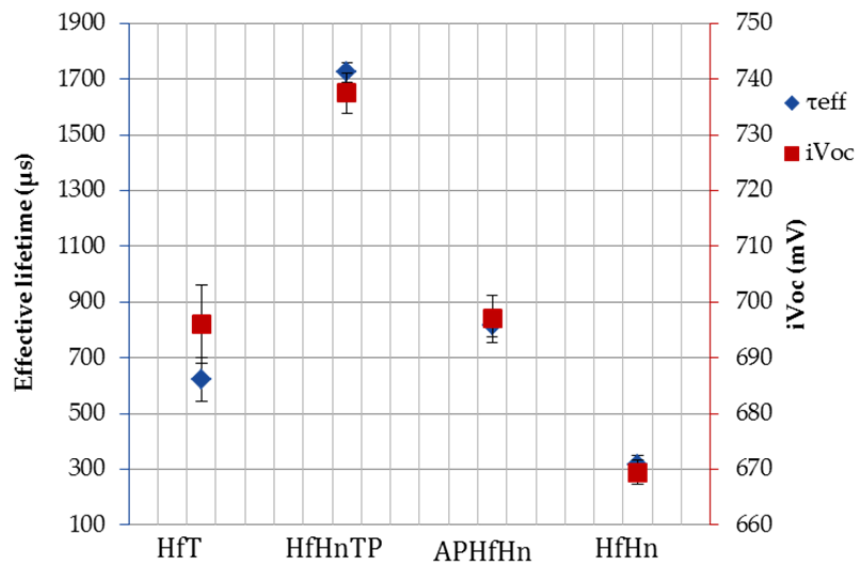


Figure 3.13:  $\tau_{\text{eff}}$  and  $iV_{\text{OC}}$  result from 10 nm i.a-Si:H passivated surfaces of four selected conditions to demonstrate the effect of TMAH residue removal step [63].

The poor performance of HfT samples in Figure 3.13 arises from the absence of TMAH residue removal, which is more noticeable with i-a-Si:H layer than with QH-MeOH. APHfHn and HfHn conditions illustrates the importance of TMAH texturing as both conditions lack TMAH texturing step, while HfHnTP condition benefits from both TMAH texturing and residue removal step, thereby recording the highest  $\tau_{\text{eff}}$  and  $iV_{\text{OC}}$ . Thus, the TMAH residue removal step is critical for sample preparation geared towards solar cell fabrication. HfHnTP is hereafter used as the simplified cleaning process for our solar cells.

### **3.8 Summary**

In this chapter, I have presented a systematic study to evaluate the critical steps for silicon wafer preparation prior to SHJ solar cell fabrication. XPS was used to characterize wafer surfaces at strategic points in the preparation sequence to determine the elemental composition of known silicon impurities. It was shown that HNA SDE, which removes a few microns of contaminated layers from the wafer surface, appears to be the first critical step in removing surface contaminants. Thus, other surface treatment prior to HNA etch can be excluded as they offer little or no benefit to the final surface quality. TMAH texturing step proved to be another critical step in the cleaning process, with marked improvement in  $\tau_{\text{eff}}$  and  $iV_{\text{OC}}$ . This was validated by XPS data and  $\tau_{\text{eff}}$  data with both QH-MeOH and PECVD-grown 10 nm i.a-Si:H layer passivation. TMAH residue removal was also found to be essential for samples intended for device fabrication. It is understood that the solvents and Piranha used during the TMAH residue removal process also help with removing any organic contaminant on the wafer surface.

## Chapter 4

### IMPROVING THE CHEMICAL AND FIELD EFFECT PASSIVATION OF CRYSTALLINE SILICON SOLAR CELL

#### 4.1 Introduction

The performance of a solar cell depends on how well the losses due to recombination; series resistance and light coupling are minimized. This chapter focuses on reducing recombination loss by reducing interface defect density. The influence of the surface and bulk recombination affect the implied  $V_{OC}$  and equivalently minority carrier lifetime, and can be attributed to the interface defect densities, and the bulk silicon quality, respectively. The samples used for this study were from high quality Si wafers with bulk lifetime  $> 5$  ms, thus surface recombination is the limiting factor to realizing high effective lifetime. PECVD conditions and parameters were extensively studied to derive deposition conditions that yield a-Si:H films with high quality chemical and field effect passivation.

Since the bulk defects distribution of these a-Si:H films consist of the valence and conduction band tail states, and Gaussian mid-gap states, the thicker these layers are, the more recombination that is expected in these layers once they exceed the minimum thickness needed for complete coverage and uniform passivation on the textured surface. This is not surprising, given that the transport lengths in such defective layers are very short, due to low carrier mobility. It is also noteworthy that in front junction cells, these layers contribute to the parasitic absorption losses (i.e. optical losses), together with the overlying TCO layers, and hence should be made as

thin as possible. To that effect the thickness of the heterojunction layers were optimized to achieve excellent passivation with thinner a-Si:H films.

Optical emission spectroscopy was used extensively to study the plasma kinetics of the dc-plasma process during PECVD growth of the a-Si:H films. This study enabled the correlation of the changes in current, pressure, temperature and gas flow rate to growth mechanism and properties of the corresponding a-Si:H films.

Our effort to improve the c-Si surface passivation, which resulted in the development of a bi-layer deposition approach with hydrogen post deposition plasma treatment, is presented in this chapter. To minimize the loss in passivation after doped layer deposition, the p- and n-layers that form the heterojunction and back surface field, respectively, were also optimized for excellent chemical and field effect passivation. In order to fabricate high efficiency silicon heterojunction solar cells, it is necessary to achieve heterojunction layers that have excellent transparency, conductivity, and passivation (both chemical and field-effect passivation). A detailed doped layer characterization is presented in this chapter.

## **4.2 Optical Emission Spectroscopic (OES) Study of PECVD Plasma Kinetics**

Time resolved optical emission spectroscopy was extensively used to investigate the plasma kinetics of our PECVD process to better understand the role of the different input parameters like plasma current, pressure, temperature, gas flow rate and dilution ratio on the transient behavior of the resultant plasma. The OES was done in-situ during PECVD process. As detailed in section 2.2.1.7, an optical fiber mounted on the PECVD chamber window was used to collect the multiple optical emission lines from the plasma into the spectrometer, where a diffraction grating separates the incoming light into element-specific wavelengths. A corresponding detector measures

the intensity of light for each wavelength. The optical fiber is connected to a computer system that acquires the measured intensities and processes the data through a predefined calibration to determine the concentrations of different species.

To begin this study, the emission wavelength for the different species in the a-Si:H plasma is first identified by performing a survey using DC plasma. Figure 4.1a shows Si peaks at 288 nm and 390 nm, SiH<sub>x</sub> at 413 nm, H<sub>β</sub> at 485 nm, H<sub>α</sub> at 656 nm and Ar at 750 nm respectively. The peaks at ~ 670 nm and ~ 740 nm emanates from stray light and background noise in the OES system. The actual emission lines are formed by the excitation of silane molecules through electron impact, resulting in the creation of charged species. The subsequent relaxation of these charges species is accompanied by photon emission. Figure 4.1b shows the plasma kinetics for a typical a-Si:H DC plasma, which indicates that the entire duration of an i-layer deposition (approx. 40-50 secs) occur at the non-equilibrium transient phase of the plasma, thus making it difficult to control.

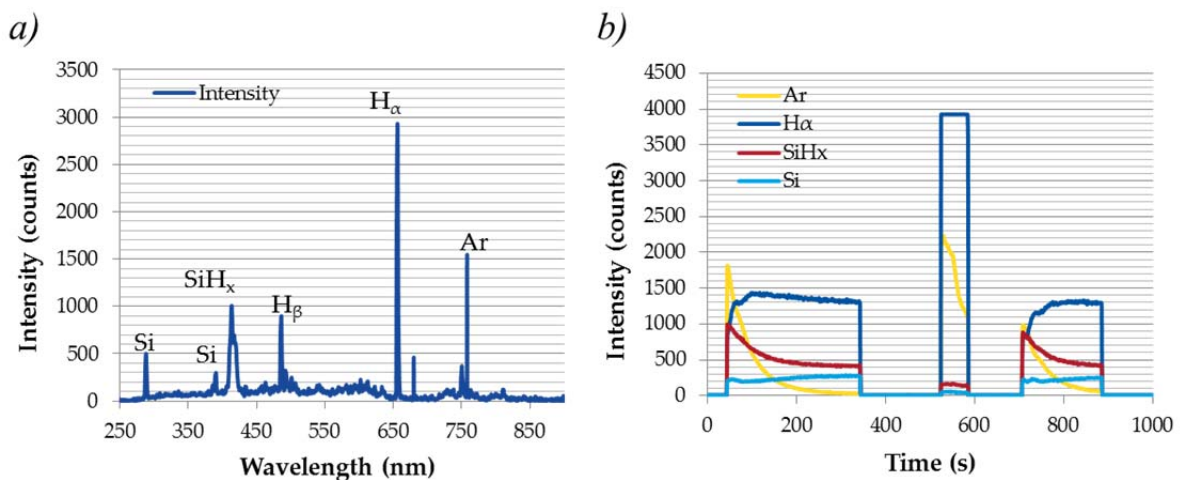
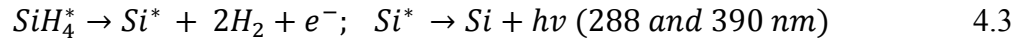
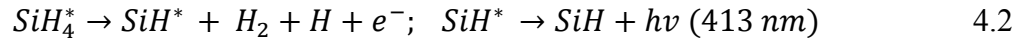


Figure 4.1: a) OES survey spectral and b) Typical a-Si:H plasma during deposition using a DC plasma.

The excitation and radiative transition for silane gas can be described as follows:



which can decay in one of two ways:



$\text{H}_\alpha$  (at 656 nm) and  $\text{H}_\beta$  (485 nm) photons, on the other hand, are produced when an excited hydrogen atom relaxes from energy level  $n=3$  to  $n=2$  and  $n=4$  to  $n=2$  respectively. The transition from energy level  $n=3$  to  $n=2$  is more common for hydrogen, thus making  $\text{H}_\alpha$  photon a predominant evidence of hydrogen ionization.

The emission density is proportional to the species concentration which is determined by the electron density, electron energy distribution function (EEDF) and gas mixtures. Figure 4.2 shows the difference in peak intensities of radiative transitions between DC and RF sources due to the different in the EEDF. The EEDF for an RF source is a maximum at low energy (long wavelength), thus low emission intensities for RF sources at long wavelength (with high electron density) are common as is the case for  $\text{H}_\alpha$  at 656 nm (blue line). However, at high energy (short wavelength), where the EEDF for RF is low, RF sources require higher intensities to achieve equivalent electron density, thus higher emission intensity can be seen for  $\text{SiH}_4$  at 413 nm (blue line). The reverse is true for DC sources with high emission intensities at low energy (long wavelength) as is the case for  $\text{H}_\alpha$  at 656 nm (red line) and low emission intensities at high energy (short wavelength) as can be seen for  $\text{SiH}_4$  at 413 nm (red line).

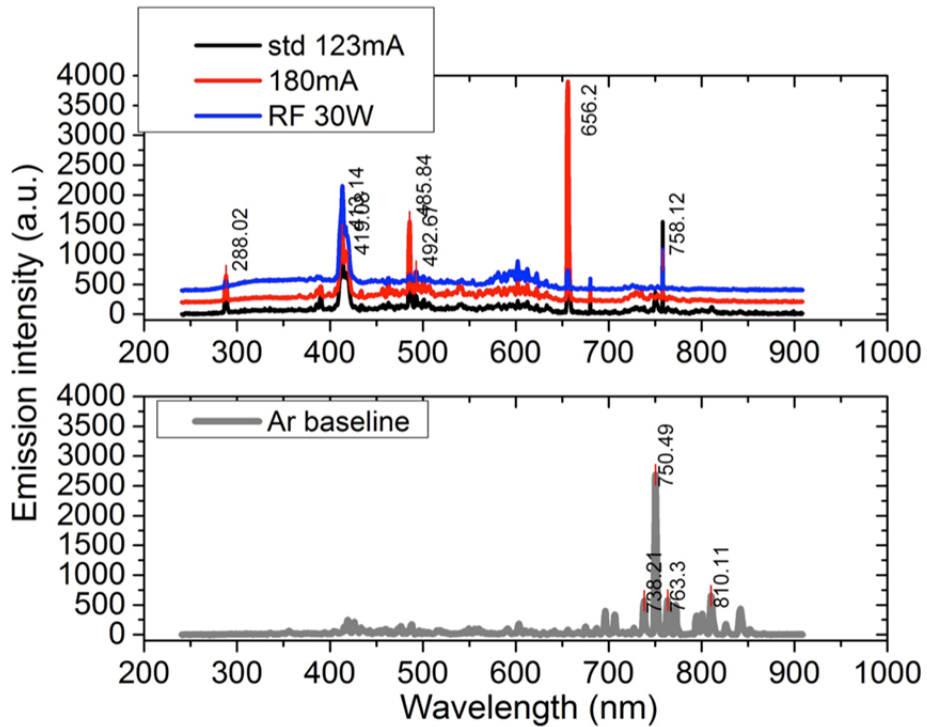


Figure 4.2: OES survey spectral showing the effect of electron energy distribution, EED on DC (black and red lines) and RF (blue line) sources on the peak intensity of the plasma species (upper section), and the peak position for Ar used as purge and vent gas (lower section).

Equipped with the knowledge of the individual species and their respective emission wavelengths, we set out to design an experiment that correlates plasma properties to deposition conditions and establish device applicable sub-10 nm i.a-Si:H layer with excellent passivation. Table 4.1 shows details of this experimental set up.

Table 4.1: Experimental set up for studying the effect of varying input parameters on plasma transient behavior. Highlighted number represents our standard process conditions.

Parameters	Characterization
DC current (mA): 180, 150, <b>120</b> , 90, 60	OES spectrum, time acquisition & voltage monitoring
RF power (W): 60, 50, 40, <b>30</b> , 20	OES spectrum, time acquisition & voltage monitoring
H <sub>2</sub> dilution ratio, (R=H <sub>2</sub> /SiH <sub>4</sub> ): 4, 3.5, 3, <b>2.5</b> , 2	OES spectrum, time acquisition & voltage monitoring
Pressure (torr): 2, 1.75, 1.5, <b>1.25</b> , 1	OES spectrum, time acquisition & voltage monitoring
Combinations: During which plasma transition behavior is modified	OES spectrum, time acquisition & voltage monitoring

All parameter variations were implemented with fixed substrate temperature ( $T_{\text{sub}}$ ) of 200 °C. OES spectral, time acquisition and plasma voltage were recorded for varying DC current, RF power, H<sub>2</sub> dilution and pressure. The plot of their respective plasma transient behavior is shown in Figure 4.3. It is clear from Figure 4.3a that reducing the DC plasma current has the net effect of reducing the transient behavior of the a-Si:H plasma, which improves the overall controllability of the plasma process, especially critical for typical layer depositions of ~ 40 sec . RF power series also shows transient behavior in the plasma species, which reduces as the power is reduced. However, the challenge of matching the forward and reflected power in RF plasma

discourages the use of RF power for these short (on the order of seconds) plasma processes. This challenge is evident from the ripples in the SiHx spectral line and the inability to sustain plasma for the entire duration of the 20 W-condition in Figure 4.3b. Other parameters show some degree of transient behavior regardless of their variation. Figure 4.3c shows that higher pressure tends to promote steady state condition, while hydrogen dilution ratio as shown in Figure 4.3d has no net effect on the transient behavior of the plasma.

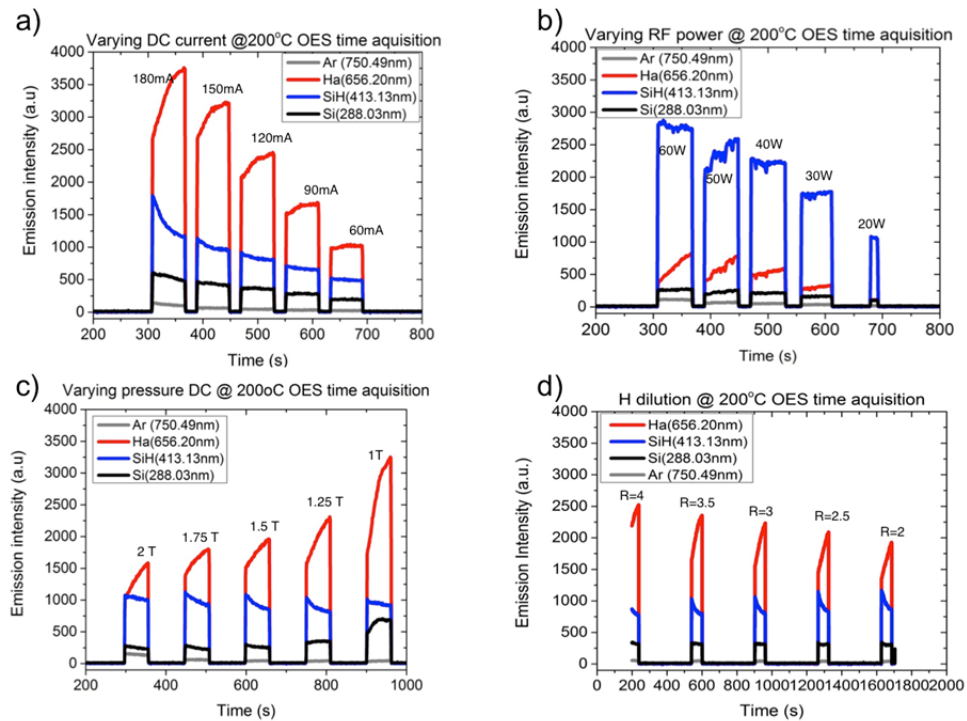


Figure 4.3: OES spectral for varying a) DC current, b) RF power, c) pressure and d) hydrogen dilution ratio, at  $T_{sub}$  of  $200^\circ\text{C}$ . For each parameter variation, other parameters were fixed at 123mA, 1.25 T and H dilution of 2.5.

The trends from this experiment were further combined to either reduce or increase transient behavior during a plasma process. Figure 4.4 and 4.5 shows such plots.

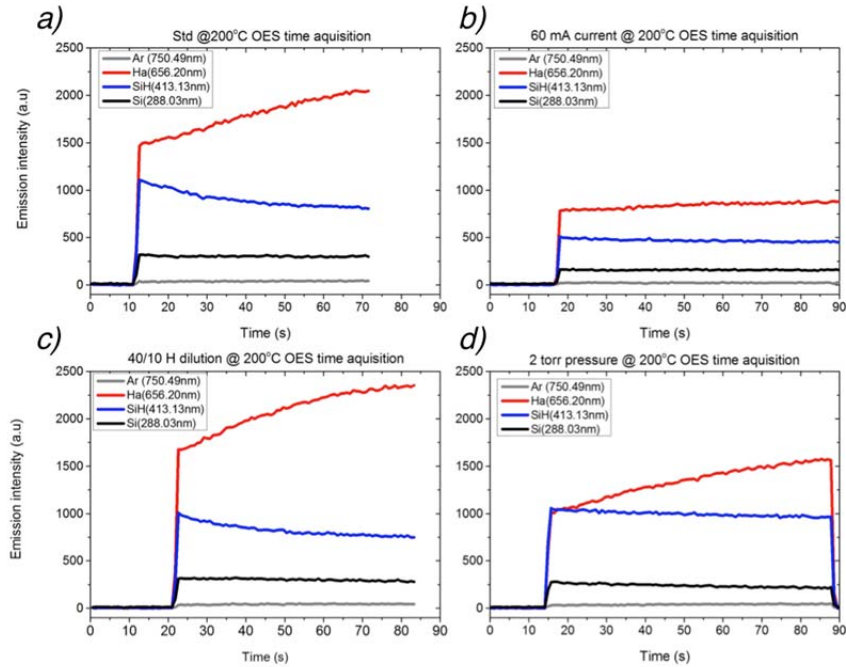


Figure 4.4: Parameter combinations to reduce DC plasma transient behavior at  $T_{\text{sub}}$  of 200 °C: a) std. i.a-Si:H (ref. condition), b) low plasma current, c) high hydrogen dilution ratio and d) high pressure.

Figure 4.4a shows the transient behavior for our standard plasma process (123 mA, 1.25T and R=2.5) at  $T_{\text{sub}}$  of 200 °C. Figures 4.4b, 4.4c and 4.4d show different parameter combinations, based on the OES study, which can reduce the transient behavior of the DC plasma. Reducing the DC current to 60 mA and increasing the pressure to 2T appears to be the most effective way of achieving stable plasma. These conditions also create a low plasma voltage ( $V_{\text{pl}}$ ), corresponding to low acceleration

potential and ion bombardment energy, and therefore create minimal damage to the wafer surface. Increasing the hydrogen dilution on the other hand has minimal effect.

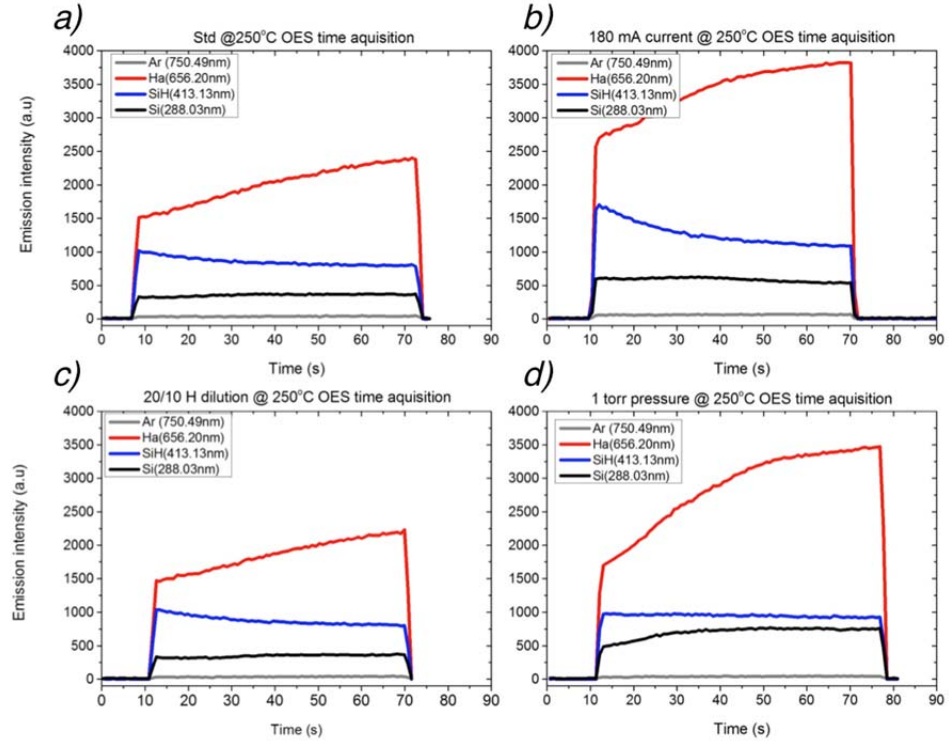


Figure 4.5: Parameter combinations to increase DC plasma transient behavior at  $T_{\text{sub}}$  of 250 °C: a) std. i.a-Si:H (ref. condition), b) high plasma current, c) low hydrogen dilution ratio, and d) low pressure.

Figure 4.5a shows the transient behavior for our standard plasma process (123 mA, 1.25T and R=2.5) at  $T_{\text{sub}}$  of 250 °C. Figures 4.5b, 4.5c and 4.5d show different parameter combination, based on the OES study, which can increase the transient behavior of the DC plasma. Increasing the DC current to 180 mA and reducing the pressure to 1T appears to be the most effective method of promoting transient

behavior of the plasma. These conditions occur at high plasma voltage ( $V_{pl}$ ), corresponding to high acceleration potential and ion bombardment energy, and therefore create damages to the wafer surface. Reducing the hydrogen dilution in this case also has minimal effect on the plasma behavior.

With this study, a new i-layer condition was established that more quickly reaches steady state condition and reduces plasma voltage, corresponding to reduced ion bombardment energy during deposition. The new i-layer recipe consists of DC current of 60 mA, pressure of 1.75 T, and hydrogen dilution ratio of 2.5 at a  $T_{sub}$  of 200 °C. For easy distinction, the new i-layer recipe is hereafter referred to as low-current-high-pressure i-layer (LCHP-i), while our standard i-layer plasma process (consisting of DC current of 123 mA, pressure of 1.25 T, hydrogen dilution ratio of 2.5 at a  $T_{sub}$  of 200 °C) will be referred to as high-current-low-pressure i-layer (HCLP-i).

### **4.3 Hydrogen Plasma Post-Deposition Treatment**

Hydrogen plasma post deposition treatment has been considered as an effective and manufacturable method to saturate the surface dangling bonds, thereby reducing the recombination losses leading to higher  $iVoc$  [<sup>74</sup>][<sup>75</sup>]. These treatments are usually very short on the order of 10-30 seconds because increased exposure of the ultra-thin (<10 nm) i.a-Si:H layer to hydrogen plasma can result in etching and consequent degradation of the passivation qualities [<sup>76</sup>]. Such short duration hydrogen plasma treatment occurs at the non-equilibrium transient phase of the plasma, hence, it is critical to monitor the plasma kinetics using time resolved OES. The correlation between hydrogen plasma composition and passivation quality of the i.a-Si:H films was investigated using OES and effective minority carrier lifetime. The relation

between the hydrogen plasma process parameters to the  $H^*$  concentration was investigated by monitoring the  $H_\alpha$  spectral line at 656 nm. The effective minority carrier lifetime of c-Si wafers after the hydrogen plasma treatment of the i.a-Si:H layers was co-related with the  $H_\alpha$  to explain the passivation quality of the films. The improved passivation of the films is attributed to an increase in  $H^*$  concentration and a reduced ion bombardment energy as reported in [77]. This study also highlights the effect of annealing in relaxing the i.a-Si:H film. Much of the work in this section has been adapted from [77].

In order to study the dependence of  $H^*$  species on different process conditions, 3 series of experiment that constitute the variation of dc plasma current, pressure and hydrogen flow rate was performed. In each series, 2 of the parameters were kept constant while 1 was varied and its effect on the  $H^*$  concentration and induced plasma voltage ( $V_{pl}$ ) was observed. The  $V_{pl}$  relates to the acceleration potential of the ions and thus the ion bombardment energy. Figure 4.6 shows the plots for the 3 series that were studied. It can be inferred from Figure 4.6a that increasing the DC plasma current has the net effect of increasing  $H_\alpha$  with little or no change in  $V_{pl}$  during hydrogen plasma treatment. Figure 4.6b shows that both  $H_\alpha$  and  $V_{pl}$  can be reduced significantly by increasing the pressure. Finally, Figure 4.6c shows that the hydrogen flow series has no observable effect on either  $H_\alpha$  or  $V_{pl}$ .

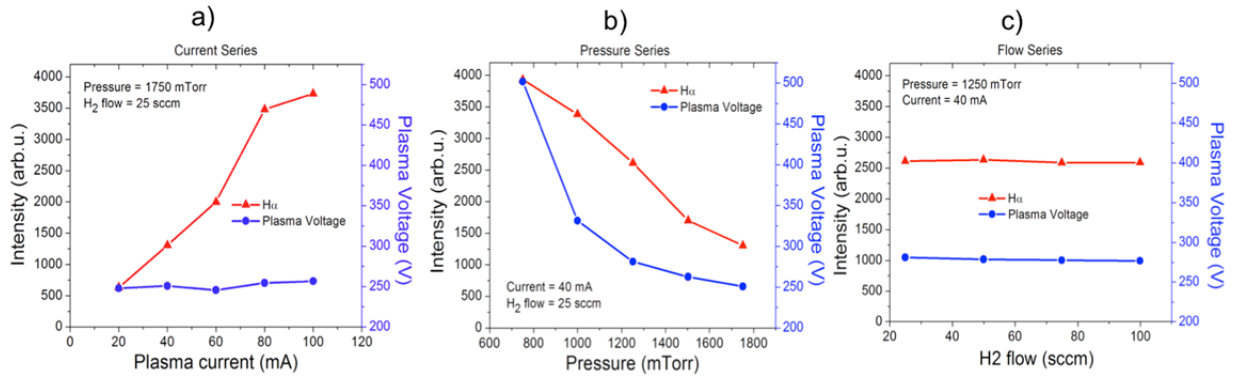


Figure 4.6: Effect of varying a) dc plasma current, b) pressure and c) hydrogen flow, on  $H_{\alpha}$  conc. and  $V_{pl}$  [77].

Figure 4.6a shows that increasing the dc plasma current from 20 to 100 mA have a strong positive correlation with  $H_{\alpha}$  but no effect on plasma voltage hence increasing the power density from 3 to 18  $\text{mW}/\text{cm}^2$ . Similarly, Figure 4.6b shows that when the pressure is increased from 750 to 1750 mTorr, the plasma voltage and  $H_{\alpha}$  decreases, and the power density decreases from 14 to 7  $\text{mW}/\text{cm}^2$ . From the above results we can conclude that: 1) increasing the dc plasma current increases the concentration of  $H_{\alpha}$  species; 2) increasing the pressure decreases  $V_{pl}$ , which in turn reduces the ion bombardment energy and the acceleration potential of the particles, and similarly reduces  $H_{\alpha}$  species; and 3) Increasing the hydrogen flow has no net effect on  $V_{pl}$  or  $H_{\alpha}$  concentration.

Based on the OES results, a second set of experiments were conducted to study the effect of changing  $H_{\alpha}$  concentration and  $V_{pl}$  on passivation during HPT. By varying current and pressure as shown in Table 4.2 we can understand the effect of ion bombardment energy as measured by  $V_{pl}$  and the total  $H^*$  available for saturation of dangling bonds, on the passivation quality of a-Si:H films.

Table 4.2: Process conditions for studying the effect of varying  $H_{\alpha}$  conc. and  $V_{pl}$  on passivation [77].

Process conditions	LV	HV
LH	20 mA, 1.75 T	20 mA, 0.75 T
HH	100 mA, 1.75 T	100 mA, 0.75 T

In Table 4.2, LV and HV signifies low and high plasma voltage, while LH and HH signify low and high  $H_{\alpha}$  conc. Thus LVLH condition implies a condition that yields a plasma state with low  $V_{pl}$  and low  $H_{\alpha}$  concentration. Applying the result from the earlier experiment, which suggests that  $H_{\alpha}$  conc. can be controlled by dc plasma current and  $V_{pl}$  can be controlled by pressure, this 2x2 matrix was developed. This study also investigated the effect of post deposition thermal annealing in restructuring the i.a-Si:H film after HPT. The thermal annealing step was performed at a temperature of 300 °C for 25 mins.

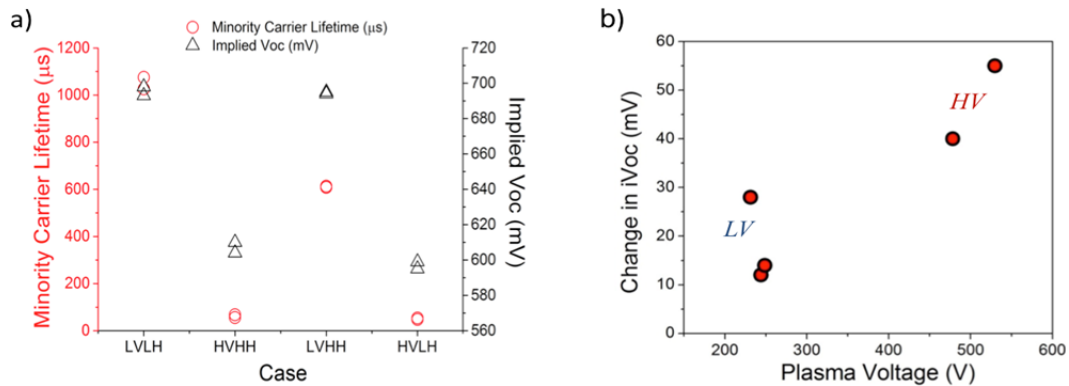


Figure 4.7: a)  $\tau_{eff}$  and  $iVoc$  of both side i.a-Si:H passivation samples treated with hydrogen plasma with varying  $H_{\alpha}$  conc. and  $V_{pl}$  before thermal annealing. b) Change in  $iVoc$  after thermal annealing as a function of the  $V_{pl}$  during hydrogen plasma treatment [77].

Figure 4.7a shows a plot for the 4 conditions outline in Table 4.2, where the  $H_{\alpha}$  concentration and  $V_{pl}$  values were varied between high and low points. The 4 conditions are LVLH, LVHH, HVLH and HVHH respectively. Figure 4.7a shows  $\tau_{eff}$  and  $iVoc$  data of 2 samples for each condition. It is clear that the passivation quality is poor for both high voltage (HV) conditions evident by the low  $\tau_{eff}$  and  $iVoc$  values, whereas at low voltage (LV) conditions the samples show better passivation quality with  $iVoc \sim 700$  mV before annealing. This could be explained by the fact that  $V_{pl}$  relates to the ion bombardment energy, thus HV conditions which corresponds to high  $V_{pl}$  results in increased surface damage due to high ion bombardment energy. For LV conditions, it has been shown that varying the current from 20 mA to 100 mA changes the  $H_{\alpha}$  concentration, which does not bode well for passivation. Figure 4.7a confirms that the LH condition, corresponding to a low plasma current condition, is preferred for better passivation quality. It is also interesting to note that despite the LVHH condition having a higher power density ( $16 \text{ mW/cm}^2$ ) than the HVLH condition ( $5.9 \text{ mW/cm}^2$ ), the LVHH condition still showed better lifetime. This suggests a strong dependence of passivation quality on  $V_{pl}$  than on  $H_{\alpha}$  conc. The power density for the other 2 conditions - LVLH and HVHH are  $3 \text{ mW/cm}^2$  and  $34 \text{ mW/cm}^2$  respectively.

In order to quantify the amount of degradation due to the high  $V_{pl}$ , we compared the high and low  $V_{pl}$  samples with a reference sample in Table 4.3. The reference sample is coated with identically deposited 10 nm-thick i.a-Si:H layer but without hydrogen plasma treatment. We find that annealing considerably improves  $\tau_{eff}$  and  $iVoc$ . The effect of annealing, shown in Table 4.3, highlights the improvement in  $iVoc$  for different  $V_{pl}$  conditions. The improvement is more significant for HV samples, which initially had very low  $\tau_{eff}$  and  $iVoc$  values. These samples had an

increase in  $iV_{oc}$  of 40 to 55 mV while the LV samples increased considerably less in the range of 10-30 mV as can be seen in Figure 4.7b. Thus, annealing HV samples show greater improvement in  $iV_{oc}$  but cannot completely recover the damage due to ion bombardment. Hence these samples have significantly lower  $iV_{oc}$  even after annealing. The maximum  $\tau_{eff}$  and  $iV_{oc}$  obtained after annealing are  $\sim 2$  ms and  $\sim 740$  mV for the LVLH sample. Thus LVLH condition was used for hydrogen plasma treatment hereafter. Note that annealing a-Si films above  $300^{\circ}\text{C}$  is not advisable since it risks effusion of H from the film creating more dangling bond defects.

Table 4.3: Implied Voc from varying plasma voltage condition during hydrogen plasma treatment. Reference sample has i-layer without hydrogen plasma treatment [77].

Voltage Conditions	Plasma Voltage (V)	Chamber pressure (T)	$iV_{oc}$ before annealing (mV)	$iV_{oc}$ after annealing (mV)
Low Vpl	231	2.75	706	739
Low Vpl	244	1.75	699	711
High Vpl	530	0.75	600	655
Reference	N.A	N.A	699	726

#### 4.4 Bi-Layer Deposition of Intrinsic Amorphous Silicon

The passivation of c-Si surface involves the reduction of the rate at which electrons in the conduction band recombine with holes in the valence band, thus improving the effective carrier lifetime. A common method of achieving excellent

passivation of the dangling bonds on the c-Si surface is by growing a thin layer of silicon dioxide ( $\text{SiO}_2$ ) [78], amorphous silicon nitride ( $\text{a-SiN}_x\text{:H}$ ) [79], amorphous silicon carbide ( $\text{a-SiC}_x\text{:H}$ ) [80], aluminum oxide ( $\text{AlO}_x$ ) [81], or intrinsic amorphous silicon ( $\text{i.a-Si:H}$ ) [82] on both sides of the c-Si surface. Amorphous silicon, however, is predominantly used because it can be easily doped to form p- and n-type contacts with improved carrier transport properties. It is also possible to further improve passivation by utilizing hydrogen or argon post deposition plasma treatment [83] to achieve very low surface recombination velocity. Results from the hydrogen plasma treatment experiment from the previous section were applied in this study to boost passivation quality.

A common challenge with PECVD-grown thin films is the random formation of voids and pinholes in the  $\text{i.a-Si:H}$  network due to mixed-phase silicon growth [83]. This emergence of pinholes and voids provides a pathway for possible hydrogen effusion. Some researchers have used residual silane molecules in hydrogen plasma to grow a dense silicon capping layer on top of the as-deposited  $\text{i.a-Si:H}$  film to inhibit the effusion of free H atoms from the low-mass-density  $\text{i.a-Si:H}$  network [84]. Others have used some form of bi-layer stack structure with varying hydrogen and silane dilution ratio to achieve similar feat [85]. Our effort in this regard will mirror some of these techniques.

Researchers from Sanyo have previously shown the effect of utilizing increased hydrogen dilution ratio to improve passivation quality and the optical properties of  $\text{i.a-Si:H}$  films [85]. Figure 4.8 show a comparison between standard method for crystalline silicon passivation using  $\text{i.a-S:H}$  film and the approach undertaken by Sanyo. Using this passivation scheme they achieve better passivation

and front surface optical properties as indicated by the high  $V_{oc}$  and  $J_{sc}$  values they obtained. By creating a stack i-layer and increasing the hydrogen dilution ratio on the i-layer in contact with the doped layer, they were able to increase the bandgap of that i-layer and thus reduce parasitic absorption. This higher hydrogen content films ensure better hydrogen termination of dangling bonds at the c-Si/i.a-Si:H interface during annealing, thus improving passivation quality. Our approach did mirror this method.

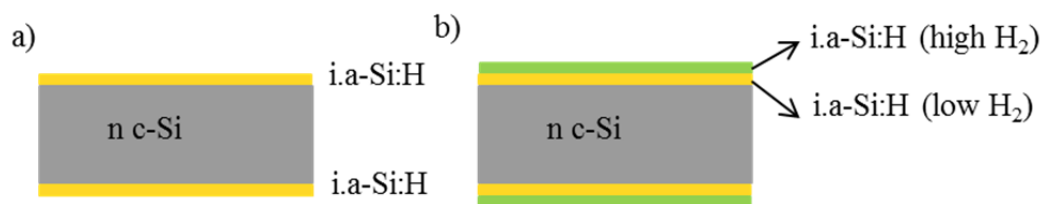


Figure 4.8: i.a-Si:H passivation of n-type crystalline silicon surface: a) prior art; b) according to Sanyo patent.

In our case, we utilized a stacked i-layer structure comprising of our old and new i-layer recipes, and then treat the whole stack with hydrogen plasma afterwards. This combination of stacked i-layer approach together with post deposition hydrogen plasma treatment proved to be a superior passivation scheme to our standard single layer process as measured by the very high  $iV_{oc}$  that was achieved. Figure 4.9 shows a depiction of our i-layer passivation scheme. Both passivation sequences in Figure 4.9a and 4.9b have shown relatively equal passivation quality and cell parameters, thus the order of the stack is not critical as long as the top layer is treated with hydrogen plasma. Using this deposition technique, we have achieved state-of-the-art  $iV_{oc} \sim 750$  mV for 10 nm-thick i.a-Si:H and well over 750 mV for 12 nm-thick i.a-Si:H [86].

Figure 4.10 shows a comparison between our standard single layer depositions with the bi-layer interrupted deposition with varying thickness and application of post deposition hydrogen plasma treatment.

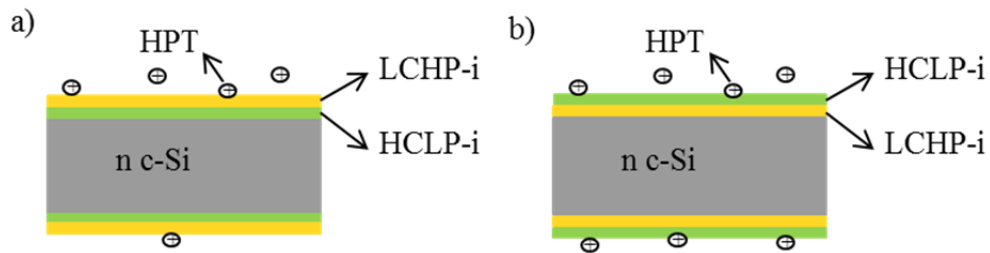


Figure 4.9: i.a-Si:H passivation of n-type crystalline silicon surface developed at IEC: a) low  $V_{pl}$  LCHP-i in contact with the c-Si surface; b) high  $V_{pl}$  HCLP-i in contact with the c-Si surface.

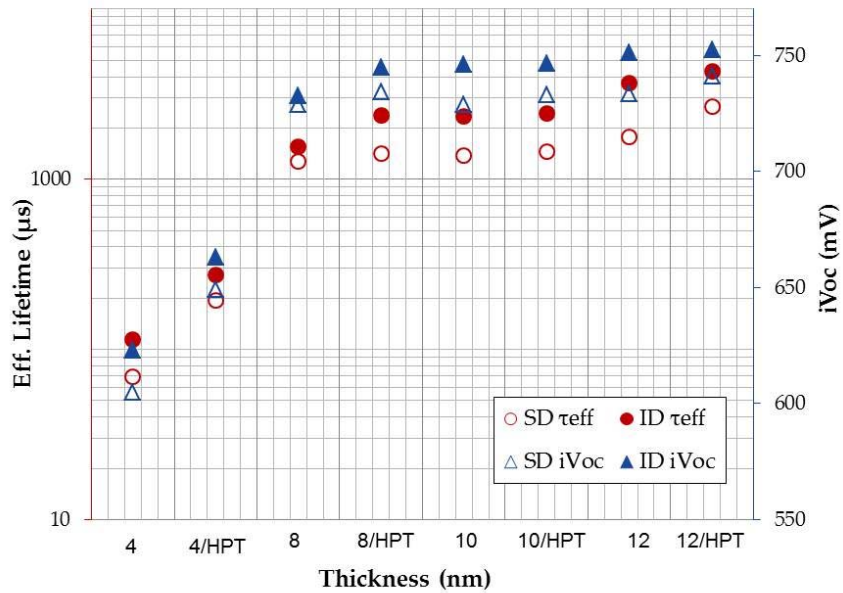


Figure 4.10: Variation of  $\tau_{eff}$  and  $iV_{oc}$  with thickness for single deposition, SD (open symbols) and bi-layer deposition, ID (closed symbols), before and after the HPT [86]. Numbers on the x-axis refer to total i-layer thickness in nm.

The results of varying the passivation via i-layer processing and thickness are shown in Figure 4.10. The passivation metrics,  $\tau_{\text{eff}}$  and  $iV_{\text{oc}}$ , for single deposition, SD, and bi-layer interrupted deposition, ID, films show a steady improvement with i.a-Si:H film thickness. However, the ID films have consistently higher values of  $\tau_{\text{eff}}$  and  $iV_{\text{oc}}$  at every film thickness. Hydrogen plasma treatment improves both ID and SD films but the ID films retain their superior passivation. This additional improvement in passivation is more pronounced for thinner films and appears to saturate around 12 nm-thick films. To achieve high efficiency SHJ solar cell, certain trade-offs are necessary. In this case, increasing the i.a-Si:H film thickness invariably improved the passivation quality with  $\tau_{\text{eff}} > 5$  ms and  $iV_{\text{oc}} > 750$  mV. However, this is known to result in a reduction of fill factor, due to decrease in carrier collection, and in short circuit current, due to an increase in light absorption, both arising from the thicker i.a-Si:H film. Thus, a trade-off is established based on achieving the best possible passivation with the minimum i.a-Si:H film thickness. We found this optimal thickness, from previous works, to be around 8-10 nm. Beyond this thickness, the decrease in FF and  $J_{\text{sc}}$  negates any slight increase in  $V_{\text{oc}}$ . With the introduction of the bi-layer/interrupted deposition technique (ID in Figure 4.10) we show that the  $iV_{\text{oc}}$  and  $\tau_{\text{eff}}$  of an 8 nm i.a-Si:H film can be improved by  $\sim 10$  mV and  $\sim 1$  ms respectively, when compared to single deposition after HPT.

We carried out ellipsometry measurements to characterize the optical properties of the i.a-Si:H films. The measured parameters were fitted with a Tauc-Lorentz model to extract the film thickness,  $n$  &  $k$  values and band gap ( $E_g$ ). The error margins of the measured film thickness were within 5%. Figure 4.11 shows the variation of band gap with i.a-Si:H film thickness for both single and interrupted

deposition after HPT. The chart shows two trends: 1) a steady increase in band gap with respect to thickness; and 2) samples with interrupted deposition showed a consistently higher band gap by 2-4 meV except an outlier (circled region). The lower band gap for the 4 nm-thick film can be attributed to thinner i.a-Si:H film exhibiting non-conformal film deposition, thereby giving rise to voids. All samples showed equivalent or higher band gap after HPT except for the 4 nm-thin films. The presence of hydrogen in i.a-Si:H films is known to increase the band gap arising from the replacement of weak Si-Si bonds contributing to the valence band tail state with more stable and energetically deep Si-H bonds [85]. This causes a widening of the band gap due to a retreat of the valence band edge as hydrogen content increases. Thus, the higher band gap of the samples with ID supports our proposition of a closely-packed film with higher hydrogen content in the i.a-Si:H network.

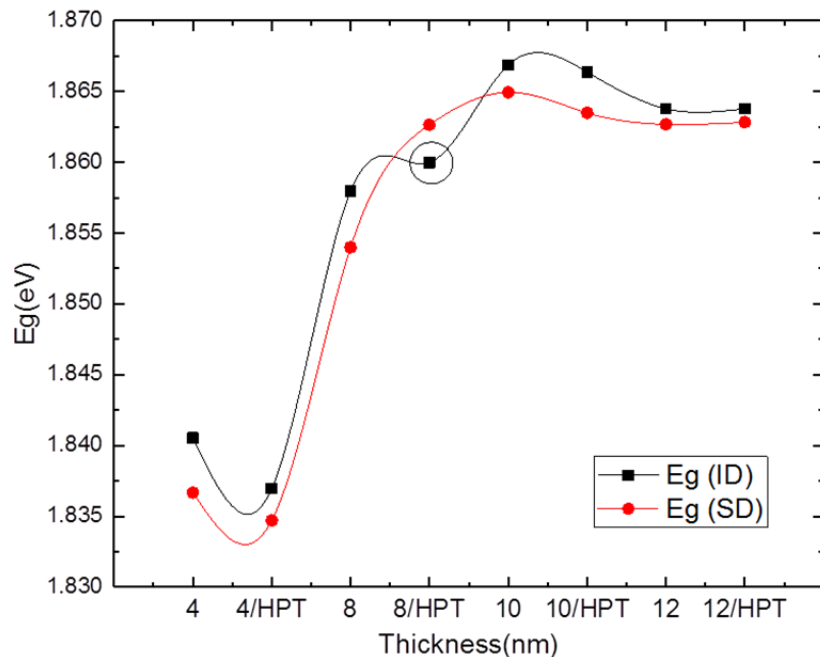


Figure 4.11: Eg variation with thickness for SD and ID with and without HPT [86].

To understand the nature of the Si-H bond in the i.a-Si:H film, FTIR measurements were obtained for both SD and ID samples. The absorption coefficient spectra for the infrared measurement are shown in Figure 4.12. The vibration of a single silicon to hydrogen bond (Si-H) peaks around the low stretching mode (LSM) of wavenumber,  $\omega = 2000 \text{ cm}^{-1}$ , while two or more hydrogen atoms usually bonds to silicon at a void surface and peaks at the high stretching mode (HSM) of wavenumber  $\omega = 2090 \text{ cm}^{-1}$ . Thus, di-hydride bonds resulting in HSM peaks indicate void formation. Figure 4.12a shows a high HSM vibration at  $2090 \text{ cm}^{-1}$  for a 4 nm thin i.a-Si:H film due to poor film coverage and voids associated with very thin films. Figure 4.12b and 4.12c compares SD and ID films with increased thickness. Both shows reduced HSM peak indicating a lower fraction of void. However, ID film showed higher LSM peak. The increased intensity of Si-H bonds for ID films compared with their SD counterparts was consistent for all thickness studied, with lower or equivalent HSM. This supports our observation of increase in band gap for all ID films due to the replacement of weak Si-Si bonds by Si-H bonds and thereby reduces valence band tail states. The microstructure parameter  $R^*$ , defined in Eqn 2.7, for all film thickness and for both deposition techniques after HPT are shown in Figure 4.13. The  $R^*$  trend with thickness and HPT is consistent in both SD and ID films. However, ID films, are consistently lower than those of the SD films – an indication of better quality film with fewer voids.

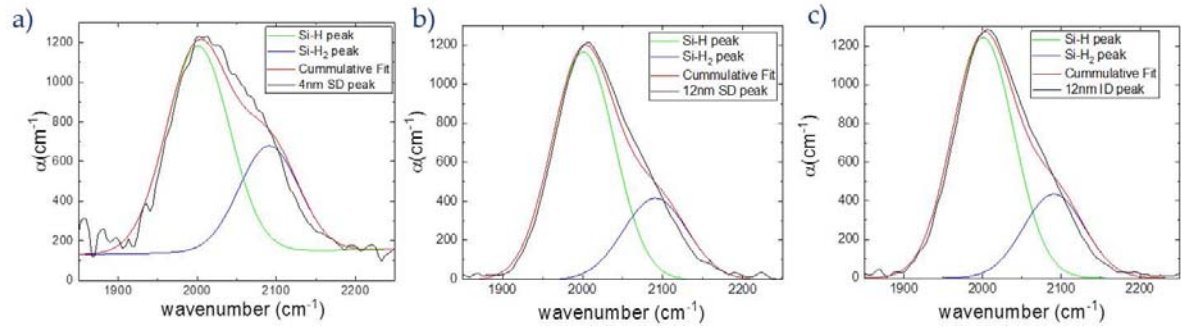


Figure 4.12: FTIR absorption coefficient spectral for: a) 4 nm SD i.a-Si:H film, b) 12 nm SD i.a-Si:H film and c) 12 nm ID i.a-Si:H film showing improved microstructure properties for ID film [86]. This trend is consistent for samples with HPT.

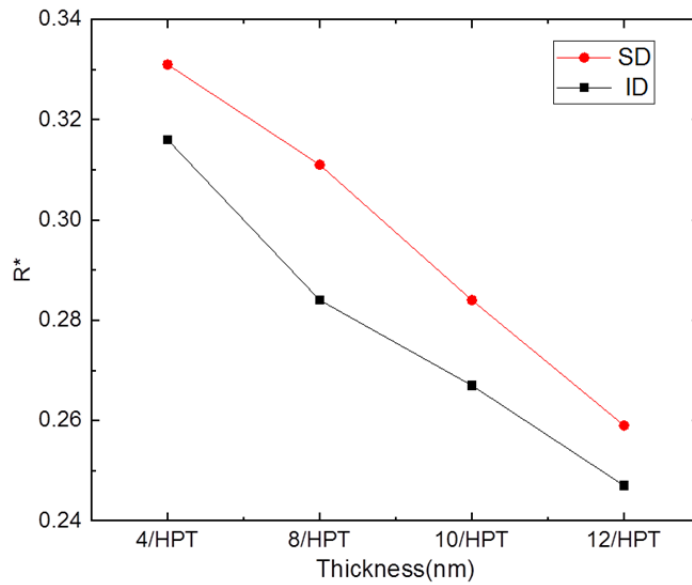


Figure 4.13: Variation of microstructure parameter with increasing thickness for SD and ID films after HPT [86].

#### 4.5 Reducing Process Dependent Voc and Jsc losses

The state-of-the-art iVoc achievable by our deposition technique, though very promising, only indicate the upper limit of our device Voc. The actual measured Voc

can be up to 50 mV lower depending on subsequent processing steps, which involves doped layer deposition and metal contact formation for FHJ cells, or downstream patterning of the emitter and base region for IBC cell. The chart in Table 4.4 shows the typical range in  $iV_{oc}$  and measured  $V_{oc}$  trends from multiple samples processed over time.

Table 4.4: Average  $iV_{oc}$  and measured  $V_{oc}$  trends from multiple samples after doped layer deposition and metallization.

$iV_{oc}$ after i-layer (mV)	$iV_{oc}$ after doped-layer (mV)	Measured FHJ $V_{oc}$ (mV)
730-750	710-720	700-705

It is clear from Table 4.4 that the limiting step to achieving very high measured  $V_{oc}$  in our FHJ cells is the doped layer deposition step. One of the effects of doped layer deposition is the formation of field effect passivation, which helps with carrier collection. These doped layers however do not have the same capability for excellent chemical passivation as the intrinsic layers. The doping mechanism in a-Si is also very different from c-Si. It involves forming a defective energy state, not simply donating electron. Thus, doped a-Si films by default are highly defective. Figure 4.14 shows the effective lifetime from p.a-Si:H, n.a-Si:H and i.a-Si:H (with and without HPT). Many studies have attributed this low chemical passivation to the presence of boron (p-doped) and phosphorus (n-doped) impurities in the film, with the p-doped layer showing the least chemical passivation quality. This is also true for both side i/p.a-Si:H and i/n.a-Si:H passivation scheme as shown in Figures 4.15 and 4.16. In these configurations, the p-layer reduces the effective passivation of the i/p stack more than

the i/n stack, where the overall passivation quality is slightly increased or unchanged compared to the i.a-Si:H layer. This increase in interface recombination after doped layer has been attributed to Fermi level dependent Si-H bond rupture [88].

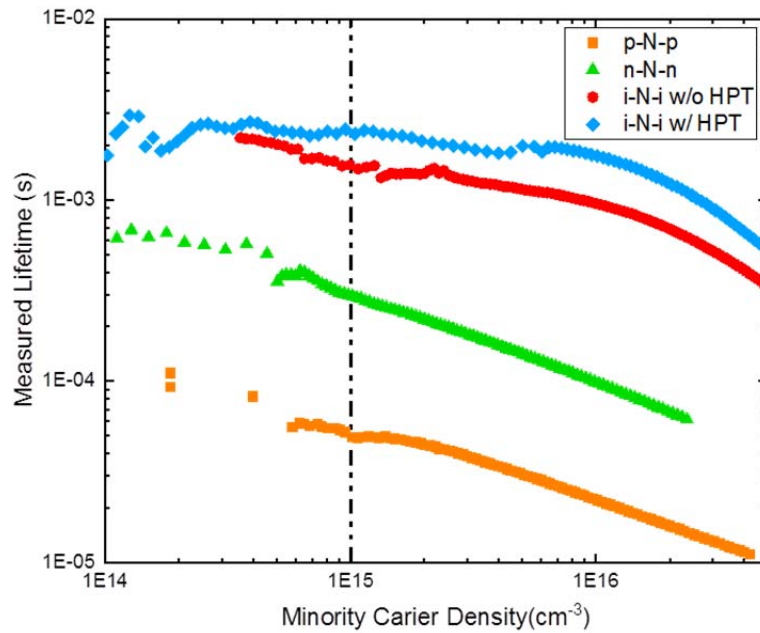


Figure 4.14: Effective minority carrier lifetime for both-side p, n and i-layer (w/ and w/o HPT) passivation. Dashed line shows the standard reporting condition for the minority carrier density of 1E15.

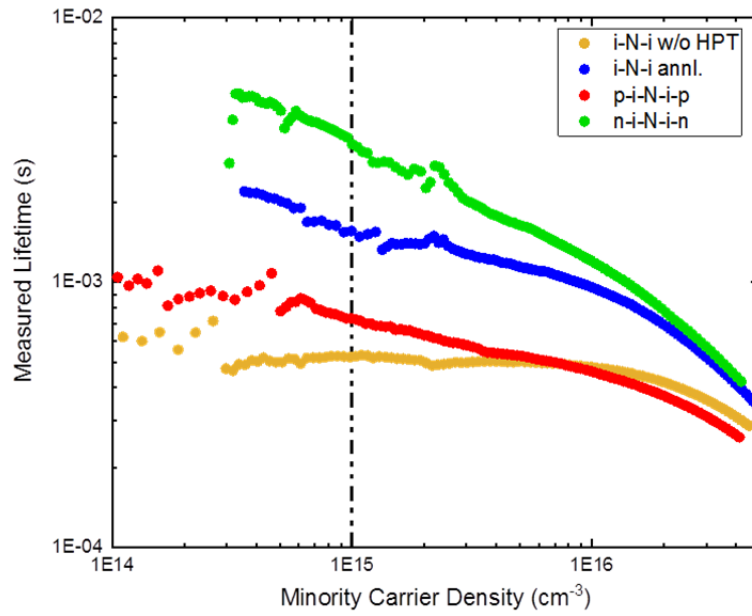


Figure 4.15: Effective minority carrier lifetime for both side i/p, i/n and i-layer (w/o HPT) passivation.

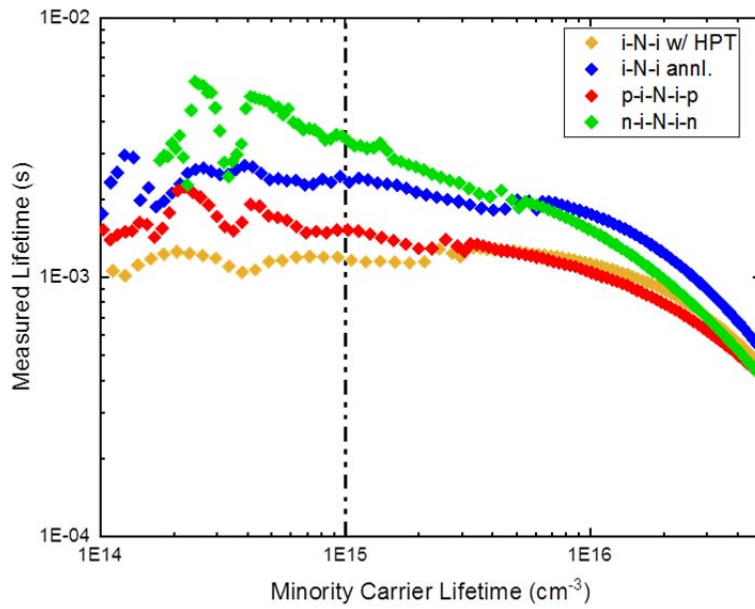


Figure 4.16: Effective minority carrier lifetime for both side i/p, i/n and i-layer (w/ HPT) passivation.

The addition of HPT in Figure 4.16 is shown to improve the initial i-layer passivation from 0.5 ms at  $1E15$  in Figure 4.15 to 1 ms in Figure 4.16 where the dashed line shows the standard reporting condition for the minority carrier density of  $1E15$ . This improved passivation is consistent after thermal annealing and dope layer deposition. Thus, returning a better net passivation for both cases of p-i-N-i-p and n-i-N-i-n.

Due to the critical nature of the doped layers to the overall passivation of the c-Si sample, we carried out studies to improve the doped layer deposition conditions. The following sub-section will detail our work to optimize doped layer deposition conditions and minimize the loss in passivation.

#### **4.5.1 Doped Layer Characterization**

It is common to experience a reduction in passivation quality after the deposition of the doped layers. Given that the intrinsic Si layer is very thin ( $\sim 10$  nm), the deposition of the doped layer (if not optimized) has the potential to damage the i.a-Si:H layer as well [<sup>89</sup>], causing a decrease in the passivation quality. An excellent passivation quality is a combination of both chemical passivation and field-effect passivation. To get an efficient chemical passivation, a significant reduction of the interface defect densities by a saturation of the dangling bonds at the c-Si/i.a-Si:H interface is required. To get an efficient field-effect passivation, the doped layer should exhibit a high level of doping efficiencies (i.e. a high concentration of activated dopants) which will increase the surface band bending and the electric field present at the interface to collect the photo-generated charge carriers. Merely increasing of doping gas flows during deposition is not able to deliver on this requirement since it

leads to significant increase in internal film stress [<sup>89</sup>] and defect formation in the doped layers. Thus, a careful optimization is required for the doped layers.

Also the film crystallinity of the doped layers is important. The silicon heterojunction solar cells benefit from the heterojunction layers adjacent to it, and the high band offsets leading to a high  $iV_{oc}$ , and lower recombination rates. However, if the deposition condition leads to films with even a fraction of crystallinity approaching the c-Si substrate (i.e. microcrystalline, nanocrystalline, protocrystalline), the band-offset conditions are reduced, and the  $iV_{oc}$  drops naturally. This may however be tradeoff with an improvement in the doping efficiencies of the doped films, which improves collection efficiencies and fill factor. Hence an optimization is required. If the film crystallinity increases, the band gap approaches c-Si substrate, and parasitic absorption increases as a result, leading to drop in  $J_{sc}$ .

Our efforts to optimize the doped layers centered on modifying the conductivity, microstructure and doping efficiency of our standard p-doped and n-doped a-Si:H layers, while monitoring the loss in  $iV_{oc}$  from these doped layers. Five deposition conditions that comprised of our standard doped layers, the addition of HPT, bi-layer with increasing hydrogen dilution, tri-layer with varying doping concentration and reduction of ion bombardment energy were studied. Table 4.5 and 4.6 detail the parameter modification and the purpose for each of the five conditions for p-doped and n-doped layers.

Table 4.5: Input parameter variations for p-doped layer study.

P-layers	Parameters	Purpose
Std-p	H <sub>2</sub> /SiH <sub>4</sub> =6, 123mA, 1.25T, 10 nm	Reference
Std-p w/HPT	H <sub>2</sub> /SiH <sub>4</sub> =6, 123mA, 1.25T + HPT, 10 nm	Effect of HPT
Bi-layer w/incr. H <sub>2</sub> dilution	H <sub>2</sub> /SiH <sub>4</sub> =6 (7 nm); H <sub>2</sub> /SiH <sub>4</sub> = 10 (3 nm); 123mA, 1.25T	Incr. crystallinity with incr. H dilution
Tri-layer low/high/nc-Si	B <sub>2</sub> H <sub>6</sub> /SiH <sub>4</sub> =0.5 (4 nm); B <sub>2</sub> H <sub>6</sub> /SiH <sub>4</sub> =1.5 (4 nm); SiH <sub>4</sub> depletion (~2 nm); 123mA, 1.25T	Varying doping conc.
Low Vpl	H <sub>2</sub> /SiH <sub>4</sub> =6, 60mA, 1.75T, 10 nm	Reduced plasma damage

Table 4.6: Input parameter variations for n-doped layer study.

N-layers	Parameters	Purpose
Std-n	H <sub>2</sub> /SiH <sub>4</sub> =6, 123mA, 1.25T, 10 nm	Reference
Std-n w/HPT	H <sub>2</sub> /SiH <sub>4</sub> =6, 123mA, 1.25T + HPT, 10 nm	Effect of HPT
Bi-layer w/incr. H <sub>2</sub> dilution	H <sub>2</sub> /SiH <sub>4</sub> =6 (7 nm); H <sub>2</sub> /SiH <sub>4</sub> = 10 (3 nm); 123mA, 1.25T	Incr. crystallinity with incr. H dilution
Tri-layer low/high/nc-Si	PH <sub>3</sub> /SiH <sub>4</sub> =0.5 (4 nm); PH <sub>3</sub> /SiH <sub>4</sub> =1.5 (4 nm); SiH <sub>4</sub> depletion (~2 nm); 123mA, 1.25T	Varying doping conc.
Low Vpl	H <sub>2</sub> /SiH <sub>4</sub> =6, 60mA, 1.75T, 10 nm	Reduced plasma damage

Temperature dependent conductivity measurement and FTIR were used to characterize the conductivity and microstructure of these films. Using Eqn. 2.24, the

conductivity and activation energy  $E_a$  of the doped layers can be calculated, which indicates the Fermi level position in the film. The doped layer films for the conductivity measurement were deposited on  $\sim 1$ mm-thick Corning glass samples, after which two rectangular aluminum contacts were thermally evaporated onto the layers. To ensure reliable electrical measurement, the thickness of the doped layers were set at  $\sim 100$  nm, which is 70 nm and 90 nm thicker than our standard n-doped and p-doped layer thicknesses for devices. By applying a voltage  $V$  between the aluminum contacts, and measuring the corresponding current  $I$  through the films at different substrate temperature, using a 2-point probe measurement, the conductivity  $\sigma$  was determined according to Eqn. 2.23. Figure 4.17 show the current-voltage graph for all doped layers that was studied. The straight line confirms the Ohmic conductor properties of the films.

In both p- and n-doped layer cases, it is clear that the low  $V_{pl}$  condition, with the sharpest tilt, is the most conductive of the doped layers. Of the 5 conditions studied, this was the only condition performed at a different plasma current and plasma voltage, and hence power density. The improved conductivity is attributed to the resultant low ion bombardment energy of this condition due to the low  $V_{pl}$ , which may have led to a better doping efficiency. Note that the next most conductive film in both cases was our previous standard condition.

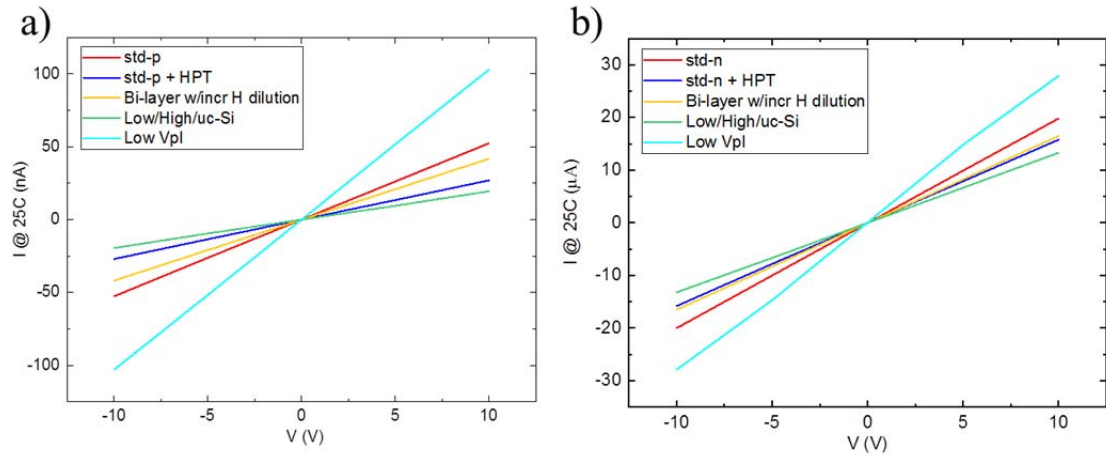


Figure 4.17: Current-voltage relationship for a) p-doped layers, and b) n-doped layers, showing straight lines, typical for Ohmic conductors, for all doped layer variation studied.

Using Eqn. 2.24 or 2.26, we derived the temperature dependent conductivity plots of Figure 4.18a and 4.18b for p-doped and n-doped layers respectively. By fitting this plot with Eqn. 2.25 or 2.27, the conductivity at room temperature and  $E_a$ , recorded in Table 4.7 and 4.8, were derived accordingly.

As can be seen from both Figure 4.18 and Tables 4.7 and 4.8, the most variation across doped layers occurred on the p-doped layers, which confirms our initial conviction that modifying the p-doped layer will be more beneficial in improving device performance. The n-doped layer, though with some variation in conductivity, still fell within the same order of magnitude.

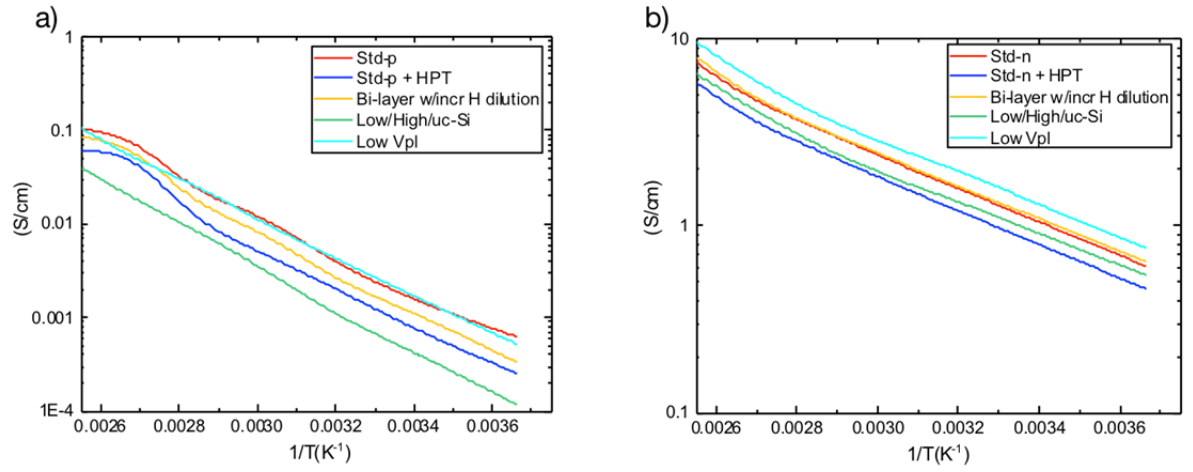


Figure 4.18: Temperature dependent conductivity plots for a) p-doped layers and b) n-doped layers for all doped layer conditions studied.

Table 4.7: Activation energies and conductivities for varying p-doped layers.

	Std-p	Std-p+HPT	Bi-layer w/incr H <sub>2</sub> dilution	Low/Hi/nc-Si	Low Vpl
E <sub>a</sub> (eV)	0.414	0.440	0.442	0.455	0.412
σ <sub>RT</sub> (S/cm)	1.25E-3	6.0E-4	1.05E-3	5.70E-4	1.50E-3

Table 4.8: Activation energies and conductivities for varying n-doped layers.

	Std-n	Std-n+HPT	Bi-layer w/incr H <sub>2</sub> dilution	Low/Hi/nc-Si	Low Vpl
E <sub>a</sub> (eV)	0.190	0.192	0.189	0.188	0.191
σ <sub>RT</sub> (S/cm)	5.26E-1	4.20E-1	4.77E-1	3.89E-1	6.67E-1

In the same plasma CVD run,  $\sim 300$   $\mu\text{m}$ -thick polished CZ c-Si samples were also inserted for FTIR analysis of the microstructure of the doped films. Figure 4.19 and 4.20 shows the infrared spectra of the doped amorphous silicon for the stretching mode absorption regions (mono-hydride centered at  $\sim 2000$   $\text{cm}^{-1}$  and di-hydride centered at  $\sim 2090$   $\text{cm}^{-1}$ ). The stretching modes were mainly studied while characterizing the amorphous silicon film due to the nature of the predominant amorphous silicon vibration and the range of our FTIR system. The mono-hydride and di-hydride peaks are then fitted on the raw data to allow the estimation of the hydrogen concentration in each peak using Eqns. 2.5 and 2.6, after which the microstructure parameter is estimated using Eqn. 2.7. Table 4.9 and 4.10 detail the hydrogen concentration and microstructure parameters for both cases of doped layer study.

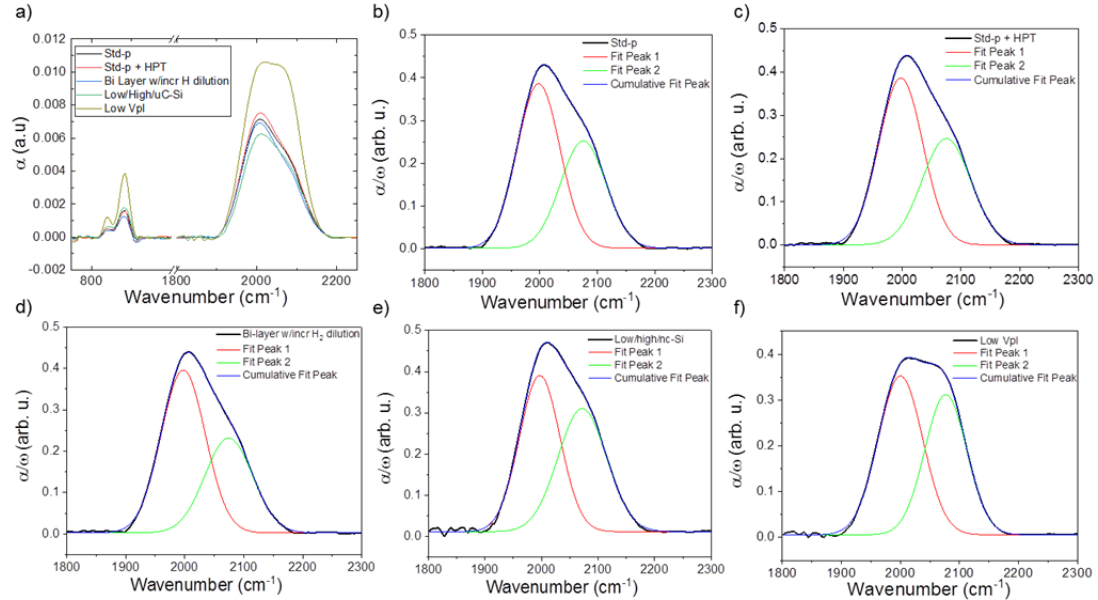


Figure 4.19: Infrared spectra for p-doped layers showing: a) Raw; and fitted data for: b) std-p, c) std-p +HPT, d) bi-layer w/incr.  $\text{H}_2$  dilution, e) low/high/nc-Si, and f) low  $V_{\text{pl}}$ .

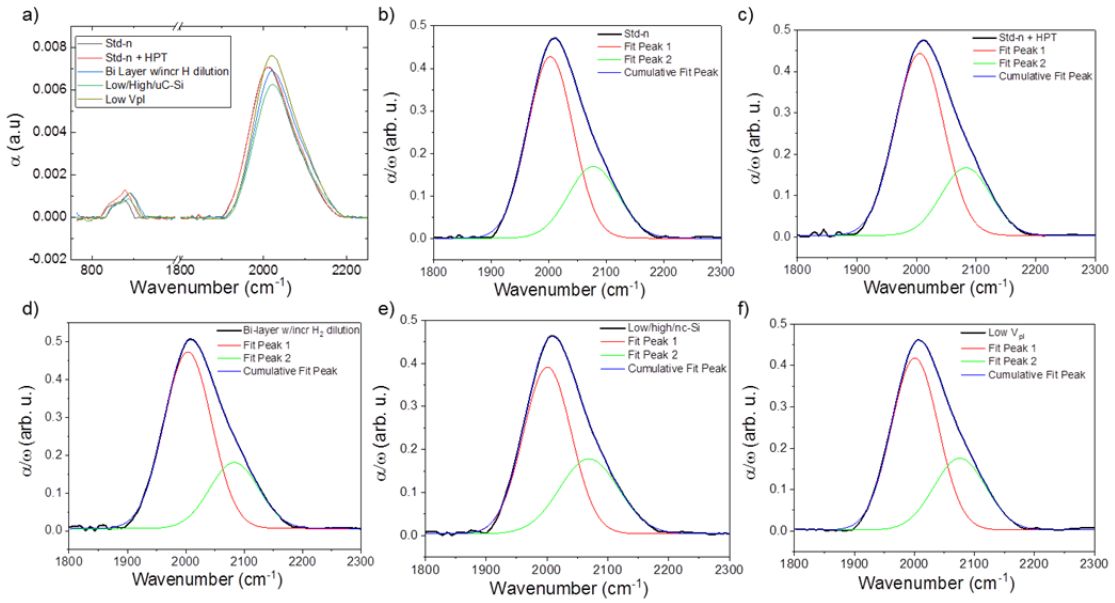


Figure 4.20: Infrared spectra for n-doped layers showing: a) Raw; and fitted data for: b) std-n, c) std-n +HPT, d) bi-layer w/incr. H<sub>2</sub> dilution, e) low/high/nc-Si, and f) low V<sub>pl</sub>.

Figure 4.19a and 4.20a shows the raw data for the two stretching modes at  $\sim 2000 \text{ cm}^{-1}$  and  $2090 \text{ cm}^{-1}$ , and a doublet due to di-hydride bending and scissor modes around  $840 - 890 \text{ cm}^{-1}$ . However, our focus was mainly on the stretching modes. As stated earlier on section 4.4, the vibration of a single silicon to hydrogen bond (Si-H) peaks around the LSM of  $\omega = 2000 \text{ cm}^{-1}$ , while two or more hydrogen atoms usually bonds to silicon at a void surface and peaks at the HSM of  $\omega = 2090 \text{ cm}^{-1}$ . Thus, di-hydride bonds resulting in HSM peaks indicate void formation. Figure 4.16f indicates that the low V<sub>pl</sub> p-doped layer (grown at low plasma current and high pressure) has a significantly different microstructure than the rest of the p-doped layers. This condition is also unique because it is the only condition performed at a different plasma current and pressure. It does conform to our previous findings that films grown

at higher pressure are less dense and more amorphous. Other p-doped layer conditions show little distinctions, while the bi-layer condition with increasing hydrogen conc. (Figure 4.19d) appears to have the least microstructure parameter. It is also interesting to note that this same condition has the least hydrogen concentration (14.4 %). Thus, merely having an increased hydrogen concentration in the a-Si:H film does not necessarily translate to better microstructure. The nature of the silicon to hydrogen bond is also important. Apparently, the additional hydrogen atoms in the other films were bonded to silicon at void surfaces. For the n-doped layer conditions, the microstructure parameter appears to show minimal changes between conditions. Table 4.9 and 4.10 outlines the microstructure parameters for the p-doped and n-doped layers respectively.

Table 4.9: Microstructure parameters for different p-doped layers.

Layer variations	R* parameter
Std-p	0.372
Std-p + HPT	0.375
Bi-layer w/incr. H <sub>2</sub> dilution	0.341
Tri-layer low/high/nc-Si	0.428
Low V <sub>pl</sub>	0.454

Table 4.10: Microstructure parameters for different n-doped layers.

Layer variations	R* parameter
Std-n	0.374
Std-n + HPT	0.395
Bi-layer w/incre. H <sub>2</sub> dilution	0.357
Tri-layer low/high/nc-Si	0.379
Low V <sub>pl</sub>	0.335

The p-doped layers were applied to our LCHP both side stack i.a-Si:H passivated samples with HPT, to estimate their effect on iVoc. Basically, a p-i-N-i-p structure was made with the 5 p-layer variance and a reference condition, after which the effective iVoc was recorded. The reference condition had our single deposited i-layer without HPT. Figure 4.21 shows results from 3 samples per condition used for this study. It is clear that our standard p-doped layer gave the lowest drop in Voc, with as little as 1 mV drop in one instance. It is important to note that some recent samples have shown a net positive gain after the p-doped layer deposition.

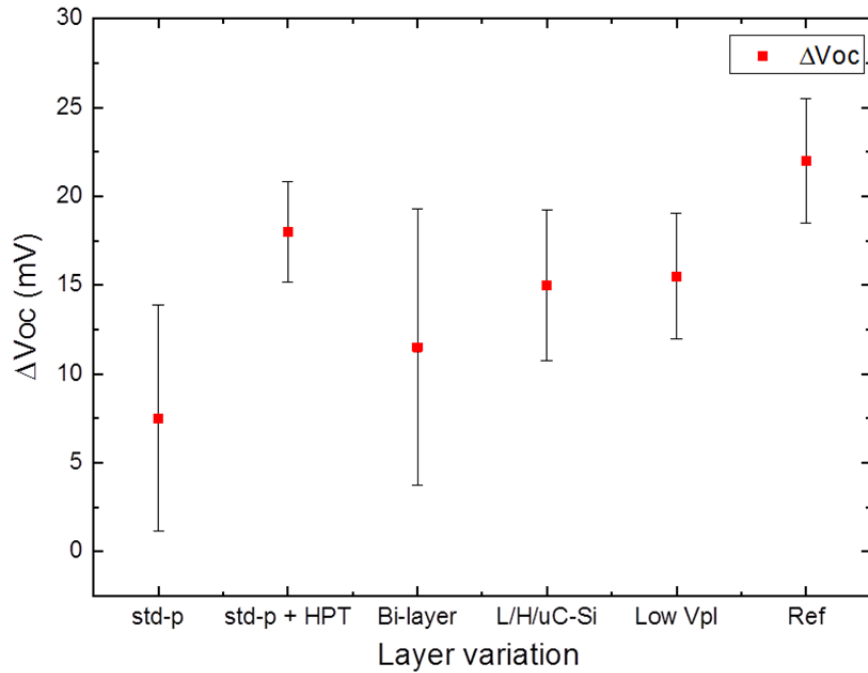


Figure 4.21: Loss in iVoc after p-i-N-i-p structure different p-doped-layer variance and a reference condition with a single deposited i-layer without HPT.

The result from this study was used to rank the p- and n- doped layers according to their relative performance. Each film was ranked according to their performance across 3 metrics – conductivity, microstructure parameter and  $\Delta V_{OC}$ . Tables 4.11 (for p-layers) and 4.12 (for n-layers) outline the film performance on a scale of 1 to 5, where 1 represent the best performer and 5 represent the worst performer on a given metric. A lower sum value represents a film with superior overall tradeoffs across the 3 metrics. Following this result, 3 p-layer conditions (Std-p, Bi-layer and Low  $V_{pl}$ ) and 2 n-layer conditions (Std-n and Low  $V_{pl}$ ) were selected for FHJ cell to verify their performance on a complete cell.

Table 4.11: P-doped layers ranked according to their conductivity, microstructure parameter and  $\Delta V_{OC}$ .

P-layer	$\sigma$	R*	$\Delta V_{OC}$	Sum
Std-p	2	2	1	5
Std-p + HPT	5	3	5	13
Bi-layer w/incr. H <sub>2</sub> dilution	3	1	2	6
Tri-layer low/high/nc-Si	4	4	3	11
Low V <sub>pl</sub>	1	5	4	10

Table 4.12: N-doped layers ranked according to their conductivity, microstructure parameter and  $\Delta V_{OC}$ .

1	$\sigma$	R*	$\Delta V_{OC}$	Sum
Std-n	2	3	-	5
Std-n + HPT	4	5	-	9
Bi-layer w/incr. H <sub>2</sub> dilution	3	2	-	5
Tri-layer low/high/nc-Si	5	4	-	9
Low V <sub>pl</sub>	1	1	-	2

While the Std-p layer condition showed better performance in terms of  $\Delta V_{OC}$ , it could also be seen that all 5 conditions showed reduced  $V_{OC}$  drop as compared to the reference condition in Figure 4.21. The primary difference between the 5 variations and the reference sample is the underlying i-layer surface on which the p-layers were grown. This data does suggest that apart from the p-layer condition, the i/p interface is

critical in determining the nature of the doped a-Si:H film and its effect on the  $iV_{oc}$ . A quick literature search reveals that other researchers have found the nucleation properties of doped microcrystalline silicon thin film to be strongly dependent on the substrate – be it glass, c-Si or i-a-Si:H [90] [91] [92]. Doped layers grown on different surfaces have shown different variation of film crystallinity with respect to increasing thickness. The above referenced articles also indicate that a hydrogen plasma pretreatment of an i.a-Si:H substrate can help create Si microcrystallites at the i.a-Si:H surface, which act as initial nuclei for enhancing doped microcrystalline silicon thin film growth. A Raman spectroscopy study of our hydrogen plasma treated i.a-Si:H film did not confirm the presence of Si microcrystallites. However, we did observe an increase in short range order [93] – a positive step towards crystallinity. Thus, it can be said that the addition of a post deposition hydrogen plasma treatment step to the i.a-Si:H serves the dual purpose of improving the c-Si/i.a-Si:H interface passivation and enabling the deposition of better quality doped amorphous silicon layers. Results of incorporating these doped layers into FHJ and IBC solar cells will be presented in Chapter 5.

#### **4.5.2 Indium Tin Oxide (ITO) Optimization**

To improve metal-semiconductor contact on the less conductive p-doped front surface, a transparent conductive oxide, TCO (Indium Tin Oxide, ITO in this case) is deposited prior to the formation of a Ni/Ag metal grid on the front surface of our SHJ solar cells. The ITO film used in this study also acts as an anti-reflection (AR) coating for reducing front surface reflection with refractive index ranging from 2.4 to 1.8, corresponding to wavelength range of 300 – 800 nm. This layer, though transparent, can increase the parasitic absorption of impinging light on the front surface but

improves lateral conductivity at the metal-semiconductor interface for effective carrier collection. To prevent parasitic absorption, this layer is required to have high optical transparency to solar radiation spectrum [94]. An ITO film deposited by sputtering was used as the TCO for the cells in this study. Our baseline cells are fabricated with ITO only on the front i/p emitter surface, where it is essential to enable good lateral carrier collection since the a-Si doped layers have such poor conductivity [95]. In this study we investigated the effect of backside ITO film on the reflection of long wavelength light back into the absorbing layer. Varying the oxygen content of the chamber during sputtering has been shown to be an effective method of modifying the optical and electrical properties of ITO [96] [97]. We applied this concept to the deposition of ITO films on the back i/n.a-Si:H surface. Front side ITO with high electrical conductivity and optical transparency were sputtered in an oxygen-filled ambient, while backside ITO was sputtered in an oxygen-free ambient for this study. The resultant effects on actual cells are discussed in chapter 5.

#### **4.6 Summary**

In this chapter, I have detailed an extensive OES studies that informed the development of the plasma processes for intrinsic and doped a-Si:H films, and post deposition hydrogen plasma treatment. A low-current-high-pressure (LCHP) condition was found to produce stable plasma with reduced plasma voltage and superior passivation quality. Hydrogen plasma treatment was shown to be an effective approach to saturate the surface dangling bonds and reduce the recombination losses at the interface. We also investigated the relation between the hydrogen plasma properties to the passivation quality of c-Si surface. The relation between H\* species and plasma voltage to the process parameters was discussed. A low plasma voltage

treatment condition during hydrogen plasma treatment was found to reduce the damage due to ion bombardment resulting in higher  $\tau_{eff}$  and  $iV_{oc}$  values.

To further improve the c-Si surface passivation, a two-step bi-layer i.a-Si:H deposition process was developed. State-of-the-art  $iV_{oc}$  exceeding 750 mV has been achieved using ~10 nm thin i.a-Si:H film when this process is complemented with a post deposition hydrogen plasma treatment.

A comprehensive doped layer study was also performed to reduce the loss in passivation after doped layer deposition. To achieve an optimized i/p.a-Si:H passivation that reduces loss in  $V_{oc}$  with superior optical and electrical properties, the nature of the i.a-Si:H surface was found to be critical. Studies have shown that hydrogen plasma pretreatment of an i.a-Si:H substrate can help create Si microcrystallites at the i.a-Si:H surface, which act as initial nuclei for enhancing doped microcrystalline silicon thin film growth. Micro Raman measurement of our hydrogen plasma treated i.a-Si:H film did not show the formation of Si microcrystallites, but showed an increase in short range order, which improves the optical and electrical properties of the doped layers grown afterwards.

Finally, the importance of ITO as an AR coating for reducing front surface reflection, and a conducting oxide for improving lateral conduction was discussed. A study to investigate the effect of backside ITO film on the reflection of long wavelength light back into the absorbing layer was presented.

## Chapter 5

### CELL STRUCTURES AND PERFORMANCE

The knowledge gained from the simplified sample cleaning experiments and the improvements from the intrinsic and doped a-Si:H passivation were applied towards making SHJ solar cells with FHJ and IBC-SHJ architectures. The improvements in measured  $V_{oc}$ ,  $J_{sc}$ , FF and overall efficiencies are outlined in the subsequent subsections:

#### 5.1 Front Heterojunction (FHJ) Solar Cell

The FHJ solar cell, as the name implies, involves the formation of a PN heterojunction by growing a thin doped amorphous silicon film of opposite polarity to that of the absorber on the front surface. In this case a p-doped layer is deposited on the front surface of an n-type c-Si wafer. The heterojunction architecture is very popular due to its high open circuit voltage ( $V_{oc}$ ) emanating from a high valence band offset between the crystalline and amorphous phases of the c-Si/a-Si:H interface. The p-doped layer and an n-doped back surface field (BSF) layer are formed on either side of the solar cell in this architecture, along with passivating i-layers on both sides, which eliminates the need for any downstream patterning after the doped layers are deposited. However, they suffer from shading loss from front surface metal grids, as do all front junction cells. This architecture offers a quick and easy way of realizing the effects of changes in process conditions to an actual solar cell.

Thin i.a-Si:H films were deposited on chemically polished n-type CZ wafers having (100) orientation with resistivity of 5-8  $\Omega$ -cm and thickness of 150  $\mu$ m. Wafers were cut and processed as 25x25 mm square samples and underwent a simplified wafer cleaning procedure as described elsewhere [63]. The effects of the improved i-layer passivation, p- and n-doped layer variations and single or both side ITO depositions on a solar cell are presented in this section. All samples started out with both-side i-layer passivation, after which p- and n-type doped a-Si:H layers were deposited on the front and back surface respectively. The cells were then completed with sputtered ITO for improved AR properties and lateral conduction, electron beam deposited Ni/Ag grids for front contact designed to have  $\sim$  6% shading loss, and electron beam deposited Al as back contact.

### **5.1.1 Front Emitter Junction Passivation**

We have found from experience that optimizing the front surface i/p amorphous silicon passivation as a pair is a better approach than individual optimization of the i.a-Si:H and p.a-Si:H layers separately. While modifying the front surface passivation, both layers were optimized simultaneously. A 2x2 matrix shown in Table 5.1 outlines the two different film deposition methods used for the intrinsic and p-doped amorphous silicon layers and their corresponding cell results are presented in Table 5.2 respectively.

Table 5.1: 2X2 Matrix for cells with SD and ID deposition methods for intrinsic and p-doped a-Si:H layers.

	SD p-layer	ID p-layer
SD i-layer	CELL A	CELL B
ID i-layer	CELL C	CELL D

Table 5.2: Measured cell parameters for cells A, B, C and D made from MC1652-02, MC1650-01, MC1657-20 and MC1642-09 respectively.

Cell	$i V_{OC}$ (mV)	$V_{OC}$ (mV)	$J_{SC}$ (mA/cm <sup>2</sup> )	FF (%)	Eff (%)
Cell A	722	717	34.9	75.8	19
Cell B	707	698	35.6	73.9	18.4
Cell C	737	727	35.7	70.7	18.4
Cell D	728	725	36.7	75.9	20.2

Tables 5.1 and 5.2 shows four SHJ cells that were processed as earlier described with front side i/p/ITO/Ni/Al-grid and backside i/n/Al. To illustrate the effect of the front surface passivation to  $V_{oc}$  and  $J_{sc}$ , the four cells were fabricated with different i/p deposition method. Single and interrupted deposition (SD and ID) of intrinsic and p-doped amorphous silicon was alternated across the four cells as shown in Table 5.1. The same i-layer conditions were used for both front and rear passivation in each case, while a unique n-doped layer condition (SD) was used for all 4 cases.

The passivation quality of cells with interrupted deposition of i-layer (Cells C and D), with measured  $V_{oc} \geq 725$  mV, clearly outperforms their single deposition

counterparts (Cells A and B). Except for Cell B, all cells showed a measured  $V_{oc} > 700$  mV. Cell D, the cell with both intrinsic and p-doped layers deposited by interrupted deposition approach, showed best  $J_{sc}$  value. This is followed by cell B and C, with either intrinsic or p-doped layers deposited by interrupted deposition, which shows lower  $J_{sc}$ . Cell A having traditional single-layer deposition of intrinsic and p-doped layers shows the lowest  $J_{sc}$  value however with a decent  $V_{oc}$  and comparable FF with cell D. Figure 5.1 shows the measured quantum efficiency of cells A, B, C and D. The most significant improvement between the cells appears to be in the short wavelength range, which correspond to changes in the front surface optical properties. The widest margin in blue response exists between cell A and D, corresponding to cell with two extreme deposition methods while cells B and C falls somewhere in-between as expected. Thus, the improvements in material properties, i.e. band gap, hydrogen content and microstructure parameter of interrupted (bi-layer) deposition discussed in section 4.4, are in fact transferable to a finished cell.

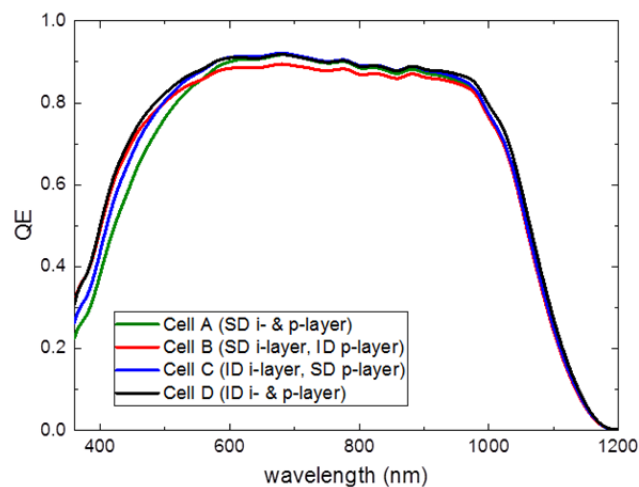


Figure 5.1: Measured quantum efficiencies for cell A (green), cell B (red), cell C (blue) and cell D (black) showing their respective optical response.

### 5.1.2 Doped Layer Optimization

The excellent passivation achievable by the high  $iV_{oc}$  from the ID method sets the upper limit for the device  $V_{oc}$ . The actual measured  $V_{oc}$  can be 10-50 mV lower depending on the subsequent processing steps, which involves doped layer deposition and metal contact formation. In section 4.5.1, valuable information was presented regarding changing the doped layer deposition parameters on the conductivity and microstructure parameter of the film, and also the resultant loss in  $iV_{oc}$  when deposited on an i-layer passivated sample. Based on that experiment, 3 p-layer conditions (Std-p, Bi-layer and Low  $V_{pl}$ ) and 2 n-layer conditions (Std-n and Low  $V_{pl}$ ) were selected for FHJ cell in order to verify their performance on a complete cell. The cell descriptions and measured parameters are detailed in Table 5.3, while their JV curves are shown in Fig 5.2.

Table 5.3: Descriptions and measured cell parameters for cells E to J with unique p- and n-doped layer deposition conditions. Initial  $iV_{oc}$  before doped layers. All had the new ID i-layer stack on front and back.

Cell	N condition	P condition	$iV_{oc}$ (mV)	$iV_{oc}$ after doped layer (mV)	Measured $V_{oc}$ (mV)	$J_{sc}$ (mA/cm <sup>2</sup> )	FF (%)	Eff (%)
Cell E	Std. n	Std. p	740	730	712	36.8	66.7	17.5
Cell F	Std. n	Bi-layer p	738	729	723	37.2	63.9	17.2
Cell G	Std. n	Low $V_{pl}$ p	736	729	719	37.7	68.6	18.6
Cell H	Low $V_{pl}$ n	Std. p	733	721	710	37.2	65.0	17.1
Cell I	Low $V_{pl}$ n	Bi-layer p	734	724	715	37.3	69.3	18.5
Cell J	Low $V_{pl}$ n	Low $V_{pl}$ p	739	725	724	37.8	69.5	19.0

Cells E to J were made from MC1679:11, MC1690:03, 04, 05, 08 and 09 respectively. Table 5.3 shows that before doped layers, all samples had comparable and high  $iV_{oc}$  (733-740 mV). For both the std. (cells E-G) and low  $V_{pl}$  (cells H-J) n-doped layer deposition, the measured  $V_{oc}$  and  $J_{sc}$  improved as the p-doped layer condition is changed from std-p to bi-layer p and finally to low  $V_{pl}$  p. Thus, the IV performance for cell J with both p and n doped layer conditions at low  $V_{pl}$  showed the best cell parameters, while cell E with both p and n doped layer conditions at standard conditions (corresponding to high  $V_{pl}$ ) showed low  $V_{oc}$  and  $J_{sc}$  values. The loss in  $V_{oc}$  after doped layer deposition was also reduced significantly from 20-25 mV to approximately 10 mV in all cases. However, the loss in  $V_{oc}$  after metal deposition varied across the 6 conditions. All conditions showed roughly 10 mV loss except the std. n/std. p condition (cell E), which showed a loss of 18 mV and low  $V_{pl}$  n/low  $V_{pl}$  p condition (cell J), which showed a loss of 1 mV. In both types of n.a-Si:H layer, the low  $V_{pl}$  condition showed better FF. This result is in agreement with the doped layer study in section 4.5.1, which shows high conductivity for the low  $V_{pl}$  p and n doped layers, with relatively the same effect on  $V_{oc}$  as the other conditions. The microstructure parameter was essential the same for the n-doped layers but the p-doped films grown at this condition showed high microstructure parameter. Apparently, this does not have any negative effect on the cell. We posit that the low plasma voltage, which results in low acceleration voltage and low ion bombardment, is the key factor to the tangible improvements in cell parameters similar to the findings in [77].

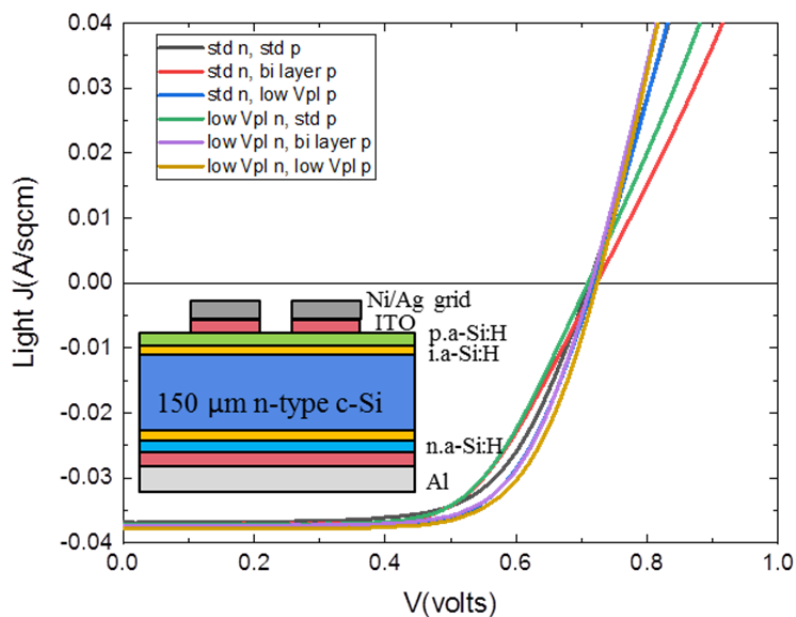


Figure 5.2: Light JV curves for cells E to J. Insert shows cell architecture with front and backside ITO.

### 5.1.3 Improving Light Trapping Scheme

In section 3.6.3, we detailed the benefit of improving the light trapping mechanism of the c-Si samples by texturing the front and back surfaces of the wafers. A 1% TMAH solution was used to achieve orientation dependent pyramids, which reduces hemispherical reflection by increasing the optical path length of incident light on the c-Si surface. To quantify this improvement, a polished wafer and a textured wafer were used in making a front HJ cell and the difference in their  $J_{sc}$  is observed. Also the a-Si/Al contact is well known to have high parasitic plasmonic absorption, which can be reduced by inserting a dielectric layer with an index of about 2 like ITO. TCO/Al ‘back contact reflectors’ have been reported in FHJ cell fabrication.

Another common light trapping mechanism is the use of a TCO, in this case an ITO layer, on the rear side of the cell to improve the reflection of long wavelength

incident light. Nearly all FHJ cells including ours are made with a front surface ITO, which helps to improve carrier collection across the less conductive p.a-Si:H layer as well as reduce front surface reflection due to its nearly perfect index match to a-Si and c-Si. It has been shown in the past; using p-i-n a-Si FJ solar cells [<sup>98</sup>], that a backside ITO (or other TCOs having similar index) can improve the overall Jsc of a cell. However, this can come at the expense of a loss in Fill factor, which is hypothesized as being due to the contact barrier.

To better utilize these light trapping schemes for the case of our c-Si/a-Si:H FHJ, we made cells on both polished and textured wafers having either front side ITO or both side ITO. This enabled us to establish the difference in Jsc between a polished and textured wafer, and also to weigh the tradeoffs between Jsc and FF for front side and both side ITO. Std. n and std. p doped layer conditions were used for these cells. The 2 x 2 matrix for this experiment is presented in Table 5. 4.

Table 5.4: 2x2 matrix for light trapping experiment comparing polished vs textured wafers, and front vs both side ITO.

Wafer type	ITO deposition	
	Front side	Both side
Polished wafer	Front side	Both side
Textured wafer	Front side	Both side

The cell descriptions and measured parameters are detailed in Table 5.5, while their JV curves are shown in Fig 5.3.

Table 5.5: Descriptions and measured cell parameters for cells K to N with different wafer surface finish and ITO depositions. Cells K to N were made from MC1679:23, 24, 10 and 11 respectively.

Cell descriptions	$\tau_{\text{eff}}$ ( $\mu\text{s}$ )	$iV_{\text{OC}}$ (mV)	$iV_{\text{OC}}$ after doped layer (mV)	Measured $V_{\text{OC}}$ (mV)	$J_{\text{SC}}$ ( $\text{mA}/\text{cm}^2$ )	FF (%)	Eff (%)
Polished w/front side ITO (Cell K)	2795	731	731	712	24.7	25.5	4.5
Polish w/ both side ITO (Cell L)	2345	735	736	709	32.8	33.0	7.7
Textured w/ front side ITO (Cell M)	1746	737	732	713	35.7	71.7	18.3
Textured w/ both side ITO (Cell N)	1776	740	732	712	36.8	66.7	17.5

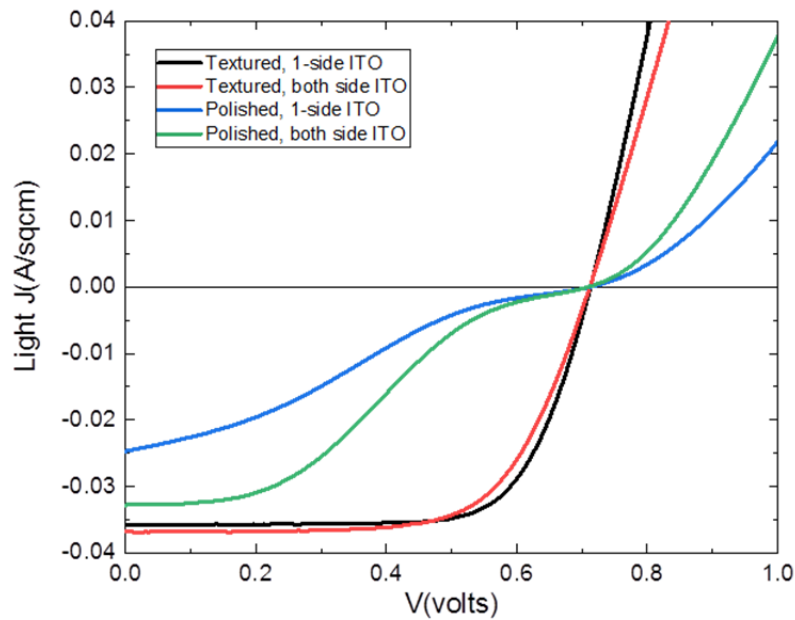


Figure 5.3: Light JV curves for cells K to N showing different diode characteristics for FHJ cells on different surface finish and ITO depositions.

The importance of surface texturing is easily noticed in the cell results for the polished and textured samples. Though having approximately the same measured Voc, the Jsc for the textured samples was greatly improved due to the reduction in front surface reflection, thus ensuring an increase in absorption of incident light. The significantly low Fill factors on the polished samples were rather unexpected as the same intrinsic and doped a-Si:H layers, ITO and metal layers were deposited on both types of sample surface. We note that similar S-shaped JV curves are commonly observed on samples with thicker intrinsic and/or doped a-Si layers, which limits effective carrier collection. These S-shaped JV curves suggest a possible difference in growth rate and thickness on the polished wafer than on the textured wafers. The hypothesized thicker i-layer is also consistent with the much higher lifetime where it would provide better passivation. Figure 5.3 also shows a clear tradeoff between Jsc and FF on the cells with textured surface having 1-side ITO versus both side ITO depositions. The cell with both side ITO (cell N) showed better Jsc values than its counterpart (cell M) but with lower FF. This tradeoff is clearly depicted in the red and black JV curves in Figure 5.3. The improvement in Jsc, and consequently reduction in FF, appears to originate from the addition of the backside ITO, which is supposed to improve the reflection of long wavelength light. The impact of surface texture in reducing front reflection losses and rear ITO in boosting rear contact internal reflection is clearly shown in the QE curves for all 4 cells, shown in Figure 5.4, highlighting the improved optical response in the red region.

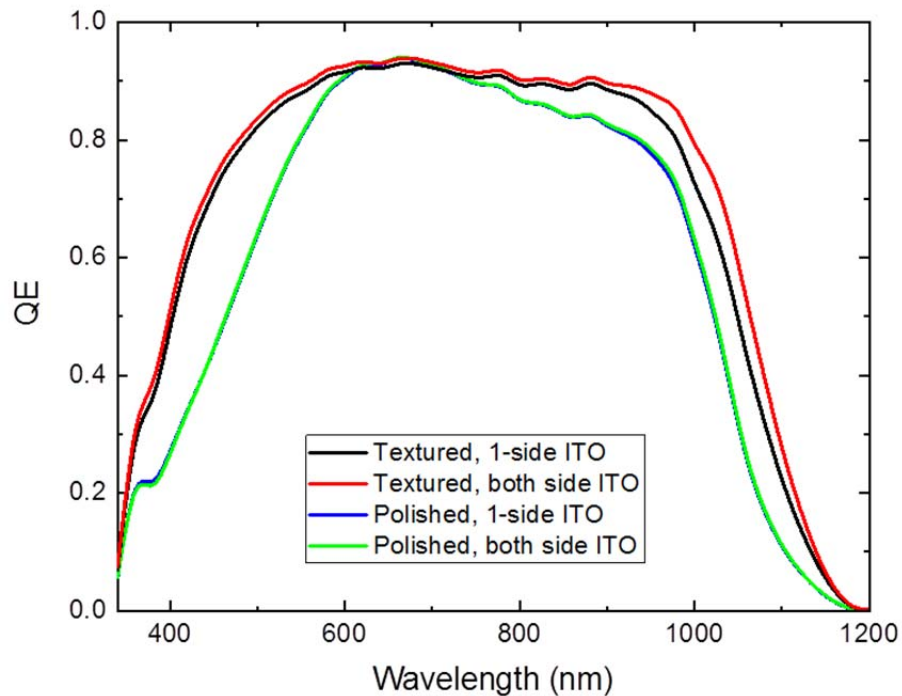


Figure 5.4: External quantum efficiency (EQE) measurement on all 4 cells from Table 5.5. Cells on polished surface show poor short and long wavelength response irrespective of backside ITO due to high front surface reflection and poor internal light trapping. Cells on textured surface show better short wavelength response due to reduced front surface reflection and improved long wavelength response for the cell with backside ITO due to rear contact reflection.

Given the cell results in Table 5.5, it is clear that a better tradeoff to achieve an overall higher cell conversion efficiency on a textured wafer will require only front side ITO or an improved n.a-Si:H/ITO contact if both side ITO is used.

## 5.2 Interdigitated Back Contact Silicon Heterojunction (IBC-SHJ) Solar Cell

IBC-SHJ solar cells have consistently been the structure for record efficiencies in single junction cells for the last couple of years. As noted in chapter 1, the IBC-SHJ structure combines the high  $V_{oc}$  of HJ cell architecture with the high  $J_{sc}$  of the

IBC structure to improve the overall conversion efficiency of a cell. The p-doped emitter layer and an n-doped back surface field (BSF) layer are both formed on the backside of the solar cell in this architecture. With both contacts on the back, they avoid all shading loss from front surface metal grids but introduce the challenge of patterning the isolated emitter and base regions typically in an alternating pattern of long thin strips. It is the reliable, low cost, high throughput lateral structuring of the alternating strips of the two regions with less than 100  $\mu\text{m}$  separation that has been most challenging to their manufacturability. Our approach to making IBC-SHJ cells that are manufacturable and cost effective is detailed in this section. It involves the use of laser-based and/or PECVD shadow mask processes to rapidly pattern the backside emitter and base regions. The intrinsic and doped a-Si:H layers developed in chapter 4 were used in making these IBC cells. All the devices reported here were completed with shadow mask metal deposition. An alternative method for patterning metal contacts, involving direct laser isolation of a blanket metal deposition, was also introduced in this section.

### **5.2.1 Laser Processed IBC Cells**

The IBC-SHJ cell fabrication process begins with the passivation of the c-Si surface by the deposition of a thin i.a-Si:H film on both sides of the c-Si sample, after which the optical properties of the front surface is enhanced by the deposition of an anti-reflection (AR - a stack layer of 80 nm a-SiNx:H and 20 nm a-SiC:H) coating. Subsequent steps involve the critical challenge of patterning the p and n strips on the backside. Our effort to simplify this process using laser-processing techniques to dope and/or define the emitter and base regions on the backside are presented in this section. These processes involve localized laser-fired contacts (LFC), laser ablation of

a sacrificial etch barrier layer, laser ablation of PECVD emitter or base contact layers and laser ablation of metal layers to define the contact electrodes. The first three are used to form the alternating interdigitated pattern of base or emitter contact or doped layer strip, while the fourth is used to create the interdigitated metal electrodes out of a blanket metal layer. The UV laser ablation work presented in this section were performed with our collaborators at the Research Center for Lasers and Plasmas, University of Virginia (Prof. Mool Gupta and graduate student Zeming Sun) and has been reported in [99] and [100].

#### **5.2.1.1 Laser Fired Contact (LFC)**

Laser fired contact on an n-type c-Si using a novel metal stack consisting of Ti/Sb/Al has been shown to be a viable technology that utilizes laser-processing technique to achieve high efficiency and throughput [101]. Most LFC on c-Si solar cells has involved the simple firing of Al into p-Si wafers. Localized contact allows over 99% cell area to have good passivation, and firing through insulating passivation allows simple structure without having to form metal contact. We explored this option in making high efficiency IBC-SHJ solar cell. IEC had previously developed LFC using Sb doping for n-Si wafers [101] and had planned to use it as an integral part of a manufacturable advanced IBC-SHJ structure. The device fabrication process is outlined as follows:

- 1) Sub 10 nm i.a-Si:H layer is deposited on both sides of an n-type CZ wafers having (100) orientation with resistivity of 5-8  $\Omega$ -cm and thickness of 150  $\mu$ m. These wafers were prepared using the same wafer cleaning process as reported in [63].

- 2) A stack dielectric layer consisting of 80 nm-thick a-SiN<sub>x</sub>:H and 20 nm-thick a-SiC:H is then deposited on the front side as an anti-reflection (AR) coating.
- 3) An 80 nm-thick a-SiN<sub>x</sub>:H blocking layer is deposited on the back side using a deposition mask to define the 350 μm n-strip.
- 4) A 5 nm-thick i.a-Si:H layer is deposited to protect the a-SiN<sub>x</sub>:H layer from subsequent HF wet chemical etch.
- 5) This is followed by a blanket p.a-Si:H layer deposition on the backside to form the HJ emitter.
- 6) A blanket Ti/Sb/Al metal stack is then deposited on the backside of the sample for carrier collection.
- 7) An LFC contact to the n-type c-Si is then formed by using either a 7 ns, 532 nm, pulsed laser or a 25 ns, 355 nm pulsed laser to drive the metal stack through the a-SiN<sub>x</sub>:H along the n-strip.

All dielectric layers were grown in a MC-PECVD chamber, where each chamber is dedicated to a unique dielectric film to prevent cross contamination. The metal stack was deposited in an e-beam PVD system with a rotating source for different metal. The device structure and an SEM image of the laser-fired region are shown in Figure 5.5.

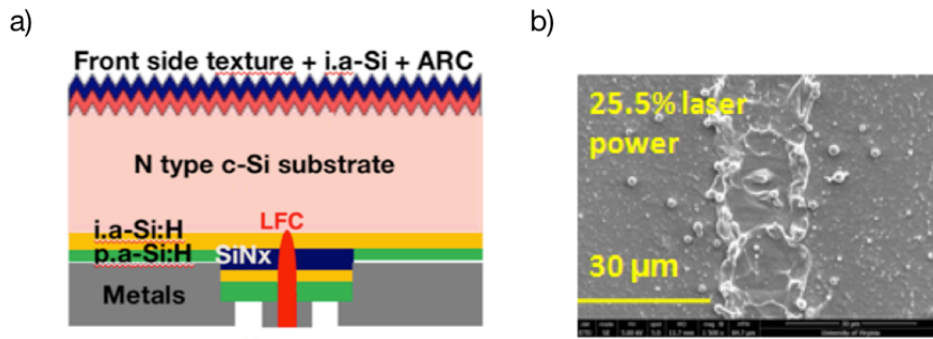


Figure 5.5: a.) Device architecture for IBC-SHJ with LFC through the n-strip, b.) SEM image of laser spots using 25.5% laser power optimized for LFC.

The JV curve for the best cell in this experiment, from MC1658-05, is shown in Figure 5.6. A significant decrease in  $V_{oc}$  can be observed on the measured cell compared to the  $iV_{oc}$  (after i-layer) suggesting a substantial recombination lost during LFC. This can be attributed to the i.a-Si:H/a.SiN<sub>x</sub>:H insulating layer possibly causing inversion layer that increases recombination.

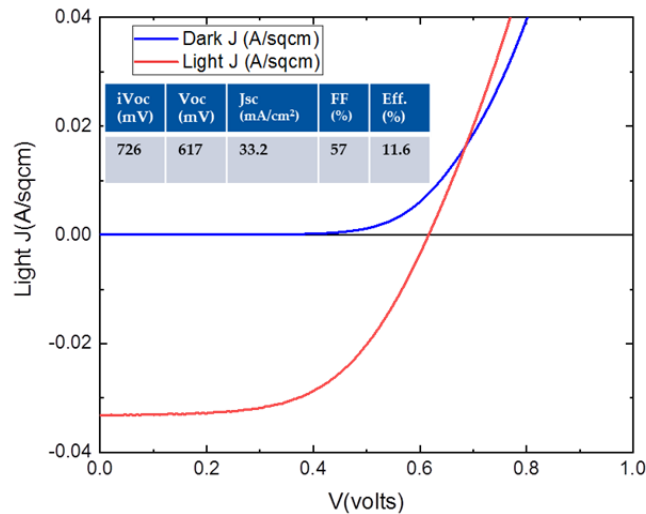


Figure 5.6: Light and dark JV curve of an IBC-SHJ solar cell with laser-fired contact through Ti/Sb/Al metal stack (MC1658-05). Insert shows cell parameters. Reported  $iV_{oc}$  measured after i-layer passivation.

To determine the source of these losses, LFC through two types of passivation stacks, i.a-Si:H/n.a-Si:H and i.a-Si:H/a-SiNx:H, were investigated on an n-type silicon front HJ solar cell. The front HJ cells were fabricated as described in section 5.1. A p.a-Si:H film was deposited on the front surface to form the HJ, while either a-SiNx:H or n.a-Si:H was deposited on the back surface as a dielectric layer for formation of LFCs. A sputter deposited 80 nm ITO and an e-beam evaporated metal grids form the front contact, while a metal stack of 5nm Ti / 50nm Sb / 500 nm Al is deposited on back dielectric layers. The n.a-Si:H on the back surface forms a passivated back surface field with an ohmic contact to the metal stack and therefore already a fully formed solar cell even before LFC. Studies of LFCs on this structure allow us to investigate degradation of cell performance with various laser-processing conditions.

The LFC's were formed by firing a 7ns pulse width, 532 nm wavelength, Nd-YAG pulsed laser through the back metal stack, forming a 50- $\mu$ m-diameter point contact. The repetition frequency of the laser and the laser diode current can be adjusted, both of which adjust the average power delivery ( $P_{avg}$ ). The spacing between the spots determines the total laser affected area on the contact pad (0.56 cm<sup>2</sup>). Given that the energy per spot and number of spots were both variable, we developed the concept of energy delivered per unit area ( $E_A$ ) to parameterize the impact of the laser conditions. Analysis of the dark and illuminated diode characteristics after the LFC offered some insight into laser damage, degradation to Voc and the inversion layer surrounding the LFC spots. A single diode lumped circuit approximation according to [62] was then used to extract circuit parameters like series resistance ( $R_S$ ), diode ideality factor ( $n$ ), and saturation current density ( $J_0$ ).

Figure 5.7 shows the changes in Voc and FF of FHJ cells as a function of laser

energy delivered per unit area ( $E_A$ ) during LFC through n.a-Si:H and a-SiN<sub>x</sub>:H dielectric layers. Note the opposing trend with increasing  $E_A$ . For LFC through n.a-Si:H, there is a ~15 mV and ~50 mV decrease in  $V_{oc}$  after LFC with  $E_A$  of 0.1 and 0.2 J/cm<sup>2</sup> respectively. This decrease in  $V_{oc}$  is solely due to laser damage caused by the LFC. A  $V_{oc}$  of ~ 690 mV and ~ 660 mV is achieved with an  $E_A$  of 0.1 and 0.2 J/cm<sup>2</sup> respectively for LFC through n.a-Si. However, devices with a-SiN<sub>x</sub>:H dielectric layers shows even lower  $V_{oc}$  of ~ 640 mV with  $E_A$  of 0.1 – 0.2 J/cm<sup>2</sup>, despite both structures having very similar passivation quality with similar  $iV_{oc}$  of 715 mV before LFC.

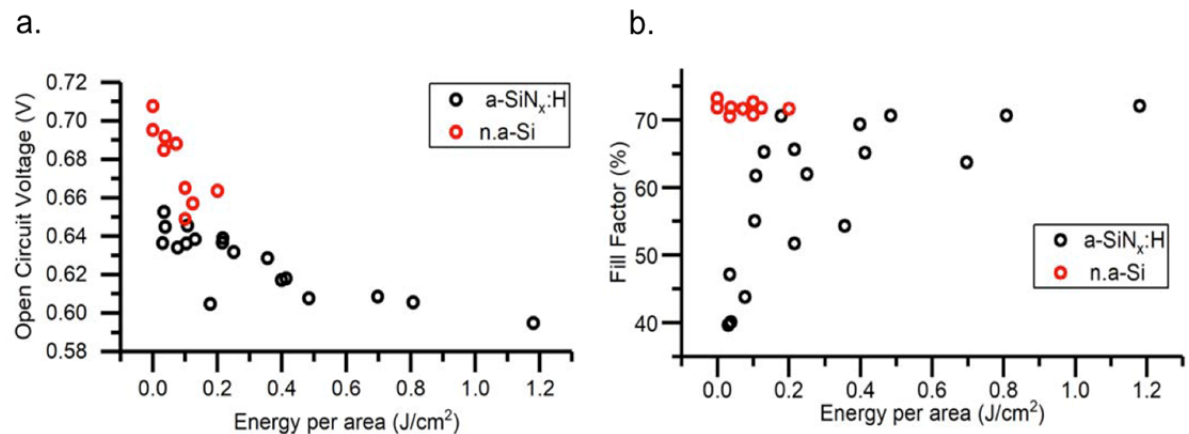


Figure 5.7: Changes in (a)  $V_{oc}$  and (b) FF of FHJ cells as a function of laser energy delivered per unit area during LFC through n.a-Si:H (red symbols) and a-SiN<sub>x</sub>:H (black symbols) [100].

Figure 5.8 shows the variations in  $n$  and  $J_0$  values for both cells under dark and light condition. The  $n$  and  $J_0$  for the LFC through n.a-Si:H, with values of ~1.7 and ~ 10 nA/cm<sup>2</sup> respectively, are rather insensitive to  $E_A$  in both dark and light. However, the cells with LFC through insulating a-SiN<sub>x</sub>:H dielectric layer show diode parameters

in dark similar to those of n.a-Si:H but exhibits an increase in the light parameters at low  $E_A$ . Abnormally high values of  $n$  and  $J_0$  found only under illumination indicates that the minority carrier (hole in this case) collection suffers from non-ideal back contacts despite an acceptable ohmic back contacts for the majority carrier electrons in dark. This can be attributed to the band bending and presence of a weak inversion layer formed by i/a-SiN<sub>x</sub>:H layer at the regions surrounding the LFC spots. This inversion layer acts as an additional back HJ for the minority carriers.

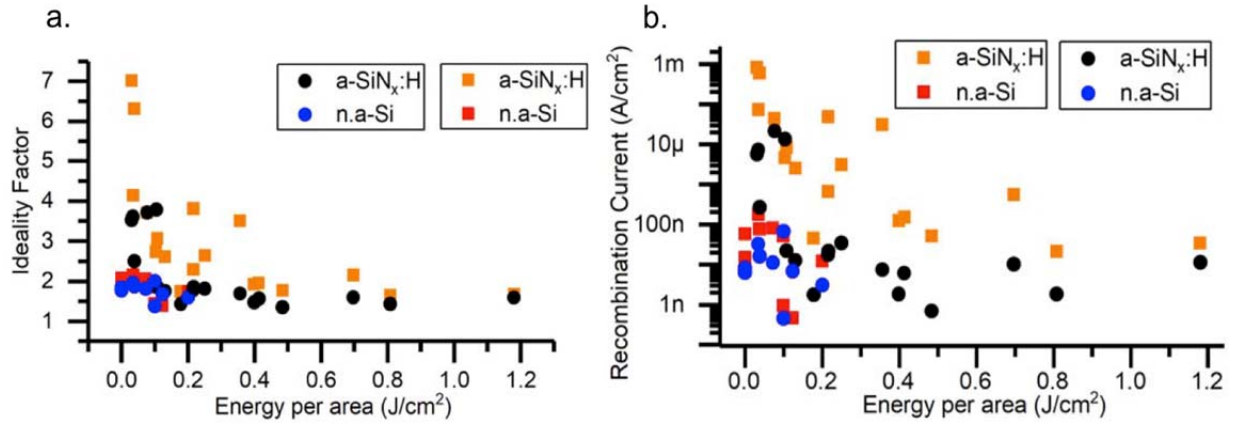


Figure 5.8: Estimated (a) Ideality factor,  $n$ , and (b) recombination current,  $J_0$ , for dark JV (blue and black symbols) and light JV (red and orange symbols) for cells with either a-SiN<sub>x</sub>:H (black and orange symbols) or n.a-Si:H (blue and red symbols) rear dielectric layer as a function of  $E_A$  [100].

On the other hand, the i.a-Si:H layer forms a weak inversion layer on n-type c-Si due to the band alignment. The charge introduced by the n.a-Si:H layer on top of the i-a-Si:H, in the case of i/n.a-Si:H dielectric stack, transforms this inversion layer into an accumulation layer and effectively creates a BSF. This avoids formation of back HJ for the LFC cell with i/n.a-Si:H stack that results in identical  $n$  and  $J_0$  values

in both dark and light.

In general, this study confirms that a low resistance contact could be formed by LFC through various dielectric layers. However, to achieve high efficiency Si cells using HJ and LFC, the band bending, band alignment and charge distribution at the interface surrounding LFC requires critical re-evaluation. HJ structures are more sensitive to degradation by LFC due to their inherent induced junction formation mechanism. To minimize the LFC damage, the surrounding regions need to have a back surface field to repel minority carrier away from the defective LFC spots. Thus, our device structure has been modified to i.a-Si:H/n.a-Si:H/a-SiNx:H dielectric stack and is currently utilized in subsequent cell structures, shown in Figure 5.9, for an ongoing project with the U.S. Department of Energy.

#### **5.2.1.2 Plasma Masked Laser Process (PMLP)**

To eliminate the negative effects of laser damage during LFC, we developed a new IBC device structure shown in Figure 5.9. This structure is realized using masked deposition of the n-region to define the base contact. It replaces the LFC with selective ablation of the p.a-Si:H/i.a-Si:H stack followed by the etching of a-SiNx:H blocking layer to open up the base region. Using this stack structure, we have achieved  $\tau_{\text{eff}}$  of  $\sim 1$  ms and  $iV_{\text{oc}}$  of 723 mV after laser processing and subsequent wet chemical etch – a good indication of minimal laser damage. The PMLP IBC-SHJ cells were fabricated in the following sequence:

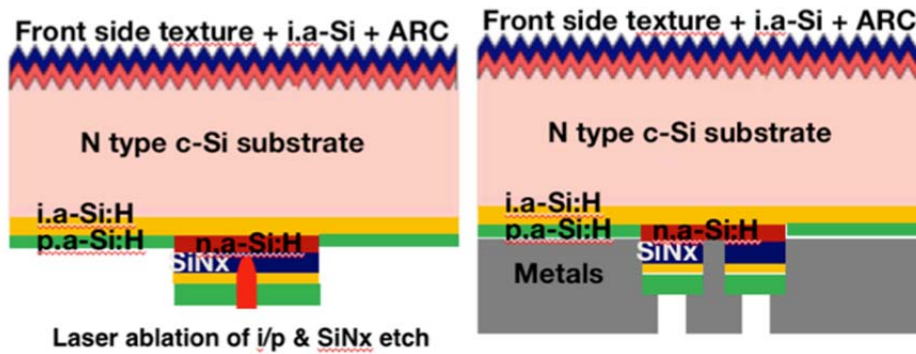


Figure 5.9: Modified IBC-SHJ device structure with the addition of an i.a-Si:H/n.a-Si:H BSF to repel minority carrier around the laser processed area. The device fabrication process involves laser ablation of the i/p.a-Si:H layer, (indicated by red vertical region in the middle of the n region), followed by an a-SiNx:H etch (left) and metal deposition to contact the n.a-Si:H layer (right).

1. Sub 10 nm i.a-Si:H layer is deposited on both side of an n-type CZ wafers having (100) orientation with resistivity of 5-8  $\Omega$ -cm and thickness of 150  $\mu$ m.
2. A stack dielectric layer consisting of 80 nm-thick a-SiNx:H and 20 nm-thick a-SiC:H is deposited on the front side as an anti-reflection coating.
3. A stack layer of 50 nm-thick n.a-Si:H/120 nm-thick Si-rich a-SiNx:H/5 nm-thick i.a-Si:H stack is deposition through the n-strip mask on the back surface. The a-SiNx:H acts as a blocking layer, while the i.a-Si:H protects the a-SiNx:H layer from HF etch.
4. A 20 nm p.a-Si:H layer is then deposited everywhere on the backside.
5. The p.a-Si:H/i.a-Si:H/a-SiNx:H stack is selectively ablated over the base region using a UV laser. Ideally a soft laser power is sufficient to ablate the sacrificial p/i.a-Si:H completely and nitride layer partially, after

which 2% HF solution is used to complete the removal of any residual nitride to allow contact to the n-layer.

6. Finally, 2  $\mu\text{m}$ -thick Al metal electrodes are deposited by e-beam evaporation using gap mask.

This structure, despite the promise of high  $iV_{oc}$  after laser processing and etching, has its limitations – accurate alignment and control of the masked deposition process. The fabrication of this structure depends on the successful deposition of the n.a-Si:H/a-SiN<sub>x</sub>:H stack through the n-strip mask without contaminating the p-strip. Experience has shown this to be the technical limitation with this approach. Post-deposition diagnostics of the PECVD masked patterns and masked regions reveal the presence of thin plasma films on the masked regions due to plasma ‘leaking’ laterally under the mask during PECVD deposition. These unwanted layers contaminate and interfere with the formation of the intended device structure on the adjacent supposedly protected region. The JV measurement for these cells, shown in Figure 5.10, consequently, have shown rather mediocre values suggesting a poor HJ formation consistent with the above description of plasma leakage. Figure 5.11a and b shows the front and back view respectively of the shadow mask after several PECVD depositions. The coatings on the backside of the fingers in Figure 5.11b confirm the presence of lateral ‘leakage’ during plasma deposition resulting in the contamination of adjacent regions. This ‘leakage’ film is also non-uniform, as can be seen in Figure 5.11b, with a greater proportion occurring close to the bus bar where the fingers are more flexible, thus providing a route for plasma films into the adjacent protected regions and under the mask.

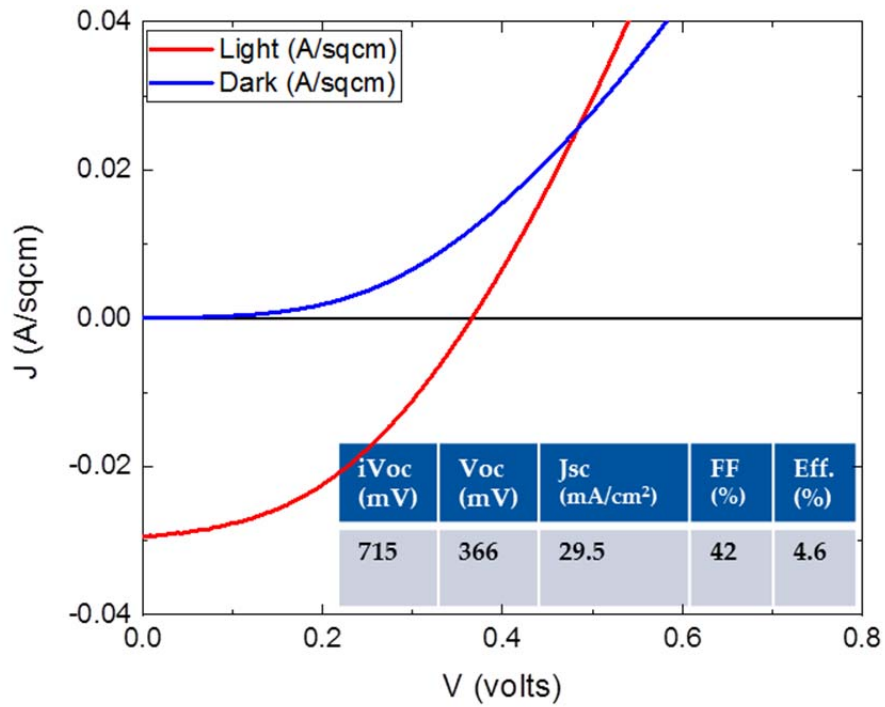


Figure 5.10: Light and dark JV curve of an IBC-SHJ solar cell with PMLP fabrication process (MC1679-02). Insert shows cell parameters. Reported iVoc measured after plasma mask deposition of n- and p-doped layers.

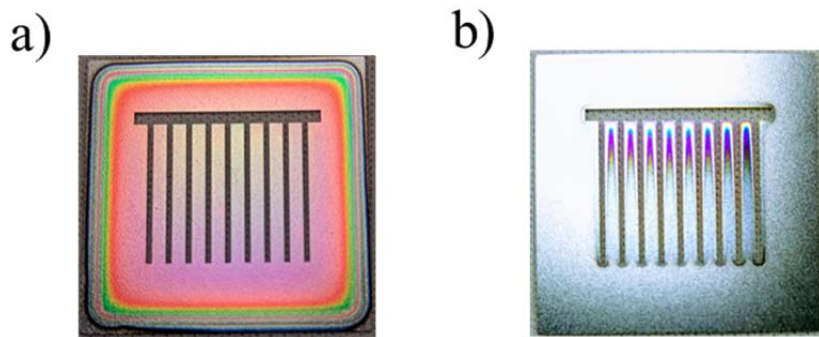


Figure 5.11: a) Front view and b) back view of the n-strip shadow mask used during PECVD masked deposition.

To mitigate this effect, we proposed an intermediate etch of the plasma films with HNA solution after the mask deposition of n.a-Si:H/a-SiNx:H to remove any plasma leakage on the protected surface (p-strip in this case). A 3-terminal front junction device with rear side IBC structure was used as a test structure for this study. Figure 5.12 shows the 3 terminal test structure, which was made with the same fabrication steps as the PMLP IBC device except that the front AR coating was replaced with a front base contact and ITO/metal grids. This allowed us to analyze the device as a front junction cell in conjunction with the rear emitter contacts. The rear base contact, with an a-SiNx:H blocking layer, represents the same base region in the PMLP IBC cell. It would require a laser process to open up the n-strip to be functional. It is a ‘dummy’ contact that is unused in this set up but allowed us to evaluate the effect of etching any leakage films under the mask during its deposition. We also prepared a control sample without intermediate HNA etch.

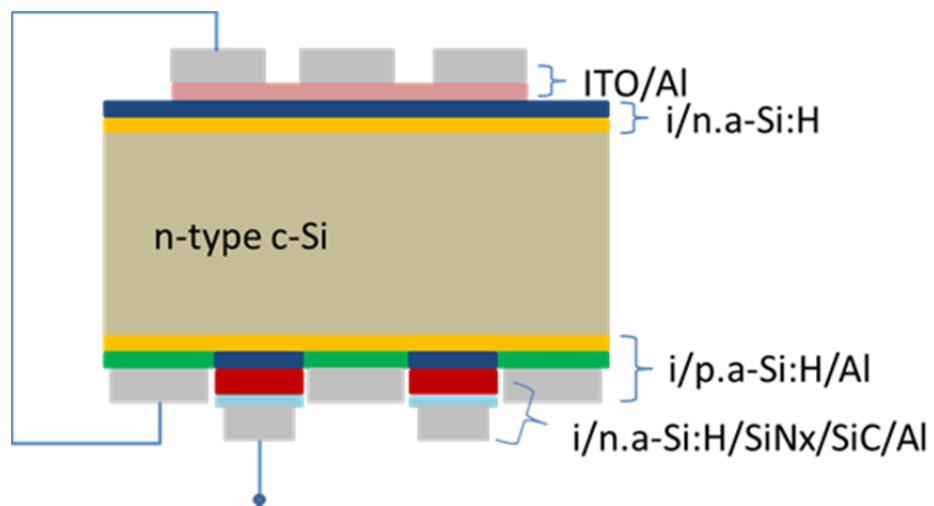


Figure 5.12: 3-Terminal front HJ test structure for diagnosing plasma leakage during PECVD masked deposition.

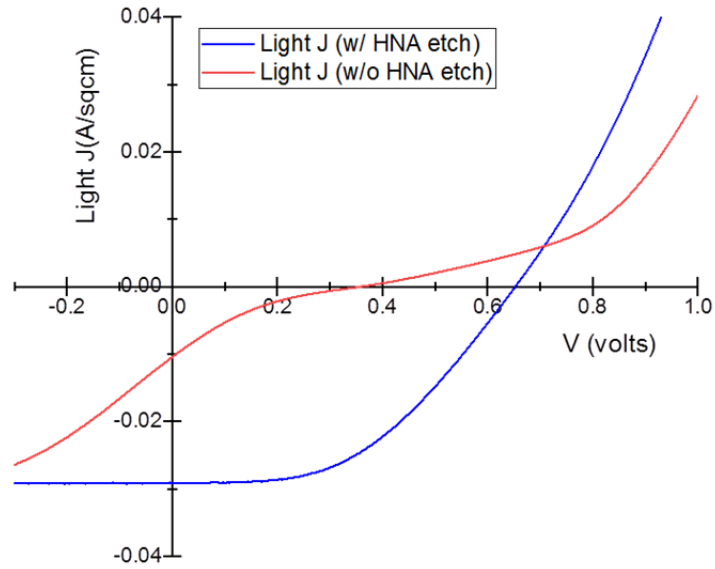


Figure 5.13: Light JV curves for the 3-terminal front HJ test structure with and without HNA etch of plasma leakage films.

Figure 5.13 shows the JV curves for the two processing conditions with and without an intermediary HNA etch. The introduction of the intermediate HNA etch clearly helps to remove the plasma leakage films and thus enables a better HJ contact formation. However, the HNA etch is non-uniform because the plasma leakage itself is non-uniform. Thus, resulting in a non-uniform surface topography after the HNA etch that is difficult to re-passivate.

To successfully utilize CVD masked deposition to realize this structure, a significant effort must be dedicated to making robust masks and sample holder units that eliminate plasma leakage completely or develop fabrication process that only utilizes masked deposition for films that are easily etched with good selectivity (e.g. HF etch of a-SiN<sub>x</sub>:H on a-Si:H layers). A revised fabrication process, termed PMLP2, that utilizes masked deposition of a-SiN<sub>x</sub>:H instead of n.a-Si:H/a-SiN<sub>x</sub>:H stack for

step 3 was developed. This structure is similar to PMLP except that only a-SiNx:H was first deposited through n-strip mask in step 3 above and n.a-Si:H was deposited through the n-strip mask and nitride opening after laser ablation and nitride etch of the n-region. Results from the PMLP2 structure have shown conversion efficiency up to 15.1% with measured  $V_{OC}$  up to 667 mV, which is very promising. The JV curve for the best PMLP2 cell (MC1699-18) is shown in Figure 5.14. Preliminary JV analysis showed that the  $R_s$  for this cell is equivalent to that of our best FHJ cells thus, FF loss Table 5.6 outlines the steps we took to address different fabrication limitations with marked improvements in cell performance after each of the iterations.

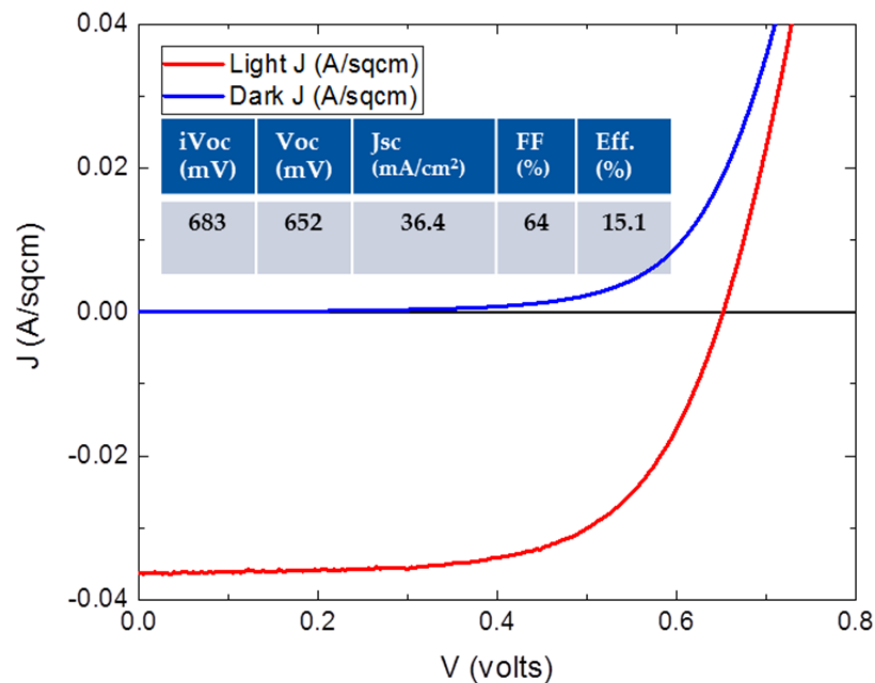


Figure 5.14: Light and dark JV curve of an IBC-SHJ solar cell with PMLP2 fabrication process (MC1699-18). Insert shows cell parameters. Reported  $iV_{OC}$  measured after plasma mask deposition of p- and n-doped layers, laser ablation and chemical etching.

Table 5.6: Summary of device iterations geared towards solving process dependent technical difficulties with PMLP structures. These steps have led to over 3-fold improvement in cell efficiency.

Cell ID	Description	Cell result	Challenges
MC1679-02 (PMLP)	n/SiNx stack through n-mask, blanket p, laser ablation of n-strip, nitride etch and metallize.	iVoc= 717 mV, Voc= 366 mV, Jsc= 29.5 mA/cm <sup>2</sup> , FF=42.2%, Eff.=4.6%	Plasma ‘leakage’ of n/SiNx films on the p-strip before p-layer deposition leading to poor HJ contact.
MC1687-01 (PMLP)	Introduced HF/HNA etch to remove plasma leakage of SiNx/n films.	iVoc= 681 mV, Voc= 537 mV, Jsc= 33.8 mA/cm <sup>2</sup> , FF=47%, Eff.=8.5%	HNA etch improved the cells but introduced another challenge as it also etch the passivating i-layer. Low iVoc.
MC1697-08 (PMLP2)	SiNx through mask, blanket p, laser ablation of n-strip, nitride etch, n-dep. thru mask and metallize.	iVoc= 722 mV, Voc= 565 mV, Jsc= 33.3 mA/cm <sup>2</sup> , FF=57.1.2%, Eff.=10.7%	Plasma ‘leakage’ of n-layer films on top the p-layer resulting in increased recombination.
MC1697-07 (PMLP2)	Introduced TMAH etch to remove plasma leakage of n-layer films.	iVoc= 719 mV, Voc= 580 mV, Jsc= 33.4 mA/cm <sup>2</sup> , FF=56.3%, Eff.=10.9%	TMAH plasma ‘leakage’ etch most certainly removes some p-layer. Voc decreased after HT.
MC1697-04 (PMLP2)	Increased p-layer thickness to 20 nm.	iVoc= 710 mV, Voc= 636 mV, Jsc= 34.3 mA/cm <sup>2</sup> , FF=59.5%, Eff.=13%	Low iVoc. Better field effect passivations after TMAH etch. Voc improved after HT

MC1699-18 (PMLP2)	Increased p-layer thickness to 40 nm.	iVoc= 703 mV, Voc= 652 mV, Jsc= 36.4 mA/cm <sup>2</sup> , FF=63.6%, Eff.=15.1%	Low iVoc. Better field effect passivations after TMAH etch. Voc improved after HT.
-------------------	---------------------------------------	--	--

### 5.2.1.3 All Laser Process (ALP)

The all laser process approaches the patterning of the emitter and base regions solely by laser processing. There is no plasma masking. A 355 nm wavelength (UV) laser with 25 ns pulse width and 8 W full-scale power was used for this process. This short wavelength laser is best suited for this application because it minimizes laser damage due to the strong absorption of the UV laser. This process also lends itself to easy manufacturing because of its heavy dependence on laser processing. The IBC-SHJ cells were fabricated in the following sequence:

1. Sub 10 nm i.a-Si:H layer is deposited on both side of an n-type CZ wafers having (100) orientation with resistivity of 5-8  $\Omega$ -cm and thickness of 150  $\mu$ m.
2. A stack dielectric layer consisting of 80 nm-thick a-SiNx:H and 20 nm-thick a-SiC:H is then deposited on the front side as an anti-reflection (AR) coating.
3. A stack layer of 30 nm-thick n.a-Si:H/120 nm-thick Si-rich a-SiNx:H/5 nm-thick i.a-Si:H stack is deposition on the back surface. The a-SiNx:H acts as a blocking layer, while the i.a-Si:H protects the a-SiNx:H layer from HF etch. An n.a-Si:H can also be used as a nitride protecting layer.

4. The i.a-Si:H/a-SiNx:H stack is selectively ablated over the emitter region using a UV laser. Ideally a soft laser power is sufficient to ablate the sacrificial i.a-Si completely and nitride layer partially, after which 2% HF solution is used to complete the removal of any residual nitride. A hydrophobic surface along the emitter region confirms the complete removal of the nitride layer.
5. The exposed n./i.a-Si:H stack on the emitter region is etched off using a solution containing 1-5 % TMAH and <1 % polyalkylene glycol in 95-99 % water or in HNA.
6. A blanket i/p.a-Si:H layer is then deposited to re-passivate the c-Si surface and form the HJ contact on the emitter region.
7. The same 355 nm laser used for selective ablation of the emitter region is once again used to selectively ablate the i/p.a-Si:H on top of the base region, after which a 2% HF is used to etch off the nitride blocking layer to open up the n-stripe.
8. Finally, 2  $\mu\text{m}$ -thick Al metal electrodes are deposited by e-beam evaporation, using the same mask and dimensions as the previous PMLP design. Note that this requires the laser ablation pattern to be very closely matched to the metal mask within the  $\sim 80 \mu\text{m}$  alignment tolerance.

The rear surface of the device is similar to that shown in Figure 5.9 and the fabrication process flow is detailed in Figure 5.15.

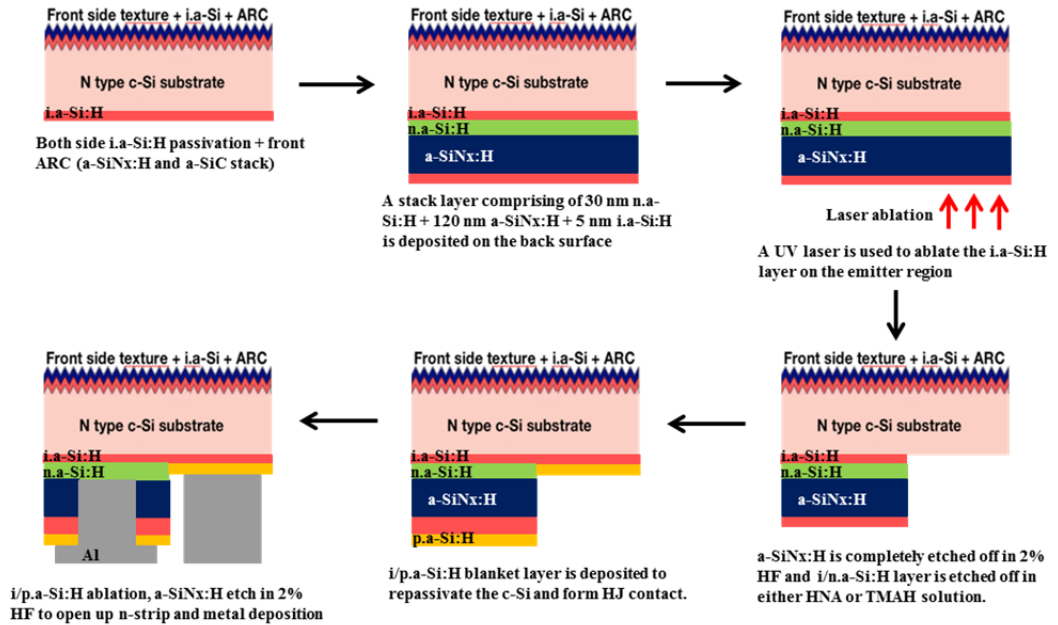


Figure 5.15: Fabrication process-flow for an all laser process (ALP) for making an IBC-SHJ solar cell.

The critical challenges with this process involves the successful ablation of the emitter region (which comprises of  $\sim 90\%$  of the cell area) without degrading passivation, successful alignment of the n and p regions, complete etching of the emitter region without contamination and subsequent i./p.a-Si:H re-passivation, and finally, the selective ablation of the base region and nitride etch to open up the n-strip. Fabrication of 2 exploratory ALP cells indicated they both suffered from one or more of these challenges. Thus, an active device is yet to be measured as at the time of writing this dissertation. Changes to the fabrication process to resolve these problems are being implemented and currently in progress. SF6 assisted ablation of the stack structure for ALP is being considered as an option to minimize laser damage, as this

will require lower laser power. The main interest, however, for this process is the ease of incorporating it into a process line for mainstream manufacturing of IBC-SHJ cells.

In general, the PMLP and ALP IBC structures described in sections 5.2.1.2 and 5.2.1.3 respectively, only differs in the patterning of the i/n.a-Si:H layer. After that the process sequence is identical. ALP process flow has 2 laser steps and no masking, while PMLP has a masked deposition and a laser ablation step. Figure 5.16 shows the process flow and final device cross-section for the two concepts. Both devices have same front passivation and AR coating, a-Si:H i/p HJ emitters and a-Si:H HJ i/n contacts. Step 6 (laser ablation of i/p over the n a-Si:H strip) can expose 1-100% of the a-Si n-contact ranging from localized ‘point contacts’ to the entire n contact.

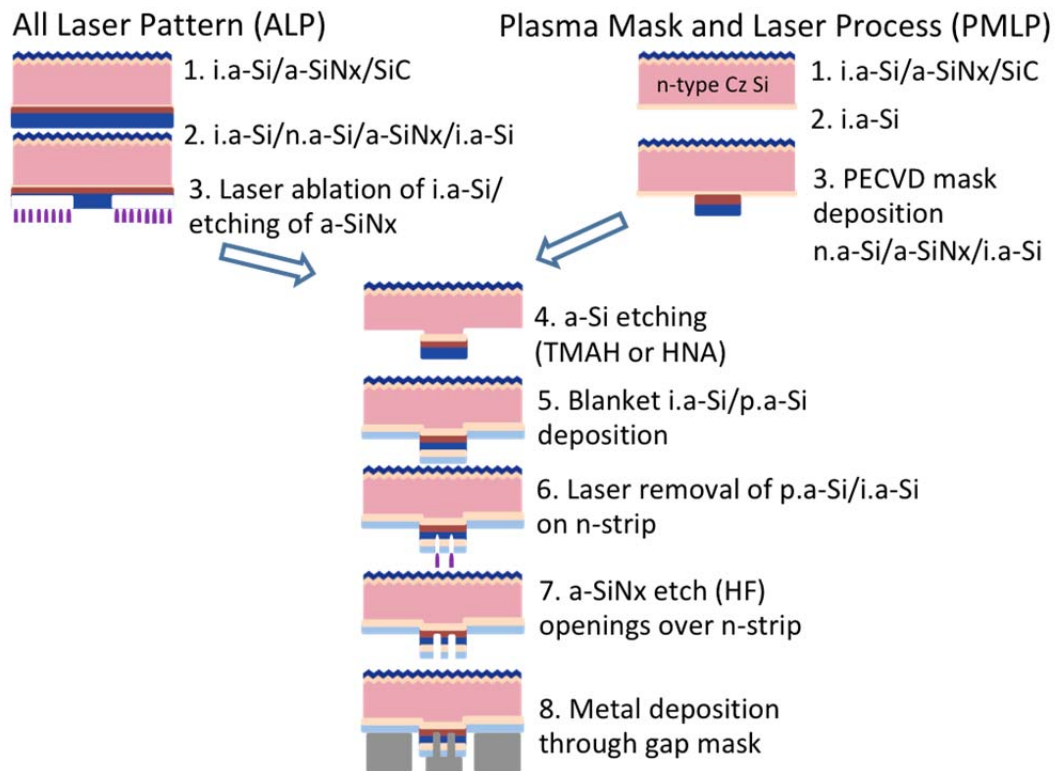


Figure 5.16: Process flow and final device cross-section for both the ALP and PMLP fabrication sequences.

#### 5.2.1.4 Direct Laser Isolation for Patterning Metal Contacts

The metal contacts in the previous three sections have been created using shadow mask during metal deposition. An alternative method for patterning metal contacts involves direct laser isolation of a blanket metal deposition. Laser based patterning techniques have attracted increasing attention due to their capability of simplifying the very complex and slow photolithography process which has been widely used to define the emitter and base region on the rear side of an IBC-SHJ cell. Our effort towards utilizing a laser based process for patterning involves the complete isolation of selected regions of the seed metal or sacrificial layers with negligible degradation of the initial passivation quality while maintaining high shunt resistance ( $R_{SH}$ ). A wide range of laser parameters was applied to create an IBC pattern by isolating p and n metal regions. The objective was to obtain  $R_{SH} > 1E3$  Ohms between metallized regions with minimal damage to the passivation under the laser ablated region as determined by surface recombination velocity (SRV).

The laser isolation experiments were carried out on a simple test structure as shown in Figure 5.17. We investigated the feasibility of laser patterning of two different e-beam deposited metal layers - a 65 nm thick Ni and a metal stack comprising of 5 nm Ti / 50 nm Sb / 10 nm Ni. Such a metal stack, as detailed in [101], provides good adhesion (by the 5 nm Ti), an n-type dopant to form good ohmic contact by LFC (by the 50 nm Sb, an n-type dopant) and a seed layer for subsequent Cu electro-deposition (by the 10 nm Ni). The metal was deposited by e-beam evaporation on an a-Si/SiNx/SiC dielectric passivation stack, which was deposited by PECVD process on semi-polished and textured c-Si wafers. The goal of this experiment was to effectively use a laser ablation process to remove the Ni or metal

stack, thus forming the interdigitated electrode pattern from a single layer of metal without degrading the passivation of the underlying dielectric layers.

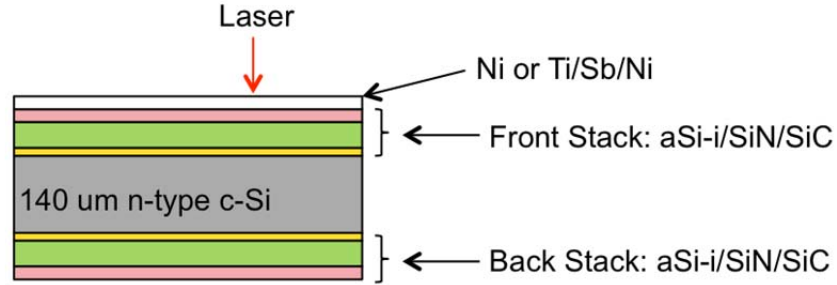


Figure 5.17: Test structure for direct laser isolation experiment of Ni and Ti/Sb/Ni stack metal on a well-passivated c-Si surface.

A 355 nm UV laser (Coherent MATRIX 355-8-50) with 25 ns pulse width and 8 W at full power was used to ablate the metals under different laser powers. An IBC pattern was laser scribed onto the metal contact surface. After the laser patterning process, I-V curves were measured to confirm the isolation resistance by placing probes on the two bus bars. Optical microscopy and scanning electron microscopy (SEM) were carried out to investigate the quality of the laser-scribed line. Finally, lifetime measurements were used to evaluate the induced damage after laser patterning and after chemically etching away the metal. The measured lifetime after the laser process enabled the estimation of the surface recombination velocity (SRV), which is derived from the extension of Eqn. 2.12 where:

$$\tau_s = \frac{W}{2S_{eff}} + \frac{1}{D} \left( \frac{W}{\pi} \right)^2 \quad 5.1$$

$$S_{eff} = \frac{W}{2} * \frac{1}{\tau_{eff}} \tag{5.2}$$

W is the wafer thickness,  $\tau_s$  is the surface lifetime,  $\tau_b$  is the bulk lifetime,  $\tau_{eff}$  is the measured effective minority carrier lifetime,  $S_{eff}$  is the effective surface recombination velocity and  $D$  is minority carrier diffusion coefficient. For very large  $\tau_b$  value, as is the case with our c-Si wafer, the  $1/\tau_b$  term in Eqn. 2.12 is negligible and can be eliminated. The second term in Eqn. 5.1 is on the order of 1  $\mu$ s and can equally be eliminated, thus simplifying the interpretation of effective lifetime to being dependent only on SRV and wafer thickness as shown in Eqn. 5.2.

Table 5.7: Isolation resistances after patterning of Ni coated samples.

Laser power (%)	0	26	27	28	29
Resistance (ohms)	20	25	2E8	1E7	8E7

Table 5.8: Isolation resistances after patterning of Ti/Sb/Ni coated samples.

Laser power (%)	0	25	25.5	26	26.5
Resistance (ohms)	114	740	2E5	2E6	3E5

Tables 5.7 and 5.8 show very low lateral resistance on the metal surfaces before the laser isolation process. As the laser power is increased gradually, the isolation resistance starts to increase. A complete isolation is observed at 27% power (for the Ni coated samples) and at 25.5% (for the Ti/Sb/Ni coated samples), with very high isolation resistance of 2E8 Ohms and 2E5 Ohms respectively, well above the 1E3

Ohms required. Further increase of the laser power reduces the isolation resistance by driving in some of the metal into the c-Si wafer and degrades the underlying passivation layers. Figure 5.18 shows the SEM and optical microscopy image of the patterned surface. The optical microscopy image shows a blue coloration (reflection from low a-SiNx:H thin film) underneath the ablated metal; indicative of the nitride layer still intact after the laser ablation process.

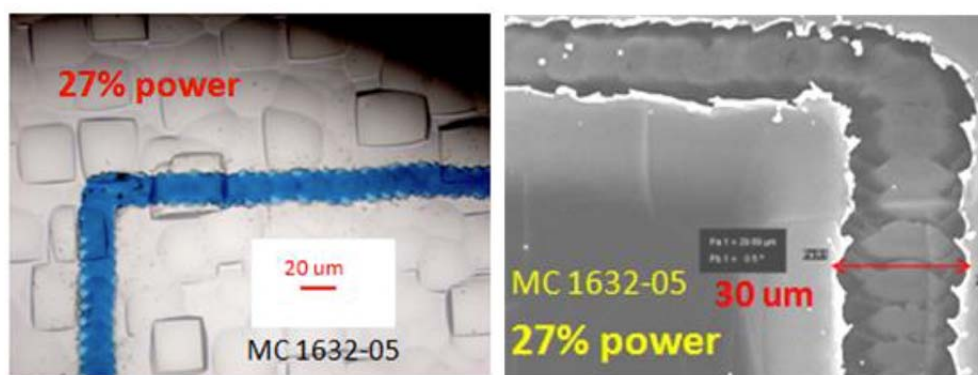


Figure 5.18: Left: Optical microscopy image of laser ablation region with exposed nitride pattern (blue coloration), Right: SEM image showing complete metal isolation along the laser scribed line with 27% laser power.

After the laser patterning and isolation resistance measurement, the metals were etched and lifetime re-measured. The lifetime decreased from  $\sim 4.3$  ms to  $\sim 1.6$  ms, and  $iV_{oc}$  from 746 mV to 720 mV however, a very low SRV of  $\sim 5$  cm/s was estimated [99]. This data demonstrates that careful adjustment of laser power enables complete isolation with negligible degradation to passivation.

Other alternative laser processing approach involves the use of a sacrificial layer to reduce the laser damage on the underlying passivation. The laser power and resistances shown in Tables 5.6 and 5.7, indicates that the processing window to

achieve good isolation and with minimal damage to passivation, using direct laser isolation, is very narrow. Thus, we explored the feasibility of using a sacrificial NiO layer, photoresist layer or low laser power combined with chemical etching to achieve good isolation. Our studies have shown isolation resistance as high as  $5.5E8$  Ohms, while preserving the passivation quality [99].

### **5.2.2 All PECVD-Masked Process (APMP)**

An alternative method to making IBC-SHJ cells is the use of only in-situ mask deposition to define the n- and p-strip during the PECVD process. This all PECVD masked process eliminates the use of any post deposition patterning steps like photolithography or laser processing thus should be fast, simpler and less expensive. It also eliminates any possible laser induced effect from previous structures like PMLP.

To make the n-strip, p-strip and gap masks, the same 7ns, 532 nm, Nd-YAG pulsed laser, used for LFC at the IEC, was used to scribe the n-pattern, p-pattern and gap pattern on a  $\sim 150$   $\mu\text{m}$  c-Si sample. After which the c-Si sample was etched in 45% KOH solution at  $\sim 70$   $^{\circ}\text{C}$  until the mask openings were created. Figure 5.19 shows the 3 deposition masks developed with this process for defining the n-strip, p-strip and gap region for metallization of an IBC structure. The same n-strip and gap masks were also used for PMLP.

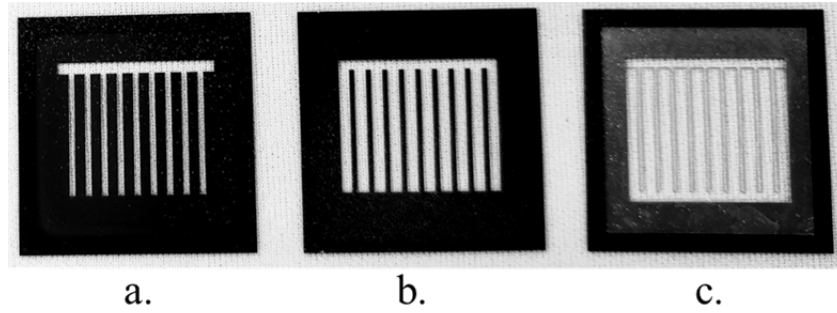


Figure 5.19: PECVD and PVD deposition masks used in making the IBC-SHJ discussed in this section. They are defined on a 150- $\mu\text{m}$  Si wafer using combination of laser patterning and chemical etching. a) n-strip mask, b) p-strip mask, and c) gap mask for metal deposition.

The dimensions of the n-strip and p-strip are 500  $\mu\text{m}$  and 1200  $\mu\text{m}$  respectively, while the opening on the gap mask for metal deposition is 300  $\mu\text{m}$  for n-contact, 1000  $\mu\text{m}$  for p-contact and 100  $\mu\text{m}$  gaps on each side. The n-strip mask defines the base region, the p-strip mask defines the emitter region and the gap mask defines the base and emitter metal contacts. Using these masks, the IBC-SHJ cells were fabricated in the following sequence:

1. Sub 10 nm i.a-Si:H layer is deposited on both side of an n-type CZ wafers having (100) orientation with resistivity of 5-8  $\Omega\text{-cm}$  and thickness of 150  $\mu\text{m}$ .
2. A stack dielectric layer consisting of 80 nm-thick a-SiN<sub>x</sub>:H and 20 nm-thick a-SiC:H is then deposited on the front side as an anti-reflection (AR) coating.
3. A PECVD masked deposition of 120 nm-thick Si-rich a-SiN<sub>x</sub>:H is then deposited over the emitter region through the p-strip mask. A short etch in 2% HF ensures the base region is free from any nitride leakage through the

p-strip mask. A hydrophobic surface along the base region confirms the complete removal of any nitride contaminant.

4. Another PECVD masked deposition is performed where a 50 nm-thick n.a-Si:H/160 nm-thick Si-rich a-SiN<sub>x</sub>:H stack is deposited on the base region using the n-stripe mask.

5. A longer etch in 2% HF is performed this time to completely remove the nitride on the p-stripe and thus open up the emitter region for the subsequent deposition. A hydrophobic surface along the emitter region confirms the complete removal of the nitride layer. The base region, however, should remain hydrophilic as it has a thicker a nitride layer. It is critical that some of this nitride layer on top of the n.a-Si:H remain intact after this etch as it prevents contamination of the base region from any lateral plasma leakage during the p.a-Si:H deposition.

6. The third and final PECVD masked deposition is performed using the p-strip mask to deposit a 20 nm-thick p.a-Si:H layer on the emitter region to form the HJ contact.

7. A third and final etch in 2% HF is now performed. This time until all the nitride on the n-strip is completely etched off. The etch process is complete when the n-strip becomes hydrophobic. The p-strip, with p.a-Si:H, will however remain hydrophilic.

8. An e-beam evaporator system is then used to metallized the sample. Using the gap mask, a 2 μm-thick Al is deposited on the emitter and base regions.

The front and back surface of a finished IBC-SHJ solar cell is shown in Figure 5.20, while the device structure and fabrication process flow is shown in Figure 5.21.

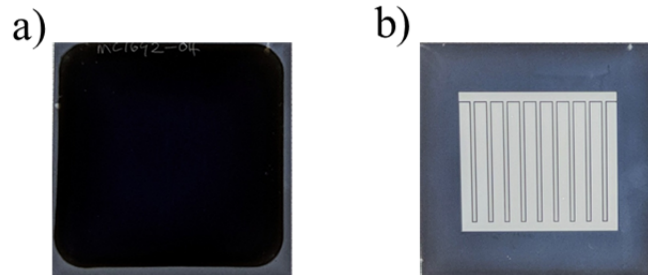


Figure 5.20: a) Front surface with AR coating and b) rear interdigitated emitter and base pattern of a complete IBC-SHJ cell.

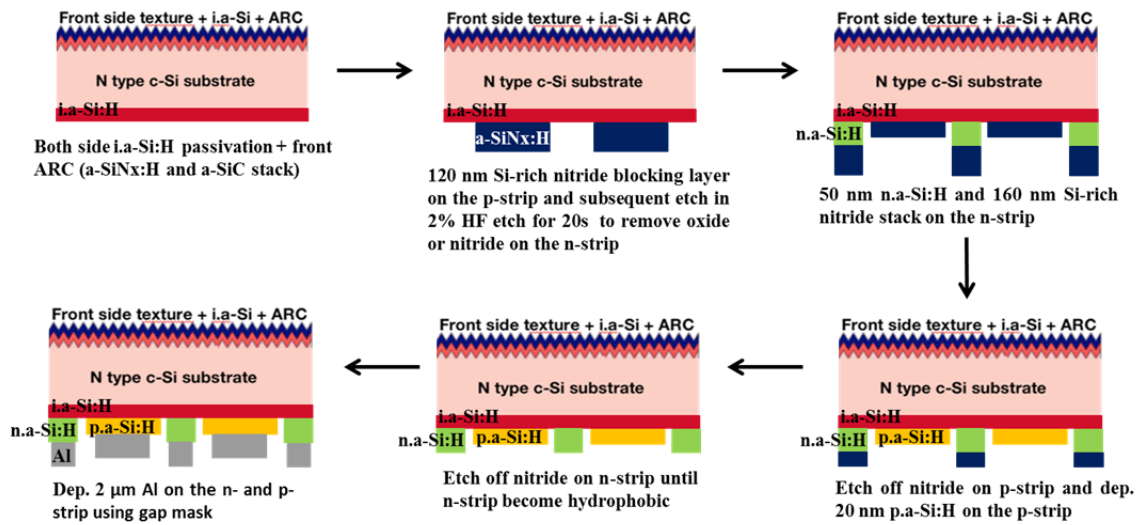


Figure 5.21: Fabrication process flow for an in-situ PECVD mask deposition process for making an IBC-SHJ solar cell.

The challenge with this method is similar with those described in section 5.2.1.2 – leakage of plasma films through the masked regions. Given that this structure

requires 3 shadow mask depositions, the negative consequences of plasma ‘leakage’ is intensified. Any attempt of making IBC-SHJ with this method would require a robust masks and sample holder units that can eliminate plasma leakage completely. Fabrication of exploratory APMP cells has shown conversion efficiency reaching only 11.1 %. The JV curve for this cell, from MC1661-11, is shown in Figure 5.22. Changes to the fabrication process to resolve these problems are being implemented and currently in progress.

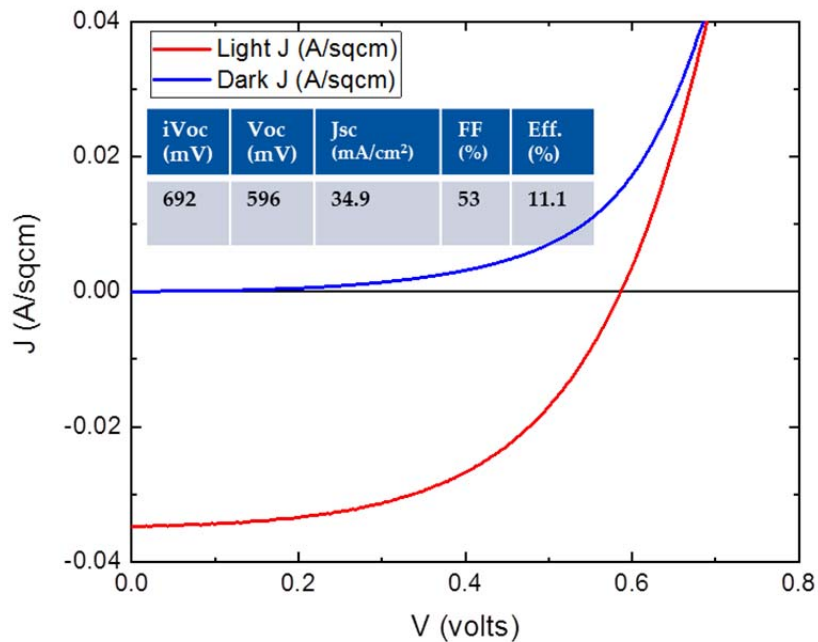


Figure 5.22: Light and dark JV curve of an IBC-SHJ solar cell with APMP fabrication process (MC1661-11). Insert shows cell parameters. Reported  $iV_{oc}$  measured after plasma mask deposition of nitride, p- and n-doped layers, and chemical etching.

Table 5.9 summarizes the different IBC structure discussed in this section, describing their processes, benefits and technical difficulties.

Table 5.9: Summary of IBC structures, outlining their fabrication processes, advantages and challenges. The process steps described here pertain to the rear side, as the front side is the same for all cases.

IBC structure	Process	Advantages	Challenges
LFC	Deposit blanket i-layer; SiNx/i through n-strip mask; Blanket deposit p-layer; Deposit Ti/Sb/Al metal stack through gap mask; Make localized n-contacts by laser firing the metal stack.	Localized contact allows over 99% cell area to have good passivation. Firing through insulating passivation allows simple structure without having to form metal contact	Weak inversion layer formed by i/a-SiNx layer at the regions surrounding the LFC spots leads to high recombination of minority carrier.
PMLP	Deposit blanket i-layer; n/SiNx/i through mask; Blanket deposit p-layer; Laser ablate some or all i/p over i/n/SiNx fingers; HF etch residual SiNx to expose i/n.	One less laser and chemical etching step compared to ALP. Already demonstrated < 10 mV $\Delta$ iVoc after patterning & etching. Well-passivated gap.	Plasma leakage under mask. Control alignment of subsequent laser ablation steps.
ALP	Blanket deposit i/n/SiNx/i; Laser ablate i-layer on emitter region; Etch of SiNx/n/i in HF + HNA to expose c-Si surface; Blanket deposit i/p; Laser ablate i/p over i/n fingers; HF etch residual a-SiNx to expose i/n.	No masking. Well-passivated gaps. Uses similar process already demonstrated for PMLP.	Create well-passivated i/p HJ emitter after laser and chemical etch of i/n/SiNx layers. Control alignment of subsequent laser ablation steps.

APMP	Deposit SiN <sub>x</sub> through p-mask; Etch plasma leakage; Deposit n/SiN <sub>x</sub> through n-mask; Etch off SiN <sub>x</sub> completely on p-strip; Deposit p-layer through p-mask; Etch off SiN <sub>x</sub> completely on n-strip to expose i/n	Eliminates the use of any post deposition patterning steps like photolithography or laser processing thus should be fast, simpler and less expensive.	This process utilizes 3 mask depositions, thus eliminating the plasma leakage under mask is very critical.
------	---	---	--

Table 5.10 summarizes the current best conversion efficiencies of these IBC structures discussed in this section, while describing their primary limitations.

Table 5.10: Summary of IBC structures, outlining their present conversion efficiencies and primary limitations.

IBC structures	Conversion Efficiency (%)	Primary Limitation
LFC	11.6	High recombination of minority carriers around LFC spot.
PMLP2	15.1	Plasma leakage under mask.
ALP	-	Laser damage. Alignment of p- and n- strips after laser ablations.
APMP	11.1	3-fold plasma leakage under mask.

### 5.3 Summary

The improvements in intrinsic and doped a-Si:H depositions, coupled with a simplified c-Si wafer cleaning process has been shown to be transferrable to front HJ solar cells with improved conversion efficiency from 17.5%, on our previous front HJ cells, to 20.2% on our best front HJ cells. The improvement in light trapping from

surface texturing and ITO deposition was shown on polished and textured wafers having either front side ITO or both-side ITO. The difference in  $J_{sc}$  between a polished and textured wafer was observed as expected, while the best tradeoff between  $J_{sc}$  and FF was found to require only front side ITO.

On the other hand, the challenges of successfully patterning the emitter and base region of the IBC structure using non-photolithography process has been the drawback for the IBC structure. Our first approach was an LFC structure with conversion efficiency up to 11.6%. By including an n-type BSF to repel minority carrier from laser processed regions, we have shown that an excellent passivation ( $iV_{oc}$  up to 723 mV) can be realized after laser processing using the i.a-Si:H layer developed in chapter 4. Other advance device structures discussed include PMLP, ALP and APMP. Results from PMLP structures utilizing both shadow mask and laser process have shown conversion efficiency up to 15.1%, APMP structures with only shadow mask process have shown conversion efficiency up to 11.1%, while ALP structures with only laser process is still in progress – due to laser damage and misalignment challenges. SF6 assisted ablation of the stack structure for ALP is being considered as an option to minimize laser damage, as this will require lower laser power. We have also demonstrated that a careful adjustment of laser power can enable complete isolation ( $R_{SH}$  up to 2E8 Ohms, well above the 1E3 Ohms required) of the emitter and base region with negligible degradation to passivation ( $SRV \sim 5$  cm/s). Currently there are intensive efforts underway between IEC and collaborators at UVa to fabricate each of these types of IBC cells, to resolve the challenges identified above, and to push the performance.

## Chapter 6

### PASSIVE TUNING OF OPTICAL COUPLERS FOR DUAL OUTPUT MODULATORS

This chapter of my dissertation focuses on a different aspect of my research work that centers on waveguides, modulators and optical couplers. In the sub-sections of this chapter, I report the demonstration of a novel method to passively tune the splitting ratio of a Ti-indiffused lithium niobate ( $\text{LiNbO}_3$ ) 3-dB directional coupler by the addition of a cladding material whose refractive index can be varied. Plasma enhanced chemical vapor deposition (PECVD) of such cladding layer onto an optical coupler is here shown to alter the effective index of the odd and even modes in the coupled waveguide. By varying the thickness of the thin-film cladding layer, we have shown the capability of precisely controlling the coupling ratio and compensating for variations arising from fabrication tolerances that can significantly impact coupling. This chapter has been adapted from a previous published work [<sup>102</sup>].

#### 6.1 Introduction

$\text{LiNbO}_3$  has been shown to be an important material for many optical networking applications due to its ferroelectric, piezoelectric, photo-elastic, birefringent and electro-optic (EO) properties [<sup>103</sup>]. Its low propagation loss at telecommunication frequencies ( $\sim 0.1$  dB/cm) [<sup>104</sup>] and high electro-optic figure of merit allows for the fabrication of high speed modulators up to 300GHz [<sup>105</sup>], switches [<sup>106</sup>], and waveguides [<sup>107</sup>]. In particular lithium niobate is extensively used in integrated optics to make directional couplers, splitters, switches and EO phase and

intensity modulators based on Mach-Zehnder Interferometers (MZIs). In the development of MZI modulators, 3-dB directional couplers are required. Ideally, a 3-dB directional coupler made of Ti-indiffused LiNbO<sub>3</sub> waveguide splits an incoming optical signal in half and gives equal outputs to both output ports. However, in actual implementation of these splitting devices, achieving precise and repeatable 3-dB splitting in a directional coupler usually presents a challenge due to slight variations in the fabrication process conditions. In MZI modulators, this deviation in splitting ratio results in poor extinction ratio and low modulation depth. Our approach to solving this problem is detailed in subsequent sections.

## **6.2 Ti-indiffused LiNbO<sub>3</sub> Channel Waveguide**

LiNbO<sub>3</sub> is a compound composed of lithium, niobium and oxygen that exists in crystalline form with very unique properties useful in many optical integrated circuits. It is arguably one of the most thoroughly characterized optical materials. Single crystals of LiNbO<sub>3</sub> are grown using Czochralski process, after which they are cut into wafers with different crystal orientations (x-cut, y-cut or z-cut). LiNbO<sub>3</sub> is commonly used to form channel waveguides by the in-diffusion of titanium.

Titanium is in-diffused to increase the index of a particular region within the LiNbO<sub>3</sub> substrate to produce a waveguide. A stripe of titanium pattern on the LiNbO<sub>3</sub> substrate is slowly heated in a diffusion furnace at temperatures between 900<sup>0</sup>C - 1050<sup>0</sup>C for about 10 – 12 hrs to drive the titanium ions into the LiNbO<sub>3</sub> substrate as shown in Figure 6.1a and 6.1b. These conditions are maintained with sufficient flow of oxygen to prevent the out-diffusion of lithium ions, which often accompanies the in-diffusion process and results in the formation of surface waveguide [108]. The titanium ions penetrate the host substrate to form a graded index region having the

shape of a Gaussian distribution as illustrated in Figure 6.1b and 6.1c. The high index core is then used to guide a beam of light by total internal reflection as illustrated in Figure 6.2.

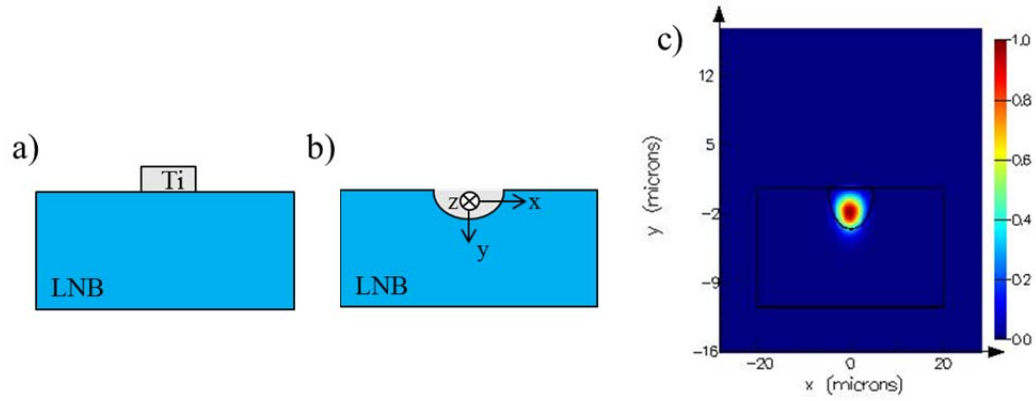


Figure 6.1: a) Patterned titanium stripe on LNB sample before diffusion, b) After titanium-indiffusion, and c) Optical simulation of guided mode in the titanium-indiffused region.

The in-diffusion of the titanium is the prevalent method of creating a channel waveguide in LiNbO<sub>3</sub>. In a z-cut LiNbO<sub>3</sub> substrate, the presence of the titanium ions causes a change in both the ordinary (axis parallel to the substrate surface) and extraordinary (axis perpendicular to the substrate surface) refractive indices in the optical wavelength range according to [109] [110] [111]. These changes can be expressed as:

$$n_x = n_z = n_o = n_{os} + \Delta n_o [f(x)g(y)]^{0.55} \quad (6.1)$$

$$n_y = n_e = n_{es} + \Delta n_e f(x)g(y) \quad (6.2)$$

$$f(x) = \frac{\operatorname{erf}\left(\frac{2x+W}{2d_x}\right) - \operatorname{erf}\left(\frac{2x-W}{2d_x}\right)}{2 \operatorname{erf}\left(\frac{W}{2d_x}\right)} \quad (6.3)$$

$$g(y) = \exp\left[-\left(\frac{y}{d_y}\right)^2\right] \quad (6.4)$$

where  $n_{os}$  is the ordinary refractive index of LiNbO<sub>3</sub>,  $n_{es}$  is the extraordinary refractive index of LiNbO<sub>3</sub>,  $\Delta n_o$  is the maximum ordinary refractive index change,  $\Delta n_e$  is the maximum extraordinary refractive index change,  $W$  is the width of the titanium stripe before in-diffusion,  $d_x$  is the diffusion length in the x direction and  $d_y$  is the diffusion length in the y direction.

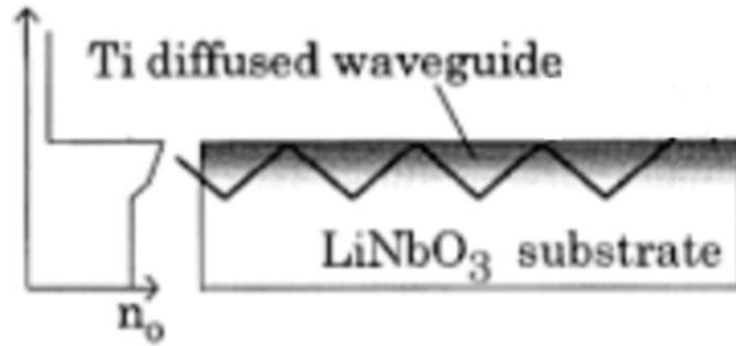


Figure 6.2: Index profile across the titanium-diffused region (core) and LiNbO<sub>3</sub> substrate (left). Incident beam of light guided by total internal reflection (TIR) through the core. The core is formed by graded refractive indices in the x- and y-axes corresponding to ordinary and extraordinary axes respectively in a z-cut LiNbO<sub>3</sub> substrate (right).

### 6.3 Electro-optic (EO) Modulation

After achieving a waveguide in our optical material of interest, a phase shift is introduced onto an optical wave using an electro-optic modulator that is controllable with an electrical signal. Electro-optic modulators utilize the first order Pockels effect

(linear EO effect) and the Kerr effect (quadratic EO effect) to bring about a change in an optical beam. The Pockels effect, expressed in Eqn. 6.5, denotes a linear relationship between the change in the refractive index and the magnitude of the applied electric field, while the Kerr effect, expressed in Eqn. 6.6, denotes a quadratic relationship between the change in the refractive index and the magnitude of the applied electric field:

$$n(E) = n_o - \frac{1}{2} \Gamma n_o^3 E, \quad (6.5)$$

$$n(E) = n_o - \frac{1}{2} \Gamma n_o^3 E - \frac{1}{2} \mathfrak{s} \Gamma n_o^3 E^2, \quad (6.6)$$

where  $n$  is the refractive index,  $r$  is the Pockels coefficient (linear EO coefficient),  $E$  is the electric field and  $\mathfrak{s}$  is the Kerr coefficient (quadratic EO coefficient).

Phase modulation is achieved when a beam of light is made to pass through a Pockels cell of length,  $L$  to which an electric field,  $E$  is applied, as illustrated in Figure 6.3. The change in phase experienced by the beam is represented as follows:

$$\Delta\phi = \beta l = [n(E) - n_o] k_o L = \frac{2\pi[n(E) - n_o]L}{\lambda_o} = \frac{\pi \Gamma n_o^3 E L}{\lambda_o} = \frac{\pi \Gamma n_o^3 V L}{d \lambda_o} \quad (6.7)$$

$$\text{where } V = E * d \quad (6.8)$$

which implies that the voltage  $V$ , connected across the electrode terminals of a Pockels cell separated by a distance  $d$ , will bring about a  $\Delta\phi$  change in phase on an optical beam that traverses the length  $L$ , of the Pockels cell. This expression can be modified to derive a key phase modulator figure of merit – the half wave voltage  $V_\pi$ , which is the voltage that is required to cause a  $\pi$ -phase shift as shown in Eqn. 6.9:

$$V_{\pi} = \frac{d\lambda_o}{L\Gamma n_0^3} \quad (\text{for } \Delta\phi = \pi) \quad (6.9)$$

Both wave guiding and modulation is required for fabricating a dual output modulator. LiNbO<sub>3</sub> being our optical material of interest functions both as a waveguide material and as an electro-optic material for modulation.

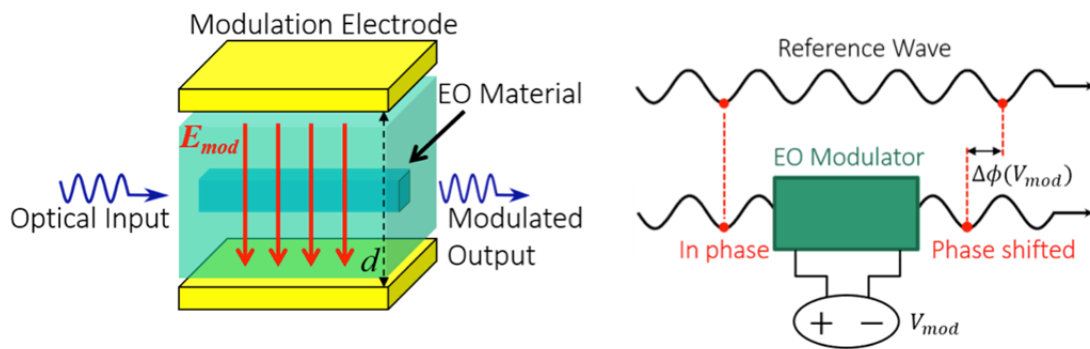


Figure 6.3: Left: Schematic showing the modulation of a beam of light as it passes through a Pockels cell of length,  $L$  to which an electric field,  $E$  is applied resulting in a  $\Delta\phi$  change in phase on the optical beam; Right: Illustration of a phase modulation using an EO modulator in a Mach Zehnder Interferometer (MZI) configuration.

#### 6.4 Balance Detection System

Most photonic links in optical systems uses single receiver detection made available by a Mach Zehnder Interferometer (MZI) shown in Figure 6.4. This set up is easily used to determine the relative phase shift between two collimated beams derived by splitting the light from a single source and recombining it afterwards. The MZI configuration is popular because it is easy to construct and deploy. However, it required high quality laser source with minimal relative intensity noise (RIN) because it amplifies the RIN together with the signal. Also optical signal is loss during the

signal mixing from two arms of the MZI to the single output arm (even to odd mode).

Figure 6.4 shows an illustration of a single detection system with a MZI configuration.

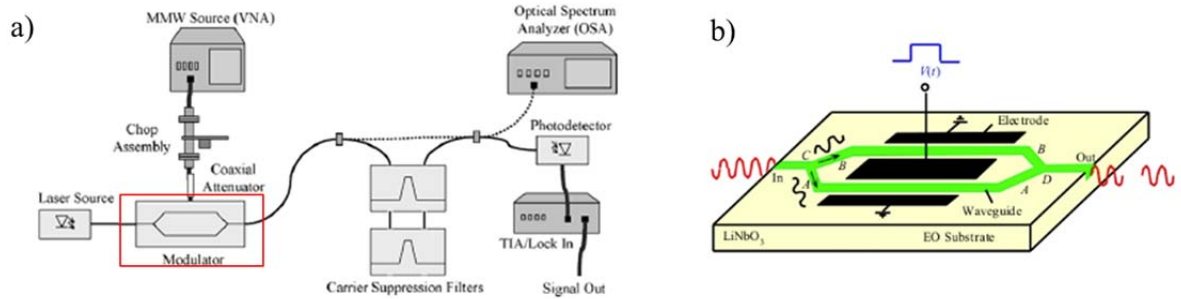


Figure 6.4: a) A photonic link with a single receiver detection system where signal mixing is done with a MZI [112], b) Illustration of signal modulation using MZI configuration.

To improve the signal to noise ratio (SNR), a balance detection system with dual output is essential. This structure preserves signal strength by maintaining signal mixing in even modes and also reduces laser RIN. Thus, a cheap laser with high RIN can be used with this configuration. Balance detection systems require equal splitting of the input light in optical domain with RF component phase shifted by 180 and optical signal (with RIN) in phase. To ensure complete cancellation of the laser RIN, an out-of-phase combiner (differential amplifier) and balance detectors (with identical figures of merit) is used in this configuration. Figure 6.5 shows an illustration of a balanced detection system using a directional coupler configuration.

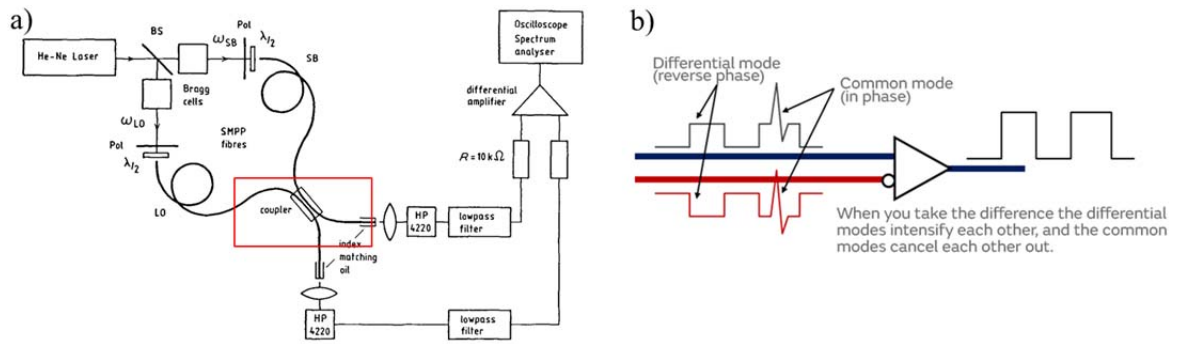


Figure 6.5: a) Photonic link with a dual output receiver system where signal mixing is done with a directional coupler [113], b) Illustration of laser RIN cancellation in a balanced detection system.

## 6.5 Directional Couplers

To achieve the dual output required for a balance detection system, a directional coupler structure was designed and fabricated. A typical directional coupler structure, as shown in Figure 6.6, starts with two parallel optical waveguides, separated by a distance,  $G$ . Two S-bends are used to bring the two waveguides towards each other over a distance,  $L_b$ . When they are brought very close to achieve a coupling gap,  $G_c$ , from each other, the optical mode evanescently couples from one to the other. After an interaction length,  $L_c$ , the two waveguides are separated back to their original parallel orientation. Light from the input waveguide splits to the adjacent waveguide by synchronous coherent coupling, otherwise known as optical tunneling via overlapping evanescent tails. For synchronous coherent coupling to occur, the light wave must travel with the same phase velocity in both single mode waveguides. The parallel waveguide can support two optical guided modes, one is even mode, and the other is odd mode. For an infinite coupling length,  $L_c$ , the optical power couples back and forth between the two waveguides as a function of length and decays exponentially as shown in the coupled mode equations below:

$$\frac{d}{dz}A_1(z) = -i\beta_1A_1(z) + \kappa_{12}A_2(z) \quad (6.10)$$

$$\frac{d}{dz}A_2(z) = -i\beta_2A_2(z) + \kappa_{21}A_1(z) \quad (6.11)$$

where  $A_1(z)$  and  $A_2(z)$  represents the complex amplitude of the optical signal, which includes the phase term  $\exp(-i\beta z)$  in waveguides 1 and 2 respectively,  $\kappa_{12}$  and  $\kappa_{21}$  represents the coupling coefficient between two guided modes,  $\beta_1$  and  $\beta_2$  are the propagation constants of the modes in the guides and  $z$  is the distance in the direction of propagation.

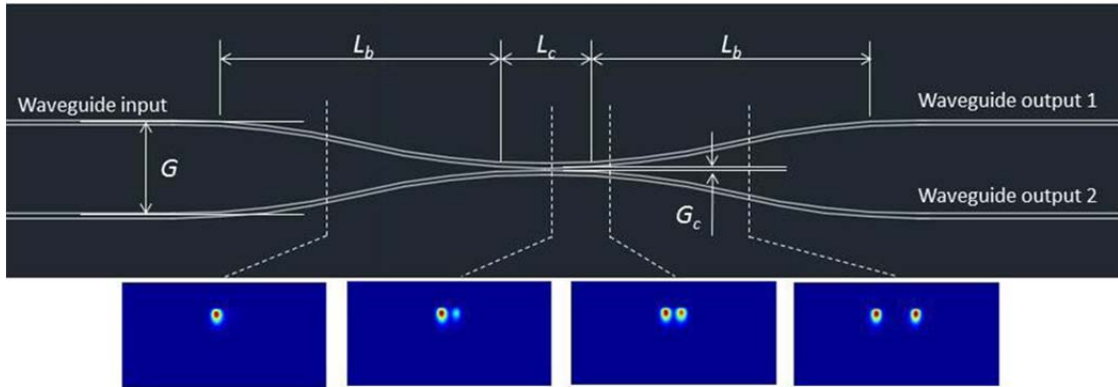


Figure 6.6: Schematic diagram of a directional coupler structure for optical splitting. Lower panels indicate computed cross-sectional mode profiles at the positions indicated by dash lines [102].

### 6.5.1 Design and Fabrication of Directional Couplers

A numeric model using beam propagation method was built to simulate the directional coupler performance following similar work reported in the literature [109]. By defining the diffusion profile, the index profile was computed, and the coupling result was analyzed based on the directional coupler. Figure 6.7 shows an illustration of a 3 dB coupling of an optical signal inputted from one of the waveguides with

different output spacing. In both cases, we found 2 mm to be an ideal coupling length for a coupling gap of 5  $\mu\text{m}$ .

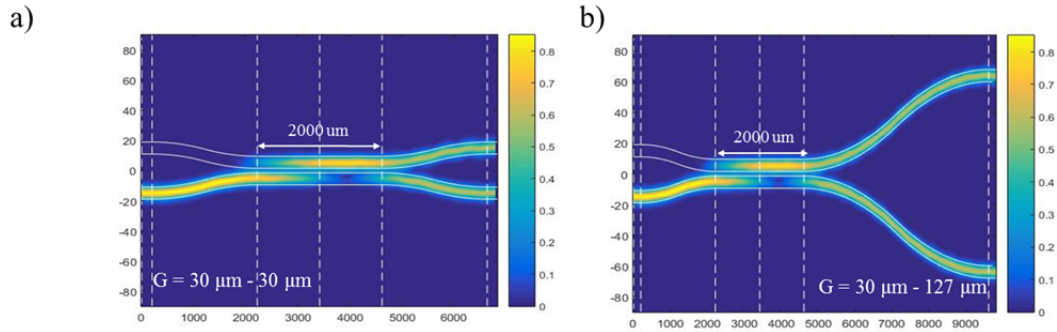


Figure 6.7: Beam propagation method showing an illustration of a 3 dB splitting between waveguides with a) 30  $\mu\text{m}$  spacing between output ports, and b) 127  $\mu\text{m}$  spacing between output ports.

In all 40 devices that we fabricated for this study, we utilized two parallel Ti-indiffused waveguides, each with a mode diameter of  $\sim 8 \mu\text{m}$ . These devices were fabricated using a similar diffusion and liftoff process recorded in [114]. Waveguides were lithographically defined with 6  $\mu\text{m}$  wide, 105 nm thick titanium stripes deposited with an electron beam evaporation system on a z-cut lithium niobate substrate. The titanium stripes were then diffused in a furnace at about 1000  $^{\circ}\text{C}$  for 10 hrs. A group of directional coupler structures, with 5  $\mu\text{m}$  coupling gap,  $G_c$ , were fabricated and tested together. The coupling lengths were varied from 100  $\mu\text{m}$  to 3600  $\mu\text{m}$  to determine the appropriate coupling length for 3-dB splitting. The samples were then diced and the end facets dice-polished at  $5.45^{\circ}$  using Disco automatic dicing saw. The splitting ratios were measured and recorded using a 6-axes fiber alignment system, shown in Figure 6.8, where polarization maintaining (PM) fiber and V-groove

assemblies were used for input and output coupling. In the V-groove assembly, the PM fiber is diced at  $5.45^\circ$  relative to the waveguide and held in place by a Pyrex V-groove together with a Pyrex lid. This angle helps to reduced back reflections and improves alignment accuracy.

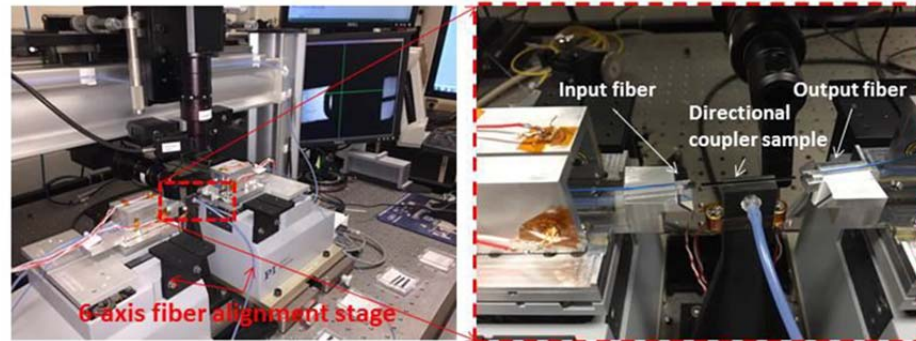


Figure 6.8: A fiber alignment system with 6 degree of freedom in the X, Y, Z, yaw, pitch and roll axes used for waveguide alignment during optical measurement.

The following procedure was used to measure the splitting ratios. First, light is coupled into the input waveguide, designated as waveguide 1 in Figure 6.9, and we measured the output power from both waveguide 1 and waveguide 2 using an optical power meter. The measured power is then normalized to the total output power to determine a percentage value. The same measurement is repeated by switching the input optical waveguide to waveguide 2 to confirm the first measurement. By comparing the output percentages of any given set of waveguide pairs, we then determine how the splitting ratio varied as a function of coupling length,  $L_c$ .

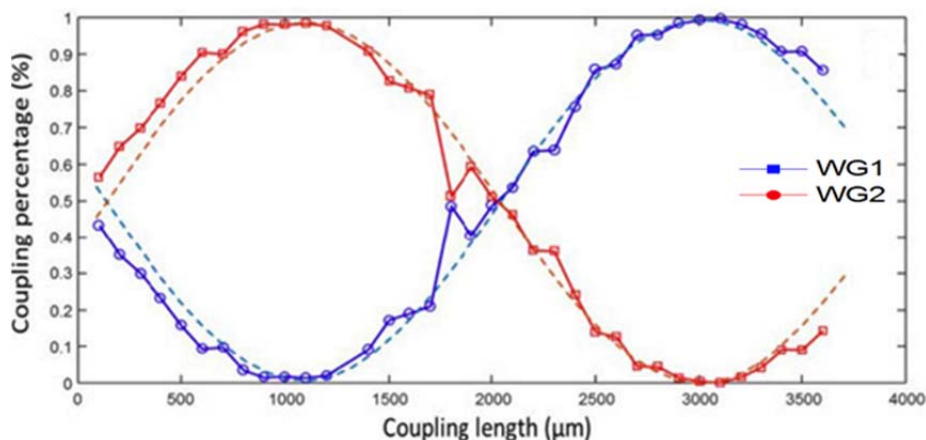


Figure 6.9: Experimental (solid) and simulated (dashed) results of directional coupler structures with varying coupling lengths [102].

### 6.5.2 Addressing Fabrication Tolerance

Achieving a consistent splitting ratio across different samples proved to be difficult because of slight discrepancies in fabrication tolerance, which has a significant effect on coupling. This appeared to be a common challenge with directional couplers as indicated by the various approaches developed to mitigate it. Different techniques that involve changing the effective index of the two waveguides have been developed over time. A common approach is the use of a set of biasing electrodes, patterned on top of the waveguides, to induce a subtle change in the local index of the diffused waveguide and as a result alter the splitting ratio. Other approaches utilize photo structural effect [115], saturation-induced optical switching [116], post-fabrication laser trimming [117], and thermo-optic control [118] to induce an index change. These processes introduce more complexities and a number of fabrication steps. In this work, a novel method for controlling the splitting ratio, namely depositing a thin-film silicon-rich nitride cladding layer, which enables post-fab trimming of the splitting ratio by varying the thickness of the silicon nitride

cladding layer through etching was investigated. We do know that the coupling coefficient is strongly dependent on the extent of the evanescent mode tail of the guided modes. By depositing a thin-film cladding layer over the waveguides, as shown in Figure 6.10, the effective index across the coupling gap can be increased due to the substitution of a low-index material (air,  $n=1.0$ ) with a higher-index cladding material (Si-rich nitride,  $n=2.258$ ). This results in the increased overlap of the mode tails, which enhances coupling.

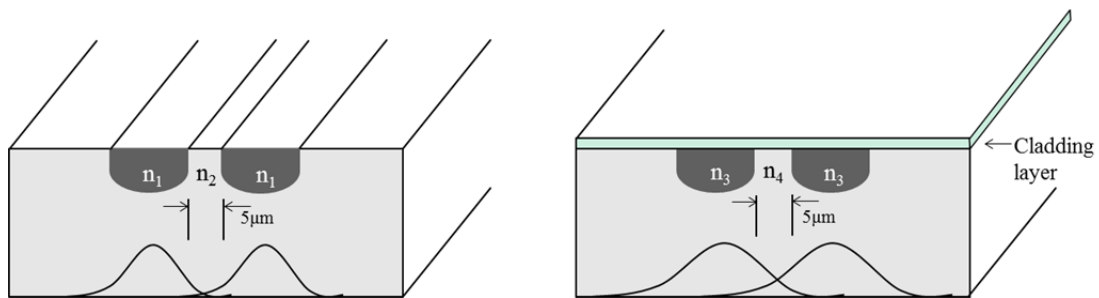


Figure 6.10: Illustration of improved mode interaction by the addition of a thin film cladding layer [102].

An ideal cladding material for this particular application will have to fulfill certain criteria. First, it must be a material with good adhesion to lithium niobate. Second, it should have low loss. Third, it should have an index close to the refractive index of lithium niobate, and finally the cladding must have well defined and repeatable deposition and etch rates. Amorphous silicon (a-Si), silicon dioxide ( $\text{SiO}_2$ ) and amorphous silicon nitride ( $\text{a-Si}_3\text{N}_4$ ) were investigated for this purpose. The high refractive index of a-Si is desirable but its poor adhesion to lithium niobate discourages its use as a cladding material for this purpose. Silicon dioxide on the other hand adheres very well to lithium niobate but with a rather low refractive index of

1.46, it hardly introduces a sufficient change in effective index. Silicon nitride, however, provide good adhesion to lithium niobate, has lower loss, has refractive index close to that of lithium niobate, and has well-established deposition and etch processes. In addition, the refractive index of PECVD-grown silicon nitride layers can be easily varied by means of modifying the silane to ammonia dilution ratio [<sup>119</sup>]. This approach was utilized here to derive a silicon-rich nitride material, by using a silane to ammonia ratio of about 3:1, yielding an index of  $n=2.258$ . Another material that could also be explored for this application is arsenic trisulphide ( $As_2S_3$ ) because of its high refractive index ( $n\sim 2.65$ ) and good adhesion to  $LiNbO_3$  as demonstrated by its usage in hybrid  $As_2S_3$ -on- $LiNbO_3$  ring resonators [<sup>120</sup>]. However,  $As_2S_3$  is easily oxidized which makes it a difficult material to process.

### **6.5.3 Effect of Thin Film Additive Cladding**

A 3D finite-difference eigenmode (FDE) solver (Lumerical) [<sup>16</sup>], well suited to treat bent waveguides, was then used to investigate the impact of additive cladding layer to the coupling. Simulations were conducted with different cladding materials and their effects on the mode profile, loss, and effective indices of the odd and even modes were observed. The simulation model was built using the same parameters reported in [<sup>109</sup>]. The meshed area for the simulation region in Lumerical was defined as: x-span = 22  $\mu m$ , y-span = 16  $\mu m$  and z-span = 1  $\mu m$ , with a mesh increment  $dx = dy = dz = 0.231 \mu m$  and with PML boundary conditions. We performed a number of simulations for different scenarios: without cladding, with 400 nm thick layer of oxide, with 400 nm thick layer of nitride and with 100 nm thick layer of amorphous silicon. The thickness of amorphous silicon was reduced to 100 nm so as to reduce the loss associated with the high-index silicon. Figure 6.11 shows a noticeably larger

change in the effective indices of the odd and even modes with amorphous silicon than with other cladding materials. However, amorphous silicon could not be used due to its poor adhesion to  $\text{LiNbO}_3$  and the increase in insertion loss from 5.8 dB to 7.4 dB. This leaves us with the option of silicon nitride, which has the next highest index change.

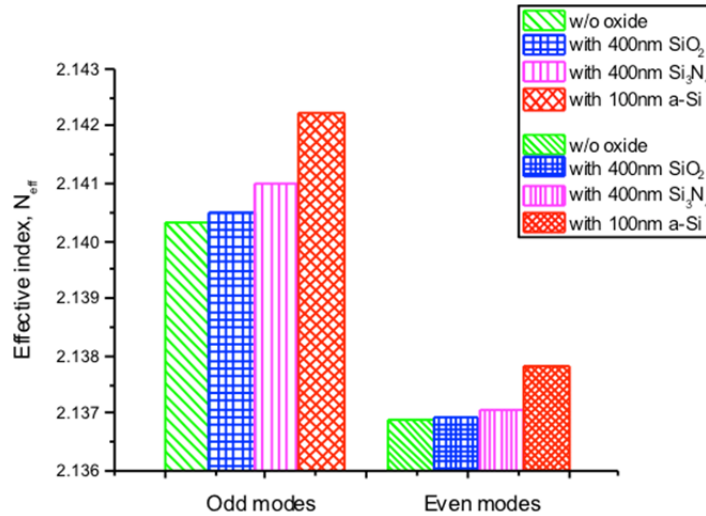


Figure 6.11: Simulated effects of different cladding materials on the change in effective index of the odd and even modes in coupled  $\text{Ti}:\text{LiNbO}_3$  waveguides [102].

To increase the effective index change with the silicon nitride, we developed a silicon-rich nitride. The silicon-rich nitride is grown in a plasma-enhanced chemical vapor deposition (PECVD) chamber using stoichiometric silicon nitride recipe that we modified to attain a high index. The composition of the non-stoichiometry silicon nitride grown in our Samco PD – 220N PECVD system [121] shows good repeatability

for the same process condition and gas flow of silane to ammonia. Table 6.1 shows the gas flow rates for the different silicon-rich nitride PECVD growth recipes.

Table 6.1: PECVD growth recipes for index tuning study showing gas flow rates, thicknesses and refractive index for silicon nitride with different silane to ammonia ratios.

S/N	Purge gas	Ammonia flow rate (sccm)	Silane flow rate (sccm)	Thickness (nm)	Refractive index, n
1	N <sub>2</sub>	6	12.6	394	2.022
2	N <sub>2</sub>	6	20	450	2.147
3	N <sub>2</sub>	12	30	460	2.170
4	N <sub>2</sub>	12	40	490	2.258

This approach was utilized here to derive a silicon-rich nitride material, by using a silane to ammonia ratio of about 3:1, which yielded an index of 2.258. Once the cladding material is deposited, the measurement procedure described earlier is repeated to study the effect of the cladding material on coupling.

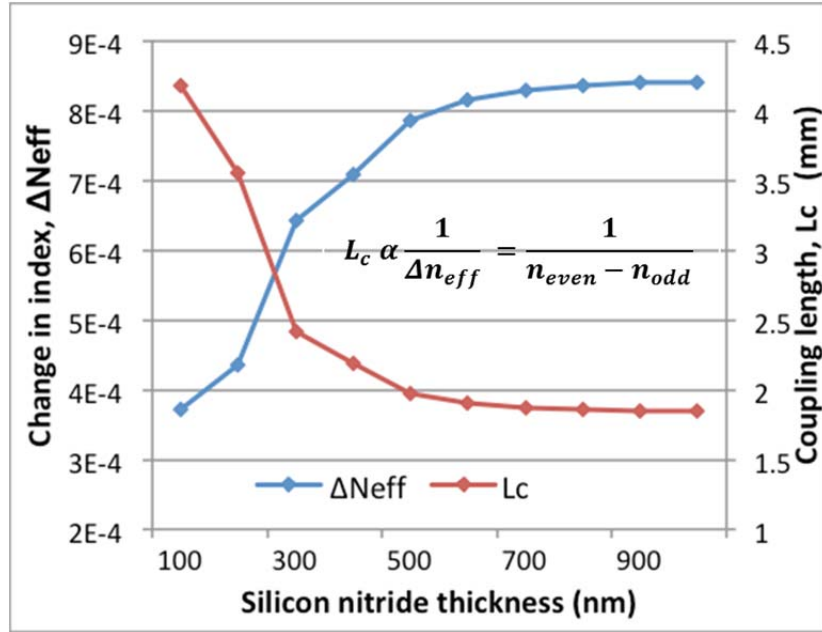


Figure 6.12: Correlation of increasing  $\text{Si}_3\text{N}_4$  thickness with change in effective index and coupling length [102].

Using silicon-rich nitride as the cladding material, we also studied numerically the changes in effective index with increasing cladding thickness and how this affects the coupling length. A cross section of the  $\text{Ti}:\text{LiNbO}_3$  waveguide model was created in Lumerical Mode Solution. The mode profile was then computed without any cladding layer. Thereafter, silicon nitride is continuously added in increments of 100 nm to this model and simulated. The change in effective index was calculated and, as expected, found to increase with increasing silicon nitride thickness. The change in effective index across the guide, with and without the silicon nitride layer, was then computed and plotted against the coupling length in Figure 6.12.

We observed that a 400 nm thick layer compensates for a 5% coupling mismatch, which translates to a 1% compensation for every 80 nm increase. This

linear approximation is consistent up to 500 nm, after which the effect saturates as illustrated in Figure 6.12.

In some cases, where the mismatch is less than 5%, the thickness of the material is varied by changing the growth time or etching away some of the material. Etching is done using hot phosphoric acid ( $\text{H}_3\text{PO}_4$ ) according to [122]. After deposition, samples were secured in airtight sample holders to prevent the formation of an oxynitride skin, which could inhibit the etch process and affect the coupling ratio.

#### **6.5.4 Passive Tuning of Optical Couplers**

The previous section indicates that the effective index change due to the addition of the silicon nitride layer is more obvious within the first few hundred nanometers up to 500 nm, after which further addition of the silicon nitride layer introduces no significant change. With this knowledge, we deposited a ~600 nm thick layer of silicon nitride on several couplers, which were previously tested and showed a coupling mismatch of about 10%. The silicon nitride layer was added in steps of 200 nm along the coupling length,  $L_c$ , and some devices on this sample were tested to observe the change in coupling. Figure 6.13 shows the increase in coupling with increasing silicon nitride thickness across four different couplers. The splitting ratio started off at around 55/45, with the input waveguide (WG1) having the higher percentage, and was corrected by the addition of the cladding layer. The cladding layer improved the interactions between the waveguides, thereby increasing the coupling efficiency. Further addition of the cladding layer overturns the splitting composition as seen in Figure 6.13 but the increased coupling saturates around 500 nm.

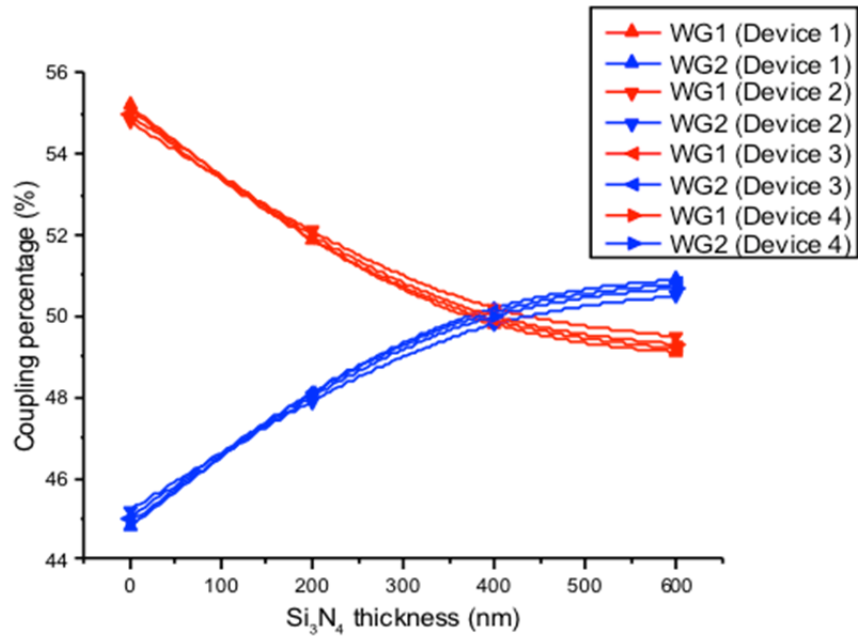


Figure 6.13: Improved coupling observed with increasing Si<sub>3</sub>N<sub>4</sub> cladding layer.

## 6.6 Summary

In summary, we have illustrated a novel and simple method to fine-tune the coupling ratio of an optical coupler by the addition of a thin-film cladding layer. The design of the optical coupler and its dependence on fabrication tolerance has been investigated. Different cladding materials were considered as options for the cladding layer but silicon nitride proved to be best suited for this application because of its good adhesion to lithium niobate, adjustable index, and ease of processing. By depositing a thin-film Si-rich nitride cladding layer on an optical coupler with mismatched coupling, the mode interaction in the Ti:LiNbO<sub>3</sub> diffused waveguides can be manipulated to control the coupling ratio between two output ports up to 10%. In order to increase the tunability range and improve the tuning precision, more material systems can be explored in the future. This post-fab trimming process will be valuable

in our fabrication of dual output modulators where accurate splitting is essential. These modulators, coupled with balanced detectors, can serve to remove relative intensity noise (RIN) in RF links and introduce significant advancement in the dynamic range of optical data and links.

## Chapter 7

### CONCLUSION AND FUTURE PERSPECTIVES

#### 7.1 Conclusion

Silicon HJ, with remarkable high open circuit voltage ( $V_{OC}$ ) and low thermal budget, enables the fabrication of high efficiency solar cells. This is evident in the fact that recent record efficiency silicon single junction cells incorporate HJ structure. The first section of this dissertation focused on optimizing the  $V_{OC}$  of HJ cells and combining it with another high efficiency concept – the interdigitated back contact (IBC) structure to make high efficiency solar cells.

Chapter 1 provided an introduction and literature review of renewable energy systems, recent trends and the principle of operation of photovoltaic devices, modules and systems. Chapter 2 detailed all the fabrication and characterization tools used in the making, testing and analysis of a solar cell.

In chapter 3, the c-Si wafer cleaning and preparation steps were covered. The fact that SHJ cells have their junctions formed by growing intrinsic and thin-doped a-Si:H layers on the silicon surface, meant that the a-Si:H/c-Si interface is an integral part of the junction, which places great emphasis on the purity of the wafer surface. I described a systematic study on the optimal conditions for silicon surface preparation to ensure excellent passivation at the a-Si:H/c-Si interface of SHJ solar cells. This study confirmed that:

1. Some form of surface damage etches (SDE), which removes a few microns of contaminated layers from the c-Si surface, is crucial for

achieving excellent passivation. SDE was done using either KOH or HNA solutions.

2. Other surface treatment prior to HNA etch can be excluded as they offer marginal or no benefit to the final surface quality.

3. c-Si surface pre-cleaning with solvents (Acetone, methanol and isopropanol, AMI) is not critical for achieving pristine surface. However, if used, a piranha step after AMI is necessary to remove carbon residue and outgassed fluoride from the Teflon sample holders.

4. TMAH texturing step is a critical step in the cleaning process, with marked improvement in  $\tau_{\text{eff}}$  and  $iV_{\text{OC}}$ . This was validated by XPS data and  $\tau_{\text{eff}}$  data with both QH-MeOH and PECVD-grown 10 nm i.a-Si:H layer passivation.

5. TMAH residue removal is essential for samples intended for device fabrication. It is understood that the solvents and piranha used during the TMAH residue removal process also help with removing any organic contaminant on the wafer surface.

6. A 7-step simplified wafer cleaning approach that utilizes minimal volume of chemicals is possible. This method has been proven to achieve equivalent surface purity as measured by  $\tau_{\text{eff}}$  and  $iV_{\text{OC}}$  from both QH-MeOH and PECVD-grown 10 nm i.a-Si:H layer passivation, and complete solar cell performance.

Chapter 4 focused on experiments and studies geared towards optimizing the chemical and field effect passivation of the PECVD-grown intrinsic and doped a-Si:H

layers. Optical emission spectroscopy was utilized to analyze the plasma kinetics of typical a-Si CVD processes. This study confirms that plasma current controls the concentration of charged species, pressure controls the plasma voltage, and temperature slightly controls the crystallinity and conductivity of the films. The passivation quality, however, appears to have a strong dependence on the plasma voltage. This could be explained by the fact that plasma voltage governs the ion bombardment energy, e.g. high plasma voltage conditions which corresponds to high acceleration potential results in increased surface damage due to high ion bombardment energy. Thus, low plasma voltage conditions, at high pressure, were found to be ideal for achieving excellent passivation as they introduce less damage to the c-Si wafer. This study enabled the development of recipes for post deposition hydrogen plasma treatment, intrinsic and doped a-Si:H layers. These recipes, combined with a bi-layer deposition technique, resulted in excellent chemical and field effect passivation, with  $iV_{oc}$  over 750 mV after both side i-layer deposition and  $iV_{oc}$  up to 741 mV after doped layer deposition. The various new-doped layer approaches had less impact on improving film properties compared to i-layers due to all the defects already present in doped layers.

Chapter 5 covered cell results from front HJ and IBC-SHJ solar cells fabricated using the wafer cleaning process developed in chapter 3 and the intrinsic and doped a-Si:H layers developed in chapter 4. Front HJ cells with conversion efficiency up to 20.2%, a record efficiency device in that category in IEC, was achieved using the optimized films and fabrication process detailed in this dissertation.

IBC-SHJ solar cells with laser-fired contacts (LFC) having conversion efficiency up to 11.6% were fabricated. The LFC IBC-SHJ cells with rear i.a-Si:H/a-

SiNx:H blocking layer suffered from Voc and FF degradation. To determine the source of these losses, LFC through two types of passivation stacks, i.a-Si:H/n.a-Si:H and i.a-Si:H/a-SiNx:H, were investigated on an n-type silicon front HJ solar cell. This study confirmed the presence of a weak inversion layer formed by i.a-Si:H/a-SiNx:H layer at the regions surrounding the LFC spots. This inversion layer acts as an additional back HJ for the minority carriers. To minimize the LFC damage, we posit that a back surface field is essential in the surrounding regions to repel minority carrier away from the defective LFC spots. Thus, i.a-Si:H/n.a-Si:H/a-SiNx:H dielectric stack structure was proposed as a better stack for LFC.

ALP, APMP and PMLP were presented as advanced device structures for rapid patterning of low cost manufacturable IBC-SHJ. The ALP process utilized only laser process to define the emitter and base regions, APMP uses only shadow mask deposition to achieve the same goal, while PMLP utilizes one shadow mask deposition step and one laser process to achieve the same task. Of the three device structures, PMLP has shown better promise with conversion efficiency up to 15.1%.

Results from laser patterning of the metal contacts to the n- and p-strip, done in collaboration with the center for laser and plasma at the University of Virginia, was also presented. High isolation resistance up to 2E8 Ohms, well above 1E3 Ohms required for these cells, was achieved using direct laser ablation of Ni or Ti/Sb/Al metal stack. Also sacrificial layer assisted ablation using NiO or photoresist, and soft laser ablation with chemical etching were also developed as alternative methods for laser isolation with high isolation resistance up to 5.5E8 Ohms.

Finally, in chapter 6, a novel and simple method to tune the coupling ratio of an optical coupler by the addition of a thin-film cladding layer was presented. The

design of the optical coupler and its dependence on fabrication tolerance was detailed. Afterwards, the idea of using a cladding material to alter the effective index in the waveguides was discussed. Different cladding materials were considered as suitable candidates for the cladding layer but silicon nitride proved to be best suited for this application because of its good adhesion to lithium niobate, adjustable index, and ease of processing. Post fabrication optical tuning up to 10% has been achieved using thin-film Si-rich nitride cladding layer on an optical coupler.

## **7.2 Future Perspective**

### **7.2.1 Manufacturable IBC-SHJ Solar Cells**

Significant work and continuous progress is still required to make photovoltaic devices more efficient, manufacturable and consequently more cost effective. IBC-SHJ solar cell, currently the record efficiency single junction cell structure, is undoubtedly a proven viable architecture to realize high efficiency cell. In the near future, we imagine the game changing component leading to mainstream manufacturing of this cell will involve a breakthrough in laser processing. Our current research contract with the U.S. Department of Energy seeks to explore the opportunities that abound with laser processing in order to address some of the challenges limiting large-scale production of IBC-SHJ solar cells. This breakthrough in laser processing will involve one or more of the following techniques - Laser fired contacts, laser patterning of emitter and base contacts, selective laser ablation, laser dicing of wafers and laser scribing for mask fabrication.

Another technique that can be harnessed to make the IBC-SHJ fabrication process easily manufacturable is the PECVD shadow mask deposition of the p- and/or

n-type a-Si:H to define the emitter and base region. Our attempt to make IBC cells using this approach, though not entirely successful, has shown significant promise in the simplification of the fabrication process and also revealed some critical challenges that can be easily fixed with improved wafer holders and masking material. We believe a robust masking material and wafer holder system that eliminates plasma leakage through the mask can help solve the principal challenge with this technique - plasma leakage and contamination of adjacent masked regions. Overall, I think laser processing of IBC-SHJ solar cells is viable and holds great promise.

### **7.2.2 Tuning of Optical Couplers**

Increasing the tunability range of the optical couplers and improving their tuning precision can improve the work on passive tuning of optical couplers. More material systems that meet the requirements of an ideal cladding material, listed in section 6.5.2, can be explored.

Apart from exploring other materials of interest for passive tuning, the structure of the optical coupler can also be redesigned. The sensitivity of the splitting ratio to the fabrication tolerance is a function of the spacing between waveguides, also known as coupling gap. As the coupling gap increasing, the coupling length for 3 dB splitting increases as well and thus, the sensitivity to slight variation in fabrication tolerance can be minimized.

### **7.3 List of Publications**

The results from my research work have been presented in the following journal publications:

1. **U. J. Nsofor**, P. Yao, S. Shi and D. W. Prather, “Passive Tuning of Optical Couplers Using a Thin Film Cladding Material”, *IEEE Photon Technol. Lett.*, vol. 29, no. 9, pp. 775-778, Mar. 2017.
2. **U. J. Nsofor**, L. Zhang, A. Soman, C. M. Goodwin, H. Liu, K. D. Dobson, U. K. Das, T. P. Beebe Jr., and S. Hegedus, “Analysis of Silicon Wafer Surface Preparation for Heterojunction Solar Cells Using X-ray Photoelectron Spectroscopy and Effective Minority Carrier Lifetime”, *Sol. Energy Mater. & Sol. Cells*, 183 (2018) 205-210.
3. **U. J. Nsofor**, A. Soman, U. K. Das, and S. Hegedus, “Minimizing Process-Induced Losses on Si HJ Solar Cells With State-of-the-art Implied Voc”, *IEEE J. Photovoltaics*, 2018 (peer review).
4. A. Soman, **U. J. Nsofor**, U.K. Das, T. Gu and S. Hegedus, “Correlation between in situ diagnostics of the hydrogen plasma and the interface passivation quality of hydrogen plasma post-treated a-Si:H in Silicon Heterojunction Solar Cells,” *ACS Materials and Interface*, 2018 (peer review).

Other aspects of my research work are presented in the following conference proceedings:

1. **U. J. Nsofor**, P. Yao, S. Shi and D. W. Prather, “Passive Tuning of Optical Couplers Using a Thin Film Cladding Material”, *IEEE Photonics Conference*, Orlando FL, Oct. 2017.
2. **U. J. Nsofor**, A. Soman, U. Das and S. Hegedus, “Improving the Interface Passivation of Si HJ Solar Cells by Interrupted Deposition of

Thin a-Si:H Film”, *7<sup>th</sup> World Conference on Photovoltaic Energy Conversion*, Waikoloa HI, Jun. 2018.

3. A. Soman, **U. J. Nsofor**, L. Zhang, U. Das, T. Gu and S. Hegedus, “Hydrogen Plasma Post-Deposition Treatment for Passivation of a-Si/c-Si Interface for Heterojunction Solar Cell by Correlating Optical Emission Spectroscopy and Minority Carrier Lifetime”, *IEEE Photovoltaic Specialist Conference*, Washington DC, Jun. 2017.

4. Z. Sun, **U. J. Nsofor**, N. Ahmed, U. Das, S. Hegedus and M. C. Gupta, “Direct Laser Isolation for Interdigitated Back Contact Heterojunction Solar Cells”, *7<sup>th</sup> World Conference on Photovoltaic Energy Conversion*, Waikoloa HI, Jun. 2018.

5. A. Soman, J. Shi, **U. J. Nsofor**, S. Hegedus, Y. Zhang, R. A. Burke and T. Gu, “Raman Spectroscopy Study of Hydrogen Plasma Treatment Effect on a Single Layer Graphene/MoS<sub>2</sub> Hybrid Structure”, *Frontier in Optics Conference*, Washington DC, Sept. 2017.

6. U. Das, C. Thompson, **U. J. Nsofor**, Z. Sun, M. C. Gupta and S. Hegedus, “Effect of Dielectric Layers on Laser-Fired-Contact Performance in a-Si/c-Si Heterojunction Solar Cells”, *7<sup>th</sup> World Conference on Photovoltaic Energy Conversion*, Waikoloa HI, Jun. 2018.

#### **7.4 List of Patent Applications**

1. **U. J. Nsofor**, P. Yao, S. Shi and D. W. Prather, “*Thin Film Passive Tuning (TFPT) of Optical Couplers*”, UD 16-41 (provisional patent), April 2016.

## REFERENCES

1. BP Statistical Review of World Energy 2016 (BP, 2016); <https://www.bp.com/content/dam/bp/pdf/energy-economics/statistical-review-2016/bp-statisticalreview-of-world-energy-2016-full-report.pdf>
2. World Energy Outlook 2015 (IEA, 2015); <http://www.worldenergyoutlook.org/weo2015>
3. Renewable Energy Data Book, National Renewable Energy Laboratory (NREL, 2018); <https://www.nrel.gov/docs/fy18osti/70231.pdf>
4. Solar Quarterly Market Update, China, United States and Japan to Lead Global Solar Installation in 2016 (Mercom Capital Group, 2016); <http://www.solareb2b.it/wpcontent/uploads/2016/04/ForecastReportsMercomSolarQuarterlyMarketUpdateApr2016.pdf>
5. 2014 Outlook: Let the Second Gold Rush Begin (Deutsche Bank, 2014); [https://www.deutschebank.nl/nl/docs/Solar\\_2014\\_Outlook\\_Let\\_the\\_Second\\_Gold\\_Rush\\_Begin.pdf](https://www.deutschebank.nl/nl/docs/Solar_2014_Outlook_Let_the_Second_Gold_Rush_Begin.pdf)
6. Global Trend in Renewable Energy Investment 2018 (FS-UNEP/Bloomberg Energy, 2018); <http://fs-unep-centre.org/sites/default/files/publications/gtr2018v2.pdf>
7. Technology Roadmap for Photovoltaic (ITRPV): 2015 Results Including Maturity Report (VDMA Photovoltaic Equipment, 2016); <http://www.itrpv.net/Reports/Downloads>
8. Battaglia, C., Cuevas, A. and Wolf, S. D. High efficiency crystalline silicon solar cells: status and perspectives. *Energy Environ. Sci.* 9, 1552–1576 (2016).
9. K. Yamamoto, D. Adachi, K. Yoshikawa, W. Yoshida, T. Irie, K. Konishi, T. Fujimoto, H. Kawasaki, M. Kanematsu, H. Ishibashi, T. Uto, Y. Takahashi, T. Terashita, G. Koizumi, N. Nakanishi and M. Yoshimi, "Record-Breaking Efficiency Back-Contact Heterojunction Crystalline Si Solar Cell and Module" in *33rd European Photovoltaic Solar Energy Conference and Exhibition, 2017*, pp. 201–204.

10. J. L. Hernandez, et al “High efficiency silver-free heterojunction silicon solar cell,” *Jpn. J. Appl. Phys.* 51, 10NB04, 2012.
11. D. Adachi et al. “Impact of carrier recombination on fill factor for large area heterojunction crystalline Si solar cell with 25.1% efficiency”, *Appl. Phys Lett.*, 107, 233506, 2015.
12. M. A. Green, “The path to 25% silicon solar cell efficiency: history of silicon cell evolution”, *Prog. Photovolt. Res. Appl.*, 2009
13. K. Yoshikawa et al, “SHJ solar cell with IBC for a photo conversion efficiency over 26%”, *Nature Energy*, Mar. 2017
14. M. Lu et al., “Interdigitated back contact silicon heterojunction solar cell and the effect of front surface passivation”, *Appl. Phys. Lett.* 91, 063507 2007.
15. L Zhang et al., “Experimental and simulated analysis of p a-Si:H defects on silicon heterojunction solar cells: trade-offs between VOC and FF”, *Proc. 42th IEEE PVSC Conf. New Orleans*, 2015.
16. Lumerical Solutions Inc., “A commercial-grade simulator based on the finite-difference time-domain method”, Vancouver, Canada. <http://www.lumerical.com/tcad-products/fdtd/>
17. J. W. Judy, “ Microelectromechanical systems (MEMS): fabrication, device and applications”, *Smart Materials and Structures*, vol. 10, no 6, 2001.
18. PRIME Faraday Partnership, “An Introduction to MEMS”, Wolfson school of Mechanical and Manufacturing Engineering, Loughborough University, Leics, LE11, 3TU. <http://www.primetechnologywatch.org.uk>
19. J. N. Pring and W. Fielding, *J. Chem. Soc.*, 1909, **95**, 1497.
20. R. Hoelbling, *Z. Angew, Chem*, 1927, **40**, 655.
21. G. K. Teal, J. R. Fisher and A. W. Treptow, *J. Appl. Phys.*, 1946, **17**, 879.
22. K. H. Storks and G. K. Teal, US Patent 2,441, 603 (1948).
23. A. C. Jones and M. L. Hitchman, in *Chemical Vapor Deposition: Precursors, Processes and Applications*, Eds. Anthony C. Jones and Michael L. Hitchman, Royal Society of Chemistry 2009, Chapter 1.
24. M. L. Hitchman and K. F. Jensen, in *Chemical Vapor Deposition*, Eds. M. L. Hitchman and K. F. Jensen, Academic Press, New York, 1989, Chapter 1.

25. R. L. Moon and Y.-M. Houg, in Chemical Vapor Deposition, Eds. M.L. Hitchman and K.F. Jensen, Academic Press, New York, 1989, Chapter 6.
26. T. T. Kodas and M. J. Hampden-Smith, Chapter 1 in The Chemistry of Metal CVD, VCH, Weinheim, 1994.
27. S. A. Campbell, in Fabrication Engineering at the Micro- and Nanoscale, Oxford University Press, New York, 2008, Chapter 12.
28. Wolfe, D.; J. Singh (2000). "Surface and Coatings Technology" **124**: 142-153.
29. I. Langmuir, General Electric Rev, **26**:731 (1923).
30. <http://www.semicore.com/news/81-what-is-thin-film-deposition>
31. L. Zhang et al., "Experimental and simulated analysis of p a-Si:H defects on silicon heterojunction solar cells: trade-offs between VOC and FF," in Proc. IEEE 42nd Photovolt. Spec. Conf., 2015, pp. 1–5.
32. W. A Kern and C. A. Deckert, "Chemical Etching," in Thin Film Processing, J. L. Vossen, ed., Academic Press, New York, 1978.
33. M. Rose, "A History of the Laser: A Trip through the Light Fantastic", Photonics Spectra, May 2010. Retrieve from <http://www.photonics.com/Article.aspx?PID=5&VID=61&IID=464&Tag=Features&AID=42279>
34. M. Gupta and D. Carlson, Laser processing of materials for renewable energy applications, MRS Energy & Sustainability. 2015.
35. C. R. Brundle, C. A. Evans and S. Wilson, Encyclopedia of materials characterization: surfaces, interfaces, thin films, Butterworth-Heinemann; Manning, Boston Greenwich, CT, 1992.
36. [https://commons.wikimedia.org/wiki/File:Schematic\\_of\\_UV-visible\\_spectrophotometer.png](https://commons.wikimedia.org/wiki/File:Schematic_of_UV-visible_spectrophotometer.png)
37. K. Vedam, Spectroscopic ellipsometry: a historical overview, Thin Solid Films, pp. 313-314, 1 (1998).
38. <https://www.jawoollam.com/products/vase-ellipsometer>
39. A. A. Langford, M. L. Fleet, and B. P. Nelson, "Infrared absorption strength and hydrogen content of hydrogenated amorphous silicon", Physical Review B, vol. 45, no. 23, 1992.

40. M. Cardona, *Phys. Status Solidi B* 118, 463 (1983).
41. M. H. Brodsky, M. Cardona, and J.J. Cuomo, *Phys. Rev. B* 16, 3556 (1977).
42. G. Lucovsky, R. J. Nemanich, and J. C. Knights, *Phys. Rev. B* 19, 2064 (1979).
43. Tsu R., González-Hernández J., Chao S.S., Lee S.C., Tanaka K., *Appl. Phys. Lett.* 40, 534 (1982)
44. J.F. Moulder, W. Stickle, P. Sobol, K. Bomben, *Handbook of X-ray Photoelectron Spectroscopy: A Reference Book of Standard Spectra for Identification and Interpretation of XPS Data*, Perkin-Elmer Corporation, Physical Electronics Division, Minnesota, USA.
45. Casa Software Ltd. UK, *CasaXPS User's Manual*, Version 2.0, Oct 2001. <http://www.casaxps.com> (accessed 15 June 2018).
46. J. H. Scofield, Hartree-Slater subshell photoionization cross-sections at 1254 and 1487 eV, *J. Electron Spectroscopy and Related Phenomena*, 8 (2) (1976) 129-137.
47. A.G. Shard, Detection limits in XPS for more than 6000 binary systems using Al and Mg K $\alpha$  X-rays, *J. Surface and Interface Analysis*, 46 (3) (2014) 175-185.
48. The University of Edinburgh (March 6, 2018). "What is Microscopy?". <https://www.ed.ac.uk/clinical-sciences/edinburgh-imaging/for-patients-study-participants/tell-me-more-about-my-scan/what-is-microscopy> (accessed 15 June 2018).
49. Helen Purtle, "History of the Microscope," *Encyclopedia of Microscopy and Micro-technique*, (New York: Van Nostrand Reinhold Co., 1973).
50. Ford, Brian J. (1992). "From Dilettante to Diligent Experimenter: a Reappraisal of Leeuwenhoek as microscopist and investigator". *Biology History*. 5 (3).
51. Lane, Nick (6 March 2015). "The Unseen World: Reflections on Leeuwenhoek (1677) 'Concerning Little Animal'." *Philos Trans R Soc Lond B Biol Sci*. 2015 Apr; 370 (1666): 20140344. [doi:10.1098/rstb.2014.0344]
52. Abramowitz M, Davidson MW (2007). "Introduction to Microscopy", *Molecular Expressions*. Retrieved 2007-08-22.

53. Von Ardenne, Manfred (1938). "Das Elektronen-Rastermikroskop. Theoretische Grundlagen" (in German). *Zeitschrift für Physik* 108: 553-572.
54. [http://en.wikipedia.org/wiki/Scanning\\_electron\\_microscope](http://en.wikipedia.org/wiki/Scanning_electron_microscope).
55. [https://hha.hitachi-hightech.com/en/blogs-events/blogs/2017/10/25/optical-emission-spectroscopy-\(oes\)/](https://hha.hitachi-hightech.com/en/blogs-events/blogs/2017/10/25/optical-emission-spectroscopy-(oes)/) Accessed 06-20-2018.
56. K. Seeger, *Semiconductor Physics, an Introduction*, Springer, 1999.
57. A. Sproul, *Journal of Applied Physics*, 76, 2851, 1994.
58. R. A. Sinton, A. Cuevas, M. Stuckings, Quasi-steady-state photoconductance, a new method for solar cell material and device characterization, in: *Proceeding of the 25<sup>th</sup> IEEE Photovoltaic Specialist Conference*, Washington DC, USA, 1996, pp. 457-460.
59. D. Abou-Ras, T. Kirchartz, and U. Rau (Eds.), 2011. "Advanced Characterization Techniques for Thin Film Solar Cells", Wiley-VCH.
60. Goetzberger, Adolf; Knobloch, Joachim; *Crystalline Silicon Solar Cells*, Bernhard © 1998 John Wiley & Sons.
61. <https://www.tek.com/keithley-source-measure-units/keithley-smu-2400-series-sourcemeater>.
62. S. S. Hegedus, W. N. Shafarman, 2004. "Thin Film Solar Cells: Device Measurements and Analysis, *Prog. Photovolt: Res. Appl.* 12: p 155-176.
63. U. J. Nsofor, L. Zhang, A. Soman, C. Goodwin, H. Liu, K. D. Dobson, U. K. Das, T. P. Beebe Jr., S. Hegedus, "Analysis of Silicon Wafer Surface Preparation for Heterojunction Solar Cells Using X-ray Photoelectron Spectroscopy and Effective Minority Carrier Lifetime", *Sol. Energy Mater. and Sol. Cells*, vol. 183, pp. 205-210, 2018.
64. D. L. Kendall, A new theory for the anisotropic etching of silicon and some underdeveloped chemical micromachining concepts, *J. Vac. Sci. Technol. A*, 8 (4) (1990) 3598-3605.
65. H. Seidel, L. Csepregi, A. Jeuberger, H. Boumgartel, Anisotropic etching of crystalline silicon in alkaline solutions, I. Orientation dependence and behavior of passivation layers, *J. Electrochem. Soc.* 137 (11) (1990) 3612-3626.
66. W. Kern, The evolution of silicon wafer cleaning technology, *J. Electrochem. Soc.* 137 (6) (1990) 1887-1892.

67. B. Chhabra, S. Bowden, R. L. Opila, C. B. Honsberg, High effective minority carrier lifetime on silicon substrates using quinhydrone-methanol passivation, *App. Phys. Letts.* 98 (6) (2010) 063502.
68. D. R. Turner, "On the mechanism of chemically etching germanium and silicon," *J. Electrochem. Soc.* 107 (10) (1960) 810-816.
69. K. Dasgupta, S. Ray, A. Mondal and U. Gangopadhyay, Review on different front surface modification of both  $n^+ - p - p^+$  and  $p^+ - n - n^+$  c-Si solar cell, *Materials Today: Proceeding*, 4 (2017) 12698-12707.
70. J. F. Moulder, W. Stickle, P. Sobol, K. Bomben, *Handbook of X-ray Photoelectron Spectroscopy: A Reference Book of Standard Spectra for Identification and Interpretation of XPS Data*, Perkin-Elmer Corporation, Physical Electronics Division, Minnesota, USA.
71. J. Goodman, S. Andrews, Fluoride contamination from fluoropolymers in semiconductor manufacture, *Solid State Technol.* July 1990, p. 65+. Academic OneFile, Accessed 7 Oct. 2017.
72. K. R. Williams, R. S. Muller, Etch rates for micromachining processing, *J. Microelectromechanical Sys.* 5 (4) (1996) 256-269.
73. R. Barrio, C. Maffiotte, J. J. Gandia, J. Carabe, Surface characterization of wafers for silicon-heterojunction solar cell, *J. Non-Crystalline Solids*, 352 (2006) 945-949.
74. L. Serenelli, R. Chierchia, M. Izzi, M. Tucci, L. Martini, D. Caputo, R. Asquini, and G. de Cesare, "Hydrogen Plasma and Thermal Annealing Treatments on a-Si:H Thin Film for c-Si Surface Passivation," *Energy Procedia*, vol. 60, no. May, pp. 102–108, 2014.
75. A. Antony and A. Soman, "Hydrogen Plasma Treatment to Enhance a-Si/c-Si Interface Passivation," in *32nd European Photovoltaic Solar Energy Conference and Exhibition*, 2016, pp. 738–741.
76. A. Descoeurdes, L. Barraud, S. De Wolf, B. Strahm, D. Lachenal, C. Guérin, Z. C. Holman, F. Zicarelli, B. Demareux, J. Seif, J. Holovsky, and C. Ballif, "Improved amorphous/crystalline silicon interface passivation by hydrogen plasma treatment," *Appl. Phys. Lett.*, vol. 99, no. 12, p. 123506, 2011.

77. A. Soman, U. J. Nsofor, L. Zhang, U. Das, T. Gu and S. Hegedus, "Hydrogen Plasma Post-Deposition Treatment for Passivation of a-Si/c-Si Interface for Heterojunction Solar Cell by Correlating Optical Emission Spectroscopy and Minority Carrier Lifetime", in *Proc. 44th IEEE Photovoltaic Spec. Conf.*, 2017.
78. Z. Chen, S. K. Pang, K. Yasutake, and A. Rohatgi, "Plasma-enhanced chemical vapor deposited oxide for low surface recombination velocity and high effective lifetime in silicon," *J. Appl. Phys.* 74, 2856, 1993.
79. A. G Aberle and R. Hezel, "Progress in low-temperature surface passivation of silicon solar cells using remote plasma silicon nitride," *Prog. Photovoltaics* 5, 29, 1997.
80. I. Martin, M. Vetter, A. Orpella, and J. Puigdollers, A. Cuevas and R. Alcubilla, "Surface passivation of p-type crystalline Si by plasma enhanced chemical vapor deposited amorphous SiC<sub>x</sub>:H films," *Appl. Phys. Lett.* 79, 2199, 2001.
81. Shubham Duttgupta, Fen Lin, Kishan Devappa Shetty, Armin G. Aberle and Bram Hoex, "Excellent boron emitter passivation for high-efficiency Si wafer solar cells using AlO<sub>x</sub>/SiN<sub>x</sub> dielectric stacks deposited in an industrial inline plasma reactor," *Prog. Photovoltaics* 21, 4, pp. 760-764, 2012.
82. Makoto Tanaka, Mikio Taguchi, Takao Matsuyama, Toru Sawada, Shinya Tsuda, Shoichi Nakano, Hiroshi Hanafusa and Yukinori Kuwano, "Development of New a-Si/c-Si Heterojunction Solar Cells: ACJ-HIT (Artificially Constructed Junction-Heterojunction with Intrinsic Thin-Layer)," *Jpn. J. Appl. Phys. Part 1* 31, 3518, 1992.
83. A. Neumuller, O. Sergeev, M. Vehse and C. Agert, "Structural characterization of the interface of amorphous silicon thin films after post-deposition argon or hydrogen plasma treatment", *Appl. Surf. Sci.*, vol. 403, pp. 200-205, 2017.
84. W. Liu, L. Zhang, S. Cong, R. Chen, Z. Wu, F. Meng, Q. Shi and Z. Liu, "Controllable a-Si:/c-Si interface passivation by residual SiH<sub>4</sub> molecules in H<sub>2</sub> plasma", *Sol. Energy Mater. and Sol. Cells*, vol. 174, pp. 233-239, 2018.
85. Nakamura et al, Sanyo Electric Co., Ltd., U.S. Patent, Apr. 2006
86. U. Nsofor, A. Soman, U. Das and S. Hegedus, "Improving the Interface Passivation of Si HJ Solar Cells by Interrupted Deposition of Thin a-Si:H Film", in *Proc. 45th IEEE Photovoltaic Spec. Conf.*, 2018.

87. M. Legesse, M. Nolan and G. Fagas, "Revisiting the Dependence of the Optical and Mobility Gaps of Hydrogenated Amorphous Silicon on Hydrogen Concentration", *J. Phys. Chem. C*, vol. 117, no. 45, pp. 23956-23963, 2013.
88. S. D. Wolf and M. Kondo, "Nature of doped a-Si:H /c-Si interface recombination," *J. Appl. Phys.* vol. 105, 103707, 2009.
89. Z. P. Ling, J. Ge, R. Standl, A. G. Aberle and T. Mueller, "Detailed Micro Raman Analysis of Doped Silicon Thin Film Layers and Its Feasibility for Heterojunction Silicon Wafer Solar Cells", *J. Material Sci., and Chem. Engr.*, vol. 1, pp. 1 – 14, 2013.
90. R. W. Collins, A. S. Ferlauto, G. M. Ferreira, C. Chen, J. Koh, R. J. Koval, Y. Lee, J. M. Pearce and C. R. Wron "Evolution of Microstructure and Phase in Amorphous, Proto-crystalline, and Microcrystalline Silicon Studied by Real Time Spectroscopic Ellipsometry," *Solar Energy Materials and Solar Cells*, Vol. 78, No. 1-4, 2003, pp. 143-180.
91. P. R. i. Cabarrocas, N. Layadi, T. Heitz, B. Drévillon and I. Solomon, "Substrate Selectivity in the Formation of Microcrystalline Silicon: Mechanisms and Technological Consequences," *Applied Physics Letters*, Vol. 66, No. 26, 1995, pp. 3609-3611.
92. H. Fujiwara, M. Kondo and A. Matsuda, "Nucleation Mechanism of Microcrystalline Silicon from the Amorphous Phase," *Journal of Non-Crystalline Solids*, Vol. 338-340, 2004, pp. 97-101.
93. A. Soman, U. J. Nsofor, U.K. Das, T. Gu and S. Hegedus, "Correlation between in situ diagnostics of the hydrogen plasma and the interface passivation quality of hydrogen plasma post-treated a-Si:H in Silicon Heterojunction Solar Cells," *Nano Energy*, 2018 (peer review).
94. M. Bivour, S. Schroer, M. Hermle and S. W. Glunz, "Silicon heterojunction rear emitter solar cells: Less restriction on the optoelectrical properties of front side TCOs", *Sol. Energy Mater. and Sol. Cells*, vol. 122, pp. 120-129, 2014.
95. Z. D. Eygi, U. Das, S. Hegedus and R. Birkmire, "Improved FF in P-Si heterojunction solar cells due to optimized ITO/emitter contact" in *Proc. 37th IEEE Photovoltaic Spec. Conf.*, 2011, pp. 001424–001428.

96. K. P. Sibins, N. Swain, P. Chowdhury, A. Dey, N. Sridhara, H. D. Shashikala, A. K. Karma and H. C. Barshilia, "Optical and electrical properties of ITO thin films sputtered by flexible FEP substrate as passive thermal control system for space applications," *Sol. Energy Mater. and Sol. Cells*, vol. 145, pp. 314-322, 2016.
97. M. S. Farhan, E. Zalnezhad, A. Bushroa and A. Sarhan, "Electrical and optical properties of indium-tin oxide (ITO) films by ion-assisted deposition (IAD) at room temperature," *Intl., J. of Precision Engr. And Manufacturing*, vol. 14, pp. 1465-1469, 2013.
98. S. S. Hegedus, W. A. Buchanan and E. Eser, "Improving performance of superstrate p-i-n a-Si solar cells by optimization of n/TCO/metal back contact," in *Proc. 26th IEEE Photovoltaic Spec. Conf.*, 1997, pp. 603-606.
99. Z. Sun, U. Nsofor, N. Ahmed, U. K. Das, S. Hegedus and M. C. Gupta, "Direct laser isolation for interdigitated back contact heterojunction solar cells," in *Proc. 45th IEEE Photovoltaic Spec. Conf.*, 2018.
100. U. Das, C Thompson, U. Nsofor, Z. Sun, M. C. Gupta and S. Hegedu, "Effect of dielectric layers on laser-fired-contact performance in a-Si/c-Si heterojunction solar cells," in *Proc. 45th IEEE Photovoltaic Spec. Conf.*, 2018.
101. J. He, S. Hegedus, U. Das, Z. Shu, M. Bennett, L. Zhang, and R. Birkmire, "Laser-fired contact for n-type crystalline Si solar cells," *Progress in Photovoltaics*, vol. 23, pp. 1091-1099, 2015.
102. U. J. Nsofor, P. L. Yao, S. Shi and D. W. Prather "Passive Tuning of Optical Couplers Using a Thin-Film Cladding Material" *IEEE Photon. Technol. Lett.*, vol. 29, no. 9, pp. 775-778, Mar. 2017.
103. R. S. Weis, and T. K. Gaylord, "Lithium Niobate: Summary of Physical Properties and Crystal Structure," *J. Appl. Phys.* vol. 37, no. 4, pp. 191-203, Aug. 1985.
104. F. Caccavale, P. Chakraborty, A. Quaranta, I. Mansour, G. Gianello, S. Bosso, R. Corsini, and G. Mussi, "Secondary-ion-mass spectrometry and near-field studies of Ti:LiNbO<sub>3</sub> optical waveguide," *J. Appl. Phys.* vol. 78, no. 9, pp. 5345-5350, Nov. 1995.
105. J. Macario, P. Yao, S. Shi, A. Zablocki, C. Harrity, R.D. Martins, C. A. Schuetz, and D.W. Prather, "Full spectrum millimeter-wave modulation," *Opt. Express* vol. 20, no. 21, pp. 23623-23629, Oct. 2012.

106. H. Kanbara, H. Itoh, M. Asobe, K. Noguchi, H. Miyazawa, T. Yanagawa, and I. Yokohama, "All-optical switching based on cascading of second-order nonlinearities in a periodically poled titanium-diffused lithium niobate waveguide," *IEEE Photon. Technol. Lett.* Vol. 11, no. 3, pp. 328-330, Mar. 1999.
107. M. N. Armenise, "Fabrication techniques of lithium niobate waveguides," in *Proceeding of IEEE J. Optoelectronics*, vol. 135, no. 2, pp. 85-91, Apr. 1988.
108. R.C. Alferness, "Titanium-Diffused Lithium Niobate Waveguide Devices", *Springer Series in Electronics and Photonics*, Vol. 26, pp. 145-210, 1988.
109. M. Koshiba, Y. Tsuji and M. Nishio, "Finite-Element Modeling of Broadband Travelling-Wave Optical Modulator", *IEEE Transaction on Microwave Theory and Techniques*, Vol. 47, No. 9, September 1999.
110. K. Noguchi, O. Mitomi, H. Miyazawa and S. Seki, "A Broadband Ti:LiNbO<sub>3</sub> Optical Modulator with a Ridge Structure", *J. Lightwave Technol.*, Vol. 13, No. 6, pp. 1164-1168, June 1995.
111. E. Strake, G.P. Bava and I. Montrosset, "Guided Mode of Ti:LiNbO<sub>3</sub> Channel Waveguides: A Novel Quasi-Analytical Technique in Comparison with the Scalar Finite Element Method", *J. Lightwave Technol.*, Vol.6, pp. 1122-1135, June 1988.
112. C. A. Schuetz et al, *IEEE Trans.Microwave Theory & Techniques*, 2005.
113. R. Stierlin et al, *Opt. & Q. Electronics* 18, (445-454), 1986.
114. R. V. Schmidt and I. P. Kaminow, "Metal-diffused optical waveguides in LiNbO<sub>3</sub>" *Appl. Phys. Lett.*, vol. 25, no.8, pp. 458-460, Jun. 1974.
115. O. Mikami, and J. Noda, "Phase tuning in optical directional coupler" *Appl. Phys. Lett.* vol. 29, no. 9, pp. 555-556, Jun. 1976.
116. J. M. Liu, and C. Yeh, "Optical switching by saturation-induced phase changes in an active directional coupler" *Appl. Phys. Lett.*, vol. 50, no. 23, pp. 1625-1627, Mar. 1987.
117. A. Chen, V. Chuyanov, F. I. Marti-Carrera, S. Garner, W. H. Steier, S. S. H. Mao, Y. Ra, L. R. Dalton, and Y. Shi, "Trimming of polymer waveguide Y-junction by rapid photo-bleaching for tuning the power splitting ratio" *IEEE Photonics Technol. Lett.*, vol. 9, no. 11, pp. 1499-1501, Nov. 1997.

118. P. Orlandi, F. Morichetti, M. J. Strain, M. Sorel, A. Melloni, and P. Bassi, "Tunable silicon photonics directional coupler driven by a transverse temperature gradient" *Opt. Lett.*, vol. 38, no. 6, pp. 863-865, Mar. 2013.
119. F. Duerinckx, and J. Szlufcik, "Defect passivation of industrial multicrystalline solar cells based on PECVD silicon nitride," *Solar Energy Mat. & Solar Cells*, vol. 72, no. 1-4, pp. 231-246, 2002.
120. M. E. Solmaz, D. B. Adams, W. C. Tan, W. T. Snider, and C. K. Madsen, "Vertically integrated  $\text{As}_2\text{S}_3$  ring resonator on  $\text{LiNbO}_3$ " *Opt. Lett.*, vol. 34, no. 11, pp. 1735-1737, Jun. 2009.
121. Samco PD – 220N PECVD system spec sheet. <http://www.cryosystems-mve.ru/dl/PD-220N.pdf>
122. W. Van Gelder, and V. Hauser, "The Etching of Silicon Nitride in Phosphoric Acid with Silicon Dioxide as a Mask," *J. Electrochem. Soc.* vol. 114, no. 8, pp. 869-872, Apr. 1967.

## Appendix A

### AM1.5 AND AM0

The efficiency of a solar cell is determined by  $\eta = P_{\text{out}}/P_{\text{in}}$ , where  $P_{\text{out}}$  is the electrical power generated per unit area and  $P_{\text{in}}$  is the power density of the solar insolation. The value for  $P_{\text{in}}$  varies considerably for different applications and different conditions.

In space the solar insolation outside the earth's atmosphere (at the mean earth-sun distance) is referred to as air mass zero (AM0) radiation, and is shown in Figure A.1 [1]. This radiation intensity is not quite the same as for the case of an ideal black body emitting at 6000 K.

At the earth's surface, the solar radiation intensity is reduced from AM0 due to scattering and absorption that occur in the atmosphere [2]. The amount by which the radiation is reduced will depend on the length of the optical path through the atmosphere, which depends on the sun's location in the sky (this will be determined by the time of day, time of year, and latitude of the observer). When the sun is directly overhead at sea level and without clouds, the radiation will be at a maximum; this is referred to as air mass one (AM1) radiation. When the sun is at other locations in the sky, the air mass is defined as:

$$\text{air mass} = \frac{1}{\cos\theta} \tag{A.1}$$

where  $\theta = 0$  corresponds to the sun being directly overhead. For terrestrial applications, AM1.5 ( $48^\circ$  from overhead) has been established as the standard solar insolation (see Figure A.1), and this corresponds to a power density of  $P_{in} = 100 \text{ mW/cm}^2$  [1].

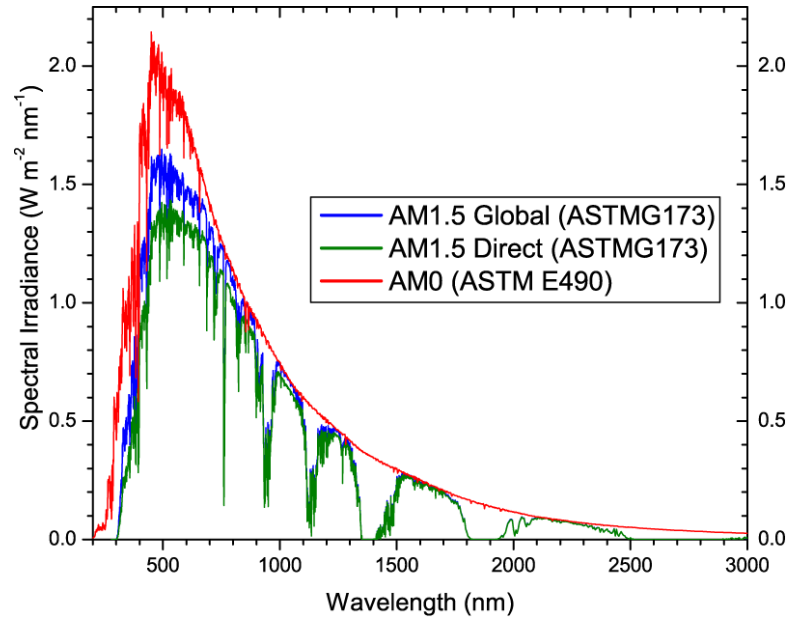


Figure A.1: Spectral distribution of sunlight for space (AM0) and terrestrial (AM1.5G and AM1.5D) applications as estimated by the American Society of Testing and Materials (ASTM).

### References:

1. M. A. Green, Solar Cells, Prentice-Hall, Englewood Cliffs, NJ, 1982.
2. P. R. Gast, Handbook of Geophysics.

## **Appendix B**

### **PECVD GROWTH RATE DEPENDENCE ON PLASMA VOLTAGE**

Achieving excellent chemical and field effect passivation with intrinsic and doped a-Si:H is the principal goal for making high efficiency HJ solar cell. Experience has shown that these layers should be very thin (preferably sub 10 nm thick) to facilitate carrier collection while minimizing parasitic absorption. Also since the bulk defects distribution of these a-Si:H films are often described in terms of the valence and conduction band tail states, and gaussian mid-gap states, the thicker these layers are, the more recombination that is expected in these layers. Thus, it is critical that the film thickness is closely monitored.

On the other hand, the a-Si:H growth rate in the MC-PECVD system described in section 2.1.1 varies over time as more dielectric films are deposited on the inner walls of the CVD chambers. As the dielectric film increases so does the resistance of the chamber walls. In order to overcome this resistance and maintain the set plasma current, the PLC system that controls the CVD increases the plasma voltage consequently. Thus, over time we have observed a linear correlation between the plasma voltage and a-Si:H growth rate, which in turn determines the thickness of the film.

The chart below was developed from growth rate estimations done over a 12 months period when we observed a significant change in plasma voltage. The chart can be used as a reference to predict the growth rate of i.a-Si:H grown in the MC-PECVD system.

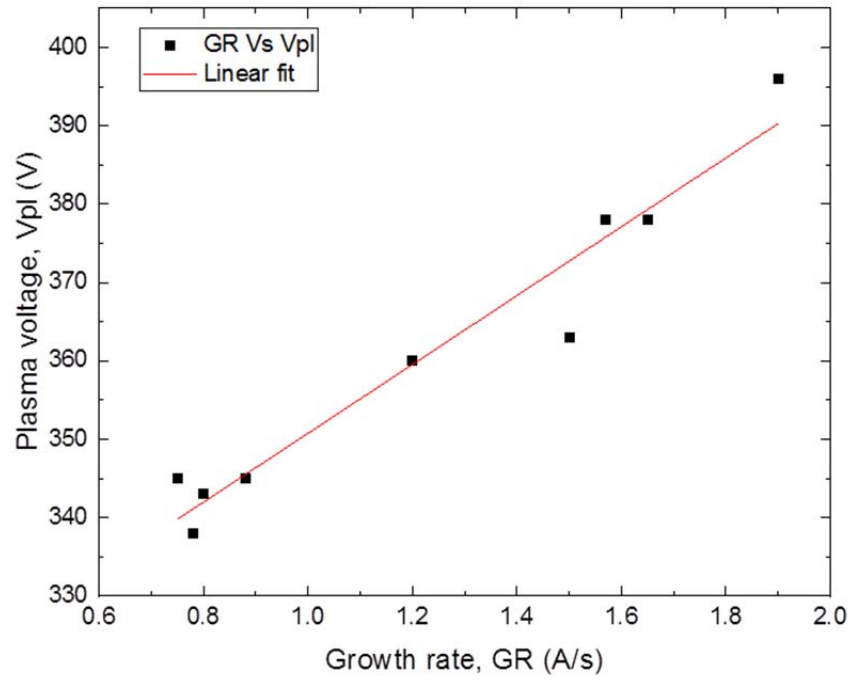


Figure A.2: Growth rate dependence on plasma voltage for i.a-Si:H deposition. Data was collected for varying deposition conditions over a period of 12 months.

## **Appendix C**

### **COPYRIGHT FOR PUBLISHED MATERIAL**

Excerpts from several of my published research works were used in developing this manuscript. Their copyright forms and letters of permission for reprinted figures are presented here.

## IEEE COPYRIGHT FORM

To ensure uniformity of treatment among all contributors, other forms may not be substituted for this form, nor may any wording of the form be changed. This form is intended for original material submitted to the IEEE and must accompany any such material in order to be published by the IEEE. Please read the form carefully and keep a copy for your files.

### Passive Tuning of Optical Couplers Using a Thin Film Cladding Material

Nsofor, Ugochukwu; Yao, Peng; Shi, Shouyuan; Prather, Dennis

Photonics Technology Letters

### COPYRIGHT TRANSFER

The undersigned hereby assigns to The Institute of Electrical and Electronics Engineers, Incorporated (the "IEEE") all rights under copyright that may exist in and to: (a) the Work, including any revised or expanded derivative works submitted to the IEEE by the undersigned based on the Work; and (b) any associated written or multimedia components or other enhancements accompanying the Work.

### GENERAL TERMS

1. The undersigned represents that he/she has the power and authority to make and execute this form.
2. The undersigned agrees to indemnify and hold harmless the IEEE from any damage or expense that may arise in the event of a breach of any of the warranties set forth above.
3. The undersigned agrees that publication with IEEE is subject to the policies and procedures of the [IEEE PSPB Operations Manual](#).
4. In the event the above work is not accepted and published by the IEEE or is withdrawn by the author(s) before acceptance by the IEEE, the foregoing copyright transfer shall be null and void. In this case, IEEE will retain a copy of the manuscript for internal administrative/record-keeping purposes.
5. For jointly authored Works, all joint authors should sign, or one of the authors should sign as authorized agent for the others.
6. The author hereby warrants that the Work and Presentation (collectively, the "Materials") are original and that he/she is the author of the Materials. To the extent the Materials incorporate text passages, figures, data or other material from the works of others, the author has obtained any necessary permissions. Where necessary, the author has obtained all third party permissions and consents to grant the license above and has provided copies of such permissions and consents to IEEE

BY TYPING IN YOUR FULL NAME BELOW AND CLICKING THE SUBMIT BUTTON, YOU CERTIFY THAT SUCH ACTION CONSTITUTES YOUR ELECTRONIC SIGNATURE TO THIS FORM IN ACCORDANCE WITH UNITED STATES LAW, WHICH AUTHORIZES ELECTRONIC SIGNATURE BY AUTHENTICATED REQUEST FROM A USER OVER THE INTERNET AS A VALID SUBSTITUTE FOR A WRITTEN SIGNATURE.

Ugochukwu Nsofor

Signature

18-03-2017

Date (dd-mm-yyyy)

## Information for Authors

### AUTHOR RESPONSIBILITIES

The IEEE distributes its technical publications throughout the world and wants to ensure that the material submitted to its publications is properly available to the readership of those publications. Authors must ensure that their Work meets the requirements as stated in section 8.2.1 of the IEEE PSPB Operations Manual, including provisions covering originality,

authorship, author responsibilities and author misconduct. More information on IEEE's publishing policies may be found at [http://www.ieee.org/publications\\_standards/publications/rights/authorrightsresponsibilities.html](http://www.ieee.org/publications_standards/publications/rights/authorrightsresponsibilities.html) Authors are advised especially of IEEE PSPB Operations Manual section 8.2.1.B12: "It is the responsibility of the authors, not the IEEE, to determine whether disclosure of their material requires the prior consent of other parties and, if so, to obtain it." Authors are also advised of IEEE PSPB Operations Manual section 8.1.1B: "Statements and opinions given in work published by the IEEE are the expression of the authors."

## RETAINED RIGHTS/TERMS AND CONDITIONS

- Authors/employers retain all proprietary rights in any process, procedure, or article of manufacture described in the Work.
- Authors/employers may reproduce or authorize others to reproduce the Work, material extracted verbatim from the Work, or derivative works for the author's personal use or for company use, provided that the source and the IEEE copyright notice are indicated, the copies are not used in any way that implies IEEE endorsement of a product or service of any employer, and the copies themselves are not offered for sale.
- Although authors are permitted to re-use all or portions of the Work in other works, this does not include granting third-party requests for reprinting, republishing, or other types of re-use. The IEEE Intellectual Property Rights office must handle all such third-party requests.
- Authors whose work was performed under a grant from a government funding agency are free to fulfill any deposit mandates from that funding agency.

## AUTHOR ONLINE USE

- **Personal Servers.** Authors and/or their employers shall have the right to post the accepted version of IEEE-copyrighted articles on their own personal servers or the servers of their institutions or employers without permission from IEEE, provided that the posted version includes a prominently displayed IEEE copyright notice and, when published, a full citation to the original IEEE publication, including a link to the article abstract in IEEE Xplore. Authors shall not post the final, published versions of their papers.
- **Classroom or Internal Training Use.** An author is expressly permitted to post any portion of the accepted version of his/her own IEEE-copyrighted articles on the author's personal web site or the servers of the author's institution or company in connection with the author's teaching, training, or work responsibilities, provided that the appropriate copyright, credit, and reuse notices appear prominently with the posted material. Examples of permitted uses are lecture materials, course packs, e-reserves, conference presentations, or in-house training courses.
- **Electronic Preprints.** Before submitting an article to an IEEE publication, authors frequently post their manuscripts to their own web site, their employer's site, or to another server that invites constructive comment from colleagues. Upon submission of an article to IEEE, an author is required to transfer copyright in the article to IEEE, and the author must update any previously posted version of the article with a prominently displayed IEEE copyright notice. Upon publication of an article by the IEEE, the author must replace any previously posted electronic versions of the article with either (1) the full citation to the IEEE work with a Digital Object Identifier (DOI) or link to the article abstract in IEEE Xplore, or (2) the accepted version only (not the IEEE-published version), including the IEEE copyright notice and full citation, with a link to the final, published article in IEEE Xplore.

**Questions about the submission of the form or manuscript must be sent to the publication's editor.**

**Please direct all questions about IEEE copyright policy to:**

**IEEE Intellectual Property Rights Office, [copyrights@ieee.org](mailto:copyrights@ieee.org), +1-732-562-3966**

# IEEE COPYRIGHT AND CONSENT FORM

To ensure uniformity of treatment among all contributors, other forms may not be substituted for this form, nor may any wording of the form be changed. This form is intended for original material submitted to the IEEE and must accompany any such material in order to be published by the IEEE. Please read the form carefully and keep a copy for your files.

**Thin Film Passive Tuning of Optical Couplers for Balanced Detection System**  
**Ugochukwu Josiah Nsofor and Peng Yao and Shouyuan Shi and Dennis Prather**  
**2017 IEEE Photonics Conference (IPC 2017)**

## COPYRIGHT TRANSFER

The undersigned hereby assigns to The Institute of Electrical and Electronics Engineers, Incorporated (the "IEEE") all rights under copyright that may exist in and to: (a) the Work, including any revised or expanded derivative works submitted to the IEEE by the undersigned based on the Work; and (b) any associated written or multimedia components or other enhancements accompanying the Work.

## GENERAL TERMS

1. The undersigned represents that he/she has the power and authority to make and execute this form.
2. The undersigned agrees to indemnify and hold harmless the IEEE from any damage or expense that may arise in the event of a breach of any of the warranties set forth above.
3. The undersigned agrees that publication with IEEE is subject to the policies and procedures of the [IEEE PSPB Operations Manual](#).
4. In the event the above work is not accepted and published by the IEEE or is withdrawn by the author(s) before acceptance by the IEEE, the foregoing copyright transfer shall be null and void. In this case, IEEE will retain a copy of the manuscript for internal administrative/record-keeping purposes.
5. For jointly authored Works, all joint authors should sign, or one of the authors should sign as authorized agent for the others.
6. The author hereby warrants that the Work and Presentation (collectively, the "Materials") are original and that he/she is the author of the Materials. To the extent the Materials incorporate text passages, figures, data or other material from the works of others, the author has obtained any necessary permissions. Where necessary, the author has obtained all third party permissions and consents to grant the license above and has provided copies of such permissions and consents to IEEE

**You have indicated that you DO wish to have video/audio recordings made of your conference presentation under terms and conditions set forth in "Consent and Release."**

## CONSENT AND RELEASE

1. In the event the author makes a presentation based upon the Work at a conference hosted or sponsored in whole or in part by the IEEE, the author, in consideration for his/her participation in the conference, hereby grants the IEEE the unlimited, worldwide, irrevocable permission to use, distribute, publish, license, exhibit, record, digitize, broadcast, reproduce and archive, in any format or medium, whether now known or hereafter developed: (a) his/her presentation and comments at the conference; (b) any written materials or multimedia files used in connection with his/her presentation; and (c) any recorded interviews of him/her (collectively, the "Presentation"). The permission granted includes the transcription and reproduction of the Presentation for inclusion in products sold or distributed by IEEE and live or recorded broadcast of the Presentation during or after the conference.
2. In connection with the permission granted in Section 1, the author hereby grants IEEE the unlimited, worldwide, irrevocable right to use his/her name, picture, likeness, voice and biographical information as part of the advertisement, distribution and sale of products incorporating the Work or Presentation, and releases IEEE from any claim based on right of privacy or publicity.

BY TYPING IN YOUR FULL NAME BELOW AND CLICKING THE SUBMIT BUTTON, YOU CERTIFY THAT SUCH ACTION CONSTITUTES YOUR ELECTRONIC SIGNATURE TO THIS FORM IN ACCORDANCE WITH UNITED STATES LAW, WHICH AUTHORIZES ELECTRONIC SIGNATURE BY AUTHENTICATED REQUEST FROM A USER OVER THE INTERNET AS A VALID SUBSTITUTE FOR A WRITTEN SIGNATURE.

Ugochukwu Nsofor

15-04-2017

Signature

Date (dd-mm-yyyy)

## Information for Authors

### AUTHOR RESPONSIBILITIES

The IEEE distributes its technical publications throughout the world and wants to ensure that the material submitted to its publications is properly available to the readership of those publications. Authors must ensure that their Work meets the requirements as stated in section 8.2.1 of the IEEE PSPB Operations Manual, including provisions covering originality, authorship, author responsibilities and author misconduct. More information on IEEE's publishing policies may be found at [http://www.ieee.org/publications\\_standards/publications/rights/authorrightsresponsibilities.html](http://www.ieee.org/publications_standards/publications/rights/authorrightsresponsibilities.html) Authors are advised especially of IEEE PSPB Operations Manual section 8.2.1.B12: "It is the responsibility of the authors, not the IEEE, to determine whether disclosure of their material requires the prior consent of other parties and, if so, to obtain it." Authors are also advised of IEEE PSPB Operations Manual section 8.1.1B: "Statements and opinions given in work published by the IEEE are the expression of the authors."

### RETAINED RIGHTS/TERMS AND CONDITIONS

- Authors/employers retain all proprietary rights in any process, procedure, or article of manufacture described in the Work.
- Authors/employers may reproduce or authorize others to reproduce the Work, material extracted verbatim from the Work, or derivative works for the author's personal use or for company use, provided that the source and the IEEE copyright notice are indicated, the copies are not used in any way that implies IEEE endorsement of a product or service of any employer, and the copies themselves are not offered for sale.
- Although authors are permitted to re-use all or portions of the Work in other works, this does not include granting third-party requests for reprinting, republishing, or other types of re-use. The IEEE Intellectual Property Rights office must handle all such third-party requests.
- Authors whose work was performed under a grant from a government funding agency are free to fulfill any deposit mandates from that funding agency.

### AUTHOR ONLINE USE

- **Personal Servers.** Authors and/or their employers shall have the right to post the accepted version of IEEE-copyrighted articles on their own personal servers or the servers of their institutions or employers without permission from IEEE, provided that the posted version includes a prominently displayed IEEE copyright notice and, when published, a full citation to the original IEEE publication, including a link to the article abstract in IEEE Xplore. Authors shall not post the final, published versions of their papers.
- **Classroom or Internal Training Use.** An author is expressly permitted to post any portion of the accepted version of his/her own IEEE-copyrighted articles on the author's personal web site or the servers of the author's institution or company in connection with the author's teaching, training, or work responsibilities, provided that the appropriate copyright, credit, and reuse notices appear prominently with the posted material. Examples of permitted uses are lecture materials, course packs, e-reserves, conference presentations, or in-house training courses.
- **Electronic Preprints.** Before submitting an article to an IEEE publication, authors frequently post their manuscripts to their own web site, their employer's site, or to another server that invites constructive comment from colleagues. Upon submission of an article to IEEE, an author is required to transfer copyright in the article to IEEE, and the author must update any previously posted version of the article with a prominently displayed IEEE copyright notice. Upon publication of an article by the IEEE, the author must replace any previously posted electronic versions of the article with either (1) the full citation to the

IEEE work with a Digital Object Identifier (DOI) or link to the article abstract in IEEE Xplore, or (2) the accepted version only (not the IEEE-published version), including the IEEE copyright notice and full citation, with a link to the final, published article in IEEE Xplore.

**Questions about the submission of the form or manuscript must be sent to the publication's editor.**

**Please direct all questions about IEEE copyright policy to:**

**IEEE Intellectual Property Rights Office, [copyrights@ieee.org](mailto:copyrights@ieee.org), +1-732-562-3966**



IEEE

## IEEE COPYRIGHT AND CONSENT FORM

To ensure uniformity of treatment among all contributors, other forms may not be substituted for this form, nor may any wording of the form be changed. This form is intended for original material submitted to the IEEE and must accompany any such material in order to be published by the IEEE. Please read the form carefully and keep a copy for your files.

**Hydrogen Plasma Post-Deposition Treatment for Passivation of a-Si/c-Si Interface for Heterojunction Solar Cell by Correlating Optical Emission Spectroscopy and Minority Carrier Lifetime**

**Anishkumar Soman, Ugochukwu Nsofor, Lei Zhang, Ujjwal Das, Tingyi Gu, Steven Hegedus**

**44th IEEE Photovoltaic Specialists Conference**

### COPYRIGHT TRANSFER

The undersigned hereby assigns to The Institute of Electrical and Electronics Engineers, Incorporated (the "IEEE") all rights under copyright that may exist in and to: (a) the Work, including any revised or expanded derivative works submitted to the IEEE by the undersigned based on the Work; and (b) any associated written or multimedia components or other enhancements accompanying the Work.

### GENERAL TERMS

1. The undersigned represents that he/she has the power and authority to make and execute this form.
2. The undersigned agrees to indemnify and hold harmless the IEEE from any damage or expense that may arise in the event of a breach of any of the warranties set forth above.
3. The undersigned agrees that publication with IEEE is subject to the policies and procedures of the [IEEE PSPB Operations Manual](#).
4. In the event the above work is not accepted and published by the IEEE or is withdrawn by the author(s) before acceptance by the IEEE, the foregoing copyright transfer shall be null and void. In this case, IEEE will retain a copy of the manuscript for internal administrative/record-keeping purposes.
5. For jointly authored Works, all joint authors should sign, or one of the authors should sign as authorized agent for the others.
6. The author hereby warrants that the Work and Presentation (collectively, the "Materials") are original and that he/she is the author of the Materials. To the extent the Materials incorporate text passages, figures, data or other material from the works of others, the author has obtained any necessary permissions. Where necessary, the author has obtained all third party permissions and consents to grant the license above and has provided copies of such permissions and consents to IEEE

**You have indicated that you DO wish to have video/audio recordings made of your conference presentation under terms and conditions set forth in "Consent and Release."**

### CONSENT AND RELEASE

1. In the event the author makes a presentation based upon the Work at a conference hosted or sponsored in whole or in part by the IEEE, the author, in consideration for his/her participation in the conference, hereby grants the IEEE the unlimited, worldwide, irrevocable permission to use, distribute, publish, license, exhibit, record, digitize, broadcast, reproduce and archive, in any format or medium, whether now known or hereafter developed: (a) his/her presentation and comments at the conference; (b) any written materials or multimedia files used in connection with his/her presentation; and (c) any recorded interviews of him/her (collectively, the "Presentation"). The permission granted includes the transcription and reproduction of the Presentation for inclusion in products sold or distributed by IEEE and live or recorded broadcast of the Presentation during or after the conference.
2. In connection with the permission granted in Section 1, the author hereby grants IEEE the unlimited, worldwide, irrevocable right to use his/her name, picture, likeness, voice and biographical information as part of the advertisement, distribution and sale of products incorporating the Work or Presentation, and releases IEEE from any claim based on

right of privacy or publicity.

BY TYPING IN YOUR FULL NAME BELOW AND CLICKING THE SUBMIT BUTTON, YOU CERTIFY THAT SUCH ACTION CONSTITUTES YOUR ELECTRONIC SIGNATURE TO THIS FORM IN ACCORDANCE WITH UNITED STATES LAW, WHICH AUTHORIZES ELECTRONIC SIGNATURE BY AUTHENTICATED REQUEST FROM A USER OVER THE INTERNET AS A VALID SUBSTITUTE FOR A WRITTEN SIGNATURE.

Anishkumar Soman

08-06-2017

Signature

Date (dd-mm-yyyy)

## Information for Authors

### AUTHOR RESPONSIBILITIES

The IEEE distributes its technical publications throughout the world and wants to ensure that the material submitted to its publications is properly available to the readership of those publications. Authors must ensure that their Work meets the requirements as stated in section 8.2.1 of the IEEE PSPB Operations Manual, including provisions covering originality, authorship, author responsibilities and author misconduct. More information on IEEE's publishing policies may be found at [http://www.ieee.org/publications\\_standards/publications/rights/authorrightrresponsibilities.html](http://www.ieee.org/publications_standards/publications/rights/authorrightrresponsibilities.html) Authors are advised especially of IEEE PSPB Operations Manual section 8.2.1.B12: "It is the responsibility of the authors, not the IEEE, to determine whether disclosure of their material requires the prior consent of other parties and, if so, to obtain it." Authors are also advised of IEEE PSPB Operations Manual section 8.1.1B: "Statements and opinions given in work published by the IEEE are the expression of the authors."

### RETAINED RIGHTS/TERMS AND CONDITIONS

- Authors/employers retain all proprietary rights in any process, procedure, or article of manufacture described in the Work.
- Authors/employers may reproduce or authorize others to reproduce the Work, material extracted verbatim from the Work, or derivative works for the author's personal use or for company use, provided that the source and the IEEE copyright notice are indicated, the copies are not used in any way that implies IEEE endorsement of a product or service of any employer, and the copies themselves are not offered for sale.
- Although authors are permitted to re-use all or portions of the Work in other works, this does not include granting third-party requests for reprinting, republishing, or other types of re-use. The IEEE Intellectual Property Rights office must handle all such third-party requests.
- Authors whose work was performed under a grant from a government funding agency are free to fulfill any deposit mandates from that funding agency.

### AUTHOR ONLINE USE

- **Personal Servers.** Authors and/or their employers shall have the right to post the accepted version of IEEE-copyrighted articles on their own personal servers or the servers of their institutions or employers without permission from IEEE, provided that the posted version includes a prominently displayed IEEE copyright notice and, when published, a full citation to the original IEEE publication, including a link to the article abstract in IEEE Xplore. Authors shall not post the final, published versions of their papers.
- **Classroom or Internal Training Use.** An author is expressly permitted to post any portion of the accepted version of his/her own IEEE-copyrighted articles on the author's personal web site or the servers of the author's institution or company in connection with the author's teaching, training, or work responsibilities, provided that the appropriate copyright, credit, and reuse notices appear prominently with the posted material. Examples of permitted uses are lecture materials, course packs, e-reserves, conference presentations, or in-house training courses.
- **Electronic Preprints.** Before submitting an article to an IEEE publication, authors frequently post their manuscripts to their own web site, their employer's site, or to another server that invites constructive comment from colleagues. Upon submission of an article to IEEE, an author is required to transfer copyright in the article to IEEE, and the author must update any

previously posted version of the article with a prominently displayed IEEE copyright notice. Upon publication of an article by the IEEE, the author must replace any previously posted electronic versions of the article with either (1) the full citation to the IEEE work with a Digital Object Identifier (DOI) or link to the article abstract in IEEE Xplore, or (2) the accepted version only (not the IEEE-published version), including the IEEE copyright notice and full citation, with a link to the final, published article in IEEE Xplore.

**Questions about the submission of the form or manuscript must be sent to the publication's editor.**

**Please direct all questions about IEEE copyright policy to:**

**IEEE Intellectual Property Rights Office, [copyrights@ieee.org](mailto:copyrights@ieee.org), +1-732-562-3966**



## Rights & Access

**Elsevier B.V.**

Article:	Analysis of Silicon Surface Preparation for Heterojunction Solar Cells Using X-ray Photoelectron Spectroscopy and Effective Minority Carrier Lifetime
Corresponding author:	Dr U. J. Nsofor
E-mail address:	<a href="mailto:nsoforuj@udel.edu">nsoforuj@udel.edu</a>
Journal:	Solar Energy Materials and Solar Cells
Our reference	SOLMAT9332
PII:	S0927-0248(18)30109-0
DOI:	10.1016/j.solmat.2018.03.006

## Your Status

- I am one author signing on behalf of all co-authors of the manuscript
- The work was performed by contractors of the US Government under contract number: DE-0007534

## Data Protection & Privacy

- I do not wish to receive news, promotions and special offers about products and services from Elsevier B.V. and its affiliates worldwide.

## Assignment of Copyright

I hereby assign to Elsevier B.V. the copyright in the manuscript identified above (where Crown Copyright is asserted, authors agree to grant an exclusive publishing and distribution license) and any tables, illustrations or other material submitted for publication as part of the manuscript (the "Article"). This assignment of rights means that I have granted to Elsevier B.V., the exclusive right to publish and reproduce the Article, or any part of the Article, in print, electronic and all other media (whether now known or later developed), in any form, in all languages, throughout the world, for the full term of copyright, and the right to license others to do the same, effective when the Article is accepted for publication. This includes the right to enforce the rights granted hereunder against third parties.

## Supplemental Materials

"Supplemental Materials" shall mean materials published as a supplemental part of the Article, including but not limited to graphical, illustrative, video and audio material.

With respect to any Supplemental Materials that I submit, Elsevier B.V. shall have a perpetual worldwide, non-exclusive right and license to publish, extract, reformat, adapt, build upon, index, redistribute, link to and otherwise use all or any part of the Supplemental Materials in all forms and media (whether now known or later developed), and to permit others to do so.

## Research Data

"Research Data" shall mean the result of observations or experimentation that validate research findings and that are published separate to the Article, which can include but are not limited to raw data, processed data, software, algorithms, protocols, and methods.

With respect to any Research Data that I wish to make accessible on a site or through a service of Elsevier B.V., Elsevier B.V. shall have a perpetual worldwide, non-exclusive right and license to publish, extract, reformat, adapt, build upon, index, redistribute, link to and otherwise use all or any part of the Research Data in all forms and media (whether now known or later developed) and to permit others to do so. Where I have selected a specific end user license under which the Research Data is to be made available on a site or through a service, the publisher shall apply that end user license to the Research Data on that site or service.

## **Reversion of rights**

Articles may sometimes be accepted for publication but later rejected in the publication process, even in some cases after public posting in "Articles in Press" form, in which case all rights will revert to the author (see

## **Revisions and Addenda**

I understand that no revisions, additional terms or addenda to this Journal Publishing Agreement can be accepted without Elsevier B.V.'s express written consent. I understand that this Journal Publishing Agreement supersedes any previous agreements I have entered into with Elsevier B.V. in relation to the Article from the date hereof.

## **Author Rights for Scholarly Purposes**

I understand that I retain or am hereby granted (without the need to obtain further permission) the Author Rights (see description below), and that no rights in patents, trademarks or other intellectual property rights are transferred to Elsevier B.V..

The Author Rights include the right to use the [Preprint](#), [Accepted Manuscript](#) and the [Published Journal Article](#) for [Personal Use](#), [Internal Institutional Use](#) and for [Scholarly Sharing](#).

In the case of the Accepted Manuscript and the Published Journal Article the Author Rights exclude Commercial Use (unless expressly agreed in writing by Elsevier B.V.), other than use by the author in a subsequent compilation of the author's works or to extend the Article to book length form or re-use by the author of portions or excerpts in other works (with full acknowledgment of the original publication of the Article).

## **Author Representations / Ethics and Disclosure / Sanctions**

### **Author representations**

- The Article I have submitted to the journal for review is original, has been written by the stated authors and has not been previously published.
- The Article was not submitted for review to another journal while under review by this journal and will not be submitted to any other journal.
- The Article and the Supplemental Materials do not infringe any copyright, violate any other intellectual property, privacy or other rights of any person or entity, or contain any libellous or other unlawful matter.
- I have obtained written permission from copyright owners for any excerpts from copyrighted works that are included and have credited the sources in the Article or the Supplemental Materials.
- Except as expressly set out in this Journal Publishing Agreement, the Article is not subject to any prior rights or licenses and, if my or any of my co-authors' institution has a policy that might restrict my ability to grant

the rights required by this Journal Publishing Agreement (taking into account the Author Rights permitted hereunder, including Internal Institutional Use), a written waiver of that policy has been obtained.

- If I and/or any of my co-authors reside in Iran, Cuba, Sudan, Burma, Syria, or Crimea, the Article has been prepared in a personal, academic or research capacity and not as an official representative or otherwise on behalf of the relevant government or institution.
- 
- Any software contained in the Supplemental Materials is free from viruses, contaminants or worms.
- If the Article or any of the Supplemental Materials were prepared jointly with other authors, I have informed the co-author(s) of the terms of this Journal Publishing Agreement and that I am signing on their behalf as their agent, and I am authorized to do so.

## Governing Law and Jurisdiction

This Agreement will be governed by and construed in accordance with the laws of the country or state of Elsevier B.V. ("the Governing State"), without regard to conflict of law principles, and the parties irrevocably consent to the exclusive jurisdiction of the courts of the Governing State.

[For more information about the definitions relating to this agreement click here.](#)

**I have read and agree to the terms of the Journal Publishing Agreement.**

**5th March 2018**

T-copyright-v22/2017

- 
- 
- 

Copyright © 2018 Elsevier Ltd. All rights reserved.

Cookies are set by this site. To decline them or learn more, visit our page.

## IEEE COPYRIGHT AND CONSENT FORM

To ensure uniformity of treatment among all contributors, other forms may not be substituted for this form, nor may any wording of the form be changed. This form is intended for original material submitted to the IEEE and must accompany any such material in order to be published by the IEEE. Please read the form carefully and keep a copy for your files.

### **Improving the Interface Passivation of Si HJ Solar Cells by Interrupted Deposition of Thin a-Si:H Film**

**Ugochukwu J. Nsofor, Anishkumar Soman, Ujjwal Das, Steven Hegedus**

**2018 IEEE 45th Photovoltaic Specialists Conference (PVSC)**

### **COPYRIGHT TRANSFER**

The undersigned hereby assigns to The Institute of Electrical and Electronics Engineers, Incorporated (the "IEEE") all rights under copyright that may exist in and to: (a) the Work, including any revised or expanded derivative works submitted to the IEEE by the undersigned based on the Work; and (b) any associated written or multimedia components or other enhancements accompanying the Work.

### **GENERAL TERMS**

1. The undersigned represents that he/she has the power and authority to make and execute this form.
2. The undersigned agrees to indemnify and hold harmless the IEEE from any damage or expense that may arise in the event of a breach of any of the warranties set forth above.
3. The undersigned agrees that publication with IEEE is subject to the policies and procedures of the [IEEE PSPB Operations Manual](#).
4. In the event the above work is not accepted and published by the IEEE or is withdrawn by the author(s) before acceptance by the IEEE, the foregoing copyright transfer shall be null and void. In this case, IEEE will retain a copy of the manuscript for internal administrative/record-keeping purposes.
5. For jointly authored Works, all joint authors should sign, or one of the authors should sign as authorized agent for the others.
6. The author hereby warrants that the Work and Presentation (collectively, the "Materials") are original and that he/she is the author of the Materials. To the extent the Materials incorporate text passages, figures, data or other material from the works of others, the author has obtained any necessary permissions. Where necessary, the author has obtained all third party permissions and consents to grant the license above and has provided copies of such permissions and consents to IEEE

**You have indicated that you DO wish to have video/audio recordings made of your conference presentation under terms and conditions set forth in "Consent and Release."**

### **CONSENT AND RELEASE**

1. In the event the author makes a presentation based upon the Work at a conference hosted or sponsored in whole or in part by the IEEE, the author, in consideration for his/her participation in the conference, hereby grants the IEEE the unlimited, worldwide, irrevocable permission to use, distribute, publish, license, exhibit, record, digitize, broadcast, reproduce and archive, in any format or medium, whether now known or hereafter developed: (a) his/her presentation and comments at the conference; (b) any written materials or multimedia files used in connection with his/her presentation; and (c) any recorded interviews of him/her (collectively, the "Presentation"). The permission granted includes the transcription and reproduction of the Presentation for inclusion in products sold or distributed by IEEE and live or recorded broadcast of the Presentation during or after the conference.
2. In connection with the permission granted in Section 1, the author hereby grants IEEE the unlimited, worldwide, irrevocable right to use his/her name, picture, likeness, voice and biographical information as part of the advertisement, distribution and sale of products incorporating the Work or Presentation, and releases IEEE from any claim based on right of privacy or publicity.

BY TYPING IN YOUR FULL NAME BELOW AND CLICKING THE SUBMIT BUTTON, YOU CERTIFY THAT SUCH ACTION CONSTITUTES YOUR ELECTRONIC SIGNATURE TO THIS FORM IN ACCORDANCE WITH UNITED STATES LAW, WHICH AUTHORIZES ELECTRONIC SIGNATURE BY AUTHENTICATED REQUEST FROM A USER OVER THE INTERNET AS A VALID SUBSTITUTE FOR A WRITTEN SIGNATURE.

Ugochukwu Nsofor

16-05-2018

Signature

Date (dd-mm-yyyy)

## Information for Authors

### AUTHOR RESPONSIBILITIES

The IEEE distributes its technical publications throughout the world and wants to ensure that the material submitted to its publications is properly available to the readership of those publications. Authors must ensure that their Work meets the requirements as stated in section 8.2.1 of the IEEE PSPB Operations Manual, including provisions covering originality, authorship, author responsibilities and author misconduct. More information on IEEE's publishing policies may be found at [http://www.ieee.org/publications\\_standards/publications/rights/authorrightsresponsibilities.html](http://www.ieee.org/publications_standards/publications/rights/authorrightsresponsibilities.html) Authors are advised especially of IEEE PSPB Operations Manual section 8.2.1.B12: "It is the responsibility of the authors, not the IEEE, to determine whether disclosure of their material requires the prior consent of other parties and, if so, to obtain it." Authors are also advised of IEEE PSPB Operations Manual section 8.1.1B: "Statements and opinions given in work published by the IEEE are the expression of the authors."

### RETAINED RIGHTS/TERMS AND CONDITIONS

- Authors/employers retain all proprietary rights in any process, procedure, or article of manufacture described in the Work.
- Authors/employers may reproduce or authorize others to reproduce the Work, material extracted verbatim from the Work, or derivative works for the author's personal use or for company use, provided that the source and the IEEE copyright notice are indicated, the copies are not used in any way that implies IEEE endorsement of a product or service of any employer, and the copies themselves are not offered for sale.
- Although authors are permitted to re-use all or portions of the Work in other works, this does not include granting third-party requests for reprinting, republishing, or other types of re-use. The IEEE Intellectual Property Rights office must handle all such third-party requests.
- Authors whose work was performed under a grant from a government funding agency are free to fulfill any deposit mandates from that funding agency.

### AUTHOR ONLINE USE

- **Personal Servers.** Authors and/or their employers shall have the right to post the accepted version of IEEE-copyrighted articles on their own personal servers or the servers of their institutions or employers without permission from IEEE, provided that the posted version includes a prominently displayed IEEE copyright notice and, when published, a full citation to the original IEEE publication, including a link to the article abstract in IEEE Xplore. Authors shall not post the final, published versions of their papers.
- **Classroom or Internal Training Use.** An author is expressly permitted to post any portion of the accepted version of his/her own IEEE-copyrighted articles on the author's personal web site or the servers of the author's institution or company in connection with the author's teaching, training, or work responsibilities, provided that the appropriate copyright, credit, and reuse notices appear prominently with the posted material. Examples of permitted uses are lecture materials, course packs, e-reserves, conference presentations, or in-house training courses.
- **Electronic Preprints.** Before submitting an article to an IEEE publication, authors frequently post their manuscripts to their own web site, their employer's site, or to another server that invites constructive comment from colleagues. Upon submission of an article to IEEE, an author is required to transfer copyright in the article to IEEE, and the author must update any previously posted version of the article with a prominently displayed IEEE copyright notice. Upon publication of an article by the IEEE, the author must replace any previously posted electronic versions of the article with either (1) the full citation to the

IEEE work with a Digital Object Identifier (DOI) or link to the article abstract in IEEE Xplore, or (2) the accepted version only (not the IEEE-published version), including the IEEE copyright notice and full citation, with a link to the final, published article in IEEE Xplore.

**Questions about the submission of the form or manuscript must be sent to the publication's editor.**

**Please direct all questions about IEEE copyright policy to:**

**IEEE Intellectual Property Rights Office, [copyrights@ieee.org](mailto:copyrights@ieee.org), +1-732-562-3966**



IEEE

# IEEE COPYRIGHT AND CONSENT FORM

To ensure uniformity of treatment among all contributors, other forms may not be substituted for this form, nor may any wording of the form be changed. This form is intended for original material submitted to the IEEE and must accompany any such material in order to be published by the IEEE. Please read the form carefully and keep a copy for your files.

**Effect of dielectric layers on laser-fired-contact performance in a-Si/c-Si heterojunction Solar Cells**

**Ujjwal Das, Christopher Thompson, Ugochukwu Nsofor, Zeming Sun, Mool C. Gupta, Steven Hegedus**

**2018 IEEE 45th Photovoltaic Specialists Conference (PVSC)**

## COPYRIGHT TRANSFER

The undersigned hereby assigns to The Institute of Electrical and Electronics Engineers, Incorporated (the "IEEE") all rights under copyright that may exist in and to: (a) the Work, including any revised or expanded derivative works submitted to the IEEE by the undersigned based on the Work; and (b) any associated written or multimedia components or other enhancements accompanying the Work.

## GENERAL TERMS

1. The undersigned represents that he/she has the power and authority to make and execute this form.
2. The undersigned agrees to indemnify and hold harmless the IEEE from any damage or expense that may arise in the event of a breach of any of the warranties set forth above.
3. The undersigned agrees that publication with IEEE is subject to the policies and procedures of the [IEEE PSPB Operations Manual](#).
4. In the event the above work is not accepted and published by the IEEE or is withdrawn by the author(s) before acceptance by the IEEE, the foregoing copyright transfer shall be null and void. In this case, IEEE will retain a copy of the manuscript for internal administrative/record-keeping purposes.
5. For jointly authored Works, all joint authors should sign, or one of the authors should sign as authorized agent for the others.
6. The author hereby warrants that the Work and Presentation (collectively, the "Materials") are original and that he/she is the author of the Materials. To the extent the Materials incorporate text passages, figures, data or other material from the works of others, the author has obtained any necessary permissions. Where necessary, the author has obtained all third party permissions and consents to grant the license above and has provided copies of such permissions and consents to IEEE

**You have indicated that you DO wish to have video/audio recordings made of your conference presentation under terms and conditions set forth in "Consent and Release."**

## CONSENT AND RELEASE

1. In the event the author makes a presentation based upon the Work at a conference hosted or sponsored in whole or in part by the IEEE, the author, in consideration for his/her participation in the conference, hereby grants the IEEE the unlimited, worldwide, irrevocable permission to use, distribute, publish, license, exhibit, record, digitize, broadcast, reproduce and archive, in any format or medium, whether now known or hereafter developed: (a) his/her presentation and comments at the conference; (b) any written materials or multimedia files used in connection with his/her presentation; and (c) any recorded interviews of him/her (collectively, the "Presentation"). The permission granted includes the transcription and reproduction of the Presentation for inclusion in products sold or distributed by IEEE and live or recorded broadcast of the Presentation during or after the conference.
2. In connection with the permission granted in Section 1, the author hereby grants IEEE the unlimited, worldwide, irrevocable right to use his/her name, picture, likeness, voice and biographical information as part of the advertisement, distribution and sale of products incorporating the Work or Presentation, and releases IEEE from any claim based on right of privacy or publicity.

BY TYPING IN YOUR FULL NAME BELOW AND CLICKING THE SUBMIT BUTTON, YOU CERTIFY THAT SUCH ACTION CONSTITUTES YOUR ELECTRONIC SIGNATURE TO THIS FORM IN ACCORDANCE WITH UNITED STATES LAW, WHICH AUTHORIZES ELECTRONIC SIGNATURE BY AUTHENTICATED REQUEST FROM A USER OVER THE INTERNET AS A VALID SUBSTITUTE FOR A WRITTEN SIGNATURE.

Ujjwal Das

21-05-2018

Signature

Date (dd-mm-yyyy)

## Information for Authors

### AUTHOR RESPONSIBILITIES

The IEEE distributes its technical publications throughout the world and wants to ensure that the material submitted to its publications is properly available to the readership of those publications. Authors must ensure that their Work meets the requirements as stated in section 8.2.1 of the IEEE PSPB Operations Manual, including provisions covering originality, authorship, author responsibilities and author misconduct. More information on IEEE's publishing policies may be found at [http://www.ieee.org/publications\\_standards/publications/rights/authorrightsresponsibilities.html](http://www.ieee.org/publications_standards/publications/rights/authorrightsresponsibilities.html) Authors are advised especially of IEEE PSPB Operations Manual section 8.2.1.B12: "It is the responsibility of the authors, not the IEEE, to determine whether disclosure of their material requires the prior consent of other parties and, if so, to obtain it." Authors are also advised of IEEE PSPB Operations Manual section 8.1.1B: "Statements and opinions given in work published by the IEEE are the expression of the authors."

### RETAINED RIGHTS/TERMS AND CONDITIONS

- Authors/employers retain all proprietary rights in any process, procedure, or article of manufacture described in the Work.
- Authors/employers may reproduce or authorize others to reproduce the Work, material extracted verbatim from the Work, or derivative works for the author's personal use or for company use, provided that the source and the IEEE copyright notice are indicated, the copies are not used in any way that implies IEEE endorsement of a product or service of any employer, and the copies themselves are not offered for sale.
- Although authors are permitted to re-use all or portions of the Work in other works, this does not include granting third-party requests for reprinting, republishing, or other types of re-use. The IEEE Intellectual Property Rights office must handle all such third-party requests.
- Authors whose work was performed under a grant from a government funding agency are free to fulfill any deposit mandates from that funding agency.

### AUTHOR ONLINE USE

- **Personal Servers.** Authors and/or their employers shall have the right to post the accepted version of IEEE-copyrighted articles on their own personal servers or the servers of their institutions or employers without permission from IEEE, provided that the posted version includes a prominently displayed IEEE copyright notice and, when published, a full citation to the original IEEE publication, including a link to the article abstract in IEEE Xplore. Authors shall not post the final, published versions of their papers.
- **Classroom or Internal Training Use.** An author is expressly permitted to post any portion of the accepted version of his/her own IEEE-copyrighted articles on the author's personal web site or the servers of the author's institution or company in connection with the author's teaching, training, or work responsibilities, provided that the appropriate copyright, credit, and reuse notices appear prominently with the posted material. Examples of permitted uses are lecture materials, course packs, e-reserves, conference presentations, or in-house training courses.
- **Electronic Preprints.** Before submitting an article to an IEEE publication, authors frequently post their manuscripts to their own web site, their employer's site, or to another server that invites constructive comment from colleagues. Upon submission of an article to IEEE, an author is required to transfer copyright in the article to IEEE, and the author must update any previously posted version of the article with a prominently displayed IEEE copyright notice. Upon publication of an article by the IEEE, the author must replace any previously posted electronic versions of the article with either (1) the full citation to the

IEEE work with a Digital Object Identifier (DOI) or link to the article abstract in IEEE Xplore, or (2) the accepted version only (not the IEEE-published version), including the IEEE copyright notice and full citation, with a link to the final, published article in IEEE Xplore.

**Questions about the submission of the form or manuscript must be sent to the publication's editor.**

**Please direct all questions about IEEE copyright policy to:**

**IEEE Intellectual Property Rights Office, [copyrights@ieee.org](mailto:copyrights@ieee.org), +1-732-562-3966**



IEEE

# IEEE COPYRIGHT AND CONSENT FORM

To ensure uniformity of treatment among all contributors, other forms may not be substituted for this form, nor may any wording of the form be changed. This form is intended for original material submitted to the IEEE and must accompany any such material in order to be published by the IEEE. Please read the form carefully and keep a copy for your files.

**Direct Laser Isolation For Interdigitated Back Contact Heterojunction Solar Cells**  
**Zeming Sun, Ugochukwu Nsofor, Nuha Ahmed, Ujjwal K. Das, Steven Hegedus, Mool C. Gupta**  
**2018 IEEE 45th Photovoltaic Specialists Conference (PVSC)**

## COPYRIGHT TRANSFER

The undersigned hereby assigns to The Institute of Electrical and Electronics Engineers, Incorporated (the "IEEE") all rights under copyright that may exist in and to: (a) the Work, including any revised or expanded derivative works submitted to the IEEE by the undersigned based on the Work; and (b) any associated written or multimedia components or other enhancements accompanying the Work.

## GENERAL TERMS

1. The undersigned represents that he/she has the power and authority to make and execute this form.
2. The undersigned agrees to indemnify and hold harmless the IEEE from any damage or expense that may arise in the event of a breach of any of the warranties set forth above.
3. The undersigned agrees that publication with IEEE is subject to the policies and procedures of the [IEEE PSPB Operations Manual](#).
4. In the event the above work is not accepted and published by the IEEE or is withdrawn by the author(s) before acceptance by the IEEE, the foregoing copyright transfer shall be null and void. In this case, IEEE will retain a copy of the manuscript for internal administrative/record-keeping purposes.
5. For jointly authored Works, all joint authors should sign, or one of the authors should sign as authorized agent for the others.
6. The author hereby warrants that the Work and Presentation (collectively, the "Materials") are original and that he/she is the author of the Materials. To the extent the Materials incorporate text passages, figures, data or other material from the works of others, the author has obtained any necessary permissions. Where necessary, the author has obtained all third party permissions and consents to grant the license above and has provided copies of such permissions and consents to IEEE

**You have indicated that you DO wish to have video/audio recordings made of your conference presentation under terms and conditions set forth in "Consent and Release."**

## CONSENT AND RELEASE

1. In the event the author makes a presentation based upon the Work at a conference hosted or sponsored in whole or in part by the IEEE, the author, in consideration for his/her participation in the conference, hereby grants the IEEE the unlimited, worldwide, irrevocable permission to use, distribute, publish, license, exhibit, record, digitize, broadcast, reproduce and archive, in any format or medium, whether now known or hereafter developed: (a) his/her presentation and comments at the conference; (b) any written materials or multimedia files used in connection with his/her presentation; and (c) any recorded interviews of him/her (collectively, the "Presentation"). The permission granted includes the transcription and reproduction of the Presentation for inclusion in products sold or distributed by IEEE and live or recorded broadcast of the Presentation during or after the conference.
2. In connection with the permission granted in Section 1, the author hereby grants IEEE the unlimited, worldwide, irrevocable right to use his/her name, picture, likeness, voice and biographical information as part of the advertisement, distribution and sale of products incorporating the Work or Presentation, and releases IEEE from any claim based on right of privacy or publicity.

BY TYPING IN YOUR FULL NAME BELOW AND CLICKING THE SUBMIT BUTTON, YOU CERTIFY THAT SUCH ACTION CONSTITUTES YOUR ELECTRONIC SIGNATURE TO THIS FORM IN ACCORDANCE WITH UNITED STATES LAW, WHICH AUTHORIZES ELECTRONIC SIGNATURE BY AUTHENTICATED REQUEST FROM A USER OVER THE INTERNET AS A VALID SUBSTITUTE FOR A WRITTEN SIGNATURE.

Zeming Sun

22-05-2018

Signature

Date (dd-mm-yyyy)

## Information for Authors

### AUTHOR RESPONSIBILITIES

The IEEE distributes its technical publications throughout the world and wants to ensure that the material submitted to its publications is properly available to the readership of those publications. Authors must ensure that their Work meets the requirements as stated in section 8.2.1 of the IEEE PSPB Operations Manual, including provisions covering originality, authorship, author responsibilities and author misconduct. More information on IEEE's publishing policies may be found at [http://www.ieee.org/publications\\_standards/publications/rights/authorrightsresponsibilities.html](http://www.ieee.org/publications_standards/publications/rights/authorrightsresponsibilities.html) Authors are advised especially of IEEE PSPB Operations Manual section 8.2.1.B12: "It is the responsibility of the authors, not the IEEE, to determine whether disclosure of their material requires the prior consent of other parties and, if so, to obtain it." Authors are also advised of IEEE PSPB Operations Manual section 8.1.1B: "Statements and opinions given in work published by the IEEE are the expression of the authors."

### RETAINED RIGHTS/TERMS AND CONDITIONS

- Authors/employers retain all proprietary rights in any process, procedure, or article of manufacture described in the Work.
- Authors/employers may reproduce or authorize others to reproduce the Work, material extracted verbatim from the Work, or derivative works for the author's personal use or for company use, provided that the source and the IEEE copyright notice are indicated, the copies are not used in any way that implies IEEE endorsement of a product or service of any employer, and the copies themselves are not offered for sale.
- Although authors are permitted to re-use all or portions of the Work in other works, this does not include granting third-party requests for reprinting, republishing, or other types of re-use. The IEEE Intellectual Property Rights office must handle all such third-party requests.
- Authors whose work was performed under a grant from a government funding agency are free to fulfill any deposit mandates from that funding agency.

### AUTHOR ONLINE USE

- **Personal Servers.** Authors and/or their employers shall have the right to post the accepted version of IEEE-copyrighted articles on their own personal servers or the servers of their institutions or employers without permission from IEEE, provided that the posted version includes a prominently displayed IEEE copyright notice and, when published, a full citation to the original IEEE publication, including a link to the article abstract in IEEE Xplore. Authors shall not post the final, published versions of their papers.
- **Classroom or Internal Training Use.** An author is expressly permitted to post any portion of the accepted version of his/her own IEEE-copyrighted articles on the author's personal web site or the servers of the author's institution or company in connection with the author's teaching, training, or work responsibilities, provided that the appropriate copyright, credit, and reuse notices appear prominently with the posted material. Examples of permitted uses are lecture materials, course packs, e-reserves, conference presentations, or in-house training courses.
- **Electronic Preprints.** Before submitting an article to an IEEE publication, authors frequently post their manuscripts to their own web site, their employer's site, or to another server that invites constructive comment from colleagues. Upon submission of an article to IEEE, an author is required to transfer copyright in the article to IEEE, and the author must update any previously posted version of the article with a prominently displayed IEEE copyright notice. Upon publication of an article by the IEEE, the author must replace any previously posted electronic versions of the article with either (1) the full citation to the

IEEE work with a Digital Object Identifier (DOI) or link to the article abstract in IEEE Xplore, or (2) the accepted version only (not the IEEE-published version), including the IEEE copyright notice and full citation, with a link to the final, published article in IEEE Xplore.

**Questions about the submission of the form or manuscript must be sent to the publication's editor.**

**Please direct all questions about IEEE copyright policy to:**

**IEEE Intellectual Property Rights Office, [copyrights@ieee.org](mailto:copyrights@ieee.org), +1-732-562-3966**



IEEE